Design of Bearingless Machines with Exact Actuation of Multiple Airgap Harmonic Fields

By

Anvar Khamitov

A dissertation submitted in partial fulfillment of
the requirements for the degree of

Doctor of Philosophy
(Electrical and Computer Engineering)

at the
UNIVERSITY OF WISCONSIN - MADISON
2024

Date of final oral examination: 1/12/2024

The dissertation is approved by the following members of the Final Oral Committee:
Eric L. Severson, Associate Professor, Electrical and Computer Engineering
Dominic Gross, Assistant Professor, Electrical and Computer Engineering
Lei Zhou, Assistant Professor, Mechanical Engineering
David A. Rothamer, Professor, Mechanical Engineering

Acknowledgments

I would like to express my sincere gratitude to my advisor, Professor Eric L. Severson, for his unwavering support, guidance, and invaluable mentorship throughout the course of my doctoral studies. His expertise and encouragement have been instrumental in shaping my academic and research endeavors. I extend my thanks to the members of my dissertation committee, Professor Dominic Gross, Professor David A. Rothamer, and Professor Lei Zhou, for their insightful feedback, which improved the quality of this research.

Special appreciation goes to the fellow students and staff at the Wisconsin Electric Machines and Power Electronics Consortium (WEMPEC). I am grateful for the countless discussions, diverse perspectives, and shared insights that have fostered a stimulating academic environment. I would like to thank Nathan Petersen for his support with the Advanced Motor Drive Controller (AMDC), Owen Coulson for helping me build a prototype motor, Anson Chan for his support in preparing the hardware setup, lab managers Kyle Hanson and Pia Strampp for their support in the lab, and Kathy Young and other staff members for their assistance with various logistical matters. Thanks to all those who have played a part, no matter how small, in the realization of this dissertation.

To my dearest friends, your continuous support has made the academic experience immensely rewarding. This Ph.D. program not only provided academic growth but also introduced me to new friendships, and I am grateful for the shared, unforgettable moments.

Lastly, I want to express my sincere gratitude to my family members in Kazakhstan. Their unwavering belief in my abilities has served as a constant source of motivation. Their support has been the foundation on which I built my academic aspirations.

Abstract

Bearingless motors provide an attractive alternative to conventional motors with contact-type bearings because of their improved lifetime, lubricant-free operation, and elimination of significant friction losses at high speeds. These machines also offer more compact size, reduced design cost and complexity, and shorter axial length compared to conventional magnetic levitation solutions (motors with active magnetic bearings). Despite this, the use of bearingless motors has been significantly limited by issues of low power density, efficiency, force capacity, and high cost. Most bearingless motor prototypes reported in the literature have been designed for low power ratings and there are few publications with bearingless motors being tested at $\geq$ 30 kW. Bearingless motors are not achieving the high speed-power capabilities that high performance motors with contact bearings have. For example, the highest speed-power capability of a surface permanent magnet (SPM) bearingless machine found from the literature is only 30% of conventional high performance SPM machines. Furthermore, published test results show that bearingless motor prototypes struggle to meet the IE4 efficiency standard with relatively few machines having experimentally tested efficiencies of above 90%. Bearingless machines also have a significantly lower force capacity compared to machines with contact bearings and active magnetic bearings (AMBs). All of these discrepancies in performance are because the design space of bearingless machines is significantly more constrained than conventional machines due to stringent levitation performance requirements.

This dissertation proposes and investigates the hypothesis that developing and implementing design and control strategies for precise actuation of multiple airgap harmonic fields can make the design space of bearingless machines less constrained and enable consideration of potentially high performance designs. This dissertation develops analytic winding design theory to create new high performance electric machines that can independently create normal forces and torque, a new and exact model of electric machines that encompasses both normal force and torque creation, and an analysis and design framework for enhancing bearingless motor performance through the control of multiple airgap field space harmonics. When these techniques are combined, high performance bearingless machines can be designed. The results demonstrate a 40% increase in force capacity for bearingless machines when controlling four airgap field harmonics, as opposed to the typical approach of controlling two harmonics. Furthermore, these machines exhibit efficiencies nearing 97% and torque densities surpassing 22 kNm/m^3. These advancements mitigate the previously identified limitations of bearingless motors, enabling a broader range of design possibilities.

First, a comprehensive comparison of bearingless motor winding configurations is conducted and a general and analytic multiphase winding design theoretical framework is developed to support the design of high performance electric machines. This is the first work to provide a formal design approach that can be used to create multiphase stator windings that are capable of producing the specified airgap field harmonics necessary for control of both torque and suspension forces. This approach can be used to realize popular winding designs, including concentrated- and fractional-slot windings. Second, a new and exact modeling framework describing both force and torque creation on a shaft of an electric motor incorporating multiple airgap harmonic field interactions is proposed and developed. The proposed model is applicable to all motor types, relies on analytical methods, and accurately represents the fundamental physics of the machine. Earlier attempts to develop exact models for magnetic bearings and bearingless motors are shown to be special cases within the broader framework established in this dissertation. Third, using the proposed exact model, potential performance benefits of controlling multiple airgap harmonics are investigated and a design study framework is developed. The findings show a force capacity increase in bearingless motors to over 15 N/cm^2, surpassing the 9.9 N/cm^2 reported in the existing literature. Bearingless machines are shown to be capable of achieving the same force capacity as AMBs by employing the exact model developed in this dissertation to utilize more than two airgap field harmonics. Finally, a 10-phase bearingless induction machine, which can independently create four airgap harmonic fields, is constructed and used to experimentally validate the theories developed in this dissertation. Hardware measurements validate the increased force capacity and enhanced force performance under varying magnetizing field and torque conditions. These results show that the control of multiple harmonics is critical to achieving high performance bearingless machine designs.

Contents

List of Figures

List of Tables

Chapter 1

Introduction

This chapter provides research background and motivation, review of the state-of-the-art, research opportunities, research contributions, and document organization. [1]

1.1 Background and Motivation

Most electric motor systems rely on journal or ball bearings to support the motor's shaft. These bearings are often the first point of failure and represent a major reliability concern [8]. They are a source of significant friction losses at high speeds and their lubrication can interfere with the operation of the entire system [9]. Over the past decades, active magnetic bearings (AMBs) have been developed as an alternative to provide contact-free and lubricant-free support of the motor shaft, eliminating conventional bearing problems. AMBs have been successful in many applications, such as compressors for gas transmission, turboexpanders, heating, ventilation, and air conditioning (HVAC) chillers, and turbomolecular vacuum pumps [10]. However, their use has been limited by high design cost and large size. This is due to the required additional sensors, feedback control, and components for fail-safe operation. The size of AMBs reduces the overall motor power density and increases the total axial length of a shaft. This is not desirable as a motor system shaft length is typically limited to avoid issues of mechanical bending modes [11, Ch. 7].

---

[1] Portions of the material in this chapter have also been published in [4].

Bearingless motors are a potential solution to solve the shortcomings of conventional motor bearings and AMBs by integrating the functionality of one or more AMBs into an electric motor. Nearly every type of motor can be transformed into a bearingless motor by modifying the stator winding. Despite recent development efforts, their usage has been significantly limited by issues of low power density, efficiency, and high cost. Unlike conventional motors, bearingless motors must be sized for both motoring and suspension operations, and design constraints must be imposed for stable levitation. Most state-of-the-art bearingless motor design and torque/force regulation techniques are based on the model that incorporates the interaction between two airgap pole-pair/harmonic fields, which requires imposing additional constraints on force vector error due to unmodeled airgap pole-pairs/harmonics. Potential advantages of controlling multiple harmonics are not studied. These factors, in turn, narrow the design space of bearingless machines and can potentially exclude high performance designs.

1.1.1 Research Overview

This research encompasses two main thrusts, aimed at helping the research community develop more compact, efficient, precise, and lower cost bearingless motors, thereby allowing this technology to reach into application spaces where magnetic levitation has historically not been successful. This dissertation proposes and investigates the hypothesis that developing and implementing design and control strategies through an actuation of multiple airgap harmonic fields can enable creation of higher performance bearingless machines. The first thrust involves a comprehensive analysis and comparison of bearingless motor winding topologies and development of a universal analytic winding design theory. The second thrust involves the proposal and development of a unified electric machine analysis framework that encompasses both force and torque creation from multiple airgap harmonic field interactions, investigations into precise force/torque regulation and enhancement using the proposed model, and the reformulation of a bearingless machine design study to explore potentially new designs. Results and analysis are presented that show the bearingless motors to be a promising solution for several potential applications. This work re-envisions the model of the electric machines to encompass both the creation of magnetic shear and normal pressure on the surface of the shaft and proposes a precise regulation of these vectors through an actuation of multiple motor airgap magnetic field harmonics.

1.2 Review of the State-of-the-Art

This section presents state-of-the-art on bearingless machines. First, theory of operation of bearingless machines is presented, covering bearingless solutions and basic operating principles. Second, design aspects considering bearingless motor types, windings, and design studies are reviewed. Finally, bearingless motor control aspects on force and torque regulation are reviewed. Following the state-of-the-art review, the following section concludes with identifying the key research opportunities.

Similar to conventional motors, most potential applications for bearingless motors desire high power and torque density, high efficiency, low torque ripple, and low cost. In addition, bearingless motors must have high force density and high force per ampere characteristics to minimize motor size and losses, and low force vector error for stable levitation. Due to these levitation performance requirements, the bearingless motor design is significantly more constrained than conventional (non-bearingless) motors. Since additional power electronic components are required for levitation, it is also important to consider bearingless drive performance, which includes the required DC-bus voltage, power factor, and voltage and current ratings of the switches.

1.2.1 Theory of Operation of Bearingless Motors

This subsection presents possible solutions using bearingless motors and AMBs, and describe basic operating principles.

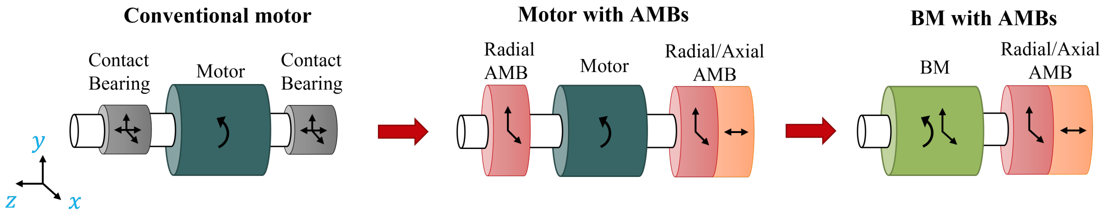

Figure 1.1: Motor bearing solutions (from left to right): motor with contact bearings, motor with AMBs, bearingless motor (BM) with AMBs.

1.2.1.1 Bearingless Motor Topologies

For full levitation of a motor's shaft, all six degrees of freedom (DOFs) must be controlled. These DOFs include translation along each axis (x, y, z) and tilting/rotation about these axes. In addition to torque (rotation about z), bearingless motors are able to create either radial or axial forces to support three DOFs and replace one or more motor bearings. AMBs, additional bearingless motors, or other bearing technology can be used to support the remaining DOFs. Figure 1.1 shows possible magnetic levitation solutions using AMBs and a bearingless motor to eliminate contact bearings and fully levitate the motor shaft. As a consequence, very high speeds [12] and encapsulated (or canned) systems with an isolated rotor can be realized. Encapsulated rotors enable a hermetic seal between the stator and rotor and have been shown to be particularly advantageous when the highest degrees of purity are required [13].

When the motor diameter to length ratio is large enough, bearingless motors can be designed as bearingless slice motors. In these motors, the radial x and y forces are controlled actively, while the remaining three DOFs are passively stabilized by the motor's magnet reluctance forces as shown in Fig. 1.2 (movement along z axis and tilting about x and y axes). This results in a simple and highly integrated system, eliminating the need for radial and axial AMBs in Fig. 1.1. Example high performance bearingless slice motors for low power applications such as bioreactor mixing and high purity applications are presented in [1, 14–16]. Studies [17, 18] reviewed bearingless slice motor concepts without permanent magnets in the rotor that have the advantage of reduced motor cost.

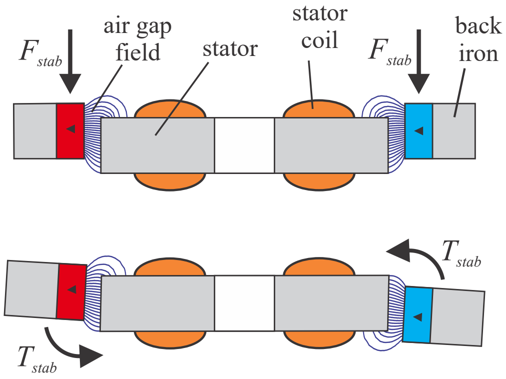

Figure 1.2: A picture (motor side view) explaining passively stabilized DOFs (movement along axial length and tilting) in a bearingless motor with an outer rotor [1], [2].

1.2.1.2 Basic Operating Principles

Bearingless motors are electromechanical devices that can simultaneously operate as a conventional motor and a magnetic bearing [19]. Similar to conventional motors, the torque in bearingless motors is created from the interaction of stator p pole pair and rotor p pole pair magnetic fields. To create suspension forces, the stator needs to additionally create $p_s = p \pm 1$ pole pair magnetic field component that interacts with a p pole pair field in the airgap and creates force. In some motors such as homopolar and consequent pole motors, p_s is equal to 1 [3].

Figure 1.3a demonstrates how force is created on a rotor of an example surface permanent magnet motor. The rotor has $p = 2$ pole pair field due to magnets and the stator winding creates $p_s = 1$ pole pair field. The distribution of these pole pair fields along the circumferential angle α is shown in Fig. 1.3b. From their interaction, the total airgap flux strengthens on the right side ($\alpha = 0$ deg.) and weakens on the left side ($\alpha = 180$ deg.) of the rotor, creating non-zero force.

1.2.2 Design Aspects of Bearingless Motors

This subsection reviews performance capabilities of bearingless machines from the design perspective. Bearingless motor types and their performance, winding topologies, and de-

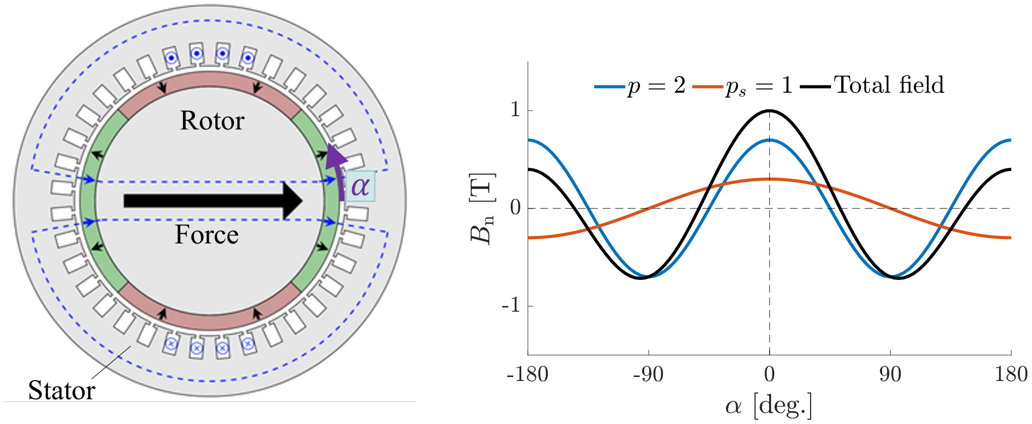

(a) (b)

Figure 1.3: Suspension force creation on an example bearingless motor with $p = 2$ and $p_s = 1$ pole pairs: (a) motor cross-section and (b) airgap field distribution.

sign studies are presented. According to [3], the number of papers on bearingless motors with experiment results has been growing quadratically since 1988, as shown in Fig. 1.5. This shows an increased interest in this technology. Advancements in power electronic semiconductor devices, magnetic materials, and computationally efficient tools have allowed the development of various bearingless motor types and winding configurations.

1.2.2.1 Bearingless Motor Types and Their Performance

Bearingless versions of nearly every motor type can be found in the literature, as reviewed in [3, 19–21]. This includes permanent magnet (PM), surface permanent magnet (SPM) and interior permanent magnet (IPM); induction motor (IM); consequent pole; synchronous reluctance; switched reluctance; AC homopolar; flux switching motor topologies. Figure 1.5 presents a summary of published bearingless motor test data of efficiency vs. output power for different motor types obtained from [3] and IE4 standard (super premium efficiency standard) curve plotted on top of these data. This plot shows that the highest reported efficiency is above 95.9% tested at 1.5 kW power for an SPM motor. There are few SPM and IPM prototype designs that satisfy IE4 efficiency requirement for powers up to approximately 2 kW. No designs have been reported to satisfy IE4 requirement for higher powers. Furthermore,

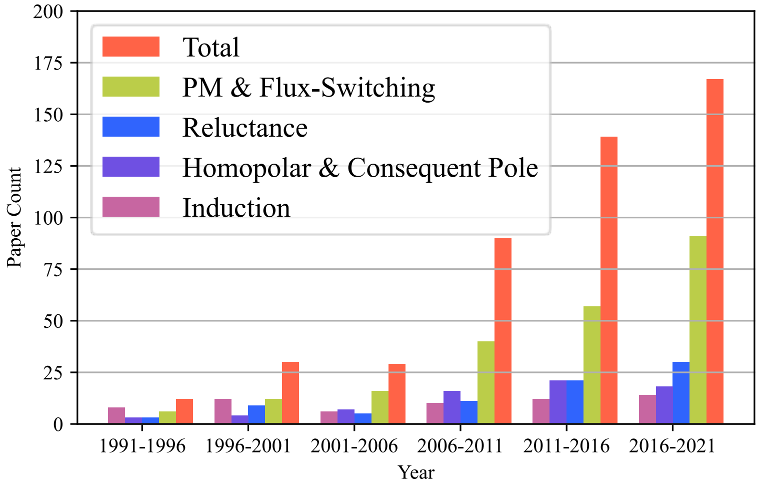

Figure 1.4: Number of papers with experimental results published by year [3].

bearingless motors are not achieving high speed-power capabilities (estimated in RPM$\sqrt{\text{kW}}$) that high performance motors with contact bearings have [3]. For example, the highest speed-power capability of a SPM bearingless machine found from the literature is only 30% of high performance SPM conventional machines (2.5×10^5 RPM$\sqrt{\text{kW}}$ vs. 8×10^5 RPM$\sqrt{\text{kW}}$). Based on these results, it can be concluded that bearingless motor technology does not yet compare well with conventional motor technology for industrial applications.

Based on the literature survey conducted in [3], bearingless PM (SPM and IPM motors) [22–26] and induction motors [27–29] are the most commonly investigated motor types for significant power levels. According to these studies, bearingless PM motors have the advantage of high power and efficiency compared to other topologies. The limiting factor for increasing the force density in bearingless SPM motors is having a comparatively large effective airgap, which is due to the magnet thickness and the retaining sleeve that protects the rotor magnets from breaking due to tension stress [30].

Both bearingless motors and AMBs are known to have a lower force capacity (specific load capacity) [31] than other bearing types. Specific load capacity is calculated by dividing the rated force (maximum force that can be created at any angle) by the projected rotor area (length × diameter) [32]. Typically, AMBs have a specific load capacity of 30-40 N/cm^2,

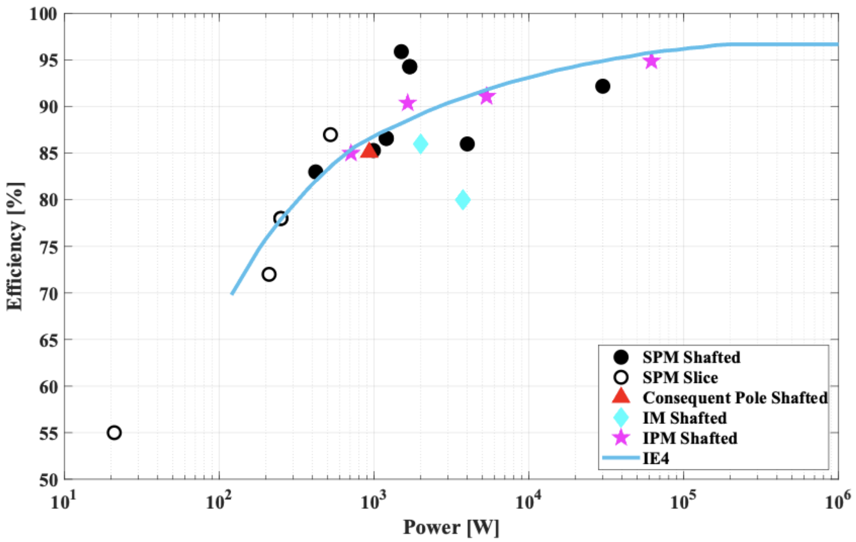

Figure 1.5: Summary of published bearingless motor test data of efficiency vs. output power for different motor types (the test data are from [3]) and IE4 standard (super premium efficiency standard).

with cobalt-alloys reaching up to 65 N/cm^2 [31,33–35]. Bearingless motors are often assumed to have a significantly lower load capacity of approximately 9 N/cm^2 [32]. This might be due to the fact that AMBs with a high number of poles have more granular control over the suspension force. Compared to other motors, bearingless IPM motors can offer advantages of high force capacity due to a small airgap as the magnets are buried into the rotor iron. Study [36] reported that 9.9 N/cm^2 of radial force density was achieved from static test results.

There are several bearingless motor prototypes found in the literature such as homopolar, consequent pole (one type of PM motor), and switched reluctance motors. AC homopolar and consequent pole motors have the advantage of suspension force creation independent of the rotor's angular position, allowing for stable levitation without the need for angular position sensing [3]. Switched reluctance bearingless motors have the advantage of reduced cost as no permanent magnets are used [17, 18].

1.2.2.2 Bearingless Motor Windings

Bearingless motor winding must create both p and p_s pole pair fields to create both torque and suspension forces, as discussed in Section 1.2.1.2. Historically, this was achieved using two separate winding sets [20]. Since the suspension winding must be dimensioned for a worst-case force requirement, the suspension winding typically occupies an order of magnitude more slot space than required during rated operation. Under normal operating conditions with a centered rotor position, minimal suspension currents are required to create suspension forces, leaving most of the slot space unused [3]. This inefficient use of slot space pushes the machine design towards larger slots which decreases the motor system power density, increases copper and iron losses, and increases leakage inductance [13, 37, 38]. Furthermore, installing two separate windings is challenging and increases the motor system cost and complexity [39, 40].

Recently, several combined winding structures have been developed, where each coil carries both torque and force producing currents, having potential to solve the aforementioned problems [41, 42]. Under rated operating conditions, when minimal force is required, the motor can use most of the slot space for torque production (or vice versa, in case of a high suspension force event, like a compressor surge scenario). Several combined winding configurations have been found in literature, which can be categorized as "multiphase" [43–46], "dual-purpose no-voltage (DPNV)" [47–49], "multi-sector" [50], and "middle-point current injection" [40] windings. Of these winding types, multiphase and DPNV winding topologies are most promising for high performance control because they completely decouple motor operation from suspension operation. Study [51] proposed a generalized winding design procedure for DPNV combined windings. Study [42] provides a list of multiphase combined winding configurations and determines whether force and torque decoupling is possible. However, the results are limited to concentrated windings with one coil per phase, and no design procedure was provided to design an MP winding for an arbitrary number of slots, poles, and phases.

Numerous publications have documented the benefits of combined windings over separated windings [13, 37, 38, 52]. For example, [37] compares these windings with the same motor topology and concludes that the combined winding has higher electromagnetic utilization, lower copper losses by approximately 36%, better dynamic performance, and reduced manufacturing effort. Analogous results have been reported in [52], which compares separate and combined windings for bearingless centrifugal pumps in terms of copper losses, power electronics losses, and maximum achievable pump pressure. The results show that a realistic reduction of approximately 30-40% in copper losses can be achieved using combined windings, while the power electronic losses and maximum achievable pressure levels are comparable in both windings for the given application.

1.2.2.3 Bearingless Motor Design Studies

Combined windings are a promising recent advancement to develop high performance bearingless motors. Studies [53–55] and [29] used optimization tools for designing bearingless PM motors and induction motors using combined windings. They have reported that efficiencies of approximately 95-97% can be achieved. Study [54] stated that an optimized bearingless motor is able to support the rotor weight with only 2.5% of the rated armature current.

According to [3], using combined windings can increase the motor torque density by approximately 40% than when using separate windings. By assuming that force vector can be regulated precisely and removing force ripple constraint (analogous to torque ripple constraint) in a bearingless motor design study, [3] showed that 30% more increase in torque density can be obtained. This performance improvement is demonstrated in Fig. 4.2b for PM and IM bearingless machines [3].

Based on the results from the literature, bearingless motor design is significantly more constrained than conventional motor design due to stringent levitation performance requirements. These requirements are mainly due to a simplified force regulation model that typically ignores the effects of airgap field harmonics, saturation, or armature reaction. Having

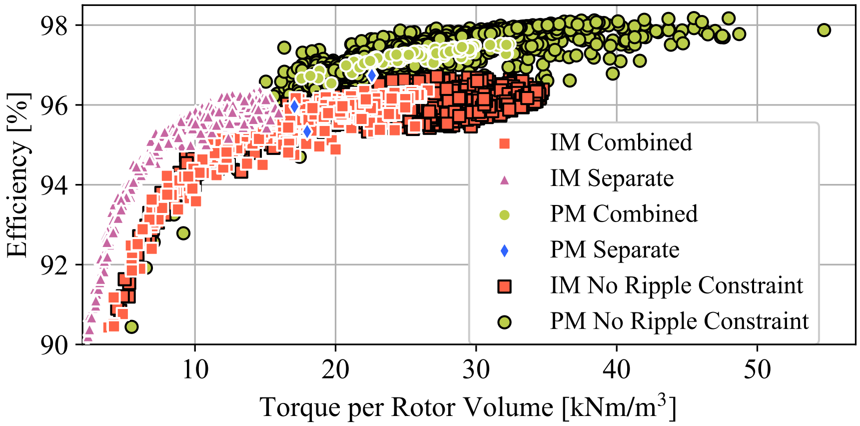

Figure 1.6: Efficiency vs. torque density plot for 100 kW, 30000 RPM bearingless motor designs obtained from the optimization in [3]. Each point represents a single design. Cases with combined vs. separate windings, and with and without force ripple constraint are compared.

these constraints restricts the design space and can exclude potential high performance bearingless motor designs from consideration.

1.2.3 Modeling and Control Aspects of Bearingless Motors

The accurate modeling of torque and force generation in bearingless machines is important for the development of design techniques and control strategies. The level of detail in the modeling process enables a thorough studying of the underlying physics, influencing the precision of torque and force vector regulation. Additionally, the modeling approach facilitates the exploration of ways for enhancing performance.

The minimization of force vector errors is a critical consideration for achieving precise force vector regulation in bearingless machines. To address this, two primary approaches can be considered: 1) designing a bearingless machine that maintains force vector errors within specified limits (though this imposes constraints on available designs), or 2) enhancing force regulation to flow phase currents in a manner that create desired force vector. In this context, force regulation, or force actuation, pertains to the translation of a desired force vector into commands for the phase currents of bearingless machines, as illustrated in Fig. 4.1d.

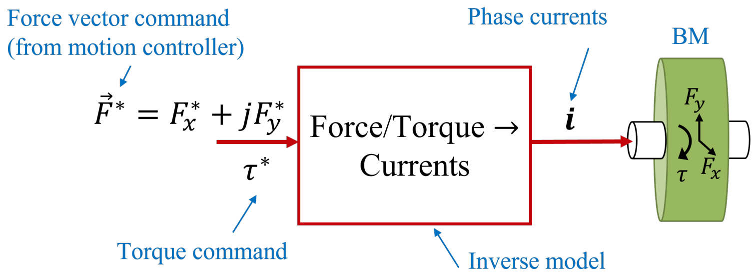

Figure 1.7: Bearingless machine force/torque regulation.

Given that the input to a bearingless motor plant is currents and the output is the force vector/torque, the red block is denoted as an inverse model of the plant. This subsection reviews force modeling and regulation efforts for high performance bearingless machines. Force vector error metrics are defined, force regulation methods found in the literature are presented, and their limitations are identified.

1.2.3.1 Force Vector Error

In a bearingless motor, it is important that the proper currents flow through the motor coils to create the desired suspension force vector with $\vec{F} = \vec{F}^*$ (Fig. 4.1d). However, due to space harmonic fields present in the motor airgap, armature reaction, sensor misalignment, etc., the force vector error may occur, deteriorating bearingless motor performance [56]. The force vector error in literature is typically characterized by two metrics [57] and demonstrated in Fig. 1.8, where the desired force $\vec{F}^*$ is along x-axis, while the actual force $\vec{F}$ can have both F_x and F_y components at any rotor angular position:

1. *Force error magnitude* E_m shows the maximum deviation in magnitude from the average force magnitude:

$$E_m = \frac{F_{\max} - F_x}{F_x} \tag{1.1}$$

2. *Force angle error* E_a shows the maximum deviation from the desired force angle (de-

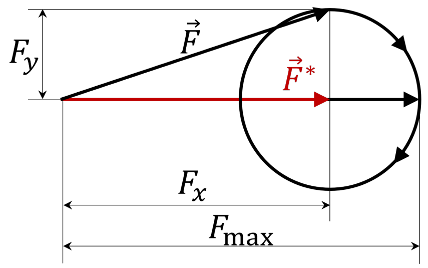

Figure 1.8: Illustration of force magnitude and angle error.

sired angle is zero in Fig. 1.8):

$$E_a = \tan^{-1}\left(\frac{F_y}{F_x}\right) \tag{1.2}$$

Bearingless motor studies suggest to keep the maximum force vector error below a certain value to avoid suspension force variations in the rotor. Study [19] reported large force angle error ($> 17°$) can cause instability in suspension regulation and [58] suggested to keep force angle error below $< 5°$.

The force regulation approaches are now reviewed.

1.2.3.2 Standard *dq*-*xy* Force Regulation

Standard bearingless motor control is based on the *dq* control theory in conventional motors [19, 42, 59]. In a bearingless motor, the motor and suspension operation can be controlled in two rotating frames. In addition to i_d and i_q current components in a *dq* frame that are used to control the magnetizing field and torque, the terminal currents responsible for force creation can be transformed into i_x and i_y current components using Generalized Clarke Transformation [60] to control F_x and F_y suspension forces. This is referred to as a "dual field oriented control" [42] and is used to implement torque and suspension force regulation independently for high performance operation. Denoting suspension and torque current space vectors as $\vec{i}_s$ and $\vec{i}_t$, force vector $\vec{F} = F_x + jF_y$ and torque vector $\vec{T} = T_d + j\tau$ (T_d is a flux weakening component) can be expressed as:

$$\vec{F} = \bar{k}_f \vec{i}_s, \quad \vec{T} = \bar{k}_t \vec{i}_t \tag{1.3}$$

where $\bar{k}_f$ and $\bar{k}_t$ are force per ampere and torque per ampere parameters. Using these equations, desired current space vectors can be found as

$$\vec{i}_s = \frac{\vec{F}}{\bar{k}_f}, \quad \vec{i}_t = \frac{\vec{T}}{\bar{k}_t} \tag{1.4}$$

and transformed back to the phase currents.

While being relatively straightforward to implement, this standard bearingless motor control method is based on the assumption of perfectly sinusoidal airgap fields and linear force/torque-current model. The unmodeled magnetic field harmonics, armature reaction, and nonlinearities are causes for large force vector error, making stable magnetic levitation infeasible [19]. The forces due to harmonics in [56] are referred to as "parasitic" forces as they create a variation in force vector angle over a complete rotor revolution. This can be solved by imposing the maximum force vector error limits as constraints in a bearingless motor [55, 61]. According to [56], decreased force vector error can be achieved by selecting radially magnetized magnets rather than parallel magnetized magnets as they have lower harmonic content. However, all of these methods impose a constraint on the bearingless machines that narrows the design space and potential high performance designs can be excluded.

1.2.3.3 $\boldsymbol{T_m/K_m}$ Matrix Based Force Regulation

Force vector error can also be minimized by further improving the force regulation. Studies [44, 62] present an approach where the required phase currents are determined based on a more accurate linear matrix model between force/torque and phase currents that takes into account the effects of higher order field harmonics. Given the phase currents $\boldsymbol{i}$ =

$\begin{bmatrix} i_1 & i_2 & ... & i_m \end{bmatrix}^T$ (m phases), the forces and torque $\boldsymbol{F} = \begin{bmatrix} F_x & F_y & \tau \end{bmatrix}^T$ are modeled to have a linear relationship with $\boldsymbol{i}$:

$$\boldsymbol{F} = \boldsymbol{T_m i} \tag{1.5}$$

where $\boldsymbol{T_m}$ is a $3 \times m$ matrix with every entry that depends on the rotor angular position (assuming centered rotor position). Force actuation using this model can be achieved by finding the pseudoinverse $\boldsymbol{K_m}$ of a $\boldsymbol{T_m}$ matrix:

$$\boldsymbol{i} = \boldsymbol{K_m F} \tag{1.6}$$

The resulting phase currents can have non-sinusoidal waveforms to compensate for the effects of harmonic fields on the force vector. This method improves force vector regulation, but the implementation in a controller requires the use of lookup tables. For accurate actuation performance, these lookup tables have to be formed using experimental static test data at many rotor angular positions and phase current values, requiring more memory and computational demands [6].

1.2.3.4 Standard *dq*-*xy* Force Regulation + Armature Reaction Compensation

A number of studies presented control efforts on improving bearingless motor performance by compensating the effects of the armature reaction field [19, 24, 25, 63]. Due to this reaction, torque winding fields affect bearingless motor force creation by changing the force vector magnitude and direction. Such change in force vector orientation is quantified as an “inclination angle” that depends on the motor torque [25, 63]. Study [63] reported that the inclination angle was approximately 3.5° for their example motor when fully loaded. This study stated that the impact of the motor operation on the suspension operation can be compensated by the knowledge of *dq* currents and stable suspension operation can be achieved. Studies [19, 24] presented control architecture that compensates the effects of the armature reaction field in IPM motors.

An expression for the suspension forces considering armature reaction is given by

$$\vec{F} = \bar{k}_f \vec{i}_s + \bar{k}_{ft} \vec{i}_s \vec{i}_t^* \tag{1.7}$$

where $\bar{k}_{ft}$ is a parameter that represents the impact of torque current on suspension operation [64]. Using this equation, desired suspension current space vector can be found:

$$\vec{i}_s = \frac{\vec{F}}{\bar{k}_f + \bar{k}_{ft} \vec{i}_t^*} \tag{1.8}$$

which shows the dependence of suspension operation on the motor torque.

1.2.3.5 Exact Force Vector Regulation

There are currently only two studies [65] and [6] that developed exact force vector regulation techniques.

Study [65] developed and implemented an exact force vector regulator for a 3-pole magnetic bearing. Both quadratic and linear dependencies on the phase currents were considered in a force vector model:

$$\vec{F} = k_1 \mathrm{SV}(\boldsymbol{i} \circ \boldsymbol{i}) + k_2 \mathrm{SV}(\boldsymbol{i}) \tag{1.9}$$

where k_1 and k_2 are constants, SV is a space vector operator, and $\boldsymbol{i} \circ \boldsymbol{i} = \begin{bmatrix} i_1^2 & i_2^2 & ...i_m^2 \end{bmatrix}^T$ is the Hadamard product. Study [65] proposed an analytic framework to find the desired coil currents using (4.33) (equivalent to solving a depressed quartic polynomial equation) and graphic techniques to study the solution space, and experimentally demonstrated the performance improvement using the proposed exact force vector regulator compared to the conventional force regulation approaches. With a 80 N force command applied to the rotor, [65] showed using experiment results that the force error magnitude and force angle error reduced by approximately 21% and 9° compared to the conventional linear regulation approach. However, this study is limited to AMBs (no torque creation) and the phase-to-phase interactions were not considered in the model.

There is another study [6,17] that developed an exact force vector regulator for bearingless machines that considered the effects of both harmonics and nonlinear force/torque-current relationship (which includes armature reaction field). This study modified the model in (1.5) to include quadratic dependence on the phase currents:

$$\boldsymbol{F} = \boldsymbol{T_Q}(\boldsymbol{i} \circ \boldsymbol{i}) + \boldsymbol{T_L}\boldsymbol{i} + \boldsymbol{T_C} \tag{1.10}$$

where $\boldsymbol{T_Q}$ and $\boldsymbol{T_L}$ are the matrices that represent quadratic and linear dependence on the phase currents, and $\boldsymbol{T_C}$ matrix represents cogging forces/torque (no dependence on the currents). Study [6] used finite-element analysis (FEA) to obtained these matrices for an example flux-switching motor.

Solving for the phase currents in this case is generally complicated and infinitely many solutions for phase currents are possible. Therefore, the desired currents in [6] are found numerically for each force/torque command and rotor angular position by solving a nonlinear optimization problem with an objective to minimize the total Ohmic losses:

$$\begin{aligned} \underset{\boldsymbol{i}}{\text{minimize}} \quad & \boldsymbol{i}^{\boldsymbol{T}}\boldsymbol{R}\boldsymbol{i} \\ \text{subject to} \quad & \boldsymbol{F} - \boldsymbol{T_Q}(\boldsymbol{i} \circ \boldsymbol{i}) - \boldsymbol{T_L}\boldsymbol{i} - \boldsymbol{T_C} = 0 \\ & \sum_{k=1}^{m} i_k = 0 \end{aligned} \tag{1.11}$$

which is known as QCQP in optimization (quadratically constrained quadratic programming) and has to be solved numerically. The optimization has to be solved for each rotor angular position and for different force/torque commands. Although this method can eliminate the force vector error, it requires additional memory and computational demands for the digital control system, resulting in m 4D lookup tables for each phase current:

$$\boldsymbol{i} = \boldsymbol{f}(\theta, F_x, F_y, \tau) \tag{1.12}$$

To reduce required memory and computation, [6] proposed an approximate solution method, which uses the results of an exact solution to perform a second order interpolation between the phase currents and the force/torque vector for each rotor angular position. This method was shown to improve force vector regulation accuracy compared to a linear $\boldsymbol{T_m}/\boldsymbol{K_m}$ matrix method described in Section 1.2.3.3 by approximately 50% [17] in force magnitude. The difference between these two regulation approaches becomes even more distinct when non-zero torque is commanded because the regulation approach in Section 1.2.3.3 does not model quadratic current dependence/armature reaction.

Although the proposed method was shown to improve force vector regulation accuracy, the model ignores the forces/torque resulting from phase-to-phase interactions and an approximate solution was implemented that causes non-zero force vector error. These assumptions limit the use of the proposed force regulation method to a specific motor topology (flux-switching motor).

Furthermore, the force regulation is completely based on the numerical techniques and the nature of the forces resulting from airgap harmonic effects and force/torque-current relationship considering these harmonics has not been investigated analytically. Because of purely numerical model, the implementation of the exact force vector regulator requires the use of multi-dimensional lookup tables, which can significantly increase computation time and require large memory as opposed to force regulation techniques based on analytic models.

1.2.4 Research Opportunities

Based on the state-of-the art review in this chapter, the following key research opportunities are identified:

1. **Opportunity to develop generalized analytic winding design theory to create new high performance bearingless machines that can operate without cross-coupling between motor and suspension operation.** Developing winding design theory makes it possible to realize popular winding designs with any number of slots, poles, and phases.

2. **Opportunity to develop a complete and unified analytic model to accurately describe torque and force creation in electric machines considering multiple magnetic field harmonics in the airgap.** This modeling framework is important to analytically understand the physics behind force and torque creation and their relation to magnetic field harmonics (sources of force vector error, possible ways to increase force density).

3. **Opportunity to develop exact force vector regulation techniques to expand the bearingless machine design space and explore high performance bearingless machines (power density, efficiency, cost, force density).** This can help exploring bearingless motor designs that have performance close to conventional machines and generate more interest in bearingless motor technology.

4. **Opportunity to enhance performance in bearingless machines through the control of multiple airgap harmonic fields.** Similar to torque enhancement through harmonic injection in standard motors, there is an opportunity to explore potential benefits of injecting additional harmonic fields for torque and force enhancement in bearingless machines.

1.3 Research Contributions

The core research contributions of this dissertation are:

1. Demonstration that all bearingless machine combined windings found in the literature are equivalent in terms of motor and suspension operating theory, but differ in power electronics implementation (Chapter 2).
2. Comprehensive comparison of the multiphase and DPNV combined winding categories and identification of machine and application characteristics that determine which combined winding is most advantageous (Chapter 2).
3. Development of a winding design theory that can be used to analyze and create new multiphase combined winding designs for bearingless machines (Chapter 3).
4. Proposal of a complete and unified model of torque and suspension force creation in electric machines from the perspective current sequences and airgap magnetic field space harmonics (Chapter 4).
5. Identification of key factors that have historically resulted in AMBs having higher force capacity than bearingless motors and proposal of a strategy for achieving comparable force capacity in bearingless machines via the control of multiple airgap harmonic fields (Chapters 4 and 5).
6. Enhancement in force performance fully decoupled from variations in magnetizing fields and torque through the implementation of multiple airgap harmonic field control (Chapters 4 and 6).
7. Design and experimental validation of a 10-phase bearingless induction machine with enhanced force creation capabilities (Chapters 6 and 7).

1.3.1 List of Publications

List of accepted publications:

1. A. Khamitov and E. L. Severson, "Design of Multi-Phase Combined Windings for Bearingless Machines," *IEEE Transactions on Industry Applications*, 2023.
2. F. Nishanth, A. Khamitov, and E. L. Severson,"Design of Multiphase Motor Windings for Control of Multiple Airgap Fields," *IEEE Transactions on Industry Applications*, 2023.
3. A. Khamitov, W. Gruber, G. Bramerdorfer, and E. L. Severson, "Comparison of combined winding strategies for radial non-salient bearingless machines," *IEEE Transactions on Industry Applications*, 2021.
4. N. Petersen, A. Khamitov, T. Slininger, and E. L. Severson, "Machine design and precision current regulation for the parallel dpnv bearingless motor winding," *IEEE Transactions on Industry Applications*, 2021.
5. A. Khamitov, N. P. Petersen, and E. L. Severson, "Combined Windings for Bearingless Motors—An Overview," *2023 IEEE Energy Conversion Congress and Exposition (ECCE)*, 2023.
6. A. Khamitov and E. L. Severson, "Analysis of Force Capacity in Magnetic Bearings and Bearingless Motors from the Perspective of Airgap Space Harmonic Fields," *18th International Symposium on Magnetic Bearings (ISMB)*, 2023.
7. A. Khamitov and E. L. Severson, "Exact Torque and Force Model of Bearingless Electric Machines," *2022 IEEE Energy Conversion Congress and Exposition (ECCE)*, 2022.

List of planned submissions:

1. A. Khamitov and E. L. Severson, "Exact Torque and Force Vector Modeling Framework for Bearingless Electric Motors," *IEEE Transactions on Industry Applications*, 2024.

2. A. Khamitov and E. L. Severson, “Design and Control of a 10-Phase Bearingless Induction Machine,” *IEEE Transactions on Energy Conversion*, 2024.

1.4 Document Organization

This document is organized as follows:

- Chapter 2 makes a comprehensive comparison between combined winding topologies for bearingless machines. State-of-the-art review on combined winding topologies is conducted, and high performance multiphase and DPNV combined winding topologies are compared with respect to modeling, regulation architecture, and drive performance. The results are experimentally validated.

- Chapter 3 develops the fundamental torque and force model for machines employing multiphase combined windings and uses this model to establish a winding analysis framework, machine design requirements, and a winding design technique. Experimental validation is provided.

- Chapter 4 develops a generalized analysis framework to relate sequence currents to the airgap harmonic fields and forces created in a bearingless machine, and uses the developed framework to investigate potential performance improvement in force vector regulation and force enhancement.

- Chapter 5 explains force capacity in AMBs from the perspective of multiple airgap harmonic fields, explains torque-force capability in bearingless machines, and demonstrates enhancement in force capacity by controlling additional harmonics.

- Chapter 6 develops a framework for an optimization design study of a 10-phase bearingless induction motor that can independently control four airgap harmonic fields to enhance motor performance. A design is selected for prototyping and simulation results are presented.

- Chapter 7 presents experimental validation of the theories and performance improvement strategies developed in prior chapters using a prototyped 10-phase bearingless induction machine. Hardware measurements validate multiharmonic combined winding design, the exact torque and force model, and performance improvement in bearingless machines. An increase in force capacity with flux-weakening and an enhanced force performance under varying magnetizing field and torque are demonstrated.
- Chapter 8 presents conclusions and potential future work.

Chapter 2

Comparison of Combined Winding Strategies for Bearingless Machines

2.1 Introduction

Recently, several combined winding structures have been developed for bearingless machines, where each coil carries both torque and force producing currents [1]. Numerous publications have documented the benefits of combined windings over separated windings. Although a number of combined winding structures have been developed, the literature lacks detailed investigations into why a bearingless machine designer may choose one combined winding topology over another. While the design and operation of combined windings is known in the research literature, existing publications treat each winding as a unique type, using distinct language and nomenclature. This chapter addresses these issues by investigating popular combined winding designs found in literature and makes a comprehensive comparison of two combined windings, the multiphase and DPNV, that are most promising for high performance control because they completely decouple motor actuation (torque and field weakening) from suspension actuation (x and y rotor forces) through the generalized Clarke transformation.

---

[1] Portions of the material in this chapter have also been published in [4].

This chapter concludes that all combined winding "types" are actually the same fundamental multiphase winding, but connected to the drive electronics in different configurations. Operating principles of multiphase and DPNV winding topologies are developed and analyzed to quantify similarities and differences. It is shown that machines with an even number of phases can have their stator coils connected in a manner that realizes either topology, resulting in identical coil currents. However, the two topologies can require significantly different VA rating and loading of the bearingless drive. To facilitate a clear presentation, the analysis is conducted for non-salient motors, but the approach taken can be used in future efforts to extend the analysis to salient motors.

The fundamental operating principles and modeling approach established in this chapter will be useful when developing a multiphase combined winding design technique in Chapter 3 and an exact bearingless motor model in Chapter 4.

2.2 Combined Windings for Bearingless Motors

This section reviews the various types of combined windings for radial bearingless machines and explains the two winding types that are investigated in this chapter. An example bearingless motor (Fig. 2.3) is introduced that can be configured as either winding type.

2.2.1 Combined Winding Drive Categories

The bearingless machine requires p pole pairs on the rotor and stator winding to create torque, and $p_s = p \pm 1$ pole pairs on the stator winding to create suspension forces. This implies that both separate and combined winding must be intentionally designed to be capable of creating magnetic field harmonics at p and p_s.

Combined windings for torque and radial force generation can be grouped into the following four distinct categories:

1. Multiphase winding [1, 2, 13–16, 39, 41–46, 66–74].

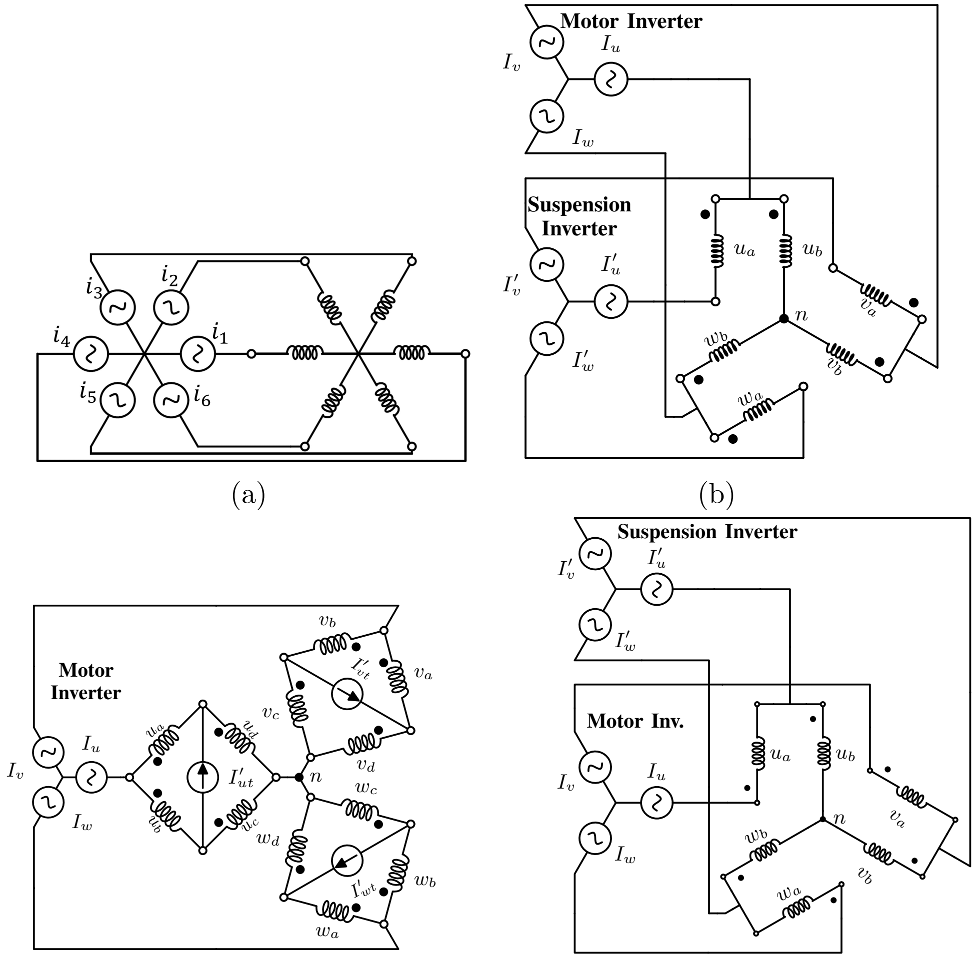

(a) (b)

(c) (d)

Figure 2.1: Bearingless motor combined winding configurations (a) multiphase, (b) parallel DPNV, (c) bridge DPNV, and (d) MCI.

2. Parallel and bridge dual purpose no voltage (DPNV) combined windings [47–49, 51, 75, 76].
3. Middle-point current injection (MCI) combined winding [38, 40].
4. Multi-sector winding [50, 77–81].

Drive configurations for these combined winding topologies are presented in Fig. 2.1.

2.2.1.1 Multiphase Combined Winding

The research community classifies the case where each winding phase terminal is connected to one phase of the drive as a multiphase winding, shown in Fig. 2.1a for $m = 6$ drive connections. It is well-known that multiphase machines can independently create multiple magnetic field space harmonics/pole-pairs in the airgap [82]. Bearingless machines use this capability to create torque p and suspension p_s pole-pair fields. Multiphase combined windings must have $m > 3$ distinct drive connections (typically, $m = 6$) to create p and p_s fields. Each phase provides both torque and suspension currents. Depending on the number of drive connections, multiple star connections can be used to reduce the number of required current measurements.

Studies [42,67,83,84] provide detailed information about the multiphase combined winding design and operation. Study [84] proposes a generalized multiphase combined winding design method that is applicable to any number of phases. Reference [42] demonstrates that the multiphase currents can be independently controlled to create torque and suspension forces in their space vector frames using the Generalized Clarke Transformation (GCT) [85].

2.2.1.2 Parallel DPNV Combined Winding

The parallel DPNV winding drive consists of two sets of inverters connected to the motor coils, as shown in Fig. 2.1b. The drive terminals are connected to the coil groups ($u_a,\ u_b, ...$) such that the suspension inverter terminals see no back-EMF. Torque is created when the currents flowing from the motor inverter are equally split between coil groups “a” and “b”, while force is created when additional currents from the suspension inverter are superimposed in the coil groups.

Reference [48] introduced a parallel DPNV combined winding structure with three-phase motor and suspension inverters. Study [86] discussed DPNV power electronics and control considerations, and [59,87] presented current regulation architecture. A generalized DPNV combined winding design procedure is proposed in [86].

2.2.1.3 Bridge DPNV Combined Winding

The bridge DPNV winding consists of a motor inverter and multiple isolated single-phase suspension inverters, as shown in Fig. 2.1c for three phases. This combined winding drive category also has the advantage of having zero back-EMF at suspension terminals, allowing for low-power, low-voltage suspension inverters. Furthermore, the control of torque and suspension inverter currents in this winding is completely independent.

Study [75] presented the operating principle and practical implementation of the bridge configured combined winding; [51] proposed a generalized winding design method, identifying motors with slot/pole/phase combinations that can be operated with the bridge DPNV winding. Reference [76] used this combined winding for noise and vibration attenuation in switched reluctance motors.

2.2.1.4 MCI Combined Winding

The MCI winding drive has a structure similar to the parallel DPNV winding drive. However, as shown in Fig. 2.1d, the motor and suspension inverters are swapped and the terminals of the coil group "a" are reversed. Unlike the parallel and bridge DPNV winding drives, the MCI winding drive does not have the advantage of zero back-EMF, making it more suitable for low-speed, high-power applications. Operation and practical implementation of the MCI winding are presented in [38, 40].

2.2.1.5 Multi-sector windings

Bearingless motors with multi-sector windings are divided into sectors (sets of poles) with each sector featuring a multi-phase winding (usually three-phase); each sector has an independent power source. Forces are produced on the shaft by controlling field weakening/strengthening independently in each sector.

Example multi-sector winding bearingless machines with 3 sectors, each having 3 phases, are presented in [50, 77–81]. Studies [50, 77–79] developed control algorithms for multi-sector machines to create forces in a manner to suppress selected vibration harmonics. Multi-sector machines particularly have the advantage of operating under fault conditions due to having several independent sectors. The problem is in the complexity and cost of the hardware due to a separate power supply in each sector and an increased number of power electronic switches.

2.2.2 Combined Windings for High Performance Motors

This work investigates the multiphase and DPNV combined windings. These two winding topologies are capable of providing completely decoupled motor operation (field weakening and torque, i_d and i_q current regulation) and suspension force operation (radial x-y forces, i_x and i_y current regulation). The basic principles of these windings are now described.

In multiphase windings, the phase currents consist of two balanced sets of currents with different phase shifts. One set produces torque and the other set produces force. An example multiphase winding configuration with six phases is shown in Fig. 2.2a. Notice that a double star connection is used. Multiple star connections are possible depending on the number of phases and can reduce the number of required current measurements.

Detailed information about the multiphase winding design and operation can be found in [67], [42] and [83]. Reference [42] shows that the multiphase phase currents can be transformed into two independent current space vectors to enable decoupled dual field oriented control (torque and suspension forces are controlled independently). In general, the phase currents of multiphase systems can be transformed into multiple independent space vectors located in independent rotating reference frames [88]. This will be explained later in this chapter.

The second winding configuration considered in this chapter is the parallel DPNV winding. This winding is driven by two sets of inverters connected to the coil groups as shown in Fig. 2.2b. As the name "no-voltage" suggests, the back-EMF seen by the suspension terminals/phases is ideally zero. Torque is produced when the current flowing from each

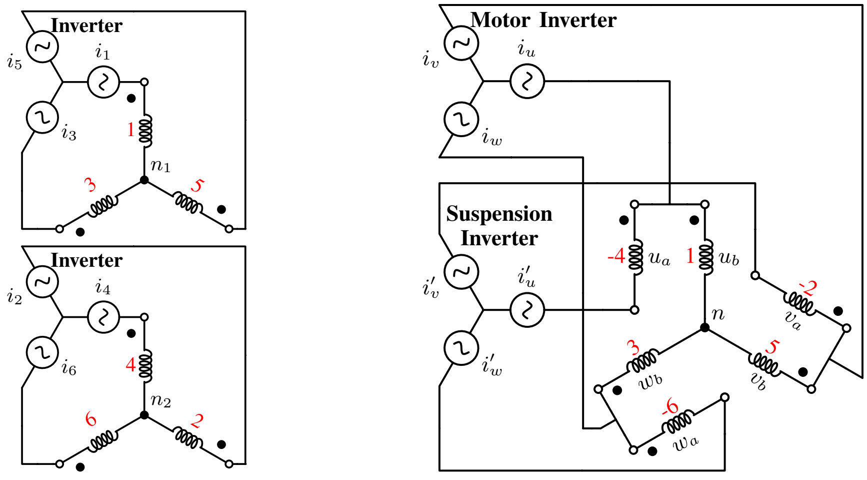

(a) (b)

Figure 2.2: Bearingless motor configured as (a) multiphase winding with two neutral points and (b) parallel DPNV winding.

motor terminal/phase (i_u, i_v, i_w) is equally distributed between coil groups "a" and "b". Force is produced when an additional current component from each suspension terminal is superimposed in the coil groups and flows to the neutral point n.

DPNV winding operation, power electronics, and control considerations were introduced in [49], and a current regulation architecture for a parallel combined winding configuration was presented in [59]. Winding design requirements and a design procedure were detailed in [89]. Any motor winding that meets these requirements can be configured as a DPNV winding by adding additional end connections to connect the bearingless drive as shown in Fig. 2.2b.

2.2.3 Example Bearingless Motor

An example bearingless motor system is used throughout this chapter to illustrate the theory that is developed and provide experimental validation in Section 2.6. The example motor is an outer rotor bearingless PM vernier slice motor shown in Fig. 2.3b. It consists of $Q = 6$ stator slots, $m = 6$ phases (concentrated coils), and $p = 17$ pole pairs. The motor characteristics are shown in Table 2.1. This machine was recently proposed in [1] for low

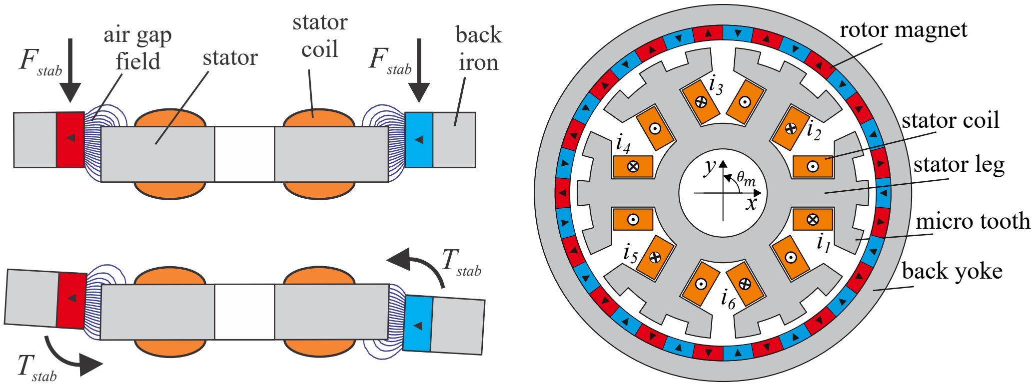

(a) (b)

Figure 2.3: Bearingless PM vernier motor with outer rotor: (a) picture explaining passively stabilized degrees of freedom and (b) cross-section plot [1], [2].

Parameter	Value	Parameter	Value
Rated torque (τ_r)	1 Nm	Torque per amp. (k_t)	0.28 Nm/A
Rated force (F_r)	26 N	Force per amp. (k_f)	7 N/A
Rated speed (ω_r)	500 RPM	Radial stiffness (k_δ)	−70 N/mm
Number of turns (N)	84	Resistance (R)	2 Ω
Equiv. self-ind. (L)	2.3 mH	Equiv. mutual ind. (M)	−0.2 mH
Pole-pairs (p, p_s)	17, 16	Phases (m)	6

Table 2.1: Vernier motor (Fig. 2.3b) characteristics

speed, high torque applications, and was designed and experimentally characterized in [2].

While this motor was designed for use with an multiphase winding, it also meets the DPNV design requirements in [89]. Figure 2.2 illustrates how the stator coils can be connected as either an multiphase winding (Fig. 2.2a) or a DPNV winding (Fig. 2.2b). For the DPNV winding (Fig. 2.2b), the coils have additional labels of u_{a}, u_{b}, etc., which indicate the phase (u, v, w) and coil group type ("a" or "b") used in the DPNV literature. For example, i_{ub} indicates the current in phase u and coil group "b". The red numbers in Fig. 2.2 indicate the coil numbers of Fig. 2.3b. Current entering the dotted terminals of Fig. 2.2 corresponds to the coil current polarity of Fig. 2.3b if the red number is positive. If the red number is negative, current entering the dotted terminals corresponds to the opposite of the current polarity in Fig. 2.3b.

This chapter will explain how the two approaches (multiphase and DPNV) actually yield equivalent coil group currents, but each implementation has different power electronics and control advantages depending on the application requirements.

2.3 Force and Torque Model

This section reformulates the operating theory for both windings using matrix models to allow the windings to be directly compared. It is shown that multiphase windings with an even number of phases can be realized as DPNV windings.

2.3.1 Generalized Force-Torque Model

A generalized matrix model of bearingless motor forces and torque is presented in [67] and is now summarized for multiphase combined windings. The model relates the total forces/-torque $\boldsymbol{F_t(x_r, i)} = [F_{xt}\ F_{yt}\ \tau_t]^T$ to the rotor radial/angular position $\boldsymbol{x_r} = [x\ y\ \theta_m]^T$ and to the stator current $\boldsymbol{i}$:

$$\boldsymbol{F_t} = \begin{bmatrix} \boldsymbol{i^T} & \mathbf{0}_{1\text{x}m} & \mathbf{0}_{1\text{x}m} \\ \mathbf{0}_{1\text{x}m} & \boldsymbol{i^T} & \mathbf{0}_{1\text{x}m} \\ \mathbf{0}_{1\text{x}m} & \mathbf{0}_{1\text{x}m} & \boldsymbol{i^T} \end{bmatrix} \boldsymbol{M_Q(x_r)i} + \boldsymbol{M_L(x_r)i} + \boldsymbol{M_C(x_r)} \tag{2.1}$$

where $\boldsymbol{i} = [i_1\ i_2\ ...\ i_m]^T$ is a current vector and $\mathbf{0}_{1\text{x}m}$ is a 1-by-m zero vector. Here, m is the number of distinct connections to the drive. In the multiphase winding, m can also be referred to as the total number of phases. In the DPNV winding, there are $m/2$ motor phases and $m/2$ suspension phases. The definition, size, and unit of each matrix are given below:

- $\boldsymbol{M_Q}$ − models quadratic force/torque-current behavior, typically caused by armature reaction. Size: $3m$-by-m. Units: first $2m$ rows [N/A^2], last m rows [Nm/A^2].
- $\boldsymbol{M_L}$− models linear force/torque-current behavior which is the typical term used to control shaft position. Size: 3-by-m. Units: first 2 rows [N/A], last 1 row [Nm/A].

- $\boldsymbol{M_C}-$ models cogging forces/torque. Size: 3-by-1. Units: first 2 rows [N], last 1 row [Nm].

In surface-mounted PM motors (non-salient), $\boldsymbol{M_Q}$ is usually negligible and $\boldsymbol{M_C}$ is typically either neglected or compensated [6]. By linearizing (2.1) about a centered rotor position [67], a simple model for controllable force/torque is obtained:

$$\boldsymbol{F}(\theta_m) = \boldsymbol{T_m}(\theta_m)\boldsymbol{i} \tag{2.2}$$

where a matrix $\boldsymbol{T_m} = \boldsymbol{M_L}(0, 0, \theta_m)$ is used to map the phase currents into the forces and torque $\boldsymbol{F} = [F_x\ F_y\ \tau]^T$ they produce on the rotor. A plot of $\boldsymbol{T_m}$ matrix entries vs. rotor angle in electrical degrees is shown in Fig. 2.4a for the example machine (of Section 2.2.3) for both winding topologies. For the multiphase winding, each column of $\boldsymbol{T_m}$ shows the force/torque produced when only one phase current is excited. For example, column one entries are obtained by only exciting i_1 to its rated value in FEA, and extracting the resulting force/torque over 360 degrees of the rotor electrical angle θ ($\theta = p\theta_m$).

When implementing the bearingless motor drive, the phase currents must be calculated to create a commanded force/torque vector on the rotor. To find these currents, an inverse map from the position regulator's force/torque command into currents is needed. This is accomplished by determining a $\boldsymbol{K_m}$ matrix as in (2.3):

$$\boldsymbol{i}(\theta_m) = \boldsymbol{K_m}(\theta_m)\boldsymbol{F} \tag{2.3}$$

There are infinitely many solutions of $\boldsymbol{i}$ for m>4 (with a star connection). Among these solutions, an optimal $\boldsymbol{i}$ with minimal total ohmic losses is found by solving the following optimization problem:

$$\begin{aligned} \underset{\boldsymbol{i}}{\text{minimize}} \quad & \boldsymbol{i^T R i} \\ \text{subject to} \quad & \boldsymbol{T_m i} - \boldsymbol{F} = \boldsymbol{0}_{3\text{x}1} \end{aligned} \tag{2.4}$$

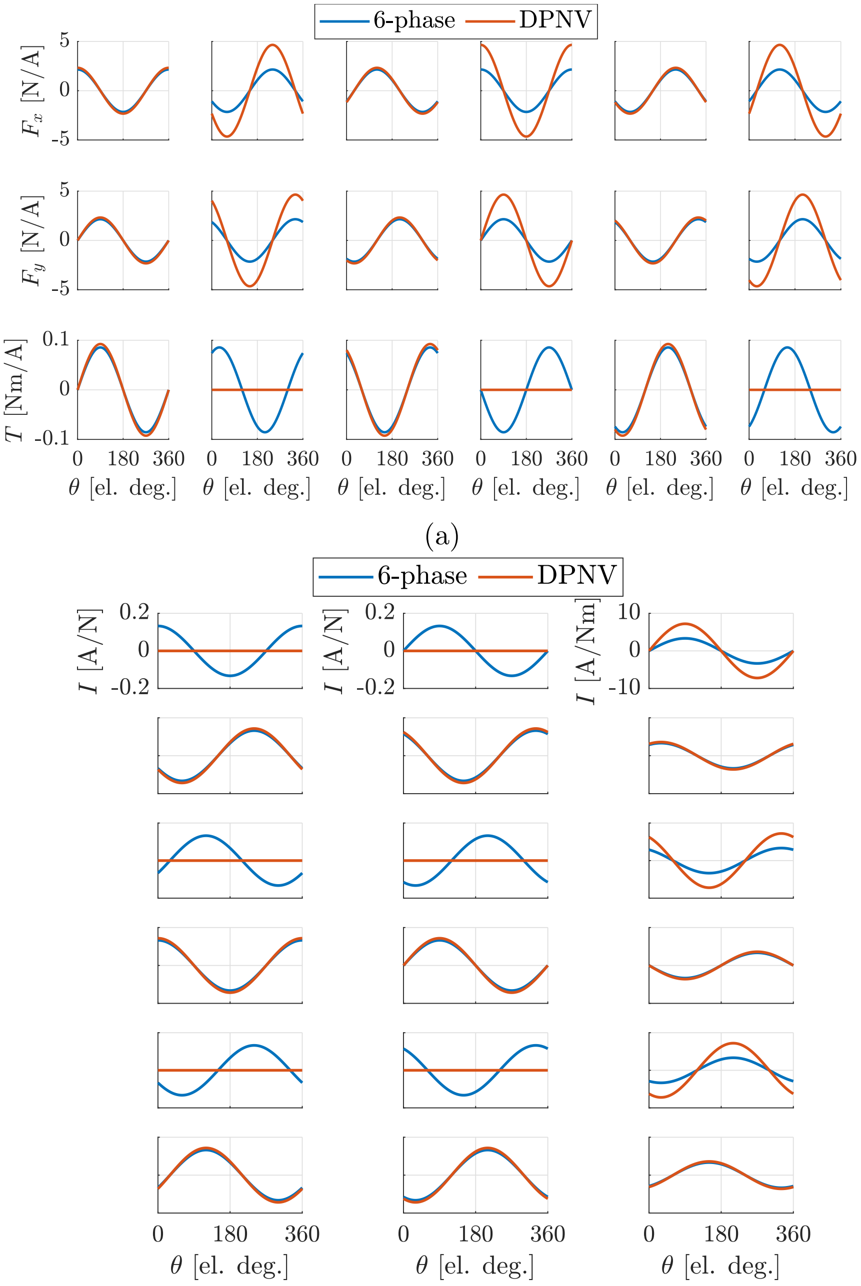

(a)

(b)

Figure 2.4: $\boldsymbol{T_m}$ and $\boldsymbol{K_m}$ matrices for 6-phase and DPNV configurations: (a) $\boldsymbol{T_m}$ matrix and (b) $\boldsymbol{K_m}$ matrix.

where $\boldsymbol{R}$ is a resistance matrix. Solving this optimization problem, the optimal $\boldsymbol{K_m}$ matrix is found to be [44]

$$\boldsymbol{K_m} = \boldsymbol{R}^{-1}\boldsymbol{T_m^T}(\boldsymbol{T_m}\boldsymbol{R}^{-1}\boldsymbol{T_m^T})^{-1} \tag{2.5}$$

The details of the resulting matrix forms will now be discussed for both winding types.

2.3.2 Multiphase Configuration

The multiphase winding resistance matrix has the diagonal form $\boldsymbol{R} = R\boldsymbol{I}$, where R is the resistance of one coil group and $\boldsymbol{I}$ is the identity matrix. Since $\boldsymbol{R}$ is a diagonal matrix, it turns out that (2.5) is the Moore-Penrose pseudo-inverse of $\boldsymbol{T_m}$ which is $\boldsymbol{K_m} = \boldsymbol{T_m}(\boldsymbol{T_m}\boldsymbol{T_m^T})^{-1}$. This is equivalent to minimizing the Euclidean norm of $\boldsymbol{i}$. As an example, the power-optimal $\boldsymbol{K_m}$ matrix for the example PM vernier machine in the 6-phase multiphase configuration is shown in Fig. 2.4b. Each column represents a set of optimal phase currents that produce 1 N in x (column 1) or y (column 2) direction or 1 Nm of torque (column 3). The total phase currents $\boldsymbol{i}$ are a scaled sum of each column based on the force/torque vector command.

This chapter is focused on high performance bearingless machines, where the columns of $\boldsymbol{K_m}$ consist of balanced, multi-phase sinusoidal functions of rotor position, with a phase angle separation between their rows of $\Delta\alpha_j$. This results in phase currents that are composed of two sets of balanced sinusoids. The first set creates torque and field weakening (but no force); the second set creates force (but no torque). This is possible because the two sinusoidal current components have different phase angles, as will now be explained. In the multiphase literature, this type of machine is described as supporting "dual field oriented control" [42], because the principles of motor field oriented control can be extended to the suspension field.

The generalized Clarke transformation, which is summarized in Appendix A, can be used to study the $\boldsymbol{K_m}$ matrix (and phase currents). Here, $\boldsymbol{x}(\theta)$ is the phase current vector $\boldsymbol{i}(\theta)$ and the $\boldsymbol{x_j}(\theta)$ vectors defined in (A.2) are currents responsible for force or torque production. These correspond to the columns of $\boldsymbol{K_m}$ (i.e. Fig. 2.4b), where the x and y force-producing current columns are combined to form a single $\boldsymbol{x_j}(\theta)$ vector. Section 2.4.1 utilizes current space vectors that this transform creates to calculate torque and suspension forces.

The properties of Appendix A can be used to identify the following requirements for $\Delta\alpha_j$ and the number of phases m so that the machine supports dual field oriented control:

- To obtain independent current components associated with torque and suspension, the phase separation $\Delta\alpha_j$ must be unique for force and torque, requiring j be unique in (A.3): $j_{\text{force}} \neq \pm j_{\text{torque}}$ (see Appendix A, property 1).
- To obtain motor currents that are able to control torque and field weakening (two independent dimensions) and force currents able to control x and y force components (two independent dimensions), the phase separation cannot use $j = 0$ or $j = m/2$ (see property 2).
- To have sufficient feasible values of phase separation, the number of machine phases (number of rows in $\boldsymbol{K_m}$ and $\boldsymbol{i}$) must be $m \geq 5$ (see property 3).

For a 6-phase bearingless machine, there are exactly two possible phase separation angles: $\Delta\alpha_1 = \pm\pi/3$ and $\Delta\alpha_2 = \pm 2\pi/3$. The machine must use one of these angles for the torque column of $\boldsymbol{K_m}$ and the other for the force columns. The optimal currents used in the example 6-phase vernier machine (see Fig. 2.4b) can be expressed as:

$$\begin{bmatrix} i_1 \\ i_2 \\ i_3 \\ i_4 \\ i_5 \\ i_6 \end{bmatrix} = \frac{F}{k_f} \begin{bmatrix} \cos(\theta - \phi) \\ \cos(\theta + \frac{2\pi}{3} - \phi) \\ \cos(\theta + \frac{4\pi}{3} - \phi) \\ \cos(\theta - \phi) \\ \cos(\theta + \frac{2\pi}{3} - \phi) \\ \cos(\theta + \frac{4\pi}{3} - \phi) \end{bmatrix} + \frac{\tau}{k_t} \begin{bmatrix} \sin\theta \\ \sin(\theta + \frac{\pi}{3}) \\ \sin(\theta + \frac{2\pi}{3}) \\ -\sin\theta \\ -\sin(\theta + \frac{\pi}{3}) \\ -\sin(\theta + \frac{2\pi}{3}) \end{bmatrix} \tag{2.6}$$

which shows that the currents need to be a function of the rotor angle θ to produce the commanded torque τ and force (magnitude F and angle ϕ). The values of k_f (force per ampere) and k_t (torque per ampere) are given in Table 2.1 for the example vernier machine. In (2.6), force and torque currents have a phase shift of $\Delta\alpha_2 = -2\pi/3$ and $\Delta\alpha_1 = -\pi/3$, respectively. These phase shifts depend on the machine design characteristics: $\Delta\alpha_1 = p\alpha_{\text{ph}}$ and $\Delta\alpha_2 = p_s\alpha_{\text{ph}}$, where α_{ph} is the mechanical angle between adjacent phases and p_s is the number of suspension pole pairs. The expression (2.6) can be adapted for any 6-phase multiphase winding by updating which column $\Delta\alpha_1$ and $\Delta\alpha_2$ appear in.

2.3.3 Parallel DPNV Configuration

To find the DPNV $\boldsymbol{T_m}$ and $\boldsymbol{K_m}$ matrices, the approach described for the multiphase configuration is used. The DPNV phase current vector $\boldsymbol{i}$ is advantageously constructed as $\boldsymbol{i} = \boldsymbol{i}_{\text{term}} = [i_u\ i'_v\ i_w\ i'_u\ i_v\ i'_w]^T$ to enable a direct comparison between the terminal currents of the two windings in Fig. 2.4. Each column of $\boldsymbol{T_m}$ is found by exciting only one terminal at a time and keeping other terminal currents zero (current is allowed to exit the neutral point). The $\boldsymbol{K_m}$ matrix is determined using (2.5) but with a new $\boldsymbol{R}$ matrix to find the ohmic losses of the DPNV winding. This new $\boldsymbol{R}$ matrix is found by first determining a $\boldsymbol{C_i}$ matrix which maps the terminal currents to individual coil group currents as

$$\boldsymbol{i}_{\text{coil}} = \boldsymbol{C_i}\boldsymbol{i}_{\text{term}},\ \ \boldsymbol{C_i} = \begin{bmatrix} 1 & 0 & 0 & 1 & 0 & 0 \\ 0 & 1 & 0 & 0 & 0 & 0 \\ 0 & 0 & 1 & 0 & 0 & 1 \\ 0 & 0 & 0 & 1 & 0 & 0 \\ 0 & 1 & 0 & 0 & 1 & 0 \\ 0 & 0 & 0 & 0 & 0 & 1 \end{bmatrix} \qquad (2.7)$$

The revised $\boldsymbol{R}$ matrix is then calculated from the ohmic losses as

$$P = \boldsymbol{i}_{\text{coil}}^{\boldsymbol{T}} \boldsymbol{R} \boldsymbol{i}_{\text{coil}} = \boldsymbol{i}_{\text{term}}^{\boldsymbol{T}} \boldsymbol{C}_{\boldsymbol{i}}^{\boldsymbol{T}} \boldsymbol{R} \boldsymbol{C}_{\boldsymbol{i}} \boldsymbol{i}_{\text{term}} \tag{2.8}$$

$$\boldsymbol{R}_{\boldsymbol{t}} = \boldsymbol{C}_{\boldsymbol{i}}^{\boldsymbol{T}} \boldsymbol{R} \boldsymbol{C}_{\boldsymbol{i}} \tag{2.9}$$

Note that $\boldsymbol{R}_{\boldsymbol{t}}$ is not diagonal, and therefore (2.5) is no longer equivalent to the Moore-Penrose inverse of $\boldsymbol{T}_{\boldsymbol{m}}$.

Alternatively, the DPNV $\boldsymbol{T}_{\boldsymbol{m}}$ and $\boldsymbol{K}_{\boldsymbol{m}}$ matrices can be derived from the multiphase matrices using $\boldsymbol{C}_{\boldsymbol{i}}$:

$$\boldsymbol{T}_{\boldsymbol{m},\text{DPNV}} = \boldsymbol{T}_{\boldsymbol{m},\text{MP}} \boldsymbol{C}_{\boldsymbol{i}},\ \boldsymbol{K}_{\boldsymbol{m},\text{DPNV}} = \boldsymbol{C}_{\boldsymbol{i}}^{\boldsymbol{-1}} \boldsymbol{K}_{\boldsymbol{m},\text{MP}} \tag{2.10}$$

The DPNV winding can be viewed as a circuit-based implementation of the multiphase winding's $\boldsymbol{K}_{\boldsymbol{m}}$ matrix, where the circuit creates the relation given by (2.7). It can be shown that any multiphase winding with even m can be implemented as a DPNV winding because of the unique phase separation requirement for torque and suspension currents described in Section 2.3.2. This is now illustrated for the example machine described by (2.6). In both DPNV and multiphase windings, the relation between coil currents in (2.11) exists when only torque is produced. When only force is produced, the currents are related as (2.12). These relations can be seen from the DPNV circuit schematic in Fig. 2.2b, and from the multiphase current expression in (2.6).

$$\text{Torque: } i_1 = -i_4,\ i_2 = -i_5,\ i_3 = -i_6 \tag{2.11}$$

$$\text{Force: } i_1 = +i_4,\ i_2 = +i_5,\ i_3 = +i_6 \tag{2.12}$$

While the multiphase winding directly connects each of these coil groups to an inverter phase, the DPNV winding provides suspension and motor terminal connections which see the coil groups as either a series or parallel connection.

2.4 Space Vector Model for Regulation

This section develops a current regulation approach that is general to both winding configurations. This is done by first formulating the operating theory into current and voltage space vector models that are related to force and torque production. The relationship between voltage and current space vectors is then used to develop a systematic current controller tuning method for the force and torque regulators.

2.4.1 Force/Torque

The bearingless motor forces and torque can be related to current space vectors through parameters $\bar{k}_t$ and $\bar{k}_f$ as

$$\begin{aligned} \vec{T} &= T_d + j\tau = \bar{k}_t \vec{i}_t \\ \vec{F} &= F_x + jF_y = \bar{k}_f \vec{i}_s \end{aligned} \tag{2.13}$$

Here, the vector $\vec{T}$ consists of a flux weakening term T_d [2] and torque τ. The space vectors $\vec{i}_t$ and $\vec{i}_s$ are created by calculating the generalized Clarke transform of the machine's phase currents $\boldsymbol{i}$ as described in Section 2.3.2 and Appendix A. It is well known in motor drives literature that the torque space vector $\vec{i}_t$ can be decomposed into two components i_d and i_q that when rotated at synchronous frequency are proportional to T_d and τ. Similarly, the suspension space vector $\vec{i}_s$ can be decomposed into two components i_x and i_y that when rotated are proportional to x and y direction forces:

$$\vec{i}_t = (i_d + ji_q)e^{j\theta_T} \tag{2.14}$$

$$\vec{i}_s = (i_x + ji_y)e^{j\theta_S} \tag{2.15}$$

These space vectors, their rotation angles θ_T and θ_S, and the two corresponding synchronous reference frames dq and xy are defined in Fig. 2.5. These two reference frames are presented separately in Fig. 2.5a and Fig. 2.5b to show that they are in orthogonal (independent) planes.

It can be shown using Fig. 2.2 and Fig. 2.4b that the same amplitude of force creating phase currents is required in both multiphase and DPNV windings. Therefore, the magnitude of $\bar{k}_f$ in (2.13) is the same in both topologies. The required amplitude of torque creating phase currents in the DPNV winding is twice that of the multiphase winding. From these observations and (2.14)-(2.15), $\bar{k}_f$ and $\bar{k}_t$ of (2.13) can be calculated as:

$$\bar{k}_f = k_f e^{-j\theta_S},\ \bar{k}_t = \begin{cases} k_t e^{-j\theta_T} & \text{for MP} \\ \frac{k_t}{2} e^{-j\theta_T} & \text{for DPNV} \end{cases} \tag{2.16}$$

The angles θ_T and θ_S are determined by the machine's torque or force creating phase currents that are input to the Clarke transform. Each angle can be equal to either θ or $-\theta$. From Appendix A property 4, if the phase currents form a positive sequence, the resulting space vector rotates counterclockwise ($e^{j\theta}$) with a speed ω_e ($\omega_e = \dot{\theta}$). If the phase currents form a negative sequence, the resulting space vector rotates clockwise ($e^{-j\theta}$) with a speed $-\omega_e$. These space vector angles may not be the same in both multiphase and DPNV topologies because of the different phase connections and the sequence of the phase currents. Calculations are now shown for the example PM vernier motor of Fig. 2.3b.

2.4.1.1 Multiphase configuration

The torque current space vector $\vec{i}_t$ is calculated from (2.6) by using (A.1) with $k = 1$, corresponding to the phase separation of $\Delta\alpha_1 = -\pi/3$ for torque currents, as given in (2.17). The suspension current space vector $\vec{i}_s$ is calculated in the same manner with $k = 2$ as (2.18).

$$\vec{i}_t = c_6(i_1 + a i_2 + a^2 i_3 + a^3 i_4 + a^4 i_5 + a^5 i_6) \tag{2.17}$$

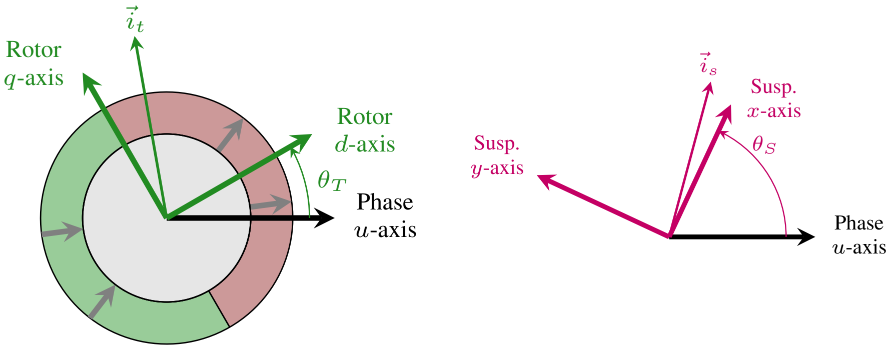

(a) (b)

Figure 2.5: Space vector diagram of synchronous reference frames: (a) torque dq-frame and (b) suspension xy-frame.

$$\vec{i}_s = c_6(i_1 + a^2 i_2 + a^4 i_3 + a^6 i_4 + a^8 i_5 + a^{10} i_6) \tag{2.18}$$

Here, $c_6 = 2/6$ for an amplitude invariant or $c_6 = \sqrt{2/6}$ for a power invariant transformation. This results in both vectors rotating CW at speed: $\omega_T = \omega_S = -\omega_e$.

2.4.1.2 Parallel DPNV Configuration

Since the DPNV winding is configured as two multi-phase systems (one for the suspension and one for the torque), (A.1) is used for each system separately. In the three-phase case observed in Fig. 2.4b, torque terminal currents $[i_u,\ i_v,\ i_w]^T$ lag each other by $2\pi/3$ (i_v lags i_u) and create a positive sequence, while force creating currents lead each other by $2\pi/3$ and create a negative sequence. The three phase Clarke transformation (A.1) with $k = 1$ is used to obtain the current space vectors as:

$$\vec{i}_t = c_3(i_u + a i_v + a^2 i_w) \tag{2.19}$$

$$\vec{i}_s = c_3[(i'_u + i_u/2) + a(i'_v + i_v/2) + a^2(i'_w + i_w/2)] \tag{2.20}$$

where $c_3 = 2/3$ for amplitude invariant and $c_3 = \sqrt{2/3}$ for power invariant transformation. Note that the suspension vector is obtained from the force creating currents ($i'_u + i_u/2$, $i'_v + i_v/2$, $i'_w + i_w/2$), not from the suspension terminal currents (see Section 2.2.2). Since the suspension currents form a negative sequence, $\vec{i}_s$ rotates CW at $\omega_S = -\omega_e$, while $\vec{i}_t$ rotates CCW at $\omega_T = \omega_e$.

2.4.2 Electric Model

Having defined the relations between force/torque and space vector currents, an equivalent electric circuit model for each winding topology is now developed to design the current regulators and facilitate comparison between the two topologies. To do this, voltage equations are derived for each topology in the dq and xy rotating reference frames defined in Fig. 2.5. Equivalent resistance and inductance terms are determined which are used for the current regulator design. For this, the torque and suspension voltages in the space vector form are first determined using

$$\vec{v}_t = R\vec{i}_t + \frac{d\vec{\lambda}_t}{dt} \tag{2.21}$$

$$\vec{v}_s = R\vec{i}_s + \frac{d\vec{\lambda}_s}{dt} \tag{2.22}$$

where $\vec{\lambda}_t$ and $\vec{\lambda}_s$ are flux linkage space vectors (flux linkage from the windings and magnets) calculated using the same order of the generalized Clarke transform as $\vec{i}_t$ and $\vec{i}_s$.

The flux linkage of each coil group (positive polarity corresponding to the dotted terminal in Fig. 2.2b) due to other coil groups can be expressed in terms of the equivalent self- and mutual-inductances L and M [87]. These equivalent inductances are defined by considering the flux linkage λ_{ua} due to all coil group currents as:

$$\lambda_{\text{ua}} = L_1 i_{\text{ua}} + L_2(i_{\text{va}} + i_{\text{wa}}) + L_3 i_{\text{ub}} + L_4(i_{\text{vb}} + i_{\text{wb}}) \tag{2.23}$$

where L_1 is a self-inductance of each coil group, L_2 is a mutual inductance between same coil groups and different phases, L_3 is a mutual inductance between different coil groups and same phases, and L_4 is a mutual inductance between different coil groups and different phases. By assuming no zero sequence currents, $i_{\mathrm{ua}} = -(i_{\mathrm{va}} + i_{\mathrm{wa}})$ and $i_{\mathrm{ub}} = -(i_{\mathrm{vb}} + i_{\mathrm{wb}})$, and defining equivalent inductances as $L = L_1 - L_2$ and $M = L_3 - L_4$, (2.23) simplifies to:

$$\lambda_{\mathrm{ua}} = L i_{\mathrm{ua}} + M i_{\mathrm{ub}} \tag{2.24}$$

The flux linkage of other coil groups can similarly be expressed in terms of L and M, and used in the derivation of the voltage equations for each configuration.

2.4.2.1 Multiphase Configuration

A 6-phase configuration is again used as an example to present the space vector voltage equations for the multiphase winding. Using (2.21), (2.24), and $a = e^{j\pi/3}$, the voltage space vector equation is:

$$\vec{v}_t = R\vec{i}_t + (L + M)\frac{d\vec{i}_t}{dt} + \vec{v}_m \tag{2.25}$$

where $\vec{v}_m$ is the back-EMF, which is determined from the coil flux linkage due to the magnets. Transforming (2.25) to the dq-frame using $\vec{v}_t = (v_d + jv_q)e^{j\theta_T}$, v_d and v_q can be found:

$$v_d = R_d i_d + L_d\frac{di_d}{dt} - \omega_T L_q i_q \tag{2.26}$$

$$v_q = R_q i_q + L_q\frac{di_q}{dt} + \omega_T L_d i_d + v_m \tag{2.27}$$

where $R_d = R_q$ and $L_d = L_q$ for non-salient machines, and are the equivalent d and q-axis resistances and inductances obtained after dq transformation. The back-EMF vector is $\vec{v}_m = jv_m e^{j\theta_T}$ with $v_m = \frac{2}{m}k_t\omega_m$ ($\omega_m = \dot{\theta}_m$ is a mechanical rotor speed and $m = 6$ for the example vernier motor).

The suspension space vector is similarly determined as (2.28):

$$\vec{v}_s = R\vec{i}_s + (L - M)\frac{d\vec{i}_s}{dt} \tag{2.28}$$

Using $\vec{v}_s = (v_x + jv_y)e^{j\theta_S}$, v_x and v_y can be found:

$$v_x = R_x i_x + L_x \frac{di_x}{dt} - \omega_S L_y i_y \tag{2.29}$$

$$v_y = R_y i_y + L_y \frac{di_y}{dt} + \omega_S L_x i_x \tag{2.30}$$

where R_x, R_y, L_x, and L_y are the equivalent x and y-axis resistances and inductances in xy-frame. Note that suspension xy voltages do not have back-EMF components as it becomes zero when transformed into suspension space vector frame. These equations are represented as space vector equivalent circuits in Fig. 2.6. All equivalent circuit parameters are summarized in Table 2.2.

2.4.2.2 Parallel DPNV Configuration

The voltage vector $\vec{v}_t$ for the parallel DPNV winding is calculated in a similar manner, but using the Clarke transform of (2.19) as:

$$\vec{v}_t = \frac{R}{2}\vec{i}_t + \frac{L+M}{2}\frac{d\vec{i}_t}{dt} + \frac{\vec{v}_s}{2} + \vec{v}_m \tag{2.31}$$

Notice that the half of the suspension voltage space vector appears in this expression. This is because the torque terminals in Fig. 2.2b are halfway between the suspension terminals and the neutral point and is examined in detail in [87]. The voltage vector $\vec{v}_t$ can be decomposed into d and q components:

$$v_d = R_d i_d + L_d \frac{di_d}{dt} - \omega_T L_q i_q + \frac{1}{2} v_x^{dq} \tag{2.32}$$

$$v_q = R_q i_q + L_q \frac{di_q}{dt} + \omega_T L_d i_d + v_m + \frac{1}{2} v_y^{dq} \tag{2.33}$$

Here, the v_x^{dq} and v_y^{dq} components are the suspension xy voltages in the torque dq reference frame. These should be compensated via a feed-forward to fully decouple the force and torque control. The back-EMF is again $v_m = \frac{2}{m} k_t \omega_m$, which is the same as the multiphase

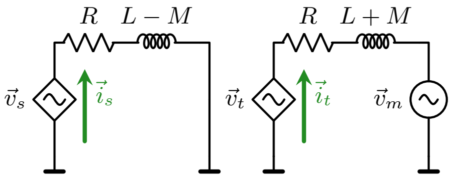

Figure 2.6: Equivalent single-phase circuit of 6-phase configuration.

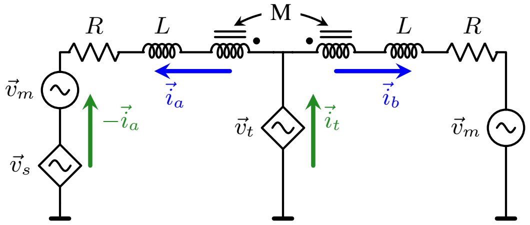

Figure 2.7: Equivalent single-phase circuit of DPNV configuration. The dotted terminals correspond to the dotted terminals of a single phase of Fig. 2.2b

winding.

The suspension voltage space vector is calculated as (2.34), with x and y components determined as (2.35) and (2.36):

$$\vec{v}_s = 2R\vec{i}_s + 2(L-M)\frac{d\vec{i}_s}{dt} \tag{2.34}$$

$$v_x = R_x i_x + L_x\frac{di_x}{dt} - \omega_S L_y i_y \tag{2.35}$$

$$v_y = R_y i_y + L_y\frac{di_y}{dt} + \omega_S L_x i_x \tag{2.36}$$

Notice that the suspension xy voltages do not have back-EMF components since this is canceled for the suspension terminals by the coil group connections.

Equations (2.31) and (2.34) are represented as a space vector equivalent circuit in Fig. 2.7.

2.4.3 Summary of Space Vector Model Parameters

The space vector model parameters from both Sections 2.4.1 and 2.4.2 are summarized in Table 2.2. The resistances and inductances in the equivalent dq and xy voltage equations are different for each configuration. It is interesting to note that these parameters for the DPNV

	MP		DPNV	
	Torque	Susp.	Torque	Susp.
L_d, L_q or L_x, L_y	$L+M$	$L-M$	$(L+M)/2$	$2(L-M)$
R_d, R_q or R_x, R_y	R	R	$R/2$	$2R$
v_m	$2k_t\omega_m/m$		$2k_t\omega_m/m$	
$\lvert\bar{k}_t\rvert$	k_t		$k_t/2$	
$\lvert\bar{k}_f\rvert$	k_f		k_f	

Table 2.2: Summary of Space Vector Model Parameters

winding appear to connect coil groups “a” and “b” in parallel for the torque terminals and in series for the suspension terminals, which matches Fig. 2.2b.

It is also interesting to note that the back-EMF magnitude v_m is identical in both winding topologies and can be expressed in terms of machine parameters as $v_m = \frac{2}{m}k_t\omega_m$.

2.4.4 Regulation Architecture

This subsection presents a generalized current regulation architecture combining both multiphase and DPNV configurations. The regulation approach is based on the equivalent space vector models developed in this section. The generalized current control architecture proposed to regulate forces and torque is shown in Fig. 2.8. The black lines/words are common to both configurations, while blue and green colored lines/words pertain only to the multiphase or DPNV configuration.

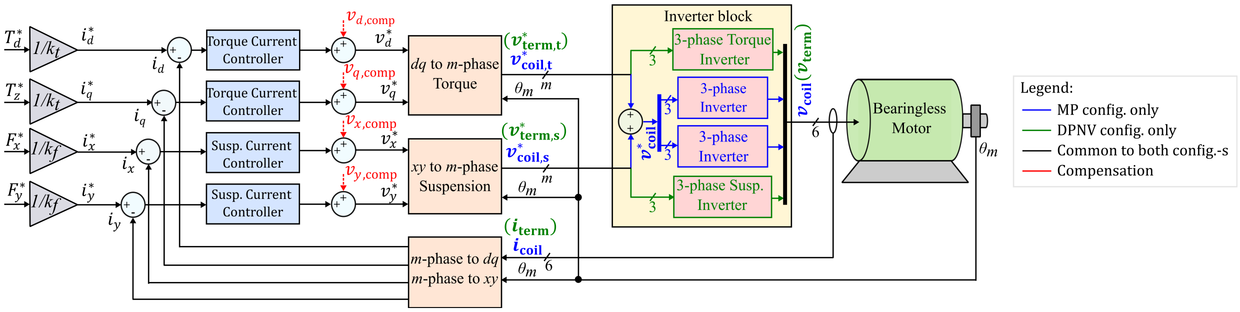

Figure 2.8: Current regulation block diagram for both configurations (* variables denote commanded values).

The torque and force commands are first translated into current dq or xy commands using k_t and k_f. After that, each current component is regulated using a PI controller. The PI controllers are tuned so that the current control closed loop transfer function becomes a first-order system through pole-zero cancellation:

$$K_p = \omega_b L_{\text{eq}},\ K_i = \omega_b R_{\text{eq}} \tag{2.37}$$

where ω_b is the desired bandwidth, and equivalent inductance L_{eq} and resistance R_{eq} terms are provided in Table 2.2.

Since the PI controllers are designed specifically assuming the RL load, compensation terms are added to the output of each PI controller (shown in red in the block diagram) to get a more accurate voltage command. These are determined based on the voltage dq equations in Section 2.4.2 for each configuration and shown below for the multiphase configuration:

$$\begin{aligned} v_{d,\text{comp}} &= -\omega_T L_q i_q,\ v_{q,\text{comp}} = \omega_T L_d i_d + v_m \\ v_{x,\text{comp}} &= -\omega_S L_y i_y,\ v_{y,\text{comp}} = \omega_S L_x i_x \end{aligned} \tag{2.38}$$

For the parallel DPNV configuration [59]:

$$\begin{aligned} v_{d,\text{comp}} &= -\omega_T L_q i_q + \frac{v_x^{dq}}{2},\ v_{q,\text{comp}} = \omega_T L_d i_d + v_m + \frac{v_y^{dq}}{2} \\ v_{x,\text{comp}} &= -\omega_S L_y i_y,\ v_{y,\text{comp}} = \omega_S L_x i_x \end{aligned} \tag{2.39}$$

After compensation, each torque dq and suspension xy voltage pair is transformed to phase voltages using the inverse dq and xy transformations. For the MP configuration, there are two m-by-1 vectors $v^*_{\text{coil,t}}$ and $v^*_{\text{coil,s}}$ resulting from the transformation, which are then added to get the final m-phase coil group voltages v^*_{coil} commanded to the m-leg inverter. For the parallel DPNV configuration, there are two $m/2$-by-1 vectors $v^*_{\text{term,t}}$ and $v^*_{\text{term,s}}$ resulting from the transformation, which are commanded to the $m/2$-leg torque inverter and $m/2$-leg suspension inverter, respectively. Finally, the actual voltages (v_{coil} or v_{term}) are modulated using inverters and applied to the motor terminals.

The currents are measured from the motor terminals and then applied to the dq and xy transformation blocks which consist of two blocks, one for the torque and another for the suspension. These dq and xy transformation blocks are based on the space vector transformations derived in Section 2.4.1. In multiphase configuration, all coil group currents are applied to both dq and xy transformations. In DPNV configuration, $i_{\text{term,t}} = [i_u,\ i_v,\ i_w]^T$ is applied to the torque dq transformation and $i_{\text{term,s}} = [i'_u + i_u/2,\ i'_v + i_v/2,\ i'_w + i_w/2]^T$ is applied to the suspension xy transformation. Transformed currents are then used as a feedback for the current regulation.

2.5 Comparison Between Multiphase and DPNV Drives

The theory developed in previous sections is now used to compare the multiphase and DPNV winding performance and drive requirements. These results apply to all machines with an even value of $m > 5$, since machines with an odd value of m cannot use DPNV windings. The $\boldsymbol{T_m}$ and $\boldsymbol{K_m}$ matrices in Section 2.3 show that both topologies use equivalent coil group currents to produce the same force and torque. Both winding topologies are able to decouple torque and suspension force regulation (2.13) through space vectors calculated with the generalized Clarke transformation (A.1), (2.17)-(2.20). As a result, a similar current regulation structure can be used in both topologies based on the voltage space vector formulation presented in Section 2.4.2, (2.25)-(2.36), with regulators designed to achieve equivalent control bandwidth in the synchronous dq and xy frames as described in Section 2.4.4, (2.37).

The main performance difference resides in the power electronic implementation of the bearingless drive. This can be investigated through the required inverter terminal current and voltage of the two topologies. Two critical differences can be identified from Fig. 2.2 and 2.4 as follows:

1. *Current:* DPNV drives carry more motor current because their suspension terminals

carry half of the motor current in addition to the motor terminals carrying twice the motor current of the multiphase approach; multiphase drives carry more suspension current because the DPNV circuit takes advantage of series connected coil groups to form $m/2$ suspension terminals.

2. *Voltage:* DPNV drives have lower voltage requirement because the DPNV suspension terminals do not see the back-EMF, while all multiphase terminals see the back-EMF.

The significance of these differences depend upon the machine parameters (m, p, R, L, M, k_t, k_f) and the expected loading and drive cycle (F, τ, and ω_m). Two performance metrics that describe the drive ratings are now developed in Section 2.5.1 and 2.5.2 to quantify when a bearingless motor developer would most advantageously select a DPNV or multiphase winding. The results, specified later in Table 2.3 and Fig. 2.9, show that machines which carry more significant suspension current (force) or have a higher rotational speed are likely to be advantageously implemented with a DPNV winding, with the multiphase winding likely being advantageous for machines which carry more torque current or operate at lower speeds. Section 2.5.3 presents a case study of selecting a winding topology for the example vernier motor in terms of the two performance metrics as well as other practical considerations.

2.5.1 Winding Performance Metric Based on Current Rating

The first metric is based on the current that the bearingless drive must be rated to handle, thereby giving an indication of the volume of drive silicon required. The metric is calculated as the ratio between the two toplogies when their phase terminal RMS current rating is summed across all phases.

In the multiphase winding, the RMS value of each phase current is found from (2.6) and shown below for a phase h:

$$I_{\mathrm{h,MP}} = \sqrt{\frac{i_{s,\mathrm{MP}}^2 + i_{t,\mathrm{MP}}^2}{2} + i_{s,\mathrm{MP}} i_{t,\mathrm{MP}} \sin\left(\phi - \frac{\pi(h-1)}{3}\right)}$$

where $i_{t,\mathrm{MP}} = \tau/k_t$ and $i_{s,\mathrm{MP}} = F/k_f$, indicating that the RMS current is not the same in all phases for a given force angle ϕ. To find the current rating for each phase, ϕ is swept from 0 to 2π and the maximum RMS current is determined. In the multiphase winding, the maximum RMS current observed in each phase is $(i_{s,\mathrm{MP}} + i_{t,\mathrm{MP}})/\sqrt{2}$. In the DPNV winding, the maximum RMS current of each suspension terminal is also equal to $(i_{s,\mathrm{MP}} + i_{t,\mathrm{MP}})/\sqrt{2}$ while the torque terminals have an RMS current of $2i_{t,\mathrm{MP}}/\sqrt{2}$.

Summing phase RMS current ratings for each topology and finding their ratio results in the following expression:

$$P_1 = \frac{\sum_{h=1}^{m} I_{h,\mathrm{MP}}}{\sum_{h=1}^{m} I_{h,\mathrm{DPNV}}} = \frac{2(i_{s,\mathrm{MP}} + i_{t,\mathrm{MP}})/\sqrt{2}}{\sqrt{2} i_{t,\mathrm{MP}} + (i_{s,\mathrm{MP}} + i_{t,\mathrm{MP}})/\sqrt{2}} \tag{2.40}$$

This expression indicates conditions when the multiphase ($P_1 < 1$) or DPNV winding ($P_1 > 1$) is advantageous. The results are summarized in Table 2.3 (row 2) and Fig. 2.9a, where F_r and τ_r are the force and torque at the rated coil current. These results show that the multiphase winding is favored when over half of the coil current is used to produce torque rather than force, while the inverse is true for the DPNV winding.

2.5.2 Winding Performance Metric Based on Volt-Ampere Rating

The second performance metric is the ratio of the total VA rating of the two drives. A similar metric is used in [16]. This metric reflects advantages in the required dc bus rating, silicon device voltage rating, and switching losses.

For each phase of the topology, the VA rating is calculated as the product of the maximum RMS voltage and maximum RMS current in steady state over all force angles. The total VA rating is then calculated as the sum of these phase VA ratings. RMS current ratings were determined in Section 2.5.1 and RMS voltage ratings are now presented in a similar manner.

In the multiphase winding, each phase voltage has a maximum RMS value of $(v_{t,\mathrm{MP}} + v_{s,\mathrm{MP}})/\sqrt{2}$ over all force angles, where $v_{t,\mathrm{MP}}$ and $v_{s,\mathrm{MP}}$ are the magnitudes of $\vec{v}_t$ in (2.25) and $\vec{v}_s$ in (2.28):

$$\begin{aligned} v_{t,\mathrm{MP}} &= \sqrt{\left(R_{dq} i_{t,\mathrm{MP}} + \omega_m \frac{2k_t}{m}\right)^2 + (p\omega_m L_{dq} i_{t,\mathrm{MP}})^2} \\ v_{s,\mathrm{MP}} &= i_{s,\mathrm{MP}} z_s,\ \ z_s = \sqrt{R_{xy}^2 + (p\omega_m L_{xy})^2} \end{aligned} \tag{2.41}$$

In the DPNV winding, the maximum RMS voltage of each torque terminal is also equal to $(v_{t,\mathrm{MP}} + v_{s,\mathrm{MP}})/\sqrt{2}$ and of each suspension terminal is $2v_{s,\mathrm{MP}}/\sqrt{2}$. Finally, the ratio of the total VA rating of each topology is calculated as:

$$P_2 = \frac{\sum_{h=1}^{m} S_{h,\mathrm{MP}}}{\sum_{h=1}^{m} S_{h,\mathrm{DPNV}}} = \frac{(v_{s,\mathrm{MP}} + v_{t,\mathrm{MP}})(i_{s,\mathrm{MP}} + i_{t,\mathrm{MP}})}{v_{s,\mathrm{MP}} i_{s,\mathrm{MP}} + (v_{t,\mathrm{MP}} + 2v_{s,\mathrm{MP}}) i_{t,\mathrm{MP}}}$$

Similar to the analysis in Section 2.5.1, a preferred set of operating points (force, torque, and speed) based on the total VA rating can be determined for the multiphase and DPNV windings. By using $v_{s,\mathrm{MP}} = i_{s,\mathrm{MP}} z_s$, the following is obtained (subscripts "MP" are removed for easier notation):

$$P_2 = \frac{z_s i_s^2 + v_t i_t + v_t i_s + z_s i_s i_t}{z_s i_s^2 + v_t i_t + 2 z_s i_s i_t} \begin{cases} < 1 & \text{multiphase preferred} \\ > 1 & \text{DPNV preferred} \end{cases}$$

which simplifies to

$$\begin{aligned} v_t &< z_s i_t \quad \text{multiphase preferred} \\ v_t &> z_s i_t \quad \text{DPNV preferred} \end{aligned} \tag{2.42}$$

This shows that the boundary between when the multiphase and DPNV windings are preferred depends on the machine's torque and speed (through the voltage v_t), but not on the force. However, note that other regions where $P_2 \neq 1$ do depend on the suspension force (in addition to torque and speed). This inequality can be more advantageously expressed as (2.43) by substituting (2.41) into (2.42), squaring both sides, and rewriting as a quadratic inequality in terms of ω_m.

$$a(\tau)\omega_m^2 + b(\tau)\omega_m + c(\tau) \begin{cases} < 0 & \text{multiphase preferred} \\ > 0 & \text{DPNV preferred} \end{cases} \tag{2.43}$$

Here, a, b, and c are the coefficients expressed in terms of the torque and machine parameters of the multiphase winding (Table 2.2):

$$\begin{aligned} a(\tau) &= (mp\tau)^2 LM + k_t^4,\ b(\tau) = R_{dq}\tau m k_t^2 \\ c(\tau) &= \frac{1}{4}(R_{dq}^2 - R_{xy}^2)\tau^2 m^2 \end{aligned} \tag{2.44}$$

where $c = 0$ because $R_{dq} = R_{xy} = R$ in the multiphase winding. The two roots of the equation $a\omega_m^2 + b\omega_m = 0$ (solution to (2.43)) represent the boundary between when the multiphase or DPNV winding has a lower VA rating:

$$\omega_{m,1} = 0,\ \omega_{m,2} = \omega_c(\tau) = -\frac{b(\tau)}{a(\tau)} \tag{2.45}$$

From (2.45), it is evident that zero speed is a boundary and the other boundary speed is a function of torque.

The results in terms of these parameters are summarized in Table 2.3 for each winding. In the authors' experience, all practical machine designs have $k_t^4 \gg (mp\tau)^2 LM$ over their entire operating range, meaning that a is approximately constant at $a \approx k_t^4$. This results in an almost linear dependence of $\omega_c(\tau)$ on τ. The results for this case are presented graphically

Criterion	multiphase preferred when		
P_1	$\tau/k_t > F/k_f$		
P_2		$a > 0$	$a < 0$
	$\tau > 0$	$\omega_c < \omega_m < 0$	$\omega_m < 0$ or $\omega_m > \omega_c$
	$\tau < 0$	$0 < \omega_m < \omega_c$	$\omega_m < \omega_c$ or $\omega_m > 0$

DPNV winding is preferred in all other conditions

Table 2.3: Summary of Winding Type Comparison

in Fig. 2.9b on a torque-speed map (ω_r is the rated rotor speed). Unlike Fig. 2.9a, this plot has two $P_2 = 1$ boundary lines that separate the multiphase and DPNV winding regions. These two lines represent the two critical speeds given in (2.45), one line always being at zero speed for any torque value (vertical line) and another line described by $\omega_c(\tau)$. Figure 2.9b shows that the multiphase winding drive can only be rated for a lower total VA when the machine is a generator. In a hypothetical machine with $a < 0$, the multiphase winding would have a lower total VA rating in the motoring mode–see Table 2.3.

Finally, it is evident from the definition of P_2 that if no suspension force is utilized ($i_s = 0$), $P_2 = 1$ for all torque and speed operating points. This means that for bearingless machines which nominally require very little suspension current (relative to torque current), there will likely be no meaningful VA rating difference between the two winding topologies.

2.5.3 Drive Comparison Case Study Using Example Motor

The multiphase and DPNV drives are now compared for the example vernier motor to validate the theoretical developments of this chapter and provide an example of the practical considerations involved in selecting the winding topology. The section concludes that the multiphase winding is preferred for this motor.

2.5.3.1 Comparison in terms of P_1 and P_2

Figure 2.10a shows a plot of P_1 for a range of force and torque values. As expected from Fig. 2.9a, the $P_1 = 1$ boundary line corresponds to $\tau/k_t = F/k_f$, the region below it being

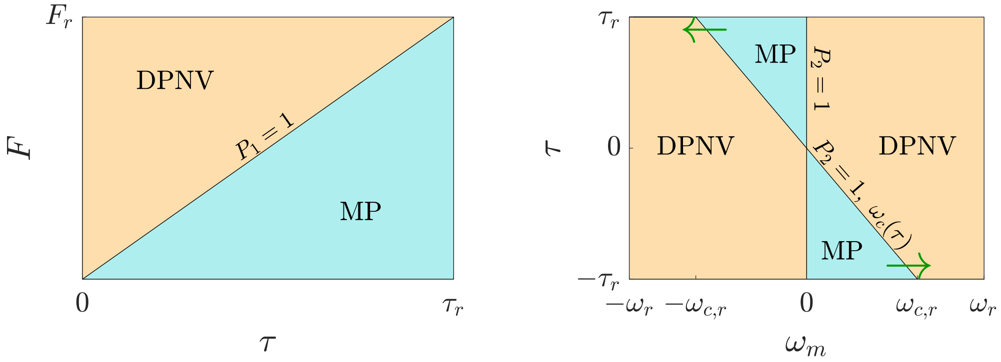

(a) (b)

Figure 2.9: Preferred regions of each winding (a) P_1, (b) P_2 when $a > 0$.

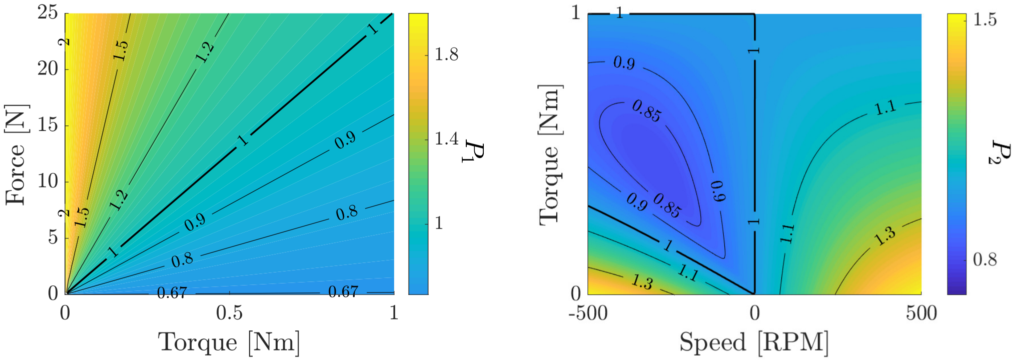

(a) (b)

Figure 2.10: Performance metrics of Fig. 2.9 for the example vernier machine.

preferred for the multiphase winding and the region above for the DPNV winding. The Fig. 2.9b plot is reproduced in Fig. 2.10b for the vernier motor, which has $\omega_{c,r} = 1491$ RPM $> \omega_r$. The force output is adjusted depending on the torque so that the coils carry rated current. As expected, there are two lines of $P_2 = 1$, one at zero speed and one determined by the torque.

This analysis shows that the DPNV driving is at a substantial advantage when suspension current comprises over 50% of the total coil current and the speed is close to its rated value. When suspension current is less than 50%, although the DPNV winding has lower total VA rating than the multiphase winding (at positive speeds), the difference is comparatively small and the multiphase winding might be preferred due to lower total RMS current rating.

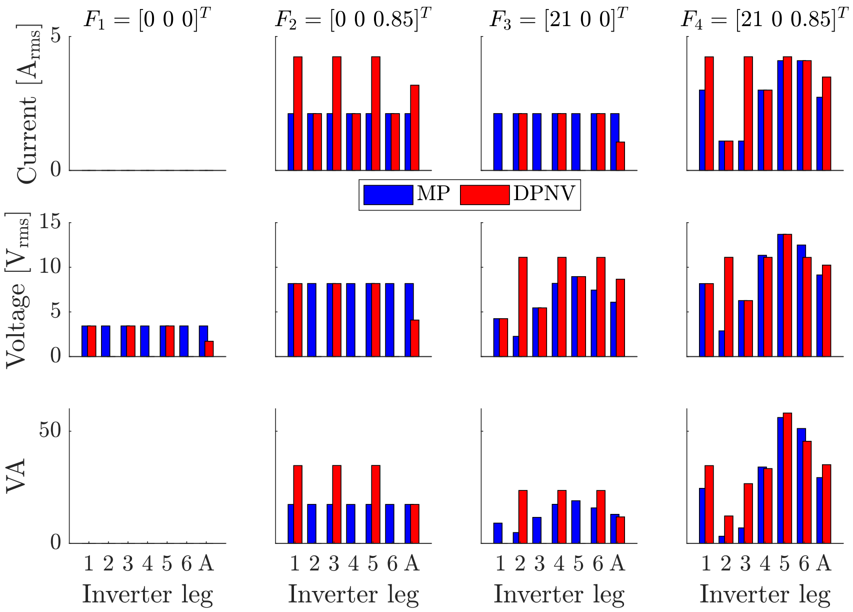

Figure 2.11: Performance comparison at 500 RPM. DPNV inverter torque phases: 1, 3, 5; suspension: 2, 4, 6. $\boldsymbol{F} = [F_x\ F_y\ \tau]^T$ in units of [N N Nm]^T.

In addition, the multiphase winding is shown to perform better in generating mode having about 85% of the total VA rating than the DPNV winding at some torque-speed values.

2.5.3.2 Comparison at Specific Force/Torque Commands

Section 2.5.3.1 analyzed the relative merits of each winding based on the drive rating. In deciding between the two windings, a designer may also consider the inverter losses over a drive cycle. This can be calculated with knowledge of the inverter implementation (silicon devices used, switching frequency, number of inverter levels) combined with the steady state current and apparent power of each inverter phase. It should be noted that P_1 and P_2 (Fig. 2.10) do not actually indicate the steady state current and apparent power of the drive phases at individual operating points (primarily due to the dependence on force angle ϕ). These quantities are difficult to calculate for a general machine and are therefore explored for the vernier machine as an example of analysis that a designer could perform for their machine.

Figure 2.11 presents current, voltage, and apparent power of each inverter phase and the

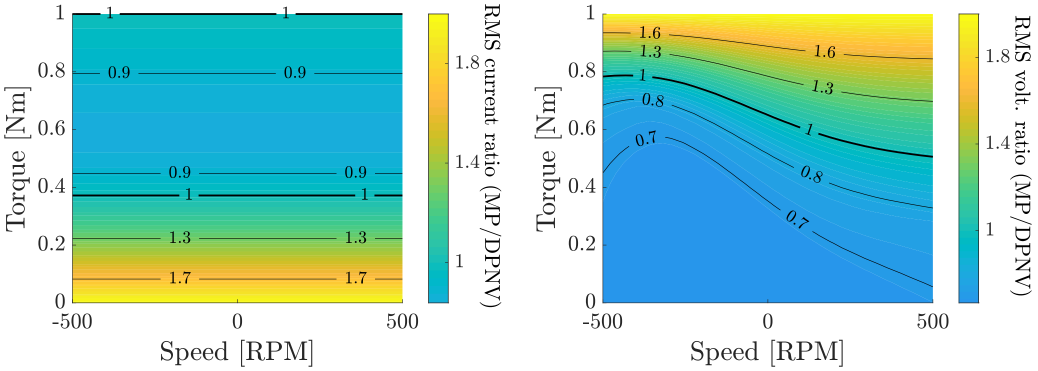

(a) (b)

Figure 2.12: Ratio of average multiphase to DPNV drive phase (a) current and (b) voltage.

same quantities averaged over all phases (denoted as "A") at four force/torque points at 500 RPM. To create torque (column 2), the multiphase drive uses 30% less average phase current, approximately matching P_1 in Fig. 2.10a. To create force (column 3), the DPNV drive uses 50% less current and 10% less apparent power, approximately matching P_1 and P_2 in Fig. 2.10. In column 4, $\tau/k_t = F/k_f$ and the multiphase drive provides 16% less apparent power and 20% less current, which does not match $P_1 = 1$ or $P_2 = 1.1$ in Fig. 2.10. However, if the machine is held in constant power while increasing the rotor speed 5 times, the DPNV drive provides 5% less apparent power and 30% less current. This analysis is extended by considering the map of average phase RMS current and RMS voltage ratios between the two topologies provided in Fig. 2.12, where force is again adjusted based on torque to keep the coils at rated current. The same general trends are observed from this analysis as from the analysis based on P_1 and P_2. That is, the DPNV winding generally performs better when operating near rated speed and higher force, while the multiphase winding performs better in other cases.

2.5.3.3 Comparison Based on DC Bus Voltage Requirement

The required DC bus voltage can be calculated for both windings by determining the value required to avoid current regulator saturation. Table 2.4 makes this comparison for different force/torque command slew rates about the force/torque command $\boldsymbol{F} = [10\text{ N},\ 5\text{ N},\ 1\text{ Nm}]^T$

Slew rate	6-phase	DPNV
0 N/ms, 0 Nm/ms	17 V	17 V torque, 10 V susp.
11.7 N/ms, 0.45 Nm/ms	31 V	29 V torque, 23 V susp.
52 N/ms, 2 Nm/ms	45 V	44 V torque, 53 V susp.

Table 2.4: DC Link Voltage Comparison for Vernier Motor

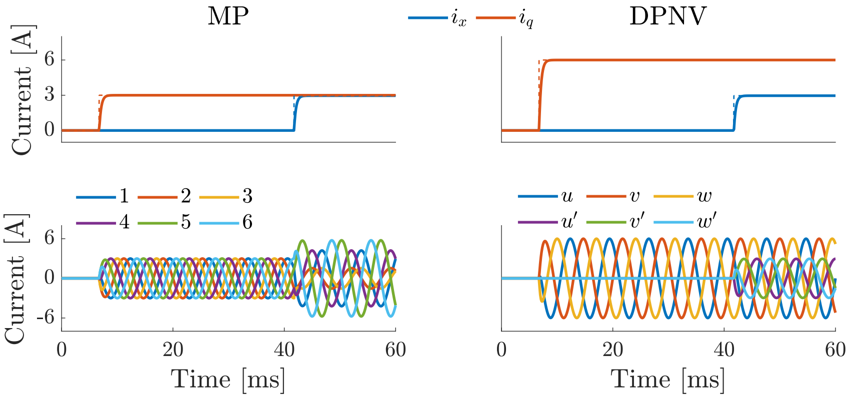

Figure 2.13: Simulation results for multiphase and DPNV with the same current regulator bandwidth ($f_b = 450$ Hz). Time-constant = 0.354 ms.

with the rotor speed of 500 RPM. The slew rates in rows two and three correspond to a ramp from zero to rated force/torque within a bandwidth of 450 Hz and 2 kHz. For both configurations, the required DC link voltage is $\sqrt{3}$ times the maximum phase voltage. The multiphase and the DPNV torque terminals require similar DC link voltage. If the DPNV winding is configured using two isolated DC voltage sources, the DPNV suspension terminals can use a lower bus voltage (rows 1 and 2), which is advantageous when a larger motor inverter DC link voltage is required.

2.5.3.4 Bandwidth Comparison

The current controllers of both topologies will have identical bandwidths and a first order system response if the controller parameters are tuned using (2.37) and Table 2.2. To demonstrate this, the current response is simulated in Simulink for torque and force step commands in the multiphase and DPNV winding configurations of the example vernier motor. The machine is modeled using the phase voltage equations in a matrix form. Direct/inverse Park and generalized Clarke transform matrices transform to/from synchronous dq and xy reference frames as shown in Fig. 2.8. All current controllers are tuned to 450 Hz and the rotor speed is 500 RPM. Figure 6.7 shows plots of i_x and i_q and the phase currents for both windings. The magnitude of i_q in the DPNV winding is twice the magnitude of i_q in the multiphase winding, as expected. The time constant is these plots is 0.354 ms in both the multiphase and DPNV topologies' force and torque currents.

2.5.3.5 Selection of Winding Topology

The most advantageous winding for this machine is now determined based on the results of Section 2.5.3.1 through 2.5.3.4. This machine is a vertically oriented slice motor and has a very minimal force magnitude requirement (typically < 5N), but substantial torque requirement (≈ 1Nm). From Fig. 2.10, the two performance metrics are evaluated as $0.7 < P_1 < 0.8$ (favoring MP) and $1 < P_2 < 1.1$ at rated speed (slightly favoring DPNV). The second row of Table 2.4 shows that to move from zero to rated force/torque within a current regulator bandwidth of 450Hz requires a similar dc link voltage for both winding topologies. The suspension inverter of the DPNV winding could be implemented with a lower voltage bus (23V instead of 29V), but the benefit of such a small reduction in voltage is minimal and would require the introduction of a second dc source (adds additional drive cost and size). In conclusion, for this high torque, low force motor, the multiphase winding more effectively utilizes the inverter current while requiring a similar dc link voltage. This makes

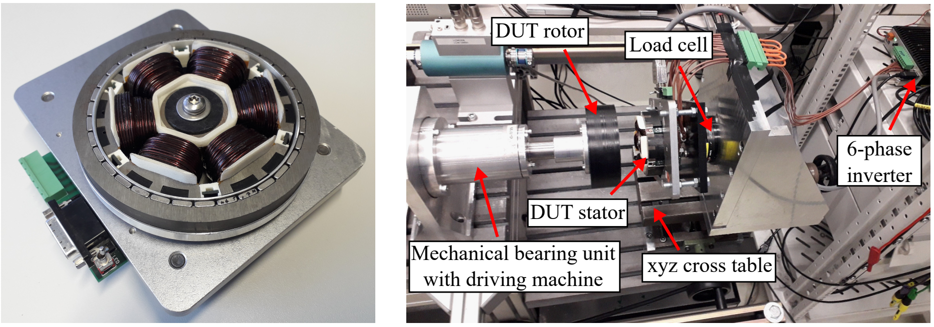

(a) (b)

Figure 2.14: (a) Bearingless PM vernier slice motor [1], and (b) experimental test setup; "DUT" is device under test.

the multiphase winding the most advantageous winding choice for this machine.

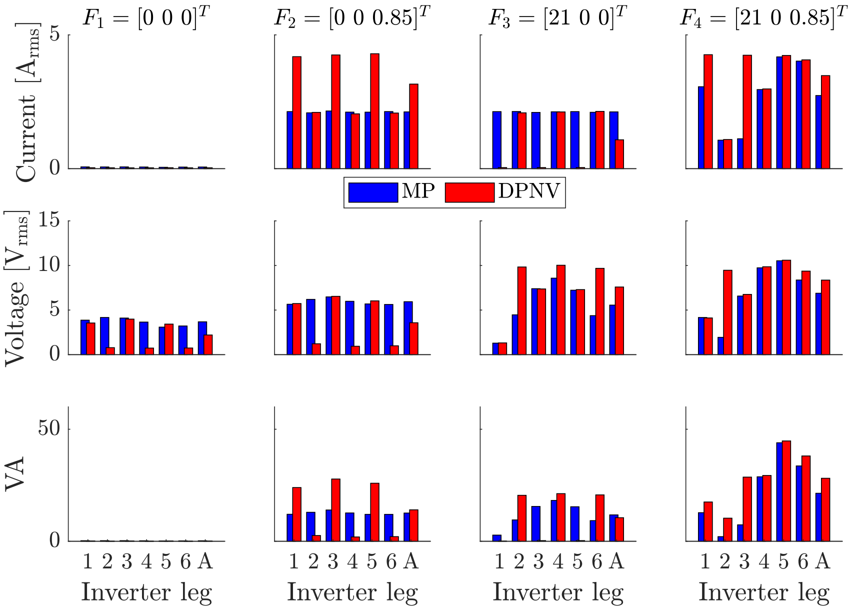

Figure 2.15: Experiment results: performance comparison at different force/torque commands with rotor speed of 500 RPM (DPNV inverter torque phases: 1, 3, 5; suspension: 2, 4, 6). $\boldsymbol{F} = [F_x\ F_y\ \tau]^T$ in units of $[\text{N N Nm}]^T$.

2.6 Experimental Validation

Experimental validation is now provided using the prototype bearingless machine and test stand shown in Fig. 2.14. Emphasis is placed on confirming the voltage and current that each drive must provide to regulate force and torque (Section 2.5.3.2) and the transient response of the two drives (Section 2.5.3.4). The motor is tested with the windings configured as both multiphase and DPNV, using the regulation architecture shown in Fig. 2.8.

In the first set of tests, the rotor was driven by an external motor at a speed of 500 RPM and the drive regulated the same torque and force commands that were previously simulated in Section 2.5.3.2. Reaction forces and torque on the stator were measured on a load cell and, across all operating points, the DPNV and multiphase configuration created the same force and torque to within 0.8 N and 0.03 Nm. The inverter phase voltage and current were measured using the bearingless drive. The results are summarized in Fig. 2.15

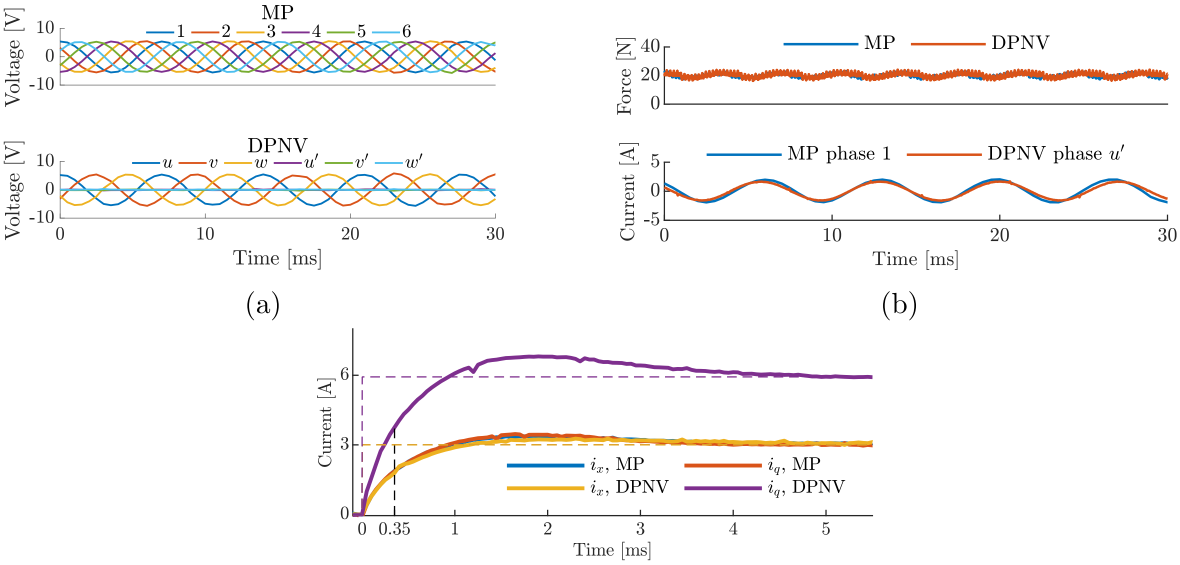

(a) (b)

(c)

Figure 2.16: Experiment results: (a) measured phase voltages at 500 RPM under no-load condition, (b) measured force and phase currents at 500 RPM for the force command of column 3 of Fig. 2.15, and (c) measured current step responses plotted on the same axis (all regulators tuned for the same bandwidth).

which can be directly compared to Fig. 2.11. The terminal voltage waveforms for column 1 of Fig. 2.15 are shown in Fig. 2.16a. As expected, the DPNV suspension terminal voltages are almost zero due to back-EMF cancellation, while the DPNV torque terminals and all multiphase terminals have a 5.2V amplitude (3.68 V_{rms}). This corresponds to 3.5 V_{rms} in simulation (Fig. 2.11, column 1). The forces / currents for column 3 of Fig. 2.15 are shown in Fig. 2.16b, which demonstrates both drives use identical coil currents.

The Fig. 2.15 data confirm the drive comparison previously reported in Section 2.5.3.2 as follows: in column 2, the multiphase drive uses less average current (hardware vs simulation: 33% vs 30%); in column 3, the DPNV drive uses less current (49% vs 50%) and less apparent power (11% vs 10%); in column 4, the multiphase drive utilizes less current (21% vs 20%) and less apparent power (23% vs 16%).

Finally, the torque and force step response of the multiphase and DPNV drives is experimentally measured. Force and torque commands are issued while the rotor is spinning at 500 RPM in the same manner as depicted in Fig 6.7. The resulting currents are plotted on a single axis in Fig. 2.16c to enable a direct comparison between the drives. All regulators were tuned using (2.37) and have a measured bandwidth of approximately 450 Hz. The slight overshoot that is observed is attributed to inaccuracies in the machine parameters R, L, and M.

The steady state experimental results of the first set of tests are shown to be in close agreement with the results of Section 2.5.3.2. This confirms the force, torque, and electric models developed in Section 2.3 and 2.4. The transient results of the second test validate the regulator architecture and tuning approach of Section 2.4.4, demonstrating that both windings can yield equivalent torque/force regulator bandwidth when sufficient voltage is available. Together, these results experimentally validate the theoretical framework that this chapter has developed and the basis for the drive comparison in Section 2.5.

2.7 Conclusion

This chapter investigates and compares the multiphase and parallel DPNV combined windings. These topologies are shown to be capable of fully actuating the machine (torque and field weakening) independent of actuating x and y suspension forces. The chapter develops analogous mathematical models to facilitate a comparison between the two windings using a prototype machine, determines power electronic drive requirements, and presents experimental validation. A primary goal of the chapter is to identify machine characteristics that determine when a designer may find either of these windings most advantageous.

Matrix-based models of the bearingless motor developed in the chapter demonstrate that the two winding topologies utilize equivalent stator coil currents to create identical torque and force vectors, while relying on significantly different terminal currents. This is combined with other fundamental properties of the bearingless machine's force and torque characteristic to establish that any multiphase winding with an even number of phases can be configured as a parallel DPNV winding. The generalized Clarke transformation for multi-phase systems is used to construct space vector models for both winding topologies. The resulting current space vectors consist of current components that can be used to independently create torque and suspension force. This finding is used as the basis for developing a generalized force and torque regulator architecture. It is shown that identical force and torque regulation bandwidth can be achieved for each winding topology by using the tuning approach presented in this chapter.

The primary performance difference identified between these two windings resides in the power electronics. Drive requirements of these windings were compared analytically and experimentally. Multiphase windings were shown to more effectively utilize drive current when over half of the coil current produces torque rather than force. The DPNV windings were shown to require a lower VA rating when operating at high speeds and low torque, high force. These results indicate that the multiphase winding is most advantageously used in bearingless motor designs that require substantially more torque than suspension current, while the parallel DPNV winding is most advantageously used in motors with high force requirements or applications with limited DC bus voltage available.

Chapter 3

Analysis and Design of Multiphase Combined Windings

3.1 Introduction

While the multiphase winding is inherently compatible with more stator designs than the DPNV winding, there is currently no generalized method that can be applied to design a multiphase combined winding. Study [42] provides a list of multiphase winding configurations and determines whether force and torque decoupling is possible. However, the results are limited to concentrated windings with one coil per phase, and no analytic design procedure was provided to design a multiphase winding for an arbitrary number of slots, poles, and phases. This chapter fills this gap by analytically deriving a set of design requirements and proposing a formal winding design procedure, which pertain to all radial-flux bearingless machines. In these machines, torque and radial suspension suspension forces are created from the interaction between radial magnetic fields. The derivations are provided for non-salient machines, using surface permanent magnet (SPM) and induction machines as examples. This work is analogous to [51], which derived design requirements and proposed a generalized design procedure for DPNV windings. [1]

The core contributions of this chapter are:

- Determination of which combinations of electric machine slots, poles, and phases can be used to design symmetric multiphase combined windings (Section 3.5).
- Identification of design criteria that allow a multiphase combined winding to be operated from a DPNV drive (Section VI).
- Proposal of a generalized multiphase combined winding design theory based on the star of slots approach and the results from Sections 3.3 and 3.5 (Section 3.7).

Section 3.2 introduces multiphase combined windings and reviews relevant literature. Section 3.3 develops a force/torque model using the Maxwell stress tensor and Section 3.4 develops winding analysis concepts for the multiphase combined winding by extending standard fractional slot winding theory [11]. Using the results from these sections, Section 3.5 develops design requirements in the form of constraint equations and Section 3.6 makes a comparison to the DPNV winding. These design requirement can also be used to determine whether existing multiphase motor designs can be transformed into bearingless machines through control action alone. Section 3.7 proposes a multiphase combined winding design procedure for symmetric windings using the star of slots approach. Section 3.8 validates the developed theory using finite element analysis (FEA) and hardware measurements from a six-phase bearingless induction machine prototype. The developments in this chapter form a basis for analysing and designing bearingless machines with multiple controllable airgap harmonic fields in the following chapters of this dissertation.

3.2 Multiphase Combined Windings

It is well-known that multiphase machines are able to produce multiple magnetic field harmonics in the airgap [90]. Bearingless motors with multiphase combined windings use this

---

[1] Portions of the material in this chapter have also been published in [84].

capability to create one field for torque and a second field for suspension. These windings have $m > 3$ distinct connections to the bearingless drive, as shown in Fig. 3.1. Depending on the drive design requirement, the phases can share a single neutral point or be grouped to have several neutral points.

The phase currents in conventional multiphase machines can be transformed into multiple independent space vectors located in independent rotating reference frames (orthogonal subspaces) [88]. Study [91] presented a Generalized Clarke transformation matrix for symmetrical multiphase windings that is used to obtain these independent space vectors. In conventional multiphase machines, a single rotating reference frame represents the torque creation, while other reference frames represent the machine's harmonic patterns which highlight the possible unbalance among the phases [90]. A number of other studies have been presented that use these reference frames for different non-traditional purposes. Study [92], for example, presented decoupled dq axes control in multi-three-phase induction machines. Study [93] surveyed innovative ways of exploiting additional DOFs of multiphase systems. One such example is series connected multiphase motors which are connected to a single inverter and the torque in each motor is created independently (represented by two independent space vectors).

The bearingless machine requires p pole-pairs on the rotor and stator winding to create torque, and $p_s = p \pm 1$ pole-pairs on the stator winding to create suspension forces. This implies that the multiphase combined winding must be intentionally designed to be capable of creating magnetic field space harmonics at p and p_s. As a result, the same theory that is used in multiphase machines can be extended to multiphase combined windings to independently control radial suspension forces and torque in two independent rotating frames. However, the following two requirements must be met to ensure that the winding is:

1. symmetric; that is, a rotating magnetic field is created when supplied from a symmetrical supply.

2. capable of independently controlling force and torque.

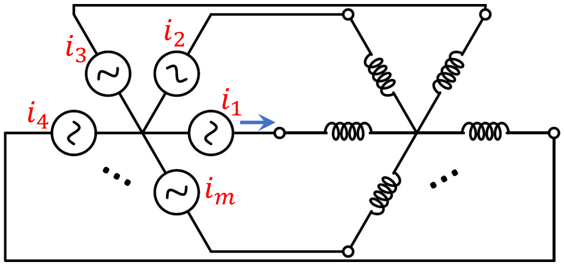

Figure 3.1: Circuit diagram with m drive connections.

The winding layout and the current excitation must be studied and used to derive these requirements in terms of the machine parameters (number of phases m, torque p and suspension p_s pole-pairs, and slots Q). For this, the bearingless machine force/torque matrix model is presented in the following section and used in later sections.

3.3 Multiphase Combined Winding Matrix Model

This section presents a bearingless machine matrix model and develops analytic expressions for the created forces and torque in terms of the phase currents and the rotor angle.

3.3.1 Force/Torque Matrix Model

The operating theory for a bearingless machine can be represented using matrices. This model shows the relationship between the created forces/torque, the drive terminal currents, and the rotor position. For a centered rotor position, this relationship can be expressed as $\boldsymbol{F}(\theta_m) = \boldsymbol{T_m}(\theta_m)\boldsymbol{i}$ and is shown in (2.2). For a machine with m phases, $\boldsymbol{T_m}$ is of the form:

$$\boldsymbol{T_m} = \begin{bmatrix} \boldsymbol{T_{mx}} \\ \boldsymbol{T_{my}} \\ \boldsymbol{T_{mt}} \end{bmatrix} = \begin{bmatrix} T_{mx,1} & T_{mx,2} & \dots & T_{mx,m} \\ T_{my,1} & T_{my,2} & \dots & T_{my,m} \\ T_{mt,1} & T_{mt,2} & \dots & T_{mt,m} \end{bmatrix} \tag{3.1}$$

Having the phase currents $\boldsymbol{i} = [i_1 \ i_2 \ \dots \ i_m]^T$ and using (3.1), the model (2.2) can be rewritten for each force and torque as

$$F_d(\theta) = \boldsymbol{T_{md}}\boldsymbol{i} = \sum_{k=1}^{m} F_{d,k}(\theta) = \sum_{k=1}^{m} T_{md,k}(\theta) i_k \tag{3.2}$$

$$\tau(\theta) = \boldsymbol{T_{mt}}\boldsymbol{i} = \sum_{k=1}^{m} \tau_k(\theta) = \sum_{k=1}^{m} T_{mt,k}(\theta) i_k \tag{3.3}$$

where $d = x$ or y, and $\theta = p\theta_m$ is an electrical rotor angle. $F_{d,k}$ and τ_k are the force and torque created by phase winding k. Each $\boldsymbol{T_m}$ matrix entry can be interpreted as a per ampere force or torque created when only a single phase is excited.

Suppose that the phase currents can be written as the sum of two current vectors for suspension $\boldsymbol{i_s}$ and for torque $\boldsymbol{i_t}$:

$$\boldsymbol{i} = \begin{bmatrix} i_1 \\ i_2 \\ \dots \\ i_m \end{bmatrix} = \boldsymbol{i_s} + \boldsymbol{i_t} = \begin{bmatrix} i_{s,1} \\ i_{s,2} \\ \dots \\ i_{s,m} \end{bmatrix} + \begin{bmatrix} i_{t,1} \\ i_{t,2} \\ \dots \\ i_{t,m} \end{bmatrix} \tag{3.4}$$

Substituting (3.4) into (3.2)-(3.3), the design requirements requirements presented in Section 3.2 can be rewritten as: 1) symmetry: $\boldsymbol{T_{md}}\boldsymbol{i_s}$ and $\boldsymbol{T_{mt}}\boldsymbol{i_t}$ are independent of the rotor angle θ, and 2) independent force and torque creation: $\boldsymbol{T_{md}}\boldsymbol{i_t} = 0$ and $\boldsymbol{T_{mt}}\boldsymbol{i_s} = 0$. Depending on $\boldsymbol{T_m}$ matrix, the desired $\boldsymbol{i_s}$ and $\boldsymbol{i_t}$ satisfying these constraints can be determined and the multiphase combined winding design requirements can be derived. The derivation of the entries of $\boldsymbol{T_m}$ is now presented.

3.3.2 Derivation of $\boldsymbol{T_m}$ matrix entries

The Maxwell stress tensor is used to calculate force/torque:

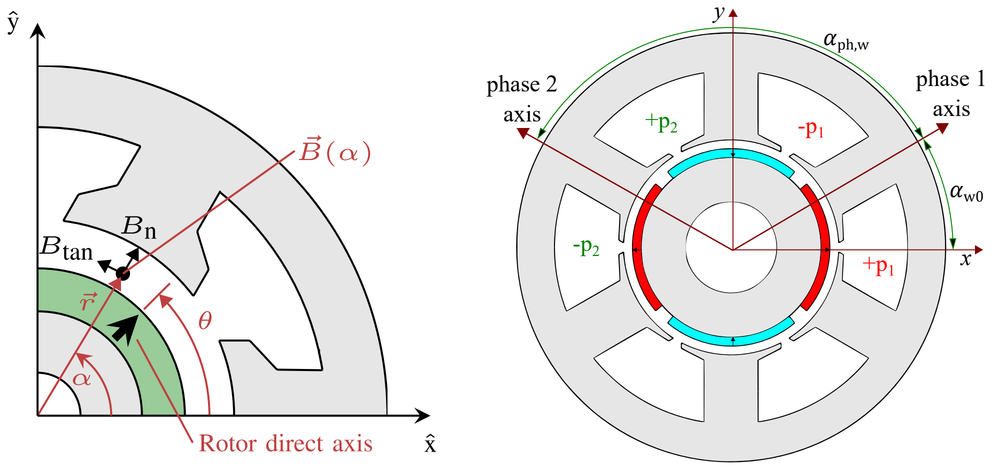

(a) (b)

Figure 3.2: Definitions of: (a) magnetic field components, unit vectors, and angles (α and θ) and (b) axes and winding phase angles ($\alpha_{\mathrm{ph,w}}$ and α_{w0}); $+\mathrm{p}_1$ and $-\mathrm{p}_1$ denote phase 1 coil sides going into and out of the page, respectively.

$$\vec{\sigma} = \begin{bmatrix} \sigma_{\mathrm{n}} \\ \sigma_{\tan} \end{bmatrix} = \begin{bmatrix} \frac{1}{2\mu_0}(B_{\mathrm{n}}^2 - B_{\tan}^2) \\ \frac{1}{\mu_0} B_{\mathrm{n}} B_{\tan} \end{bmatrix} \tag{3.5}$$

where σ_{n} and $\sigma_{\tan}$ are the normal and tangential components of the per unit area force (stress) acting on the surface of the rotor. This force is created from the interaction between the tangential ($B_{\tan}$) and normal (B_{n}) components of the magnetic field in the airgap, which are depicted in Fig. 4.1a. These stresses can be integrated over the rotor's airgap surface S to determine the net forces and torque acting on the rotor:

$$F_x = \int_S \vec{\sigma} \cdot \hat{\mathrm{x}}\, \mathrm{d}S, \;\; F_y = \int_S \vec{\sigma} \cdot \hat{\mathrm{y}}\, \mathrm{d}S, \;\; \tau = \int_S \vec{r} \times \vec{\sigma}\, \mathrm{d}S \tag{3.6}$$

where α is the airgap angle (see Fig. 4.1a), $\vec{r}$ is the airgap radius vector, and $\hat{\mathrm{x}}$ and $\hat{\mathrm{y}}$ are the unit vectors.

The $\boldsymbol{T_m}$ matrix entries are now determined using the following steps. When phase k is excited by current i_k,

1. expressions for the airgap magnetic field normal $B_{\mathrm{n},k}$ and tangential $B_{\mathrm{tan},k}$ components are determined;
2. $F_{x,k}$, $F_{y,k}$, τ_k are determined using (3.6); and
3. finally, the $\boldsymbol{T_m}$ matrix entries are calculated from $T_{mx,k} = F_{x,k}/i_k$, $T_{my,k} = F_{y,k}/i_k$, and $T_{mt,k} = \tau_k/i_k$.

As will be shown, each $\boldsymbol{T_m}$ matrix entry is a function of the fixed machine parameters and the rotor angle, but not the phase currents. The above steps are now illustrated.

3.3.2.1 Step 1

The total magnetic field in the airgap is created by rotor and stator magnetic field sources (shown for B_n):

$$B_\mathrm{n} = B_\mathrm{n,r} + B_\mathrm{n,s} \tag{3.7}$$

In SPM machines, $B_\mathrm{n,s} = B_\mathrm{n,w}$ is created by stator winding currents and $B_\mathrm{n,r}$ is created by permanent magnets described by $B_\mathrm{n,r} = B_\delta = \hat{B}_\delta \cos(p\alpha - \theta)$ (also known as the magnetizing field). Stator winding currents must create both p and p_s pole-pair fields to interact with the rotor's p pole-pair field and create torque and forces.

In induction machines, $B_\mathrm{n,s} = B_\mathrm{n,w}$ is also created by stator winding currents and $B_\mathrm{n,r}$ is created by currents induced in the rotor windings/bars. The stator winding currents create the magnetizing field B_δ and the reaction field to the rotor field $B'_\mathrm{n,r} = -B_\mathrm{n,r}$ at p pole-pairs, and suspension field at p_s pole-pairs. When a pole-specific rotor structure is used, the stator p_s pole-pair field does not induce currents in the rotor and no reaction field is created, see [7].

The total magnetic field from stator windings $B_\mathrm{n,w}$ can be expressed as the sum of fields from each phase winding. The field from each phase winding is determined using the well-known linear current density $A_k(\alpha)$ that can be expressed as the sum of all space harmonics (shows the current distribution along the inner bore of the stator),

$$A_k(\alpha) = \frac{i_k}{r} \sum_{h=1}^{\infty} A'_{c,\mathrm{ph},h} \sin\left(h[\alpha - \alpha_{\mathrm{w},k}]\right) \tag{3.8}$$

where $A'_{c,\mathrm{ph},h}$ is a normalized parameter showing the effective number of turns per radian for the space harmonic h and $\alpha_{\mathrm{w},k}$ is the angular location where the current density at harmonic h is zero. For torque and suspension pole-pairs, $A'_{c,\mathrm{ph},h}$ is denoted as $A'_{c,\mathrm{ph},t}$ and $A'_{c,\mathrm{ph},s}$.

Using (3.8), the winding magnetic field components created by a phase k can be determined as

$$B_{\mathrm{n,w},k} = \frac{\mu_0 i_k}{\delta_{\mathrm{eff}}} \sum_{h=1}^{\infty} \frac{A'_{c,\mathrm{ph},h}}{h} \cos\left(h[\alpha - \alpha_{\mathrm{w},k}]\right) \tag{3.9}$$

$$B_{\mathrm{tan,w},k} = -\frac{\mu_0 i_k}{r} \sum_{h=1}^{\infty} A'_{c,\mathrm{ph},h} \sin\left(h[\alpha - \alpha_{\mathrm{w},k}]\right) \tag{3.10}$$

These expressions are used to derive per phase forces and torque in the following steps.

3.3.2.2 Steps 2 and 3

The forces and torque $F_{x,k}$, $F_{y,k}$, τ_k created by phase k current are determined using (3.6). The torque per phase τ_k is calculated by substituting (3.5) into (3.6):

$$\tau_k = \frac{r^2 L}{\mu_0} \int_0^{2\pi} B_{\mathrm{n},k} B_{\mathrm{tan},k} \,\mathrm{d}\alpha \tag{3.11}$$

Evaluating (3.11) for harmonic p and dividing the result by i_k, entries of the row $\boldsymbol{T_{mt}}$ are obtained:

$$T_{mt,k} = -\hat{T}_{mt} \sin\left(\theta - p\alpha_{\mathrm{w},k}\right),\ \hat{T}_{mt} = \frac{V_r \hat{B}_\delta A'_{c,\mathrm{ph},t}}{r} \tag{3.12}$$

which shows created torque per ampere due to phase k.

The $\boldsymbol{T_{mx}}$ and $\boldsymbol{T_{my}}$ entries can be derived similarly. The difference from torque creation is that the force is created from the interaction between adjacent harmonics h and $h \pm 1$. At $h = p$, it can be shown that the $\boldsymbol{T_{mx}}$ and $\boldsymbol{T_{my}}$ entries are:

$$T_{md,k} = \hat{T}_{mf,h_1} f_d(\theta - h_1 \alpha_{\mathrm{w},k}) \pm \hat{T}_{mf,h_2} f_d(\theta - h_2 \alpha_{\mathrm{w},k}) \tag{3.13}$$

which shows created force per ampere due to phase k. Here, the ± term is $+$ for $d = x$ and $-$ for $d = y$; f_x and f_y are cosine and sine functions. $\hat{T}_{mf,h_1}$ and $\hat{T}_{mf,h_2}$ are (3.14), where h_s $= h_1$ or h_2.

$$\hat{T}_{mf} = \frac{V_r \hat{B}_\delta A'_{c,\mathrm{ph},h_s}}{2r} \left(\frac{1}{h_s \delta} + \frac{h_s - p}{r} \right) \tag{3.14}$$

Section 3.5 will use the results (3.12)-(3.13) and (3.2)-(3.3) to derive conditions for viable windings.

3.4 Multiphase Combined Winding Analysis

The standard fractional slot winding analysis techniques presented in textbooks such as [11] are now extended to enable analysis of multiphase combined windings for bearingless motors. The results of this analysis will be used to derive winding requirements in Section 3.5 and to develop the winding design procedure proposed in Section 3.7.

3.4.1 Star of Slots

It is common practice to design conventional stator windings (non-bearingless) using the "star of slots" diagram [11]. This diagram shows the phasor of a particular harmonic of back-EMF induced in each coil side. Using this diagram, the winding layout of the motor (phase assignment of the coil sides) can be determined. This approach can be analogously extended to multiphase combined windings, the key difference being that two winding harmonics are now considered, $h = p$ (torque) and $h = p_s$ (force creation). This document uses the terms "torque star of slots" and "suspension star of slots" to indicate that the star of slots diagram is drawn at harmonic p or p_s.

Example torque and suspension star of slots diagrams are shown in Fig. 3.3 for a motor with $Q = 8$ slots, $p = 2$, and $p_s = 3$. The phasor of the first slot is drawn horizontally and subsequent phasors lag by $p\alpha_u$ (or $p_s\alpha_u$). Depending on the values of p and p_s, Fig. 3.3 shows that several slots can have the same phasor location. Further, the angle between the phasors of adjacent slots may not be equal to the angle between adjacent phasors. For example, Fig. 3.3b shows that the angle between slots 1 and 2 is 135°, while the angle between adjacent phasors (slots 1 and 4) is 45°. This phasor angle can be determined using the following equation [11]:

$$\alpha_z = \frac{2\pi}{Q} t \tag{3.15}$$

where t is either $\gcd(Q, p)$ or $\gcd(Q, p_s)$.

The winding design procedure proposed in Section 3.7 leverages the star of slots diagram because it provides a convenient method to determine the winding's ability to create both p and p_s pole-pair fields in the airgap. The torque and suspension star of slots are used along with phasor summation properties to determine the effects of different phase-slot assignments on these harmonics, identify phase zones, and determine phase separation of current components to create the p and p_s pole-pair fields. While these aspects could be determined using winding function theory, this would require additional tools such as the Fourier Transform.

3.4.2 Winding Factor

The winding factor is useful for comparing windings. For double-layer windings, at harmonic h, it is defined as:

$$\hat{k}_{w,h} = \hat{k}_{d,h}\hat{k}_{p,h} \tag{3.16}$$

where $\hat{k}_{d,h}$ is a distribution factor that is found by summing all phasors assigned to one phase in the star of slots and $\hat{k}_{d,h}$ is a pitch factor that is determined by a coil span y:

$$\hat{k}_{d,h} = \left| \frac{1}{z_c} \sum_{i=1}^{z_c} e^{-j\alpha^e_{i,h}} \right|, \ \hat{k}_{p,h} = \sin\left(\frac{hy\alpha_u}{2}\right) \tag{3.17}$$

Here, $\alpha^e_{i,h}$ is the phasor angle in the star of slots at harmonic h. It is desired to maximize $\hat{k}_{w,h} = \hat{k}_{d,h}\hat{k}_{p,h}$ (maximum is 1) for all magnetic field harmonics h that the designer wants to create in the airgap. These metrics are used in Section 3.7.

3.4.3 Effective number of phases

This subsection introduces the notion of an "effective" number of torque and suspension phases in the multiphase combined winding, which will prove useful later for deriving sym-

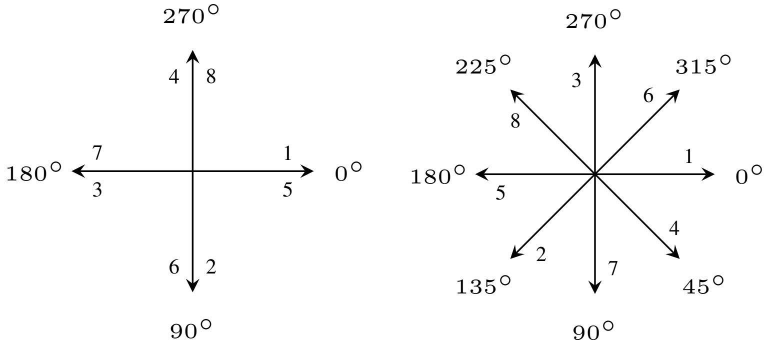

(a) (b)

Figure 3.3: Demonstration of star of slots diagrams for $Q = 8$, $p = 2$, and $p_s = 3$: (a) torque star of slots and (b) suspension star of slots.

metry requirements. In conventional multiphase windings, the angle $\alpha_{\mathrm{ph,w}}$ (see Fig. 3.2) is translated to $p\alpha_{\mathrm{ph,w}}$ in the star of slots and $\alpha_{\mathrm{ph,w}}$ is selected to ensure that $p\alpha_{\mathrm{ph,w}}$ can be reduced to $2\pi/m$. In multiphase combined windings, the angle $\alpha_{\mathrm{ph,w}}$ corresponds to the angles α_t, α_s in the torque, suspension star of slots. These angles are not necessarily $2\pi/m$ and can be expressed as

$$\alpha_t = k_1 \frac{2\pi}{m}, \ \alpha_s = k_2 \frac{2\pi}{m} \tag{3.18}$$

where k_1 and k_2 are integer numbers. In mechanical radians, it must be true that $\alpha_{\mathrm{ph,w}} = \alpha_t/p = \alpha_s/p_s$. Substituting (3.18) into this expression, it can be shown that $k_1/k_2 = p/p_s$. Since, p and p_s are co-prime, it must be true that $k_1 = cp$ and $k_2 = cp_s$, where c is an integer number. Picking the smallest positive values of $k_1 = p$ and $k_2 = p_s$, the phase separation angles for multiphase combined windings become:

$$\alpha_{\mathrm{ph,w}} = \frac{2\pi}{m}, \ \alpha_t = p\frac{2\pi}{m}, \ \alpha_s = p_s\frac{2\pi}{m} \tag{3.19}$$

This shows that $\alpha_{\mathrm{ph,w}}$ in multiphase combined windings must be constrained to $2\pi/m$. From this result, the following two observations can be drawn about multiphase combined windings:

3.4.3.1 The phases adjacent in the stator winding may not be adjacent in torque or suspension star of slots

e.g., with $p = 3$ and $m = 4$, $\alpha_t = \frac{3\pi}{2}$ and the torque phases in the star of slots have angles in the order of 0, $\frac{3\pi}{2}$, π, $\frac{\pi}{2}$ instead of 0, $\frac{\pi}{2}$, π, $\frac{3\pi}{2}$.

3.4.3.2 The effective number of phases for torque or suspension creation can be less than m

e.g., when $m = 8$, $p = 6$, and $p_s = 7$, $\alpha_t = 3 \cdot \frac{360°}{4}$ and $\alpha_s = 7 \cdot \frac{360°}{8}$. These angles show 4 effective torque and 8 effective suspension phases.

Generally, for any multiphase combined winding, the number of effective torque and suspension phases can be calculated by reducing p/m or p_s/m until the numerator and the denominator are co-prime. The resulting denominator is the effective number of phases. This can be directly calculated as (3.20), with the subscripts t and s indicating torque and suspension.

$$m_t = \frac{m}{\gcd(m, p)}, \; m_s = \frac{m}{\gcd(m, p_s)} \tag{3.20}$$

The m_t and m_s phase numbers determine the spacing between phases in the torque and suspension star of slots:

$$\alpha_{\mathrm{ph},t} = \frac{2\pi}{m_t}, \; \alpha_{\mathrm{ph},s} = \frac{2\pi}{m_s} \tag{3.21}$$

The distinction between α_t and $\alpha_{\mathrm{ph},t}$ (or α_s and $\alpha_{\mathrm{ph},s}$) is similar to the discussion in Section 3.4.2, where the phasor angle α_z is analogous to $\alpha_{\mathrm{ph},t}$ (or $\alpha_{\mathrm{ph},s}$), while the slot angles in star of slots $p\alpha_u$ and $p_s\alpha_u$ are analogous to α_t and α_s. Note that these angles are also apparent in the phase currents, which will have a phase spacing of $\alpha_{\mathrm{ph},t}$ for torque $\boldsymbol{i_t}$ and $\alpha_{\mathrm{ph},s}$ for suspension $\boldsymbol{i_s}$. However, the order that phase currents appear in an array is based on α_t for torque and α_s for suspension.

If the number of drive connections is even, the system is called "non-reduced" (non-loaded star configuration) [11, Ch 2.9.1]. In conventional winding design, the star of slots has pairs of phasors 180° apart, the phase system can be "reduced" by decreasing the original number of phases by half. If the new number of phases (after reduction) is even, a neutral point needs to be loaded. In multiphase combined windings, reducing the system is not possible because two phases that are 180° apart in the torque star of slots are $180° p_s/p \neq 180°$ apart in the suspension star of slots. Therefore, m in these derivations denotes the number of the drive connections of a non-reduced system rather than the number of torque or suspension phases.

3.5 Multiphase Combined Winding Design Requirements

Multiphase combined windings must satisfy symmetry and independent force/torque creation requirements. This section determines which combinations of electric machine slots Q, pole-pairs p and p_s, and phases m can be used to design a multiphase machine that meets these requirements. This is a primary contribution of this chapter. The design requirements are derived as constraint equations in Sections 3.5.1 and 3.5.2 and summarized in Table 3.1.

3.5.1 Symmetry Requirements

Symmetry requirements ensure that a rotating magnetic field is created when the winding is fed from a symmetrical supply. The multiphase combined winding must meet the two standard requirements (typically considered for conventional machines [11]) and new requirements, all of which are now presented.

3.5.1.1 Review of standard requirements

The first requirement is that the number of coils per phase (z_c/m) must be an integer [11]. This is listed in Table 3.1, where z_c is found as

$$z_c = \begin{cases} Q/2, & \text{single-layer winding} \\ Q, & \text{double-layer winding} \end{cases} \tag{3.22}$$

The second requirement ensures that the phase spacing $\alpha_{\text{ph}} = 2\pi/m$ in the torque star of slots is an integer multiple of the phasor angle α_z in (3.15). In a multiphase combined winding, this is analogously extended for both torque and suspension:

$$\frac{\alpha_{\text{ph},t}}{\alpha_z} \in \mathbb{N}, \ \frac{\alpha_{\text{ph},s}}{\alpha_{zs}} \in \mathbb{N} \tag{3.23}$$

where α_{zs} is analogous to α_z, but calculated with $h = p_s$. Substituting (3.15) and (3.21), the requirements are rewritten as

$$\frac{Q}{m}\frac{\gcd(m,p)}{\gcd(Q,p)} \in \mathbb{N}, \ \frac{Q}{m}\frac{\gcd(m,p_s)}{\gcd(Q,p_s)} \in \mathbb{N} \tag{3.24}$$

Since $Q/m \in \mathbb{N}$, it is also true that $\gcd(Q,p)/\gcd(m,p) \in \mathbb{N}$: $\gcd(Q,p) = b\gcd(m,p)$, where $b \in \mathbb{N}$. It can be shown that Q/m is a multiple of b. Therefore (3.24), and hence the second requirement in (3.23), is guaranteed to be satisfied for combined multiphase windings that meet the first symmetry requirement.

3.5.1.2 New requirements

Because the effective number of torque and suspension phases are not necessarily equal to m, additional symmetry requirements are needed to ensure that the multiphase combined winding can create rotating (not oscillating) p and p_s pole-pair fields. This can be articulated as that α_t and α_s cannot be multiples of π (or, equivalently: $m_t > 2$ and $m_s > 2$). Based on

(3.19), these requirements are satisfied when p and p_s are not a multiple of $m/2$. This can be rewritten as:

$$\frac{2p}{m} \notin \mathbb{N},\ \frac{2p_s}{m} \notin \mathbb{N} \tag{3.25}$$

3.5.1.3 Permissible Non-Symmetric Windings

Satisfying the conditions for a fully symmetric winding (summarized in the first two rows of Table 3.1) requires $m \geq 5$ connections to the motor drive. However, example combined winding designs can be found in literature with $m = 3$ and 4 phase connections, i.e. [16,67,94]. This section develops theory explaining these windings, showing that they can be achieved by relaxing (3.25) to allow $\frac{2p}{m} \in \mathbb{N}$. It is found that doing this can result in a viable bearingless machine, albeit with lower performance analogous to a single phase motor, with the machine having an oscillating (rather than rotating) magnetic field of p pole-pairs.

The analysis is presented through torque and force calculations. Torque is calculated by substituting (3.12) into (3.3). Each torque phase current must be in phase with $T_{mt,k}$ to create the maximum torque per ampere:

$$i_{t,k} = I_t \cos\left(\theta + \pi/2 - p\alpha_{\mathrm{w},k}\right) \tag{3.26}$$

Using complex numbers (phasors), (3.3) can be written as:

$$\tau = \frac{\hat{T}_{mt} I_t}{2} \Re\left\{ \sum_{k=1}^{m} e^{j2\left(\theta + \frac{\pi}{2} - p\alpha_{\mathrm{w}0} - [k-1]\alpha_t\right)} + m \right\} \tag{3.27}$$

If the symmetry requirements in Table 3.1 are satisfied, the torque is independent of rotor angle and (3.27) simplifies to

$$\tau = k_t I_t,\ k_t = m\hat{T}_{mt}/2 \tag{3.28}$$

where k_t is a torque per ampere constant. For windings that violate $\frac{2p}{m} \notin \mathbb{N}$ of (3.25), an oscillating field of p pole-pairs is created and the torque expression in (3.27) simplifies to

$$\tau = 2k_t I_t \sin^2 (\theta - p\alpha_{\mathrm{w0}}) \tag{3.29}$$

where the torque has so-called "single-phase characteristics". These windings have very high torque ripple because they are unable to create torque at certain rotor angular positions ($\theta = p\alpha_{\mathrm{w0}}$), but do have a non-zero average torque ($k_t I_t$) over one rotor revolution.

To study the impact on force creation, force expressions are similarly determined. Each force phase current must be in phase with the $T_{md,k}$ term of (3.13):

$$\begin{aligned} &i_{x,k} = I_x \cos (\theta - p_s\alpha_{\mathrm{w},k}),\ i_{y,k} = \pm I_y \sin (\theta - p_s\alpha_{\mathrm{w},k}) \\ &i_{s,k} = i_{x,k} + i_{y,k} = I_s \cos (\theta - p_s\alpha_{\mathrm{w},k} \mp \phi) \end{aligned} \tag{3.30}$$

where $I_s = \sqrt{I_x^2 + I_y^2}$, $\phi = \tan^{-1}(I_y/I_x)$ is the force angle, upper signs are for $p_s = h_1$ and lower signs are for $p_s = h_2$. The net force F_x is found in an analogous manner to (3.27):

$$F_x = \frac{I_x}{2} \left(\hat{T}_{mf,h1} \Re\{F_1 + F_2\} + \hat{T}_{mf,h2} \Re\{F_3 + F_4\} \right) \tag{3.31}$$

where F_1 and F_2 are the terms due to harmonic h_1, and F_3 and F_4 are the terms due to harmonic h_2:

$$F_1 = \sum_{k=1}^{m} e^{j\left(2\theta - [p_s + h_1]\alpha_{\mathrm{w},k}\right)},\ F_2 = \sum_{k=1}^{m} e^{j(p_s - h_1)\alpha_{\mathrm{w},k}} \tag{3.32}$$

$$F_3 = \sum_{k=1}^{m} e^{j\left(2\theta - [p_s + h_2]\alpha_{\mathrm{w},k}\right)},\ F_4 = \sum_{k=1}^{m} e^{j(p_s - h_2)\alpha_{\mathrm{w},k}} \tag{3.33}$$

If Table 3.1's symmetry requirements are satisfied, $F_1 = F_3 = 0$ and therefore force is constant over all rotor angles:

$$F_x = k_f I_x,\ k_f = \frac{m\hat{T}_{mf}}{2} \tag{3.34}$$

where k_f is a force per ampere constant. For windings that violate $\frac{2p}{m} \notin \mathbb{N}$ of (3.25), the net force expression becomes:

$$F_x = k_f I_x + k_{f,h} I_x \cos\left(2[\theta - p\alpha_{\mathrm{w0}}]\right) \tag{3.35}$$

which shows that these windings have an additional force ripple component as there is a dependence on the rotor angle θ (non-zero F_1 or F_3). This is due to the suspension currents creating magnetic fields at both harmonics h_1 and h_2, which rotate in opposite directions. One harmonic interacts with the rotor p pole-pair field to create non-zero average force, while another harmonic causes the force ripple.

This provides a theoretical explanation for the force ripple reported in [94] for a $m = 3$ machine. Too large of force ripple (or force vector error) can lead to suspension instability. However, by solving (3.35), advanced control techniques can be implemented to reduce the force ripple, analogous to what is proposed in [94, Sec III-B]. Apart from controls, machine design techniques may also be used to reduce force ripple by minimizing $k_{f,h}/k_f$ in (3.35). From (3.14) and (3.34), it can be shown that setting $p_s = h_2$ and constraining the machine parameters to $h_1\delta = r$ will eliminate force ripple due to h_1. This simplifies (3.35) to have the same expression as (3.34).

In summary, while it is possible to create designs with $m = 3$ or 4 drive connections, these machines will nearly always have higher torque and force ripple as compared to $m \geq 5$.

3.5.2 Independent force/torque creation requirements

Further restrictions are placed on the machine to ensure that the multiphase winding can independently control force and torque. This requires $\boldsymbol{T_{md} i_t} = 0$ and $\boldsymbol{T_{mt} i_s} = 0$. Using expressions developed for $\boldsymbol{T_m}$ matrix entries and the phase currents, the above constraint equations can be rewritten analogous to the equations (3.27) and (3.31) and used to determine conditions for independent force/torque creation. After doing these substitutions, it can be shown that the above constraints are satisfied if the following two constraints are met:

$$\sum_{k=1}^{m} e^{j(\alpha_s - \alpha_t)[k-1]} = 0 \tag{3.36}$$

$$\sum_{k=1}^{m} e^{j(2\theta - [\alpha_s + \alpha_t][k-1])} = 0 \tag{3.37}$$

Condition (3.36) is always satisfied since from (3.19) $\alpha_s - \alpha_t = \pm 2\pi/m$. Condition (3.37) is violated only if $\alpha_s + \alpha_t$ is a multiple of 2π. In this case, (3.37) is equal to $me^{j2\theta}$, resulting in a pulsating torque (at 2θ) due to force creating currents and a pulsating force due to torque currents. Otherwise, if $\alpha_s + \alpha_t$ is not a multiple of 2π, (3.37) is always satisfied because the terms in the sum form a balanced set of vectors in the complex plane with a phase separation of $\frac{2\pi}{m}(p + p_s)$. The following constraint is proposed to ensure independent force/torque creation:

$$\frac{p + p_s}{m} \notin \mathbb{N} \tag{3.38}$$

This requirement is listed in Table 3.1 (row 4 column 3).

Requirement	Standard	New[a]
Symmetry	$z_c/m \in \mathbb{N}$	$2p/m \notin \mathbb{N}$ $2p_s/m \notin \mathbb{N}$
Independent force/torque creation		$(p+p_s)/m \notin \mathbb{N}$

---

[a] While only $m \geq 5$ phases satisfy these requirements, Section 3.5.1.3 shows that $m = 3$, 4 is possible when "single-phase" characteristics are acceptable.

Table 3.1: Multiphase combined winding design requirements

3.6 Comparison to DPNV Winding

The multiphase and DPNV windings are viewed as providing the highest performance potential combined winding because of their ability to independently control field weakening as well as torque and force. Section 2.3.3 has made the observation that DPNV drives/windings [51] can be viewed as a circuit-based connection of certain multiphase combined windings. It was noted that the DPNV drive resulted in equivalent coil currents (and therefore, equivalent airgap fields, force, and torque). This implies that the DPNV winding design [51] must actually be equivalent to these multiphase combined windings. This notion is now explored by showing the equivalence (and differences) in winding design requirements between Table 3.1 and [51, Tables II-IV]. Based on this comparison, this section will identify design criteria that allow a multiphase combined winding to be operated from a DPNV drive, which is the second key contribution of this chapter.

Upon inspecting the DPNV winding, it is immediately evident that it requires an even number of connections to the motor drive electronics, and therefore winding equivalence is only possible for an even value of m. Each of the three DPNV requirement tables is now considered. In this description, m retains the definition used in this document (the total number of drive connections), which is different from the definition of m in [51]. Further, although it is not immediately obvious, it can be shown that the DPNV winding design always results in $\alpha_{\text{ph,w}} = \frac{2\pi}{m/2}$, in juxtaposition to (3.19).

3.6.0.1 Symmetry

The DPNV winding requires that $p \perp m/2$ and $p_s \perp m/2$ ($\perp$ means co-prime) [51, Table II]. While this requirement satisfies the symmetry requirements of multiphase combined windings (Table 3.1), it is more restrictive. The DPNV winding needs this more restrictive requirement to ensure that the winding always has an effective number of torque and suspension phases such that $m_t = m_s = m/2$ to support the DPNV drive connection style–see [51, Fig. 1]. The proof of this can be arrived at by noting that since $\alpha_{\text{ph,w}} = \frac{2\pi}{m/2}$, the torque and suspension phases in the DPNV winding are phase separated by $\alpha_t = p\frac{2\pi}{m/2}$ and $\alpha_s = p_s\frac{2\pi}{m/2}$. Similar to the discussion in Section 3.4.3.2, the effective number of phases in the DPNV winding are found by reducing $\frac{p}{m/2}$ or $\frac{p_s}{m/2}$ until the numerator and denominator are co-prime.

3.6.0.2 No-Voltage

[51, Table III] summarizes these requirements and it can be shown that these requirements are equivalent to multiphase winding requirements when m is even.

3.6.0.3 Non-zero suspension distribution factor

[51, Table IV] summarizes these requirements. Again, it can be shown that these are equivalent to multiphase combined windings when m is even. This means that multiphase combined windings also have the property that there will always be phasors 360° apart in the torque star that are 180° apart in the suspension star (or vice versa), matching [51, Table IV] for $p_s = p \pm 1$ machines.

In summary, the DPNV winding can be viewed as a special case of the multiphase combined winding. Any multiphase combined winding that has $p \perp m/2$ and $p_s \perp m/2$ in addition to the requirements in Table 3.1 is equivalent to a DPNV winding and can therefore be operated using the DPNV drive configurations of [51, Fig. 1].

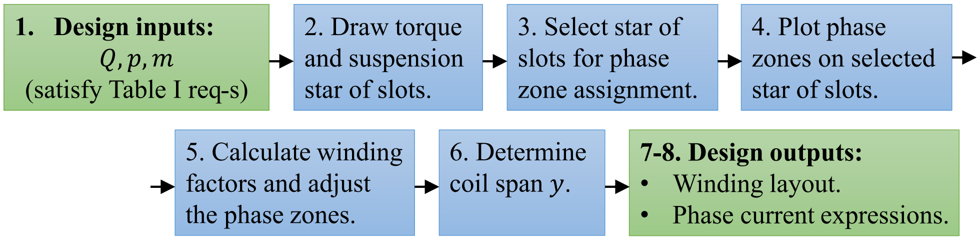

Figure 3.4: Summary of multiphase combined winding design steps.

3.7 Proposed Winding Design Approach

This section proposes a design procedure to enable a bearingless motor designer to determine a feasible winding layout for any desired multiphase combined winding. This is a third and main contribution of this chapter. A set of design steps is first provided followed by examples that utilize these steps.

3.7.1 Design Steps

The proposed winding design approach is intended for double-layer windings, where each slot holds two coil sides. The new design approach is inspired by the popular "star of slots" design used in convenional windings [11, Chapter 2.2] and makes use of the torque and suspension star of slots diagrams developed in Section 3.4.2. The proposed design steps are as followings (summarized in Fig. 3.4):

3.7.1.1 Select motor parameters that satisfy Table 3.1 requirements

Slots Q, pole-pairs (p and p_s), and phases m.

3.7.1.2 Draw torque / suspension star of slots diagrams

Refer to the procedure in the discussion accompanying Fig. 3.3.

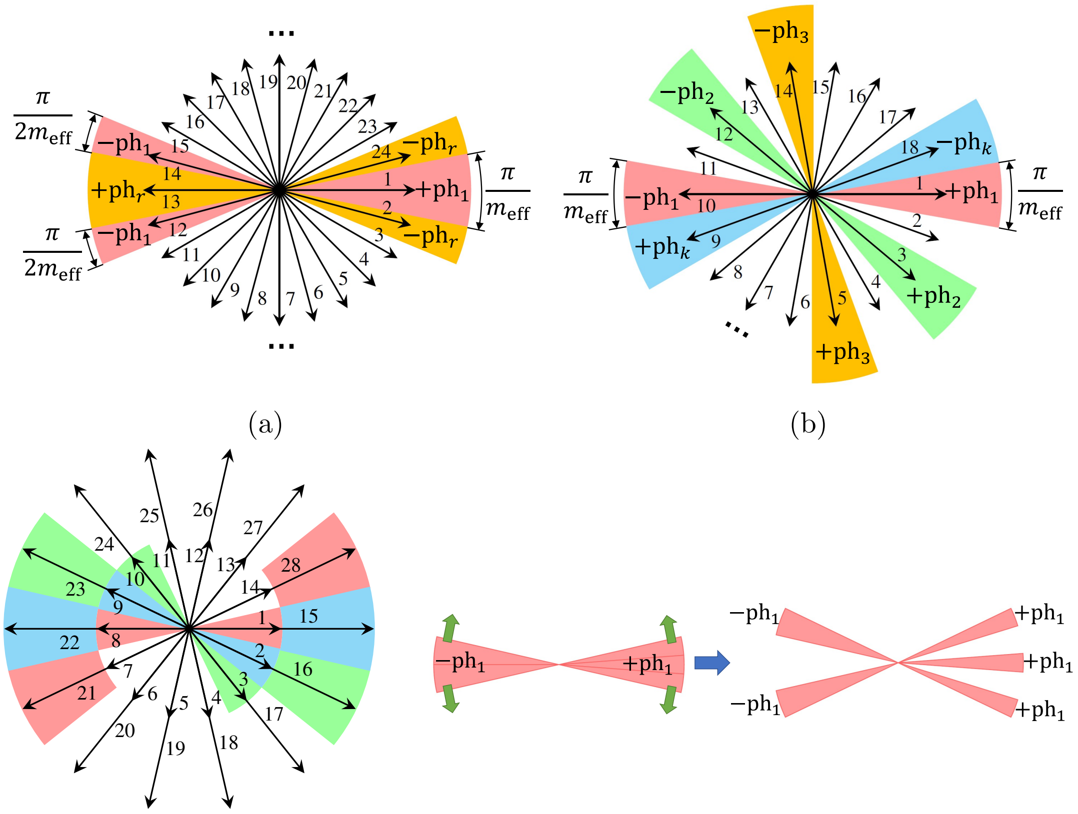

(a)

(b)

(c)

(d)

Figure 3.5: Illustration of design steps 4 and 5. Step 4: phase zones for case (a), (b), and (c). Step 5: (d) modifications to positive and negative phase zones.

3.7.1.3 Select star of slots for phase zone assignment

Identify the star with the highest number of phasors in a layer per effective number of phases: $\max\left(\frac{Q}{\gcd(Q,p)m_t}, \frac{Q}{\gcd(Q,p_s)m_s}\right)$, with m_t, m_s from (3.20). Define m_{eff} as the effective number of phases of the selected star (m_t or m_s).

3.7.1.4 Plot phase zones on selected star of slots

Assign each phasor (coil-side) in the star of slots identified in step 4 to a phase by drawing positive and negative phase zones on top of the star. Draw the phase zones following one of these cases:

a) Designs with even m_{eff}: Plot the phase zone diagram as in Fig. 3.5a. Since there are always pairs of phases separated by π radians for even m_{eff}, the negative phase zone for each phase has to be split into two parts as shown in Fig. 3.5a.

b) Designs with odd m_{eff} and with at least one of the following conditions satisfied: $m_t \neq m_s$, $\gcd(Q, p) = 1$, or $\gcd(Q, p_s) = 1$. Plot the phase zone diagram as in Fig. 3.5b. The positive and negative phase zones span π/m_{eff} and are separated by π radians. The adjacent positive (negative) phase zones are separated by $2\pi/m_{\text{eff}}$.

c) All other designs with odd m_{eff}: Draw the star of slots in several layers (in the radial direction) and plot the phase zones in each layer separately, as shown in Fig. 3.5c. Note that each layer uses the same phase zone assignment as in Fig. 3.5b, but has a different angular orientation.

3.7.1.5 Calculate winding factors and adjust the phase zones

Use (3.17) to calculate the torque $\hat{k}_{dt}$, suspension $\hat{k}_{ds}$ distribution factors. If these are unacceptably low, try the following:

First, slightly rotate the phase zones in Fig. 3.5a-3.5b clockwise or counterclockwise and select the phase-zone assignment that gives the highest distribution factors.

Next, if the distribution factors remain unacceptable, split positive and/or negative phase zones into several parts and rotate away from each other so that the net positive and negative phase zone orientations are unchanged–see Fig. 3.5d. Rotate these bands in increments that correspond to their bandwidth. This ensures equal phase band area for all phases and proper phase separation. Stop when satisfactory distribution factors are obtained. The other phases' zones can be found by rotating the phase 1 by $(k-1)2\pi/m_{\text{eff}}$ ($k = 2$ to m_{eff}).

3.7.1.6 Determine coil span

Identify a coil span y (number of slots) that achieves the preferred compromise between torque $\hat{k}_{pt}$ and suspension $\hat{k}_{ps}$ pitch factors. Calculate $\hat{k}_{pt}$ and $\hat{k}_{ps}$ for different y values by setting $h = p$, p_s in (3.17). Ensure that $yp/Q \notin \mathbb{N}$ and $yp_s/Q \notin \mathbb{N}$ to avoid zero pitch factors.

After following steps 1-6, it is possible to have multiple candidate designs for a specific slot-pole combination. To choose one design, the designer is advised to consider winding factors $\hat{k}_{w,p}$ and $\hat{k}_{w,p_s}$ for torque p and suspension p_s pole pairs. Ideally, a designer would choose an option with both highest $\hat{k}_{w,p}$ and $\hat{k}_{w,p_s}$ (if such a design exists) to obtain the maximum torque- and force-per-ampere. In other cases when there is a trade-off between $\hat{k}_{w,p}$ and $\hat{k}_{w,p_s}$ across different designs, the choice depends on the motor's required torque and force ratings. For most applications, it is suggested to select a design with a relatively higher $\hat{k}_{w,p}$ (> 0.7) and a reasonable $\hat{k}_{w,p_s}$ value ($> 0.4 - 0.5$).

3.7.1.7 Construct winding layout diagram

Determine the coil connections for each phase using the results from steps 4-6. Each phase coil has two coil sides. The slot location of one coil side is determined by the phase zone diagram, while the slot location of the other coil side is determined by the coil span y. The coils in each phase are connected in series.

3.7.1.8 Determine the phase current expressions

The phase currents consist of torque and suspension force creating components. The torque and suspension phase angles $\alpha_t = p\frac{2\pi}{m}$ and $\alpha_s = p_s\frac{2\pi}{m}$ in (3.19) determine which phase currents to flow through the coils to create two rotating magnetic field pole-pairs. The phase current k has the following expression:

$$i_k = I_t \cos\left(\phi_t - [k-1]\alpha_t\right) + I_s \cos\left(\phi_s - [k-1]\alpha_s\right) \tag{3.39}$$

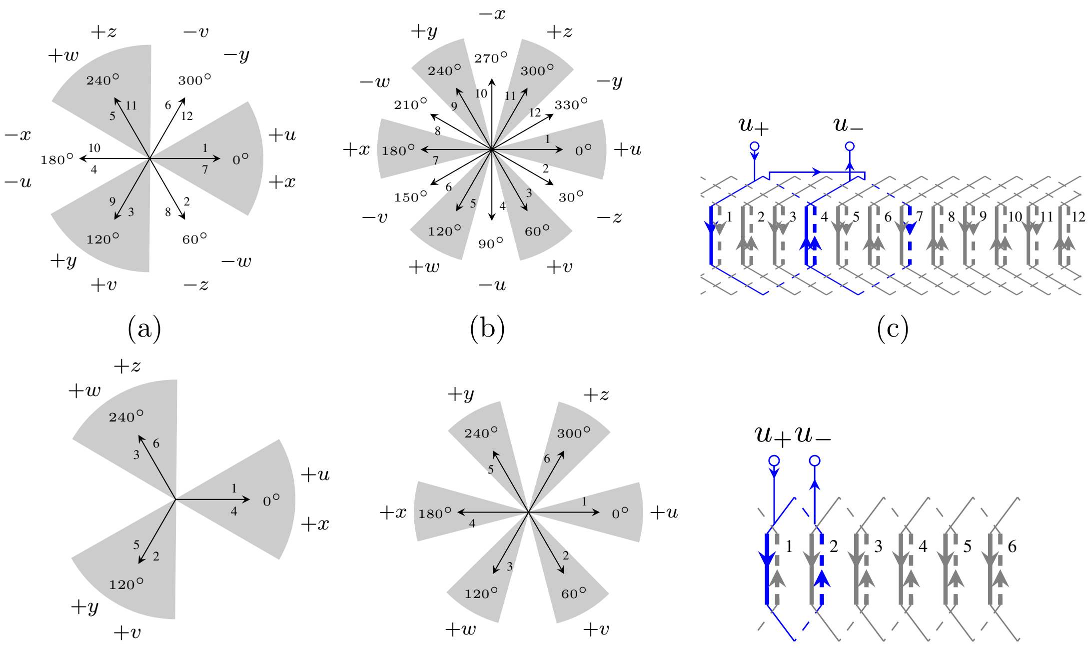

(a) (b) (c)

(d) (e) (f)

Figure 3.6: Double-layer winding designs. $Q = 12$, $m = 6$, $p = 2$, $p_s = 1$, and $y = 3$: (a) torque star of slots; (b) suspension star of slots; and (c) winding layout. $Q = 6$, $m = 6$, $p = 2$, $p_s = 1$, and $y = 1$: (d) torque star of slots; (e) suspension star of slots; and (f) winding layout.

3.7.2 Example designs

The proposed design steps are now demonstrated for a double-layer winding with $Q = 12$, $p = 2$, $p_s = 1$, and $m = 6$:

1) From (3.22), $z_c = 12$; Table 3.1 design requirements are met.

2) The diagrams are shown in Fig. 3.6a and 3.6b. The mechanical angle between adjacent slots is $\alpha_u = \pi/6$, resulting in $\pi/3$ in the torque and $\pi/6$ in the suspension star of slots.

3) Both torque and suspension stars have two phasors in a layer per effective number of phases ($m_t = 3$, $m_s = 6$). Therefore, either of the stars can be selected. For this example, the torque star of slots is selected and $m_{\text{eff}} = 3$.

4) This example uses case b) described Section 3.7.1.4 for drawing the phase zones. Since

$m_{\text{eff}} = 3$, each phase zone spans $\pi/m_{\text{eff}} = \pi/3$ radians. The positive and negative phase zones are plotted in Fig. 3.6a, where the phases are labeled from u to z. Note that each phase zone has two identical phases in the torque star. Therefore, half of the slots in each zone are assigned to each phase. The resulting star diagrams are shown in Fig. 3.6a and 3.6b.

5) The torque, suspension distribution factors are calculated as $\hat{k}_{dt} = 1$, $\hat{k}_{ds} = 0.707$. It is determined that these are satisfactory and no phase zone modification is needed.

6) The coil span is selected as $y = 3$, yielding $\hat{k}_{pt} = \sin\left(\frac{y\pi}{6}\right) = 1$ and $\hat{k}_{ps} = \sin\left(\frac{y\pi}{12}\right) = 0.707$. The resulting torque, suspension winding factors are $\hat{k}_{wt} = 1$, $\hat{k}_{ws} = 0.5$.

7) The resulting phase u winding layout is shown in Fig. 3.6c.

8) The phase current expressions are determined by (3.39) with $\alpha_t = \frac{2\pi}{3}$ and $\alpha_s = \frac{\pi}{3}$.

The design procedure can similarly be used to design any multiphase combined windings satisfying the Table 3.1 requirements. A second example design with concentrated windings is given in Fig. 3.6f (with star of slots in Fig. 3.6d and 3.6e). A third and fourth example are shown in Fig. 3.7 ($m = 7$, 8), where this time the suspension star of slots is selected in step 3 for phase zone assignment in step 4. These last two examples depict adjusting the phase zones in step 5 to increase the torque distribution factor. In a fifth example, Fig. 3.8 presents a distributed winding with $m = 6$, $Q = 24$, where only positive phase zones are used. This winding design is used in the bearingless induction machine prototype presented in Section 3.8.

3.8 Validation of Multiphase Combined Winding Design

Validation is now provided using finite element analysis and experimental measurements of a pole-specific bearingless induction motor prototype, shown in Fig. 3.11a. This machine's winding is implemented as the six-phase combined winding presented in Fig. 3.8c. The phase

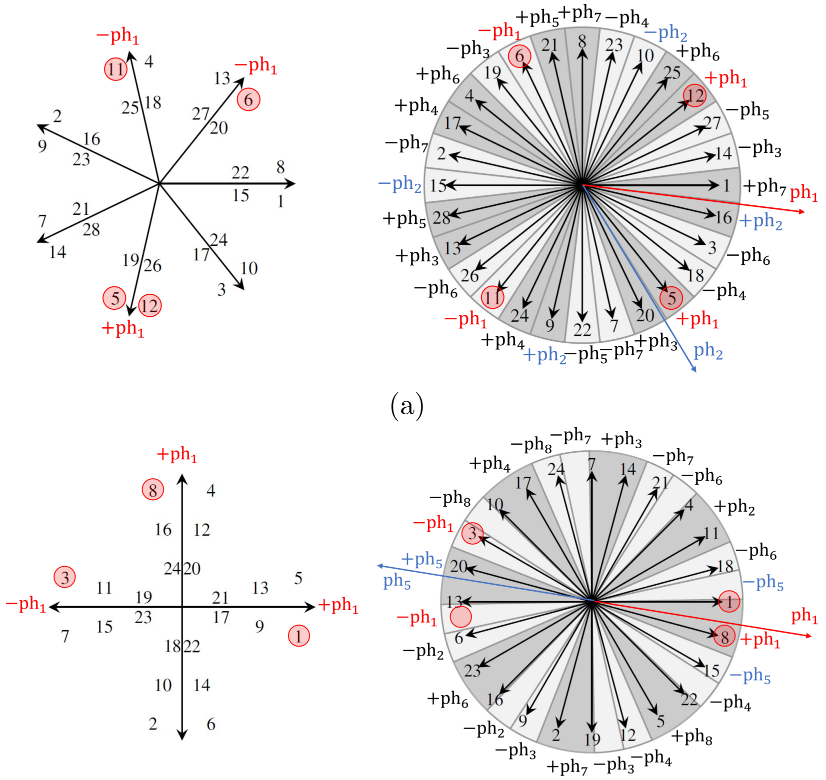

(a)

(b)

Figure 3.7: Torque (left) and suspension (right) star of slots for two examples that illustrate design steps 4 and 5 (dark gray – positive phase zones, light gray – negative phase zones): (a) $Q = 28$, $m = 7$, $p = 16$, and $p_s = 15$ ($m_t = m_s = 7$) and (b) $Q = 24$, $m = 8$, $p = 6$, and $p_s = 7$ ($m_t = 4$, $m_s = 8$). The red circles show the slots assigned to phase 1.

currents required to create $p = 1$ and $p_s = 2$ pole-pair fields in the airgap of this machine are given by the following equation–see (3.39):

$$i_k = I_t \cos\left(\phi_t - [k-1]\frac{2\pi}{6}\right) + I_s \cos\left(\phi_s - [k-1]\frac{2\pi}{3}\right) \tag{3.40}$$

where $k = 1$ to 6, $I_t = \sqrt{i_d^2 + i_q^2}$.

This winding satisfies the criteria to be operated by a DPNV drive that were derived in Section 3.6. Additional machine design information is provided in [7, 95], which presented test results obtained with the machine operated by a three-phase parallel DPNV drive. The key motor parameters are summarized in Table 7.1 when the winding is configured for operation by a six-phase drive. In the following tests, the machine is excited with various

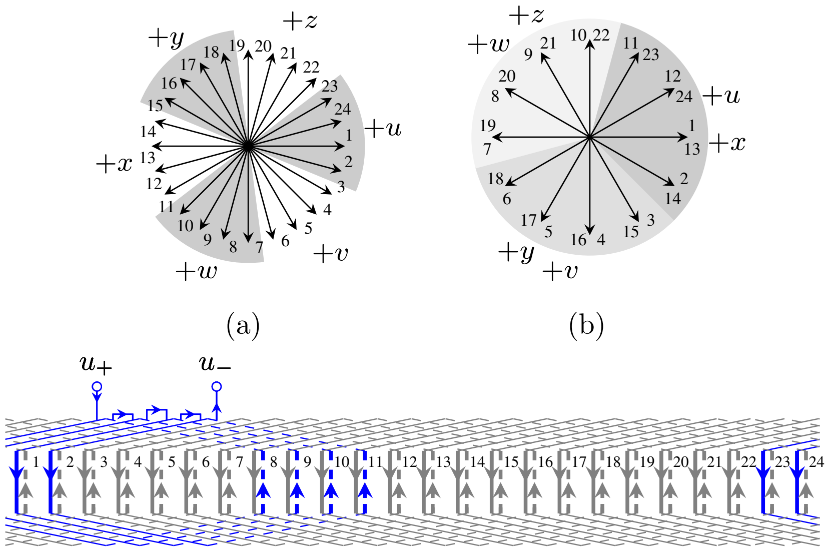

(a) (b)

(c)

Figure 3.8: Design of $Q = 24,\ m = 6,\ p = 1,\ p_s = 2,\ y = 9$ double-layer winding of the induction machine prototype used for validation in Section 3.8: (a) torque; (b) suspension star of slots; and (c) winding layout.

Rated i_d	6.75 A	Rated i_q	5.85 A
Force per current k_f[a]	13 N/A	Torque per current k_t	0.2 Nm/A
Rated slip frequency	12.5 Hz	Rated speed	29250 RPM

---

[a] k_f and k_t are measured at the rated i_d value.

Table 3.2: Induction Motor Prototype Parameters

phase currents to create desired airgap fields and torque and force vectors, with measurements compared against the findings of Sections 3.3-3.7 to confirm the theoretic developments of this chapter.

3.8.1 FEA Simulations

The proper operation of the example multiphase combined winding (if symmetry and independent force/torque creation are met) is now demonstrated using FEA simulation results for three different cases of phase currents, all described by (3.40). In all cases, currents have $\phi_t = \phi_s = 2\pi f t$ with a rated frequency of $f = 500$ Hz and a rated magnetizing current $i_d = 6.75$ A. The first column of Fig. 3.9 shows that only torque is produced when the rated

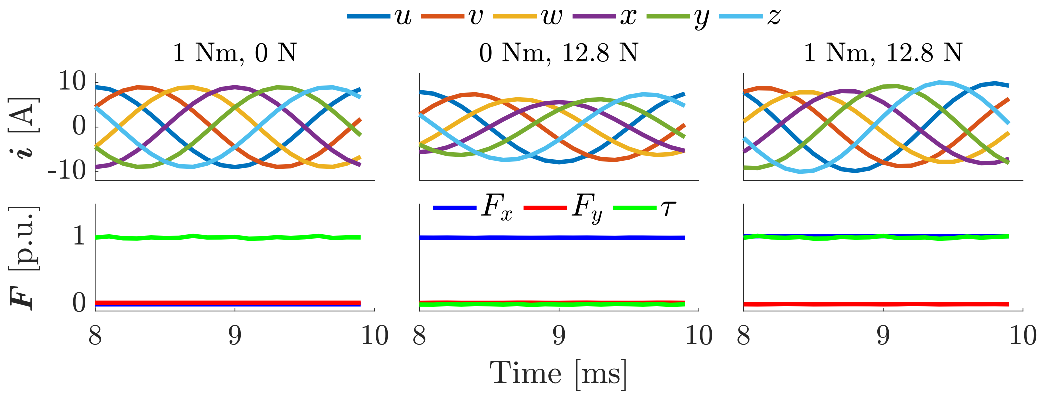

Figure 3.9: FEA results for example six-phase induction machine prototype: calculated torque and force for different currents (column 1–rated torque, column 2–rated force, column 3–rated torque and force). $F_{\text{base}} = 12.8$ N, $\tau_{\text{base}} = 1$ Nm.

torque creating current $i_q = 5.85$ A is applied (rated rotor speed and slip). The second column shows that only force is produced when the rated suspension current $I_s = 1.15$ A is applied (zero slip). The third column shows that both torque and force are produced when rated i_q and I_s are present (rated slip).

3.8.2 Experimental Validation

Three test results are presented that confirm that the airgap magnetic fields with the desired pole-pairs ($p = 1$, $p_s = 2$) can be created, that force and torque can be created independently, and that multiphase and DPNV combined windings are equivalent. These tests validate the theory developed in Sections 3.5-3.7. In all tests, the phase windings are excited by the currents described by (3.40).

3.8.2.1 Magnetic field measurements

This test is conducted to validate the multiphase combined winding symmetry requirement that two rotating p and p_s pole-pair fields are created when the phase currents are supplied by a symmetrical supply, as defined in Section 3.2 and summarized in Table 3.1. In this test, the normal airgap magnetic field B_{n} is measured with a hall probe [96] in front of each tooth (15° increment) along the inner bore of the stator (along α), as shown in Fig. 3.10a.

Despite the rotor not being present in Fig. 3.10a, it is fully inserted during the test. At each tooth, measurements are taken for the following two cases of excitation–see (3.40):

1) $I_t = 13.5$ A, $I_s = 0$ with ϕ_t swept over $0 - 2\pi$ rad. (expected to create $p = 1$ pole-pair field).

2) $I_s = 13.5$ A, $I_t = 0$ with ϕ_s swept over $0 - 2\pi$ rad. (expected to create $p_s = 2$ pole-pair field).

The result for case 1 is provided in Fig. 3.10b, which shows a 3D plot of the measured normal magnetic field B_n as a function of α and ϕ_t. This plot shows that the airgap field has $p = 1$ pole-pair when viewed along α at any fixed ϕ_t value. As an example, Fig. 3.10d plots a special case of Fig. 3.10b for $\phi_t = 60^\circ$ (in blue) to show that $p = 1$ pole-pair is created. As ϕ_t increases, the angular location of the field along α in Fig. 3.10b also increases according to $\alpha_\mathrm{peak} = \phi_t/p$ and the field behavior can be described by the rotating field equation $B_\mathrm{n} = 0.65\cos(\alpha - \phi_t)$ [T].

Figure 3.10c provides a similar 3D plot of B_n for case 2 as a function of α and ϕ_s. This plot shows that the airgap field has $p_s = 2$ pole-pairs when viewed along α at any fixed ϕ_s value. Figure 3.10d again plots the special case of Fig. 3.10c for $\phi_s = 60^\circ$ (in red) to show that $p_s = 2$ pole-pair is created. Analogous to case 1, the angular location of the field along α in 3.10c increases by increasing ϕ_s according to $\alpha_\mathrm{peak} = \phi_s/p_s$ and the field behavior is described by the rotating field equation $B_\mathrm{n} = 0.2\cos(2\alpha - \phi_s)$ [T].

The observations made above validate the multiphase combined winding symmetry requirements (see Table 3.1) that rotating p and p_s pole-pair fields can be created when motor windings are excited by balanced currents.

3.8.2.2 Force and torque measurements

The results of this test validate the multiphase combined winding independent force and torque creation requirements, as defined in Section 3.2 and summarized in Table 3.1. In this

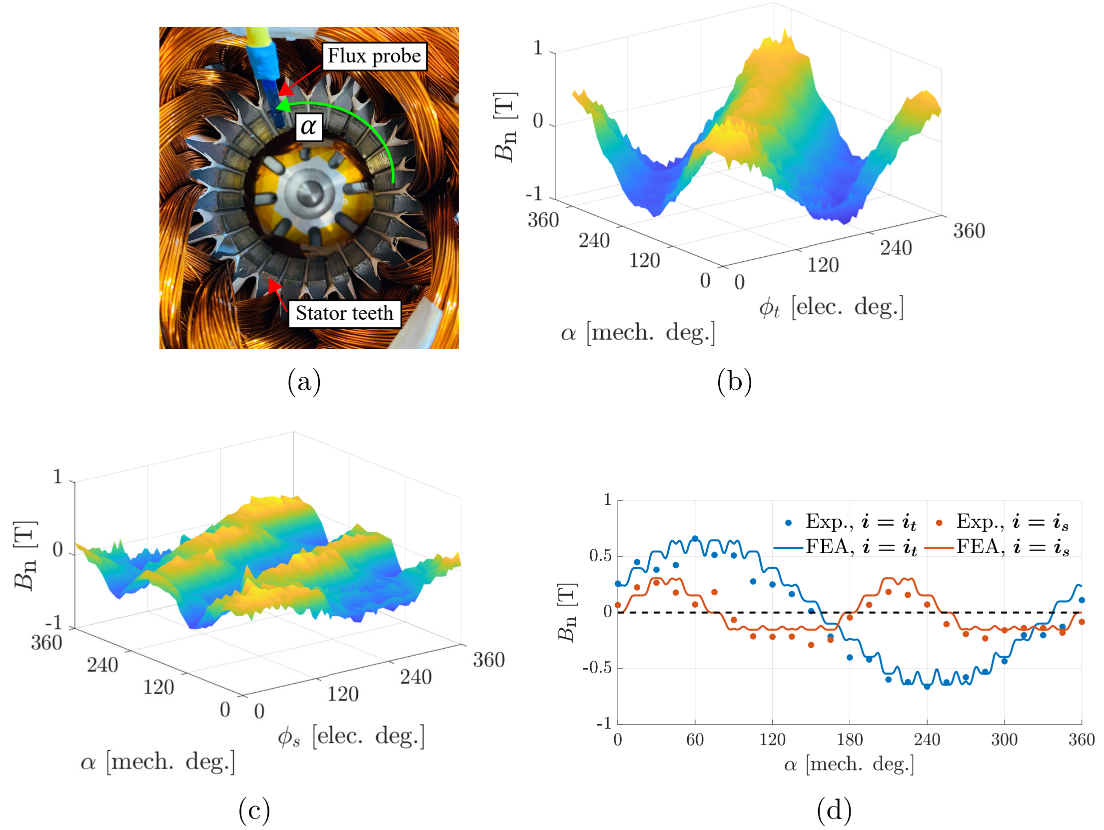

Figure 3.10: Experimentally measured magnetic field: (a) test setup; B_n when (b) torque currents are present ($\boldsymbol{i} = \boldsymbol{i}_t$); (c) suspension currents are present ($\boldsymbol{i} = \boldsymbol{i}_s$), and (d) torque and suspension currents are present with $\phi_t = 60°$ and $\phi_s = 60°$ (obtained from Fig. 3.10b-3.10c).

test, reaction torque and forces on the stator are measured using a load cell [97], as shown in Fig. 3.11a. The stator is mounted on the load cell, which is rigidly fixed. The rotor is supported by a mill's spindle and locked at the magnetic center in a manner that prevents rotation and deflection. The injected phase currents are described by (3.40) with $\phi_t = 2\pi f t$ and $\phi_s = 2\pi f t + \phi$. The measurements are taken for the following two cases:

1) $f = 0.10$ Hz, $I_t = 6.75$ A, $I_s = 1.15$ A (see Fig. 3.11b, column 1). This test verifies that rated force can be created at any angle. The frequency is set to a sufficiently low value so that no torque is created.

2) $f = 12.5$, $I_t = 9.10$ A, $I_s = 1.15$ A (see Fig. 3.11b, column 2). This test verifies that rated force can be created at any angle while torque is also produced. Since the rotor

is locked, the motor operates under rated slip frequency (see Table 7.1).

In both cases, the motor is expected to have $i_d = 6.75$ A. During the tests, ϕ is set to a fixed value, forces and torque are measured at steady state, and the average is calculated. The measurements are repeated for the values of ϕ from 0 to 2π rad. with an increment of $\pi/6$ rad.

Figure 3.11c provides measurement results of the forces F_x, F_y, and torque τ vs. ϕ for the two cases described above. Figure 3.11d is a plot of the force vector magnitude and angle obtained using the Fig. 3.11c results. These results show that the force vector angle can be changed by modifying ϕ while having no effect on torque. The reverse is also true–whether torque is being created or not, the motor can independently create force vectors with a constant magnitude at any angle. It has also been confirmed that the motor creates zero average force when $I_s = 0$ A. Together, these results indicate that force and torque creation can be created independently by controlling $(I_s,\ \phi)$ and i_q (with a constant i_d), which validate the independent force and torque creation requirements summarized in (3.38) and Table 3.1.

3.8.2.3 Comparison to DPNV Winding

This test validates equivalence between multiphase and DPNV combined windings (see Section 3.6) using suspension force measurements. As summarized in Section 3.6, an multiphase combined winding must additionally satisfy $p \perp m/2$ and $p_s \perp m/2$ to be capable of operation by a DPNV drive. The winding of this prototype (see Fig. 3.8c) meets these additional design criteria because $p = 1$, $p_s = 2$, and $m = 6$ ($1 \perp 3$ and $2 \perp 3$). The six-phase multiphase currents $[i_1,\ i_2,\ i_3,\ i_4,\ i_5,\ i_6]^T$ in (3.40) map to the DPNV coil group currents in [51] in the following order as $[i_{u_b}, -i_{w_a},\ i_{v_b}, -i_{u_a},\ i_{w_b}, -i_{v_a}]^T$–see Fig. 3.12.

The required DPNV drive torque $i_{t,k}$ and suspension $i_{s,k}$ terminal currents (see Fig. 3.12)

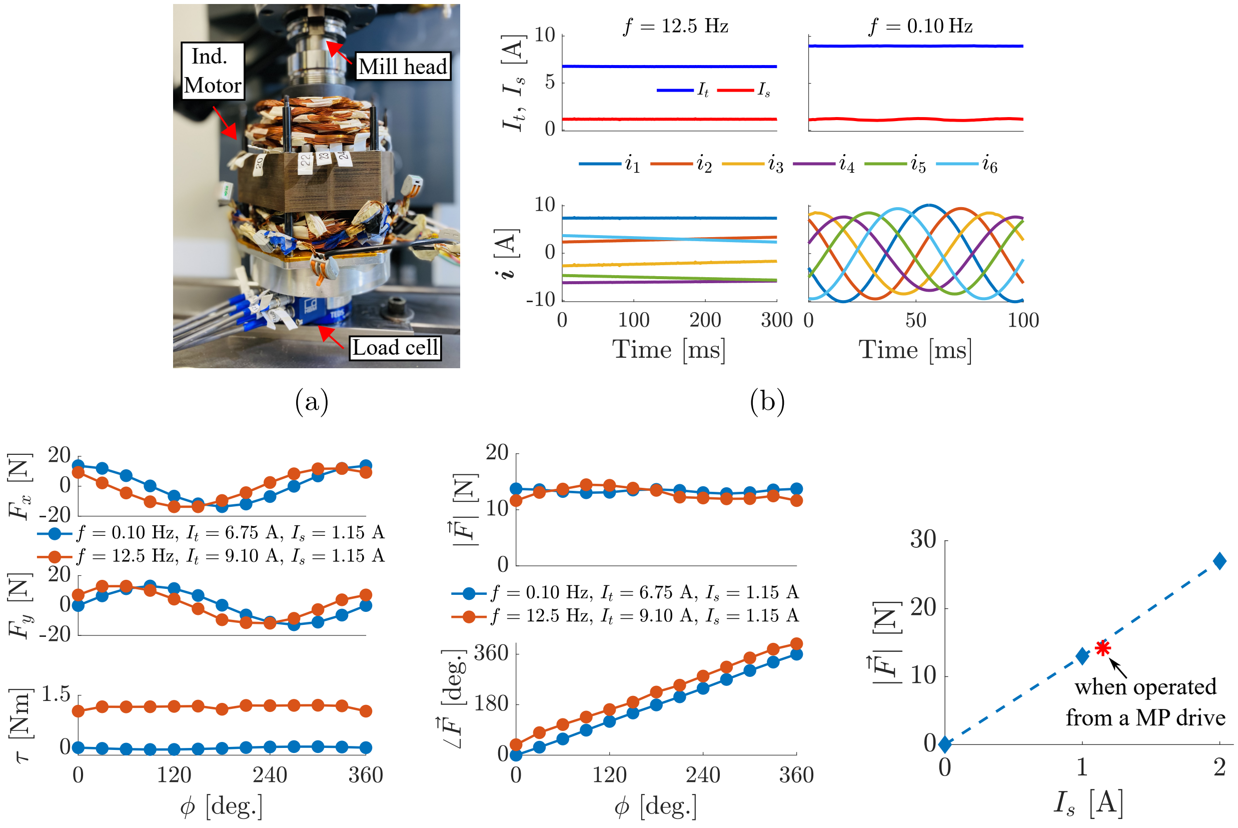

(a) (b)

(c) (d) (e)

Figure 3.11: Experiment results of the force and torque measurements: (a) test setup, (b) phase currents for two cases of test 2, (c)-(d) measured forces and torque for different ϕ values, and (e) measured force vs. suspension current for multiphase drive (red) and DPNV drive (blue).

are expressed as:

$$
\begin{aligned}
i_{t,k} &= 2I_t \cos\left(\phi_t - [k-1]\frac{2\pi}{3}\right) \\
i_{s,k} &= I_s \cos\left(\phi_s + [k-1]\frac{2\pi}{3}\right) - I_t \cos\left(\phi_t - [k-1]\frac{2\pi}{3}\right)
\end{aligned}
\tag{3.41}
$$

where $k = 1$ to 3. This drive connection configuration is compelling because it allows the inverter responsible for providing i_t to be implemented as a standard three phase motor drive without knowledge of the machine being bearingless. This is because the i_t terminals contain only a single sequence current ($2\pi/3$ spacing) as compared to the current expressions in (3.40) which have two sequences. Note that when the DPNV drive provides currents

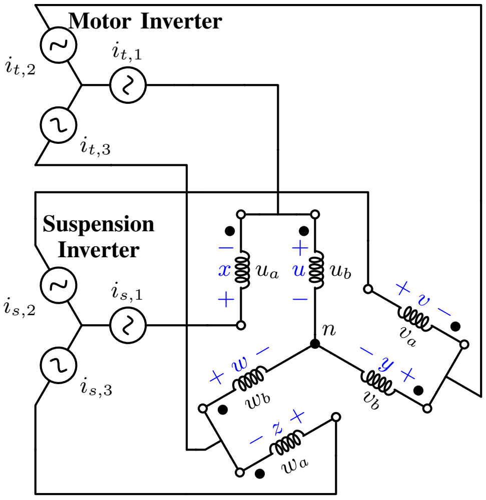

(a)

Figure 3.12: The prototype machine's winding configured for operation by a parallel DPNV drive. The 6 phases from Fig. 3.8c u, v, w, x, y, z are shown in blue to indicate their mapping to the DPNV coil groups a and b [4].

according to (3.41), the machine coils will have the same currents as when the multiphase drive provides currents according to (3.40), meaning that the machine has identical torque and force performance.

Test results are now presented to validate that the machine is capable of actuating force and torque identically, regardless of whether it is connected as a multiphase or parallel DPNV drive. First, the measured suspension force produced by the machine using both styles of drive is plotted in Fig. 3.11e, with drive phase currents determined by (3.40) and (3.41). Rated i_d current is applied, $i_q = 0$A, over a range of I_s values. The slope of this curve determines the force created per unit current $k_f = 13$ N/A, listed in Table 7.1. The red marker in Fig. 3.11e represents the force measured when the prototype is operated by the six-phase multiphase drive (tested at rated suspension current $I_s = 1.15$ A) while the blue dots correspond to measurements when the prototype is operated by the parallel DPNV drive (see Fig. 3.12). Clearly both drives result in the machine having the same force characteristic. A similar test was conducted to compare the torque capability of the machine, resulting in identical torque per unit current $k_t = 0.2$Nm/A, listed in Table 7.1. By demonstrating that both drives are able to identically actuate force and torque, these results validate the design criteria derived in Section 3.6 for when a multiphase combined winding can be operated by a DPNV drive.

3.9 Conclusion

Historically, challenges in the winding design for bearingless motors have limited the machine performance (torque density, torque and force ripple, and efficiency). Combined windings are gaining attention as a potential solution for these problems, with multiphase combined windings being widely recognized as one of the highest performance approaches. This chapter develops the fundamental force/torque model for machines employing these windings and uses this model to establish a winding analysis framework, machine design requirements, and winding design theory, which are the main contributions of this chapter. This winding design theory can be extended to design windings that can control multiple airgap harmonic fields, as will be shown in Chapters 6-7.

While it is found that many combinations of stator slots, poles, and phases can lead to viable windings, certain combinations lead to either asymmetric windings or cross-coupling between the motor and suspension operation. The highest performance multiphase winding designs have at least five connections to the drive electronics. However, this chapter's analysis framework shows that it is possible to reduce this to three or four connections (presumably to save cost) and obtain an asymmetric winding that is feasible, but with higher torque and force ripple. It is found that the classical star of slots design methodology for stator windings can be extended to aid in the design of multiphase combined windings by considering both the motor and suspension field spatial harmonics. Experimental results from a six-phase induction machine validate the multiphase combined winding analysis framework and design approach.

Motor designers will find this chapter useful as a practical guide to rapidly design multiphase combined windings for various slot-pole combination motors. Its general analysis framework and repeatable design steps enable consideration of a large number of machine variants.

Chapter 4

Exact Torque and Force Vector Modeling Framework for Bearingless Electric Machines

4.1 Introduction

As was found from the literature review in Chapter 1, bearingless motors face limitations in power density, efficiency, cost, and speed-power capabilities compared to high-performance conventional motors. The constrained design space of bearingless machines, driven by stringent levitation performance requirements, contributes to these challenges [1]. State-of-the-art models and force regulation algorithms are based on the assumption of a linear force/torque-current relationship that ignores the effects of magnetic field harmonics, saturation, or armature reaction. As a result, potentially high performance designs that do not fall under these simplified model assumptions can be excluded from consideration during design studies. Furthermore, the possibility of increasing force density using unmodeled airgap magnetic field harmonics is ignored.

---

[1] Portions of the material in this chapter have also been published in [98].

This chapter addresses the problem by proposing and developing an “exact” electric machine model that provides a new way of understanding force and torque creation. The proposed model is based on current space vectors to allow identification of current sequence components that excite specific magnetic field harmonics to increase force capacity. The chapter shows how the exact model enables the creation of force/torque regulation techniques that can precisely actuate the shaft even when multiple airgap field harmonics are present. This allows relaxing the force vector error requirement during the design stage and addressing it during the control stage. As a result, this makes the design space less constrained and enables consideration of potentially higher performance designs. Only two studies, [5] and [6], have investigated techniques that can be referred to as exact force vector regulation. They demonstrated significant performance improvement for an active magnetic bearing (AMB) and a bearingless motor. Two other studies [99] and [39] made use of multiple space vector frames to develop the models for multisector and magnetically levitated rotary-linear machines. However, the techniques they developed only work for specific machine examples and no generalized analytic model was presented.

The main contribution of this chapter is to propose, develop, and validate a new and exact electric machine model that encompasses both force and torque creation, incorporating multiple airgap harmonic field interactions. Section 4.2 reviews airgap field theory that will be used in the model derivation. Sections 4.3 and 4.4 review the textbook bearingless machine model typically used in literature, propose the exact model, and provide a detailed derivation from first principles using winding function theory, current sequences, and the Maxwell Stress Tensor. Section 4.5 compares the proposed model to the prior exact models in [5] and [6]. Sections 4.6 and 4.7 shows how to use the proposed exact model to improve bearingless machine performance for force ripple minimization and force enhancement.

4.2 Review of Airgap Field Theory

This section reviews the airgap field creation in bearingless electric machines as a special case of a more generalized multi-harmonic winding design study presented in [100]. The results summarized in (4.11)-(4.14) and (4.18) are used in Section 4.4 to develop the exact model proposed by this dissertation work. Sections 4.2.1 and 4.2.2 review magnetic field space harmonics using winding function theory and the relation to the current sequence components. Section 4.2.3 shows how to use the airgap fields to calculate the forces and torque using a reformulated form of the Maxwell Stress Tensor.

4.2.1 Harmonic Airgap Fields

This subsection reviews airgap magnetic field harmonics created by rotor magnets and stator winding currents. Winding function theory and circumferential current density are used to determine expressions for the winding fields.

The normal and tangential components of the airgap magnetic field (see Fig. 4.1a) are given by

$$B_{\mathrm{n}} = B_{\delta} + B_{\mathrm{n,w}}, \quad B_{\mathrm{tan}} = B_{\mathrm{tan,w}} \tag{4.1}$$

where B_{δ} is the rotor magnetic field, and $B_{\mathrm{n,w}}$ and $B_{\mathrm{tan,w}}$ are the winding's magnetic field components. The rotor magnetic field at harmonic h can be expressed in terms of the airgap angle α and the rotor angular position θ (defined in Fig. 4.1a):

$$B_{\delta,h} = \hat{B}_{\delta,h} \cos\left(h[\alpha - \theta]\right) \tag{4.2}$$

where $\hat{B}_{\delta,h=p} = \hat{B}_{\delta}$ is the magnetic loading. An example plot of $B_{\delta,h}$ along the airgap is illustrated in Fig. 4.1b.

The winding magnetic field depends on the winding layout and the phase currents. At space harmonic h:

$$B_{\mathrm{n,w},h}(\alpha) = \frac{\mu_0}{\delta_{\mathrm{eff}}} \sum_{k=1}^{m} N_{k,h}(\alpha) i_k, \;\; B_{\mathrm{tan,w},h}(\alpha) = -\tfrac{\mu_0}{r} \sum_{k=1}^{m} A_{c,k,h}(\alpha) i_k \tag{4.3}$$

where δ_{eff} is the effective airgap length, i_k is the phase current in phase k, $N_{k,h}(\alpha)$ is the winding function [101] harmonic h of phase k, and $A_{c,k,h}(\alpha)$ is the circumferential current density per ampere of current. The winding function describes the distribution of the per ampere magnetomotive force:

$$N_{k,h}(\alpha) = \hat{N}_h \cos\left(h\alpha - \alpha_{\mathrm{w0},h} - [k-1]h\alpha_{\mathrm{ph,w}}\right) \tag{4.4}$$

where $\hat{N}_h = \frac{2}{\pi h} z_Q z_c \hat{k}_{w,h}$ and $\alpha_{\mathrm{w0},h}$ are the winding function amplitude and phase shift at harmonic h. $\hat{N}_h$ is determined by the number of turns per coil z_Q, coils per phase z_c, and the winding factor $\hat{k}_{w,h}$. The angle $\alpha_{\mathrm{ph,w}} = \frac{2\pi}{m s_\Theta}$ is the mechanical phase separation between adjacent phases, where s_Θ is introduced in [100] to develop a generalized winding design theory to independently create multiple airgap harmonics. The value of s_Θ can be any common divisor (CD) of the space harmonic orders $\{h_1, h_2, ...\}$ that the winding needs to create [100]. In separated windings, the value of s_Θ is typically p and p_s for torque and suspension windings, respectively. However, in combined windings, $s_\Theta = \mathrm{CD}(p, p_s) = 1$ [84].

Using the winding function, the per ampere circumferential current density $A_{c,k,h}(\alpha)$ at harmonic h can be calculated:

$$A_{c,k,h}(\alpha) = -\frac{\mathrm{d}N_{k,h}(\alpha)}{\mathrm{d}\alpha} = A'_{c,\mathrm{ph},h} \sin\left(h\alpha - \alpha_{\mathrm{w0},h} - [k-1]h\frac{2\pi}{m}\right) \tag{4.5}$$

where $A'_{c,\mathrm{ph},h} = h\hat{N}_h = \frac{2}{\pi} z_Q z_c \hat{k}_{w,h}$. Substituting (4.4) and (4.5) into (4.3), the winding magnetic field components become:

$$\begin{aligned} B_{\mathrm{n,w},h}(\alpha) &= \frac{\mu_0 \hat{N}_h}{\delta_{\mathrm{eff}}} \sum_{k=1}^{m} i_k \cos\left(h\alpha - \alpha_{\mathrm{w0},h} - [k-1]h\frac{2\pi}{m}\right) \\ B_{\mathrm{tan,w},h}(\alpha) &= -\frac{\mu_0 h \hat{N}_h}{r} \sum_{k=1}^{m} i_k \sin\left(h\alpha - \alpha_{\mathrm{w0},h} - [k-1]h\frac{2\pi}{m}\right) \end{aligned} \tag{4.6}$$

The phase currents i_k in (4.6) determine the behavior of the winding magnetic field at harmonic h when summed over all phases, resulting in counterclockwise (CCW) rotating, clockwise (CW) rotating, oscillating, or zero field. The following subsection provides more details about this relationship.

4.2.2 Field Relation to Sequence Currents

This subsection reviews the relation between the airgap fields and the phase currents. Current sequence components are defined and used to determine the field harmonics that they create in the airgap.

Any set of multiphase currents $\boldsymbol{i} = \begin{bmatrix} i_1 & i_2 & ... & i_m \end{bmatrix}^T$ can be decomposed into current sequence components as

$$\boldsymbol{i} = \boldsymbol{i_0} + \boldsymbol{i_1} + ... + \boldsymbol{i_s} + ... + \boldsymbol{i}_{\boldsymbol{s}_{\mathrm{m}}} \tag{4.7}$$

and the current at sequence s and phase order k is defined as

$$i_{s,k} = \hat{I}_s \cos\left(\phi_s - [k-1]s\frac{2\pi}{m}\right) \tag{4.8}$$

where each sequence s has an amplitude $\hat{I}_s$, a phase angle ϕ_s, and a phase separation $s\frac{2\pi}{m}$.

The values of s can be

$$s = 0, \pm 1, ..., s_{\mathrm{m}}, \text{ where } s_{\mathrm{m}} = \begin{cases} \pm\frac{m-1}{2} & \text{for odd } m \\ \frac{m}{2} & \text{for even } m \end{cases} \tag{4.9}$$

The value of s is constrained between $-s_{\mathrm{m}}$ and s_{m} because any other integer values outside this range result in the same phase separation angle $s\frac{2\pi}{m}$ due to the periodicity of 2π rad. The current sequences can be decoupled from each other by applying the Generalized Clarke Transform (GCT) [60, 85]. As a result, each sequence component has an independent space vector representation. Space vectors for the sequences $s = 0$ and $s = m/2$ have 1-DOF (only real part) and a form of $\vec{i}_s = \hat{I}_s \cos\phi_s$. All other sequences have 2-DOF (real and imaginary parts) and a form of $\vec{i}_s = \hat{I}_s e^{\pm j\phi_s}$, with + for $s > 0$ (positive sequence) and − for $s < 0$ (negative sequence). This space vector representation of each sequence can be conveniently used to describe the magnetic field and force/torque creation.

Substituting (4.8) into (4.6) allows determining the magnetic field harmonics that are created due to a current sequence s (assuming that a winding factor $\hat{k}_{w,h} \neq 0$ at each harmonic). The terms inside the summation in (4.6) have the form of

$$\cos\left(\phi_s - [k-1]s\frac{2\pi}{m}\right)\cos\left(h\alpha - [k-1]h\frac{2\pi}{m}\right)$$

For any values of s, h, and m, the summation in (4.6) is non-zero only if the phase separation angles $h\frac{2\pi}{m}$ and $s\frac{2\pi}{m}$ are equal:

$$h\frac{2\pi}{m} = \pm s\frac{2\pi}{m} + 2\pi b \tag{4.10}$$

where $2\pi b$ (b is an integer) indicates periodicity. Simplifying this equation shows that the sequence s can create the following airgap field harmonics:

$$h = \begin{cases} s + mb, & \text{for CCW rotating fields} \\ -s + mb, & \text{for CW rotating fields} \end{cases} \tag{4.11}$$

and the total magnetic field expression at these harmonics is

$$\begin{aligned} B_{\mathrm{n,w},h}(\alpha) &= \hat{B}_{\mathrm{n,w},h} \cos\left(h\alpha - \alpha_{\mathrm{w0,h}} \mp \phi_s\right) \\ B_{\mathrm{tan,w},h}(\alpha) &= -\hat{B}_{\mathrm{tan,w},h} \sin\left(h\alpha - \alpha_{\mathrm{w0,h}} \mp \phi_s\right) \end{aligned} \tag{4.12}$$

where $-$ and $+$ signs indicate CCW or CW rotation. For example, a sequence $s = 2$ in $m = 5$ can create harmonics at $h = 2, 7, 12, ...$ rotating CCW and $h = 3, 8, 13, ...$ rotating CW. The magnetic field amplitudes in (4.12) are

$$\hat{B}_{\mathrm{n,w},h} = \frac{m}{2} \frac{\mu_0 \hat{N}_h \hat{I}_s}{\delta_{\mathrm{eff}}}, \; \hat{B}_{\mathrm{tan,w},h} = \frac{m}{2} \frac{\mu_0 h \hat{N}_h \hat{I}_s}{r} \tag{4.13}$$

When $s = 0$ or $s = m/2$, the magnetic field harmonics have an oscillating behavior (no rotation):

$$\begin{aligned} B_{\mathrm{n,w},h} &= \hat{B}_{\mathrm{n,w},h} \left[\cos\left(h\alpha - \alpha_{\mathrm{w0,h}} - \phi_s\right) + \cos\left(h\alpha - \alpha_{\mathrm{w0,h}} + \phi_s\right)\right] \\ B_{\mathrm{tan,w},h} &= \hat{B}_{\mathrm{tan,w},h} \left[\sin\left(h\alpha - \alpha_{\mathrm{w0,h}} - \phi_s\right) + \sin\left(h\alpha - \alpha_{\mathrm{w0,h}} + \phi_s\right)\right] \end{aligned} \tag{4.14}$$

Equations (4.11)-(4.13) show that the current sequence s ($\hat{I}_s$ and ϕ_s) can be used to control the amplitude and angular location of the airgap magnetic field at harmonic h. Analogously, injecting multiple current sequences as in (4.7) allows controlling multiple airgap field harmonics. These results are used in the following section to develop the bearingless machine model.

4.2.3 Reformulation of the Maxwell Stress Tensor

Force and torque creation in electric machines directly depend on the airgap magnetic fields and can be described by the Maxwell Stress Tensor. This dissertation reformulates the standard Maxwell Stress Tensor formula (3.6) in vector form as (4.15), which facilitates the derivation of the exact model:

$$\vec{F} = \frac{rL}{2\mu_0}\int_0^{2\pi} e^{j\alpha}\left[B_\mathrm{n} + jB_\mathrm{tan}\right]^2 \mathrm{d}\alpha,\ \tau = \frac{r^2L}{\mu_0}\int_0^{2\pi} B_\mathrm{n}B_\mathrm{tan}\mathrm{d}\alpha \tag{4.15}$$

where $\vec{F} = Fe^{j\phi} = F_x + jF_y$ is the force vector and τ is the torque, as shown in Fig. 5.1b. The parameters r and L are the rotor radius and axial length, B_n and B_tan are the normal and tangential components of the airgap magnetic field, and α is the airgap angle (see Fig. 4.1a). The airgap magnetic field consists of multiple space harmonics along α, each harmonic h having the form $\hat{B}_\mathrm{n/tan}\cos(h\alpha \pm \phi_s)$, where ϕ_s is the angular location. This can be rewritten as $0.5\hat{B}_\mathrm{n/tan}[e^{j(h\alpha\pm\phi_s)} + e^{-j(h\alpha\pm\phi_s)}]$ and used to solve (4.15) to identify harmonics that create force.

It is well-known that torque is created from the interaction between field harmonics of the same order h, while forces are created from the interaction between adjacent harmonics h and $h \pm 1$ [19]. This can be shown using (4.15). Suppose that the airgap field consists of two harmonics h_1 and $h_2 > h_1$:

$$\begin{aligned} B_\mathrm{n} &= \hat{B}_{\mathrm{n},h_1}\cos(h_1\alpha - \phi_{s_1}) + \hat{B}_{\mathrm{n},h_2}\cos(h_2\alpha - \phi_{s_2}) \\ B_\mathrm{tan} &= -\hat{B}_{\mathrm{tan},h_1}\sin(h_1\alpha - \phi_{s_1}) - \hat{B}_{\mathrm{tan},h_2}\sin(h_2\alpha - \phi_{s_2}) \end{aligned} \tag{4.16}$$

where ϕ_{s_1} and ϕ_{s_2} are the angular locations of these harmonics. By substituting these field expressions into the force equation in (4.15), it can be shown that the terms that result in non-zero integration have the form of (4.17) with $h_2 = h_1 + 1$:

$$\int_0^{2\pi} e^{j\alpha} \cos(h_1\alpha - \alpha_1)\cos(h_2\alpha - \alpha_2)\mathrm{d}\alpha = \frac{\pi}{2} e^{j(\alpha_2 - \alpha_1)} \tag{4.17}$$

where α_1 and α_2 are the angles expressed in terms of ϕ_{s_1} and ϕ_{s_2}. This result is used multiple times when solving (4.15).

Solving (4.15) results in the following force expression:

$$\vec{F}_{h_{12}} = \tfrac{V_r}{2\mu_0 r}\left(\hat{B}_{\mathrm{n},h_1} - \hat{B}_{\mathrm{tan},h_1}\right)\left(\hat{B}_{\mathrm{n},h_2} + \hat{B}_{\mathrm{tan},h_2}\right) e^{j(\phi_{s_2} - \phi_{s_1})} \tag{4.18}$$

Note that (4.18) is a general expression for force created by field harmonics h_1 and h_2. These fields can be from windings, magnets, or saliency. When the fields are created from windings, it is possible and convenient to express (4.18) in terms of normal field quantities alone. This is done by using the relation $\hat{B}_{\mathrm{tan},h} = \frac{h\delta_{\mathrm{eff}}}{r}\hat{B}_{\mathrm{n},h}$, from (4.13), in (4.18) to obtain

$$\vec{F}_{h_{12}} = \tfrac{V_r}{2\mu_0 r} C_{h_{12}} \hat{B}_{\mathrm{n},h_1} \hat{B}_{\mathrm{n},h_2} e^{j(\phi_{s_2} - \phi_{s_1})} \tag{4.19}$$

where $C_{h_{12}} = \left(1 - \frac{h_1\delta_{\mathrm{eff}}}{r}\right)\left(1 + \frac{h_2\delta_{\mathrm{eff}}}{r}\right)$ with $h_2 = h_1 + 1$. When $h_{1/2}\delta_{\mathrm{eff}} \ll r$, $C_{h_{ij}} \approx 1$. The results (4.18)-(4.19) are used in the following sections to first derive the traditional bearingless machine model (the "textbook" model) and then to derive the new exact electric machine model.

4.3 Textbook Model

This section provides an overview of the bearingless machine textbook model, i.e. [19], used in literature. The derivation of the force/torque equations is accomplished using the field calculations presented in Section 4.2 and its impact on machine design will be discussed.

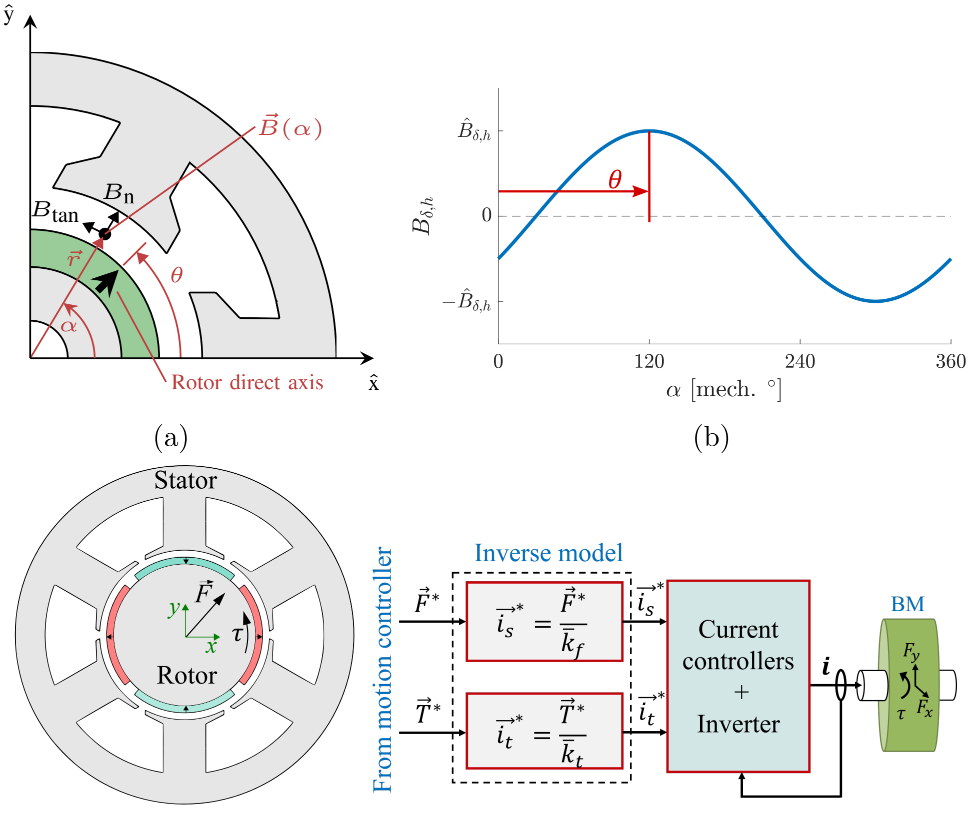

(c)

(d)

Figure 4.1: (a) Magnetic field components and angles (α and θ), (b) an example plot of the rotor magnetic field along the airgap at $h = 1$, (c) force vector $\vec{F}$ and torque τ, and (d) force/torque regulation block diagram.

4.3.1 Force/torque calculations

The textbook model assumes that the airgap field consists of only p and p_s pole pairs. Considering the fields from the magnets (4.2) and the windings (4.3), the total airgap magnetic field components have the form (the phase shift angle $\alpha_{\mathrm{w}0,p/p_s}$ is omitted for simplicity):

$$\begin{aligned} B_\mathrm{n} &= \hat{B}_\delta \cos\left(p[\alpha - \theta]\right) + \hat{B}_{\mathrm{n,w},p} \cos(p\alpha - \phi_t) + \hat{B}_{\mathrm{n,w},p_s} \cos(p_s\alpha - \phi_s) \\ B_\mathrm{tan} &= -\hat{B}_{\mathrm{tan,w},p} \sin(p\alpha - \phi_t) - \hat{B}_{\mathrm{tan,w},p_s} \sin(p_s\alpha - \phi_s) \end{aligned} \tag{4.20}$$

where the subscripts t and s denote the torque and suspension current sequences used to excite p and p_s pole pairs.

The force vector expression can be derived using (4.18). When $h_1 = p$ or $h_2 = p$ is created by the magnets, $\hat{B}_{\mathrm{n},h_1/h_2} = \hat{B}_\delta$, $\hat{B}_{\tan,h_1/h_2} = 0$, $\phi_{s_1}/\phi_{s_2} = \theta_e = p\theta$, and (4.18) simplifies to:

$$\begin{aligned}\vec{F} &= \frac{V_r \hat{B}_\delta}{2\mu_0 r}\left(\hat{B}_{\mathrm{n,w},p_s} \pm \hat{B}_{\mathrm{tan,w},p_s}\right) e^{\pm j(\phi_s - \theta_e)} \\ \tau &= \frac{V_r}{\mu_0}\hat{B}_\delta \hat{B}_{\mathrm{tan,w},p}\sin(\phi_t - \theta_e)\end{aligned} \tag{4.21}$$

where the ± signs correspond to $p_s = p \pm 1$. Note that the textbook model ignores the interaction between the stator p and p_s fields. Substituting (4.13) into (4.21), the force/torque expressions can be expressed in terms of the suspension and torque current space vectors as

$$\vec{F} = \bar{k}_f \vec{i}_s, \quad \vec{T} = \bar{k}_t \vec{i}_t \tag{4.22}$$

where the flux weakening component T_d is included in $\vec{T} = T_d + j\tau$. Parameters $\bar{k}_f$ and $\bar{k}_t$ are the per ampere force and torque

$$\bar{k}_f = \frac{\hat{B}_\delta V_r m p_s \hat{N}_{p_s}}{4r}\left(\frac{1}{p_s \delta_{\mathrm{eff}}} \pm \frac{1}{r}\right) e^{\mp j\theta_e}, \ \bar{k}_t = \frac{\hat{B}_\delta V_r m p \hat{N}_p}{2r} e^{-j\theta_e} \tag{4.23}$$

While $\vec{i}_s$ and $\vec{i}_t$ are calculated with the conventional CT for separated windings, [4] shows how this concept can be extended to multiphase (MP) and dual-purpose no voltage (DPNV) combined windings with the GCT.

4.3.2 Discussion

The textbook model (4.22) is based on the *dq* control theory. The motor and suspension operation can be controlled in two independent space vector frames [42, 60] using the GCT and Park transformations. Desired phase currents are calculated by inverting the model (see Fig. 4.1d).

This model assumes perfectly sinusoidal airgap fields and its solution results in sinusoidal phase currents. The unmodeled magnetic field harmonics, armature reaction, and nonlinear-

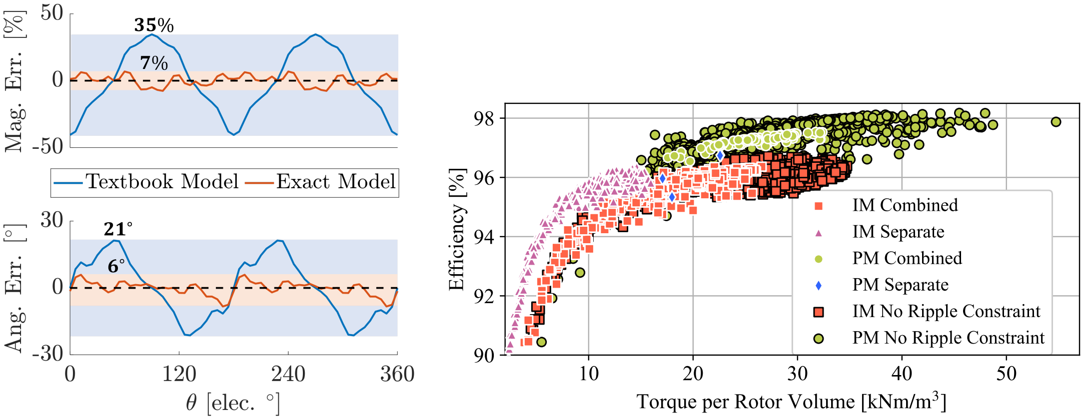

(a) (b)

Figure 4.2: (a) FEA results comparing textbook vs. exact models and (b) efficiency vs. torque density plot for 100 kW, 30 kRPM.

ities can cause large force vector error [19, 56]. This is shown in Fig. 4.2a where an example motor (described later in Fig. 4.3d) is commanded to create a x-axis force. However, the actual force obtained when phase currents are calculated using the textbook model has a large variation in the force vector magnitude and angle. This problem is typically solved in bearingless motor design studies by imposing the maximum error limits as constraints when sinusoidal phase currents are applied [55, 61]. However, this approach narrows the design space. Higher performance designs can be obtained if a more accurate machine model is used to determine the phase currents. Data from [3, Section III-E] has been replotted in Fig. 4.2b for permanent magnet (PM) and induction machines (IM) to demonstrate that 30% or more increase in torque density along with efficiency improvements up to 98% are possible when the force ripple constraint is removed.

4.4 Proposed Exact Model

This section proposes the exact electric machine model, which is the main contribution of this chapter. The model is applicable to all motor types, including PM, IM, and reluctance type motors. Section 4.4.1 provides additional force calculations that are not considered in the textbook model (4.22). Based on this, Sections 4.4.2 proposes the generalized exact model for bearingless machines, discusses its properties, and provides examples for different number of phases.

4.4.1 Additional terms in force calculation

As was previously mentioned, the suspension forces are created from the interaction between adjacent magnetic field space harmonics h and $h \pm 1$. Based on this fact and (4.11)–(4.12), this chapter identifies two additional force creation mechanisms that are not considered in the textbook model:

1. Forces from two adjacent current sequences. This can include the interaction between torque and suspension current sequences (armature reaction) or between other additional sequences that can be injected.
2. Forces from a single current sequence s_m (only occurs in machines with an odd number of phases m).

These two force creation mechanisms are now discussed. Analogous to the derivation in Section 4.3.1, the force vector expression derived in (4.18) is used.

4.4.1.1 Force from two adjacent current sequences

Force can be created by applying two adjacent current sequences s_1 and $s_2 = s_1 + 1$, as (4.11) shows that this creates pairs of adjacent harmonics h_1 and $h_2 = h_1 + 1$ which rotate in the same direction (CCW or CW). The resulting airgap field and force are given by (4.16) and (4.18). Using (4.13), (4.18) can be expressed in terms of the current sequence components:

$$\begin{aligned}
\vec{F}_{h_{12}} &= \bar{k}_{h_{12}} \hat{I}_{s_1} \hat{I}_{s_2} e^{j(\phi_{s_2} - \phi_{s_1})} = \bar{k}_{h_{12}} \vec{i}^{\,*}_{s_1} \vec{i}_{s_2} \\
\bar{k}_{h_{12}} &= \frac{\mu_0 V_r m^2 \hat{N}_{h_1} \hat{N}_{h_2}}{8r^2} \left(\frac{r}{\delta_\mathrm{eff}^2} - \frac{h_1 h_2}{r} + \frac{1}{\delta_\mathrm{eff}} \right) e^{j(\alpha_{\mathrm{w0},h_2} - \alpha_{\mathrm{w0},h_1})}
\end{aligned} \tag{4.24}$$

4.4.1.2 Force from a single current sequence

Force can be created by injecting the highest current sequence $s_{\mathrm{m}} = \frac{m-1}{2}$ in odd phase windings. Equation (4.11) shows that this creates pairs of adjacent harmonics that rotate in opposite directions: for every integer value of $c \geq 0$, harmonics exist at $h_1 = s_{\mathrm{m}} + mc$ and $h_2 = -s_{\mathrm{m}} + m(c+1)$:

$$\begin{aligned} h_2 &= -s_{\mathrm{m}} + m(c+1) = -s_{\mathrm{m}} + mc + m - 1 + 1 \\ &= -s_{\mathrm{m}} + mc + 2s_{\mathrm{m}} + 1 = h_1 + 1 \end{aligned} \tag{4.25}$$

The created pairs of harmonics are $(s_{\mathrm{m}}, s_{\mathrm{m}}+1)$, $(s_{\mathrm{m}}+m, s_{\mathrm{m}}+m+1)$, $(s_{\mathrm{m}}+2m, s_{\mathrm{m}}+2m+1)$, ...

Similar to Section 4.4.1.1, the total airgap magnetic field and the force vector due to these adjacent harmonics can be described by (4.16) and (4.18). However, since these harmonics rotate in opposite directions and are created by the same sequence s_{m}, their angular locations are $\phi_{s_1} = \phi_{s_{\mathrm{m}}}$, $\phi_{s_2} = -\phi_{s_{\mathrm{m}}}$ and their amplitudes depend on $\hat{I}_{s_{\mathrm{m}}}$, described by (4.13). This results in the following force expression:

$$\vec{F}_{h_{12}} = \bar{k}_{h_{12}} \hat{I}_{s_{\mathrm{m}}}^2 e^{-j2\phi_{s_{\mathrm{m}}}} = \bar{k}_{h_{12}} \vec{i}_{s_{\mathrm{m}}}^{*2} \tag{4.26}$$

This equation shows that the single sequence s_{m} can be used to control the force vector magnitude $F_{h_{12}} = \bar{k}_{h_{12}} \hat{I}_{s_{\mathrm{m}}}^2$ and angle $\phi = -2\phi_{s_{\mathrm{m}}}$.

The quadratic force vector component in (4.26) is not considered in other bearingless motor literature publications which is surprising given that this force also appears in bearingless machines with three-phase windings. This includes all three-phase combined windings where $s = 0$ creates torque and $s = 1$ creates force, and all three-phase separated windings with $s_\Theta = 1$ (always true when $p = 1$ or $p_s = 1$). If these quadratic terms are not accounted for, conventional design processes attempt to minimize these terms (presumably through the use of large effective airgap lengths) as they create force vector error. Instead, if these new terms are handled in the force regulator, designers can enhance these terms to increase the suspension force capability.

4.4.2 Generalized exact force model

The total force acting on the rotor due to all harmonics is now summarized in a single model. This is calculated as the vector sum of the force due to each pair of adjacent field harmonics h_i and $h_j = h_i + 1$: $\vec{F} = \sum \vec{F}_{h_{ij}}$, where each force vector component $\vec{F}_{h_{ij}}$ is described by (4.18). Based on the force/torque derivations in Sections 4.3.1 and 4.4.1, three types of force components $\vec{F}_{h_{ij}}$ are identified that differ by their dependence on current space vectors:

- Textbook model: force from stator-rotor harmonic interactions. This term has a linear dependence on the current space vector and is summarized in (4.22).
- New term 1: force from stator-stator harmonic interactions where each harmonic is created by a unique current sequence. This term depends on the product of two current space vectors, see (4.24).
- New term 2: force from stator-stator harmonic interactions where both harmonics are created by the same current sequence. This term depends on the square of a single current space vector (4.26).

This chapter proposes an exact force model that compiles the force terms created by all current space vectors that can be injected into the m-phase winding.

4.4.2.1 Matrix representation

The proposed model is written in matrix form as

$$\vec{F} = \vec{\boldsymbol{i}}^{\boldsymbol{T}} \bar{\boldsymbol{T}}_{\boldsymbol{Q}} \vec{\boldsymbol{i}} + \bar{\boldsymbol{T}}_{\boldsymbol{L}} \vec{\boldsymbol{i}} + \vec{F}_C \tag{4.27}$$

where $\vec{\boldsymbol{i}}$ is an $m \times 1$ array of the current space vectors and their conjugates calculated from the GCT matrix $\boldsymbol{C_m}$ as $\vec{\boldsymbol{i}} = \boldsymbol{C_m i}$:

$$\vec{\boldsymbol{i}} = \begin{bmatrix} \vec{i}_0 & \vec{i}_1 & \vec{i}_2 & ... & \vec{i}_2^* & \vec{i}_1^* \end{bmatrix}^T \tag{4.28}$$

and $\bar{\boldsymbol{T}}_{\boldsymbol{Q}}$ and $\bar{\boldsymbol{T}}_{\boldsymbol{L}}$ are $m \times m$ and $1 \times m$ complex matrices that model the quadratic and linear dependencies of the force on the current space vectors, and $\vec{F}_C$ is the cogging force.

Every entry of $\bar{\boldsymbol{T}}_{\boldsymbol{Q}}$ is determined by (4.24) and represents the force per ampere squared created due to two current space vectors. This includes the forces due to two adjacent current space vectors as in (4.24) ($\vec{i}_1^*\vec{i}_2$, $\vec{i}_2^*\vec{i}_3$, ...) and due to the space vector s_m as in (4.26) ($\vec{i}_{s_\mathrm{m}}^{*2}$). Every entry of $\bar{\boldsymbol{T}}_{\boldsymbol{L}}$ is a force per ampere given in (4.23), which shows an interaction between adjacent rotor-stator field harmonics created by one current space vector ($\vec{i}_1$, $\vec{i}_2$, ...). Note that the $\vec{i}_t$ and $\vec{i}_s$ space vectors of the textbook model (4.22) are present in (4.28), but indicated as a sequence number; i.e. $\vec{i}_t = \vec{i}_1$ and $\vec{i}_s = \vec{i}_2$.

The proposed exact model in (4.27) can incorporate multiple harmonics by modifying $\bar{\boldsymbol{T}}_{\boldsymbol{Q}}$ and $\bar{\boldsymbol{T}}_{\boldsymbol{L}}$ matrix entries. Every entry of $\bar{\boldsymbol{T}}_{\boldsymbol{Q}}$ is a sum of the terms in (4.24) as $\bar{K}_{s_{ij}} = \sum \bar{k}_{h_{ij}}$ for all adjacent airgap harmonics h_i and h_j created by the sequences s_i and $s_j = s_i + 1$ or the sequence s_m in odd phase machines. Similarly, every entry of $\bar{\boldsymbol{T}}_{\boldsymbol{L}}$ is the sum of the terms in (4.23) as $\bar{K}_{s_i} = \sum \bar{k}_{f,h_{ir}}$ for all adjacent harmonics h_i and h_r created by the sequence s_i and the rotor magnets. Depending on the relative rotation direction of these harmonics, some harmonic interactions result in a force ripple (having the $e^{j\pm 2\theta}$ term) or a constant force.

4.4.2.2 Space vector representation

Since only specific entries of $\bar{\boldsymbol{T}}_{\boldsymbol{Q}}$ are non-zero, the proposed model (4.27) can be rewritten using (4.22), (4.24), and (4.26) for even phase machines as:

$$\vec{F} = \sum_{i=1}^{s_\mathrm{m}-2} \bar{K}_{s_{ij}} \vec{i}_{s_i}^* \vec{i}_{s_j} + \sum_{i=1}^{s_\mathrm{m}-1} \left(\bar{K}_{s_i} \vec{i}_i + \bar{K}_{s_i^*} \vec{i}_{s_i}^* \right) \tag{4.29}$$

and for odd phase machines as,

$$\vec{F} = \bar{K}_{s_\mathrm{m} s_\mathrm{m}} \vec{i}^{\,*}_{s_\mathrm{m}}{}^{2} + \sum_{i=1}^{s_\mathrm{m}-1} \bar{K}_{s_{ij}} \vec{i}^{\,*}_{s_i} \vec{i}_{s_j} + \sum_{i=1}^{s_\mathrm{m}} \left(\bar{K}_{s_i} \vec{i}_{s_i} + \bar{K}_{s_i^*} \vec{i}^{\,*}_{s_i} \right) \tag{4.30}$$

where $\vec{F}_C$ is omitted to save space. Note that odd phase machines have an additional term that depends on the space vector s_m due to (4.26). The term $\bar{K}_{s_i^*} \vec{i}^{\,*}_{s_i}$ is a force ripple term from interaction between adjacent magnet and winding field harmonics that rotate in opposite directions. Depending on the desired model accuracy, the coefficients in (4.29) and (4.30) can be modified to include the desired number of space harmonics.

4.4.2.3 Examples

To demonstrate the use of the proposed model, a force vector equation for an example nine-phase machine is now provided by expanding (4.30) (assuming that the rotor magnetic field is purely sinusoidal):

$$\vec{F}_{\text{9-ph}} = \bar{k}_{h_{45}} \vec{i}^{\,*2}_{4} + \bar{k}_{h_{34}} \vec{i}^{\,*}_{3} \vec{i}_{4} + \bar{k}_{h_{23}} \vec{i}^{\,*}_{2} \vec{i}_{3} + \bar{k}_{h_{12}} \vec{i}^{\,*}_{1} \vec{i}_{2} + \bar{k}_{f} \vec{i}_{s} \tag{4.31}$$

This machine has four independent rotating current space vectors. Here, $\bar{k}_f \vec{i}_s$ is the force from stator-rotor interaction and $\vec{i}_s$ can be any space vector between $\vec{i}_1$ and $\vec{i}_4$ depending on p_s. Coefficients $\bar{k}_{h_{12}}$, $\bar{k}_{h_{23}}$, $\bar{k}_{h_{34}}$, $\bar{k}_{h_{45}}$ are the entries of $\bar{\boldsymbol{T}}_{\boldsymbol{Q}}$ and are calculated using (4.24). Differing from the textbook model (4.22), (4.31) shows that the proposed exact model has multiple quadratic terms. Accounting for these terms in a bearingless machine design study can potentially yield bearingless machine designs with enhanced force capability.

The proposed model (4.27) can be used to find the exact force vector expression for any m. As further examples, consider five- and six-phase machines, which have two rotating space vectors $\vec{i}_1$ and $\vec{i}_2$. When $\vec{i}_1 = \vec{i}_t$ and $\vec{i}_2 = \vec{i}_s$, force vector expressions can be obtained analogous to (4.31):

$$\vec{F}_{\text{5-ph}} = \bar{k}_q \vec{i}_s^{*2} + \bar{k}_{ft}\vec{i}_t^{*}\vec{i}_s + \bar{k}_f\vec{i}_s,\ \vec{F}_{\text{6-ph}} = \bar{k}_{ft}\vec{i}_t^{*}\vec{i}_s + \bar{k}_f\vec{i}_s \tag{4.32}$$

where $\bar{k}_q$ and $\bar{k}_{ft}$ are the entries of $\bar{\boldsymbol{T}}_{\boldsymbol{Q}}$ matrix in (4.27). As in (4.31), these equations have new quadratic terms due to two adjacent space vectors $\vec{i}_t^{*}\vec{i}_s$ and the highest space vector $\vec{i}_s^{*2}$ for $m = 5$. The $\vec{i}_s^{*2}$ term also appears in bearingless machines with three phases, as was discussed in Section 4.4.1.2. To avoid force vector error created by these quadratic terms, (4.32) can be used to implement exact force vector regulation by analytically solving for phase current commands that eliminate force vector error, as demonstrated in Fig. 4.2a for a five-phase machine.

4.5 Comparison to Prior Exact Models

This section makes a comparison between the exact model developed in Section 4.4 and the two studies [5] and [6] that developed the exact model for AMBs and bearingless motors, respectively. It will be shown that the models developed in these studies can be viewed as special cases of the exact model presented in Section 4.4.

4.5.1 Exact AMB Model

Study [5] developed the exact force vector model for a three-pole ($m = 3$) AMB, as shown in Fig. 4.3a, where the radial forces are created due to bias and control fields. Using this model, [5] proposed an analytic framework to find the desired coil currents (equivalent to solving a quartic polynomial equation) and experimentally demonstrated the performance improvement using the proposed exact force vector regulator compared to the conventional regulation approaches.

The exact force vector model in [5, eq. (19)-(20)] can be rewritten using the notation in this document as

$$\vec{F}_{\text{AMB}} = \frac{3}{2}k_1 \left(\frac{1}{2} \left(\hat{B}_{\text{n,w},1} e^{-j\phi_1} \right)^2 + 2B_{\delta,0}\hat{B}_{\text{n,w},1} e^{j\phi_1} \right) \tag{4.33}$$

where $B_{\delta,0}$ is a homopolar magnetizing field, $\hat{B}_{\text{n,w},1}$ is the amplitude of a rotating two-pole field described by (4.12), and k_1 is a constant that represents the force-field relationship. The rotating field is created by three-phase currents ($s = 1$) represented by $\vec{i}_1 = \hat{I}_1 e^{j\phi_1}$. When the constants are combined together, (4.33) can be rewritten as

$$\vec{F}_{\text{AMB}} = \bar{k}_q \vec{i}_1^{*2} + \bar{k}_f \vec{i}_1 \tag{4.34}$$

which shows the force vector has both quadratic and linear dependencies on the currents. The newly proposed exact model (4.27) can be simplified to (4.34) for this machine (three-phase winding, $s = s_{\text{m}} = 1$ creates force, $s = 0$ could create torque).

4.5.2 Exact Bearingless Flux-Switching Motor Model

Study [6] presented the exact force/torque motor model for bearingless machines. The model considers the linear (stator-rotor interactions) and quadratic (stator-stator interactions) dependence of the force/torque on the phase currents. Although the model in [6] was shown to improve force vector regulation accuracy, [6] assumed that the force components from the phase-to-phase interactions ($i_1 i_2$, $i_2 i_3$, ...) are negligible. This assumption limits the use of the model to a specific motor topology such as the flux-switching motor with flux barriers that was used for the case study in [6] (see Fig. 4.3b). Furthermore, the model is FEA-based and no analytic expressions were developed, which makes it difficult to understand the actual physics of the machine and its system properties.

Unlike the exact model (4.27) developed in this work, the model in [6, eq. (1)] is based on phase current quantities:

$$\begin{aligned} \vec{F} &= \boldsymbol{i^T} \boldsymbol{\bar{T}_{Q,xy}} \boldsymbol{i} + \boldsymbol{\bar{T}_{L,xy}} \boldsymbol{i} + \bar{T}_{C,xy} \\ \tau &= \boldsymbol{T_{L,\tau}} \boldsymbol{i} + T_{C,\tau} \end{aligned} \tag{4.35}$$

where $\boldsymbol{i} = \begin{bmatrix} i_1 & i_2 & ... & i_m \end{bmatrix}^T$ is an array of the phase currents. $\boldsymbol{\bar{T}_{Q,xy}} = \boldsymbol{T_{Q,x}} + j\boldsymbol{T_{Q,y}}$ is $m \times m$ matrix that represents quadratic dependence; $\boldsymbol{\bar{T}_{L,xy}} = \boldsymbol{T_{L,x}} + j\boldsymbol{T_{L,y}}$ and $\boldsymbol{T_{L,\tau}}$ are $1 \times m$ matrices that represent linear dependence; $\bar{T}_{C,xy} = T_{C,x} + j_{C,y}$ and $T_{C,\tau}$ are the terms that represent cogging forces/torque (no dependence on currents). Since phase-to-phase interactions were ignored, [6] set the non-diagonal entries of $\boldsymbol{\bar{T}_{Q,xy}}$ to zero and rewrote the quadratic term as $\boldsymbol{i^T} \boldsymbol{\bar{T}_{Q,xy}} \boldsymbol{i} = \text{diag}\left(\boldsymbol{\bar{T}_{Q,xy}}\right) (\boldsymbol{i} \circ \boldsymbol{i})$. Here, $\boldsymbol{i} \circ \boldsymbol{i} = \begin{bmatrix} i_1^2 & i_2^2 & ...i_m^2 \end{bmatrix}^T$ is the Hadamard product.

The exact model proposed by this research work includes all phase current interactions through space vector currents. Therefore, the model in [6] is a special case of the exact model in (4.27). Using the space vector transformation $\vec{\boldsymbol{i}} = \boldsymbol{C_m} \boldsymbol{i}$, the relationship between the matrices in (4.27) and (4.35) is determined:

$$\boldsymbol{\bar{T}_{Q,xy}} = \boldsymbol{C_m^T} \boldsymbol{\bar{T}_Q} \boldsymbol{C_m}, \quad \boldsymbol{\bar{T}_{L,xy}} = \boldsymbol{\bar{T}_L} \boldsymbol{C_m} \tag{4.36}$$

4.6 Force Ripple Minimization

This section shows how the proposed exact model can be used to minimize force ripple. Simulation results using two example five-phase machines are presented.

The force ripple in literature is typically characterized by force magnitude error E_m and force angle error E_a [57]. This is illustrated in Fig. 4.3c, where the desired force $\vec{F}^*$ is along x-axis, while the actual force $\vec{F}$ can have both F_x and F_y components at any rotor angular position. These two metrics are calculated as $E_m = \frac{F_{\max} - F_x}{F_x}$ and $E_a = \tan^{-1}\left(\frac{F_y}{F_x}\right)$,

	SPM	IM		SPM	IM
$\bar{k}_f$ (N/A)	$6.46e^{-j\theta}$	0	Outer radius (mm)	200	
$\bar{k}_{ft}$ (N/A^2)	2.84	10.6	Rated speed (kRPM)	30	
$\bar{k}_q$ (N/A^2)	-0.58	-1.92	Rated P_{out} (kW)	9.8	

Table 4.1: Example motor parameters

which show the maximum deviation from the desired force magnitude and angle. Study [19] reported large force angle error ($> 17°$) can cause instability in suspension regulation and [58] suggested to keep force angle error below $< 5°$.

The two examples used to demonstrate the benefits of the proposed exact model are a five-phase SPM machine (Fig. 4.3d) and IM (Fig. 4.3e) that have the same stator. The key parameters are given in Table 4.1, including the quadratic force coefficients of (4.32). Figure 4.2a compares the error in force vector magnitude and angle for the SPM example when the textbook (4.22) and the exact (4.32) models are used to solve for the phase currents to create a force $F_x = 20$ N. The plotted force data is obtained from FEA by using the calculated phase currents. For the exact model, solving (4.32) for the phase currents is equivalent to solving a fourth order polynomial equation, which has up to four real solutions. The solution with the lowest ohmic losses $\sum_{k=1}^{5} i_k^2$ is selected (Euclidean L^2 norm). Cogging force is not included and linear iron material is used. Figure 4.2a shows that the exact model can significantly improve force actuation accuracy. Figure 4.3f shows the polar plot of force vector components in (4.32) for the IM example when the rated suspension current space vector $\vec{i}_s$ is applied and rotated over 360 degrees. This plot shows the significance of the quadratic $\bar{k}_q$ term on the total force created on a shaft.

The proposed exact model can also be used to minimize the force ripple during the design stage. If the designer desires to eliminate the effects of the quadratic term $\bar{k}_q \vec{i}_s^{*2}$, it can be shown using (4.24) that this can happen when the machine design parameters are selected to have the relation $p_s \delta_{\text{eff}} = r$. This can be advantageous for machines with a small rotor radius or a high number of pole pairs.

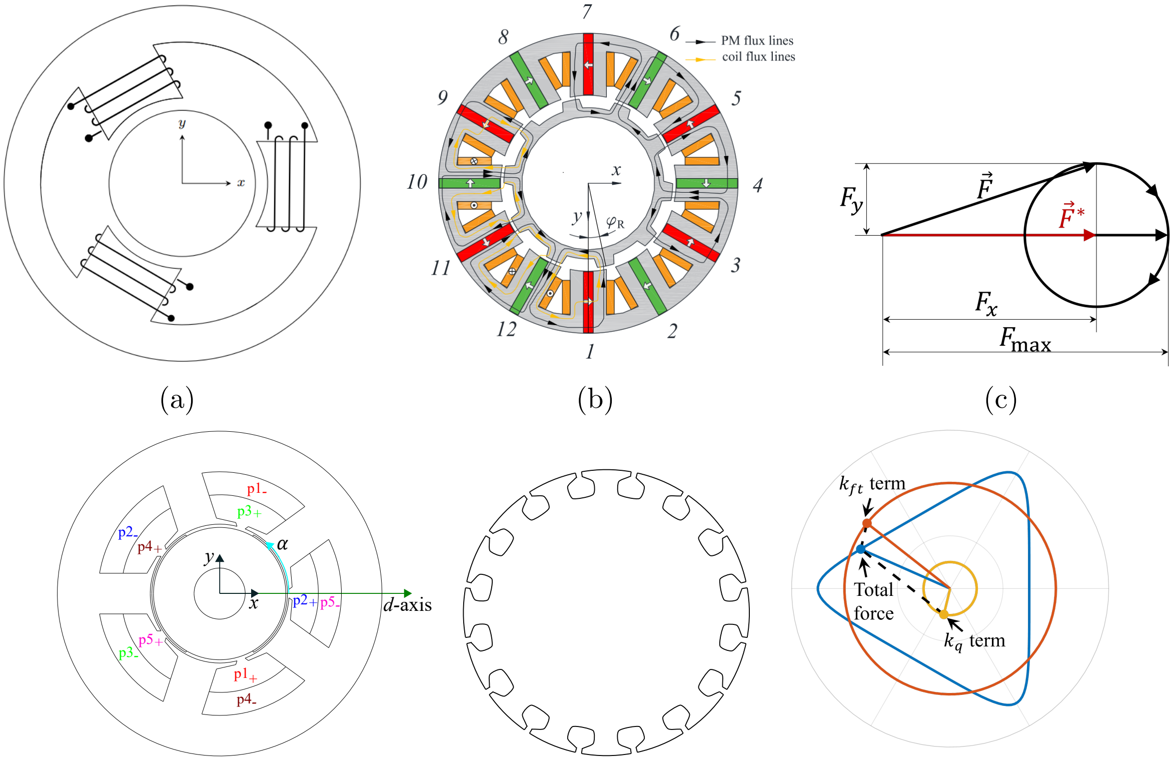

(a) (b) (c)

(d) (e) (f)

Figure 4.3: (a) and (b) electric machine cross-sections used in the development of the exact models for three-pole AMB in [5] and bearingless flux-switching motor in [6], rexpectively, (c) illustration of force magnitude and angle error. SPM and IM examples with the same stator $Q = 5$ and $m = 5$: (d) SPM example cross-section, (e) IM example rotor cross-section, and (f) polar plot of force vector components for the IM example.

4.7 Force Enhancement

This section investigates how the proposed model can be used to enhance the force capacity of bearingless motors through control of multiple airgap harmonic fields. Bearingless machines with $m = 5$ through 10 are compared in terms of their rated force capabilities, current requirements, ohmic losses, and simultaneous torque capability. The machines are compared over a range of magnetizing field $\hat{B}_\delta$. This is a critical design parameter influencing motor design sizing and its torque capability. All examples have $p = 1$, the same motor dimensions, the same total number of turns $m z_Q z_c$ (same $R_{\mathrm{ph}} m$, where R_{ph} is the phase winding resistance), and unity winding factors $\hat{k}_{\mathrm{w},h_i} = 1$ for all harmonics to allow a comparison in per-unit [p.u.] quantities. Appendix B provides the p.u. force vector model (B.1) and the base values (B.2) used in this section.

4.7.1 Force Rating

First, the proposed exact model is used to show that higher force rating can be achieved when controlling multiple harmonics in bearingless machines. Using the definition of F_{rated} in [19, Ch. 2], the dimensionless model (B.1) allows finding F_{rated} as follows:

1. Solve for the field quantities to find the maximum force profile $F'_{\text{max}}(\phi)$ over all force angles ϕ, while satisfying $\max(|B'_{\text{n}}(\alpha)|) \leq 1$ (solved as an optimization problem in Matlab).

2. Find the rated force as $F'_{\text{rated}} = \min\left[F'_{\text{max}}(\phi)\right]$, which is the force that can be created at any angle.

Using the result from these steps, force capacity/specific load capacity, which is defined as the load capacity per the projected rotor area (diameter × length) [31, Ch. 6], can be found as

$$f_c = \frac{F'_{\text{rated}} F_{\text{b}}}{DL} = \frac{\pi}{4\mu_0} B^2_{\text{max}} F'_{\text{rated}} \tag{4.37}$$

The results after following these steps are provided in Fig. 4.4a, which shows the maximum force profile and the rated force (shown as an inscribed red dashed circle for $\hat{B}'_\delta = 0.5$ p.u.). Based on this, the rated force vs. $\hat{B}_\delta$ is obtained and plotted in Fig. 4.4b (top subplot). Figure 4.4a illustrates that, unlike other phases, the $m = 5$ machine has non-convex maximum force profiles for a range of $\hat{B}_\delta$ values. This results in F_{rated} being a non-convex function of $\hat{B}_\delta$, as shown in Fig. 4.4b (two maxima at $\hat{B}'_\delta = 0$ and 0.7 p.u.). This is due to the quadratic term in (4.32), which also appears in certain three-phase separated windings and three-pole AMBs [5], as described in Section 4.5.1. Figure 4.4b also compares the current rating and the average ohmic losses per unit of the rated force (subplots 2 and 3). The currents are calculated using the p.u. field quantities and the base value I_b, as given in (B.2).

These results show that machines with $m \geq 8$ phases can maintain their force capability over a wide range of $\hat{B}_\delta$ values. Of all phase combinations, $m = 6$ has the poorest performance at $\hat{B}'_\delta \leq 0.2$ p.u. (lowest force rating, highest current rating and ohmic losses). At $\hat{B}'_\delta \approx 0$, machines with $m = 5$ have the lowest current rating and ohmic losses, while having the same force rating as other phases. This is because $m = 5$ machines can use a single sequence $s = 2$ to create suspension forces, which corresponds to the quadratic term in (4.32). It is found that the 10-phase machine can create the largest force, with the peak at $\hat{B}'_\delta = 0.5$ p.u. This is because the 10-phase machine can independently control four harmonics, which adds more degrees of freedom to simultaneously satisfy the constraint $\max(|B'_\mathrm{n}(\alpha)|) \leq 1$ and enhance the force creation.

4.7.2 Force Impact on Torque

The machines are also compared in terms of their torque capabilities. In this comparison, the motor creates a constant force (equal to the rotor weight W_r or its multiple) and the torque that the motor can create at any force angle without exceeding the maximum airgap field limit is determined. Figure 4.4c shows that the torque performance in $m = 6$ and 8 is the same in all cases (same for all other phases with $m \geq 6$), with a peak torque at $\hat{B}'_\delta = 0.7$ p.u.. The torque performance of the $m = 5$ machine is poorer, which is especially noticeable at high force values.

4.7.3 Discussion

The findings using the proposed model show that the control of multiple airgap harmonic fields can help enhance the performance of bearingless machines. By controlling four airgap harmonic fields as opposed to two ($m = 10$ vs. $m = 6$ phases), the results reveal that an increase in force rating by over 40% can be achieved at the magnetizing field $\hat{B}'_\delta = 0.5$ p.u. This corresponds to an increase in force capacity (4.37) from 10.4 to 14.3 N/cm^2 when $B_{\text{max}} = 0.8$ T. Similarly, at $\hat{B}'_\delta = 0.7$ p.u., controlling four harmonic fields instead of two improves force rating by 36%, increasing the force capacity from 8.7 to 12.2 N/cm^2 for $B_{\text{max}} = 0.8$ T. This improvement is advantageous when a bearingless machine operates near iron saturation or requires large amount of force. Furthermore, designs that support a wide range of magnetizing fields ($m \geq 8$) offer more flexibility during the design stage to meet motor design specifications and during operation to support optimal motor control via field weakening. It is also seen the machines that obtain the maximum torque and force capabilities have $m \geq 8$ and $\hat{B}'{}_\delta = 0.7$ p.u. These results suggest that the designs with at least three controllable airgap harmonic fields and $\hat{B}'{}_\delta \approx$ 0.5-0.7 p.u. can be a potential solution to improve bearingless motor performance.

4.8 Conclusion

This chapter proposes an exact force/torque model for bearingless electric machines using current space vector/sequence components and their relationship to airgap magnetic field space harmonics. It is found that previous attempts at developing the exact models for magnetic bearings and bearingless motors can be viewed as special cases of the generalized model developed in this chapter. Furthermore, this chapter finds that all three-phase combined windings and some three-phase separated windings have quadratic force vector components, which have been neglected in previous literature. The chapter finds that when these terms are ignored in the force model, substantial force vector error can result; however, when properly handled, these additional forces can increase the machine's force rating.

The proposed model is applicable to all motor types, is analytic-based, and captures the underlying physics of the machine accurately. These features equip the machine and controls designers with tools to increase the torque and levitation system performance. The chapter

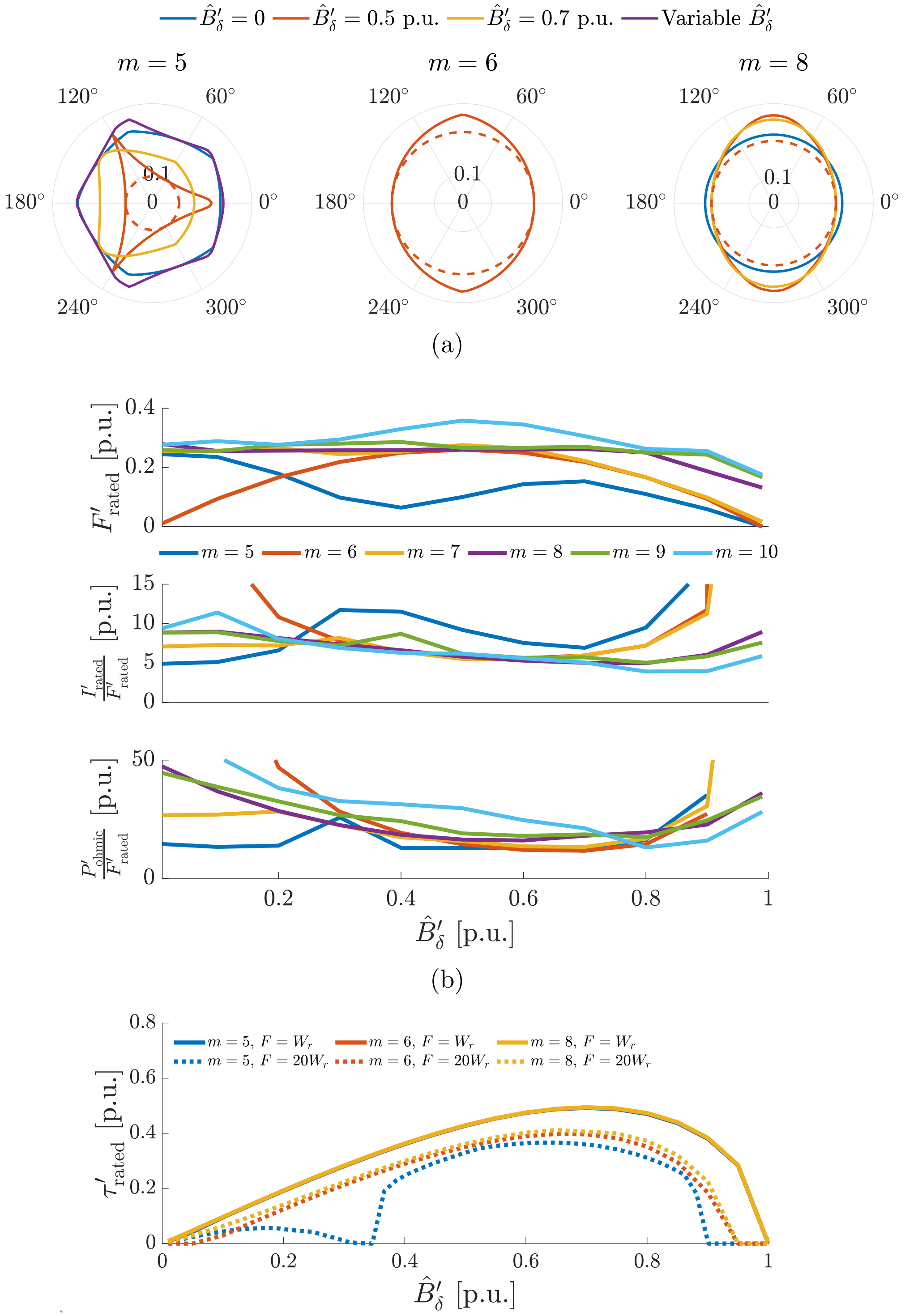

(a)

(b)

(c)

Figure 4.4: Comparison between bearingless machines with $m = 5$ to 10 phases: (a) maximum force profiles shown for different magnetizing fields, (b) force rating, current rating, and average ohmic losses vs. $\hat{B}'_\delta$, and (c) torque rating vs. $\hat{B}_\delta{}'$ for different force magnitudes.

finds that the developed model can be used to eliminate the force vector error by selecting a certain combination of machine design parameters during the design stage or by having the control system analytically solve the exact model during runtime to determine phase currents as the sum of multiple current sequences. The chapter shows how the proposed model can be used to enhance force creation in bearingless machines by controlling multiple airgap harmonic fields. Increase in force rating by approximately 40% can be achieved with 10 phases as opposed to six phases. Enhanced force performance can be advantageous in various operating conditions, including the operation under iron saturation, when a large amount of force is required, or when a machine operates under varying magnetizing field and torque.

In conclusion, the findings of this chapter provide motivation to rethink the design approach of bearingless machines to include additional force creation mechanisms and to develop regulation techniques that use the proposed exact model. These developments have potential to make the design space of bearingless machines less constrained and enable consideration of higher performance designs. Based on the findings in this and next chapters, Chapter 6 will conduct a detailed design study using a 10-phase bearingless induction machine.

Chapter 5

Analysis of Force Capacity in Magnetic Bearings and Bearingless Motors from the Perspective of Airgap Space Harmonic Fields

5.1 Introduction

This chapter builds upon the exact modeling framework developed in Chapter 4 and presents a detailed analysis of force capacity in AMBs and bearingless motors from the perspective of airgap harmonic fields. Both technologies are known to have a lower specific load capacity [31] than other bearing types. Specific load capacity is calculated by dividing the rated force (maximum force that can be created at any angle) by the projected rotor area (length × diameter) [32]. Typically, AMBs have a specific load capacity of 30-40 N/cm^2, with cobalt-alloys reaching up to 65 N/cm^2 [31, 33–35]. Bearingless motors are often assumed to have a significantly lower load capacity of approximately 9 N/cm^2 [32]. Furthermore, in most publications, force creation and control in AMBs is considered in terms of individual poles/teeth. This chapter will present an alternate analysis method from the perspective of airgap space harmonics.

The core contributions of this chapter are: 1) explanation of the force capacity of AMBs from the perspective of controllable airgap space harmonic fields, 2) explanation of the force capacity in bearingless motors when only two space harmonics are controlled, and 3) enhancement of the force capacity in bearingless motors by controlling multiple airgap space harmonics and comparison to AMB performance limits. Section 5.2 reviews pole- and space harmonic-based force models and shows relations between controllable harmonic fields, current sequences, and forces. Section 5.3 uses the harmonic-based model to explain force capacity in AMBs (contribution 1). Section 5.4 explains torque-force capability and presents force enhancement potential using multiple harmonics (contributions 2 and 3).

5.2 Force Creation from the Perspective of Airgap Space Harmonic Fields

This section briefly reviews the force creation in AMBs and bearingless motors based on the airgap space harmonic field interactions presented in Chapter 4 and identifies the relationship with the conventional method of calculating force in magnetic bearings. Section 5.2.1 reviews the force vector models and Section 5.2.2 presents the relationship between airgap harmonics, current sequences, and controllable force vectors. The model (5.2) is used in subsequent sections to calculate the force capacity in AMBs and bearingless motors.

5.2.1 Pole- and Harmonic-Based Force Vector Models

The conventional method of calculating force in AMBs is based around a magnetic equivalent circuit, where the total force is the vector sum of the forces created by individual poles/teeth [31]. This model assumes that the field is normal to the tooth surface and is constant over the tooth span. The cross-section of a general AMB with one coil per pole is depicted in Fig.5.1a.

Each pole i can create an attraction force of $F_i = \frac{A}{2\mu_0}B_i^2$, which depends on the square of flux density B_i in tooth i and the tooth surface area A facing the airgap. Under saturation operation, the pole field has a linear relationship with the pole current. When there are n_p equally spaced poles with the same surface area A as in Fig. 5.1a, the total created total force vector is (5.1), where $a^{i-1} = e^{\mathrm{j}(i-1)2\pi/n_p}$ indicates the force direction created by pole i.

$$\vec{F} = Fe^{\mathrm{j}\phi} = \frac{A}{2\mu_0}\left(B_1^2 + aB_2^2 + a^2B_3^2 + ... + a^{n_p-1}B_{n_p}^2\right) = \frac{A}{2\mu_0}\sum_{i=1}^{n_p} a^{i-1}B_i^2 \tag{5.1}$$

An AMB can be equivalently viewed as a multiphase winding with m drive connections (m independent currents), as was shown in Fig. 3.1. This equivalence allows applying the theories used to analyze multiphase windings in bearingless machines (Generalized Clarke Transformation, winding function theory) and studying force creation in AMBs from the perspective of airgap space harmonic fields. Instead of individually viewing each tooth field, the total airgap field can be studied in terms of its spatial harmonic content along the airgap angle α (see Fig. 5.1b). Each harmonic of order h is expressed as $B_{\mathrm{n},h}(\alpha) = \hat{B}_{\mathrm{n},h}\cos(h\alpha - \phi_h)$ with a magnitude $\hat{B}_{\mathrm{n},h}$ and an angular location ϕ_h/h, and the total field is the sum of all space harmonics present in the airgap. As an example, Fig. 5.3b shows a plot of the total airgap field and its space harmonics of orders 1-6 along α. Using the exact model proposed in Chapter 4.4, the total created force in AMBs can be expressed in terms of harmonic quantities as

$$\vec{F} = \sum_{h_i=1}^{n_h-1} \vec{F}_{h_ih_j} = k\sum_{h_i=1}^{n_h-1} C_{h_{ij}}\vec{b}_{h_i}^{*}\vec{b}_{h_j}, \quad \text{where } k = \frac{V_r}{2\mu_0 r} \text{ and } C_{h_{ij}} = \left(1 - h_i\frac{\delta_{\mathrm{eff}}}{r}\right)\left(1 + h_j\frac{\delta_{\mathrm{eff}}}{r}\right) \tag{5.2}$$

where $\vec{b}_{h_i} = \hat{B}_{\mathrm{n},h_i}e^{\mathrm{j}\phi_{h_i}}$ is a vector that represents the field harmonic h_i, k is a constant in terms of the rotor volume V_r and radius r, and $C_{h_{ij}}$ is a factor considering the effect of the tangential field components (δ_{eff} is the effective airgap length). $C_{h_{ij}} \approx 1$ when $h_{i/j}\delta_{\mathrm{eff}} \ll r$. Some of the harmonics in (5.2) can be directly manipulated through the control of the equivalent current space vectors/current sequences, as was discussed in Chapter 4.2.2.

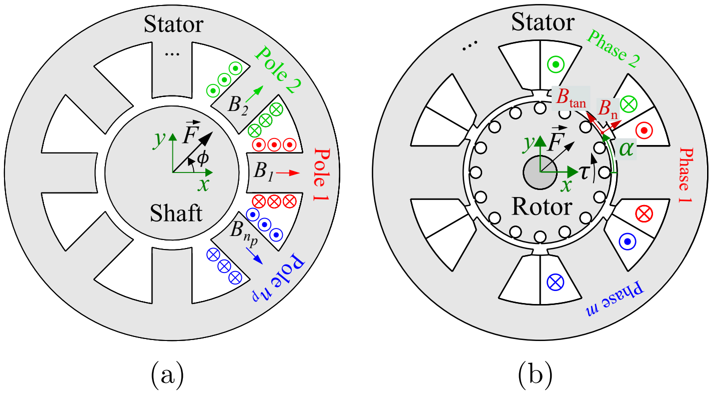

Figure 5.1: Cross-sections and definitions: (a) an example AMB (× and • indicate the coil direction into and out of the page, fields are shown for positive currents) and (b) an example bearingless motor with the definition of axes, fields components, and vectors.

5.2.2 Relationship to Current Sequences

Analogous to bearingless machines (see Chapter 4.2.2), the number of controllable currents m in AMBs directly determines the number of independently controllable harmonics and their spatial orders. These harmonics can be independently controlled by current sequences. Certain sequences can only control the magnitude of a harmonic (oscillating field), while other sequences can control both the magnitude and angle (rotating field):

$$
\begin{aligned}
&s = \pm 1,\ \pm 2,\ ...,\ \pm n_{\text{ind}} \text{ control rotating fields, } n_{\text{ind}} = \begin{cases} \frac{m-2}{2} & \text{for } m \in \mathbb{N}_{\text{even}} \\ \frac{m-1}{2} & \text{for } m \in \mathbb{N}_{\text{odd}} \end{cases} \\
&s = 0,\ \frac{m}{2} \text{ control oscillating fields}
\end{aligned} \tag{5.3}
$$

where n_{ind} is the total number of controllable rotating harmonics. AMBs with $m \in \mathbb{N}_{\text{even}}$ can control two oscillating and $n_{\text{ind}} = \frac{m-2}{2}$ rotating harmonics, while AMBs with $m \in \mathbb{N}_{\text{odd}}$ can control one oscillating and $n_{\text{ind}} = \frac{m-1}{2}$ rotating harmonics.

The force vector model (5.2) in terms of current quantities can be used to identify the number of controllable force vectors. Using the Generalized Clarke Transformation as $\vec{\boldsymbol{i}} = \boldsymbol{C_m i}$ [85], where $\vec{\boldsymbol{i}}$ is an array of all space vectors, the space vector form of (5.2) is

$$\vec{F} = \sum_{i=1}^{n_f} \bar{k}_{q,h_{ij}} \vec{i}_i^* \vec{i}_j \tag{5.4}$$

where $\bar{k}_{q,h_{ij}}$ is the force per ampere squared and n_f is the number of controllable force vectors. To control an individual force vector component $\vec{F}_{h_i h_j} = kC_{h_{ij}} \vec{b}_{h_i}^* \vec{b}_{h_j} = \bar{k}_{q,h_{ij}} \vec{i}_i^* \vec{i}_j$, at least one magnitude and one angle out of four quantities ($\hat{B}_{h_i}$, $\hat{B}_{h_j}$, ϕ_{h_i}, ϕ_{h_j}) must be controllable. This means one harmonic must be able to rotate, while the other harmonic can have a rotating or oscillating behavior. There are $n_{\text{ind}} - 1$ force vectors created independently when controlling all n_{ind} adjacent rotating harmonics. For an even m, an additional force vector can be created when the magnitude of an oscillating harmonic is controlled by sequence $s = 0$ or $\frac{m}{2}$. For an odd m, there is also an additional force vector created by a single sequence, as discussed in Chapter 4.4.1.2. This sequence creates two adjacent harmonics that rotate in opposite directions. This explains the way force is created in a three-pole AMB, where harmonics $h_i = 1$ and $h_j = 2$ create force $\vec{F}_{h_i h_j} = kC_{h_{ij}} \hat{B}_{h_i} \hat{B}_{h_j} e^{-2\phi_{h_i}}$. In summary, for any m number of independent winding currents, there are $n_f = n_{\text{ind}}$ independently controllable force vectors.

5.2.3 Force Creation in AMB Examples

Consider force creation in 4-, 8-, and 12-pole AMB examples in Fig. 5.2, where all AMBs have $m = 4$ independent currents. From (5.3), one rotating harmonic ($n_{\text{ind}} = 1$) from sequence $s = 1$ and one oscillating harmonic from $s = 0$ or $s = m/2$ can be controlled in these AMBs. Controlling one rotating and one oscillating harmonic allows controlling $n_f = 1$ force vector component. The dominant force creating harmonics depend on the winding layout of these AMBs (number of poles per drive connection). Similar to the winding analysis in electric motors, these dominant harmonics can be identified based on their winding factors. The winding factor $\hat{k}_{\text{w},h}$ can take values from zero (harmonic h cannot be created) to one (harmonic h is one of the dominant harmonics). The first dominant harmonic has order $h = n_p/2$ (oscillating), which is created when the subsequent poles in Fig. 5.2 have alternating

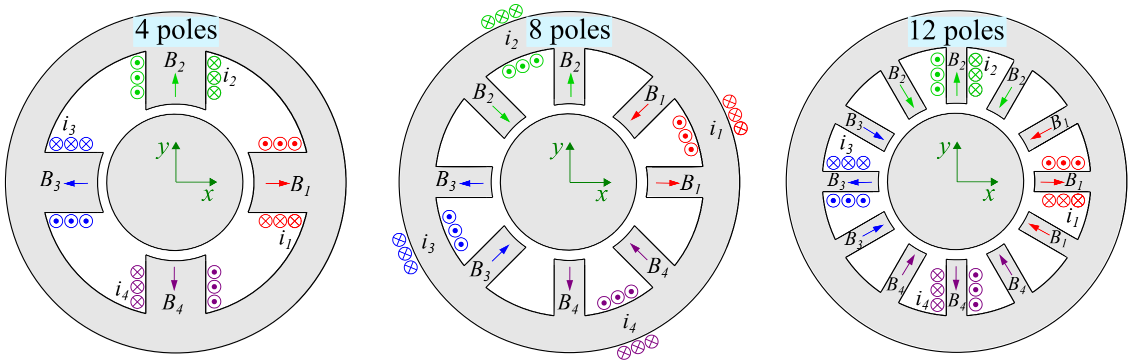

Figure 5.2: AMBs with 4, 8, and 12 poles (to apply electric motor winding analysis methods, these AMBs can be viewed as each pole wound by a coil).

magnetic field polarities. In 4- and 12-pole AMBs, this is achieved with $s = 2$ when currents are 180° phase separated (when subsequent currents are equal but opposite). However, in 8-pole AMBs, $h = n_p/2 = 4$ is created by $s = 0$ (all currents are equal). The second dominant harmonic has order of $h = n_p/2 - 1$ (rotating). This harmonic may not be trivial to visualize in 8- and 12-pole AMBs because some of its peaks are not located in front the poles. From the relation $h = \pm s + mb$, this harmonic is created by sequence $s = 1$ in 4- and 12-pole AMBs and by $s = -1$ (negative sequence) in 8-pole AMBs. Since one sequence can create multiple harmonics, sequence $s = \pm 1$ also creates harmonic $h = n_p/2 + 1$ in addition to $h = n_p/2 - 1$, which rotate in opposite directions. If the force equation (5.2) models one harmonic per sequence (harmonic with the highest magnitude), the interaction between $h = n_p/2 + 1$ and $h = n_p/2$ would be ignored, resulting in force vector error. However, since the control in AMBs is based on individual pole currents instead of particular harmonics, all harmonics (including higher order harmonics) are inherently considered in the force model.

5.3 Force Capacity of AMBs from the Perspective of Multiple Airgap Harmonic Fields

This section explains the force capacity/design sizing of AMBs from the perspective of multiple airgap space harmonics. This new explanation approach provides insight into identifying and controlling components of the total force vector from each harmonic interaction. The proposed approach to calculate force capacity is explained and the results are presented.

The force vector model in (5.2) can be used to determine the specific load capacity f_c. The procedure from Chapter 4.7.1 that calculates the rated force and the the dimensionless model from Appendix B are used and summarized below:

1. Find the maximum force magnitude $F'_{\text{max}}(\phi)$ that an AMB can create at every force angle ϕ, while keeping the peak airgap field max $\left[\left|\sum_{h_i=1}^{n_{\text{ind}}} \hat{B}'_{h_i}\cos\left(h_i\alpha - \phi_{h_i}\right)\right|\right]$ below 1 (the maximum airgap field in p.u.).

2. Calculate the force capacity as $f_c = F_{\text{rated}}/DL$, where $F_{\text{rated}} = \min\left[F_{\text{max}}(\phi)\right]$ is the rated force. D and L are the rotor diameter and axial length.

The use of the dimensionless model makes the force rating and force capacity results applicable to any DL and B_{max} values. After calculating the normalized rated force F'_{rated} using this model, the force capacity can be calculated as

$$f_c = \frac{kB_{\text{max}}^2 F'_{\text{rated}}}{DL} = \frac{\pi}{4\mu_0} B_{\text{max}}^2 F'_{\text{rated}} \tag{5.5}$$

This result shows that the force capacity does not depend on DL, but instead depends on the square of the maximum airgap field B_{max} and the harmonics present in the airgap.

This chapter shows results of force capacity calculations for AMBs considering only controllable rotating harmonics n_{ind}, resulting in $2n_{\text{ind}}$ control variables. The calculation of the force capacity for $n_{\text{ind}} \geq 2$ has to be solved as an optimization problem as infinitely many solutions exist. Furthermore, the problem has to be solved numerically due to nonlinear objective and constraints. When controlling two rotating harmonics h_i and h_j, the force magnitude and angle of (5.2) are calculated as $F = kC_{h_{ij}}\hat{B}_{h_i}\hat{B}_{h_j}$ and $\phi = \phi_{h_j} - \phi_{h_i}$. Following the procedure of calculating the specific load capacity, it is found that the rated force of $F'_{\text{rated}} = 0.32$ p.u can be obtained. Substituting this in (5.5) gives $f_c = 45$ N/cm^2 for $B_{\text{max}} = 1.5$ T (12.8 N/cm^2 for $B_{\text{max}} = 0.8$ T). This result is expected because the force capacity reported in the AMB literature is approximately 40 N/cm^2. Similarly, the force capacity for more than two independent harmonics can be calculated. Figure 5.3a summarizes the force capacity results for different numbers of harmonics when $B_{\max} = 1.5$ T. This plot shows that an approximately 31% increase in the force capacity can be obtained when increasing n_{ind} from 2 to 6, which is equivalent to increasing the number of poles from 6 to 14 according to (5.3). As an example, Fig. 5.3b shows the optimal distribution of the field harmonics when $n_{\text{ind}} = 6$ ($n_p = 14$) to create maximum force along the x-axis. The blue dots indicate the locations of the pole centers. In this case, all harmonics have their peaks located at $\alpha = \phi_{h_i}/h_i = 90°/h_i$, resulting in the total field (indicated with a solid black line) that has better iron utilization. Interestingly, Fig. 5.3b shows that poles 1 and 8 that are located along the force direction (indicated with a red dashed line at $\alpha = 0$) have zero fields, while three poles on either sides of the force direction (2-4 and 12-14) have the highest field values.

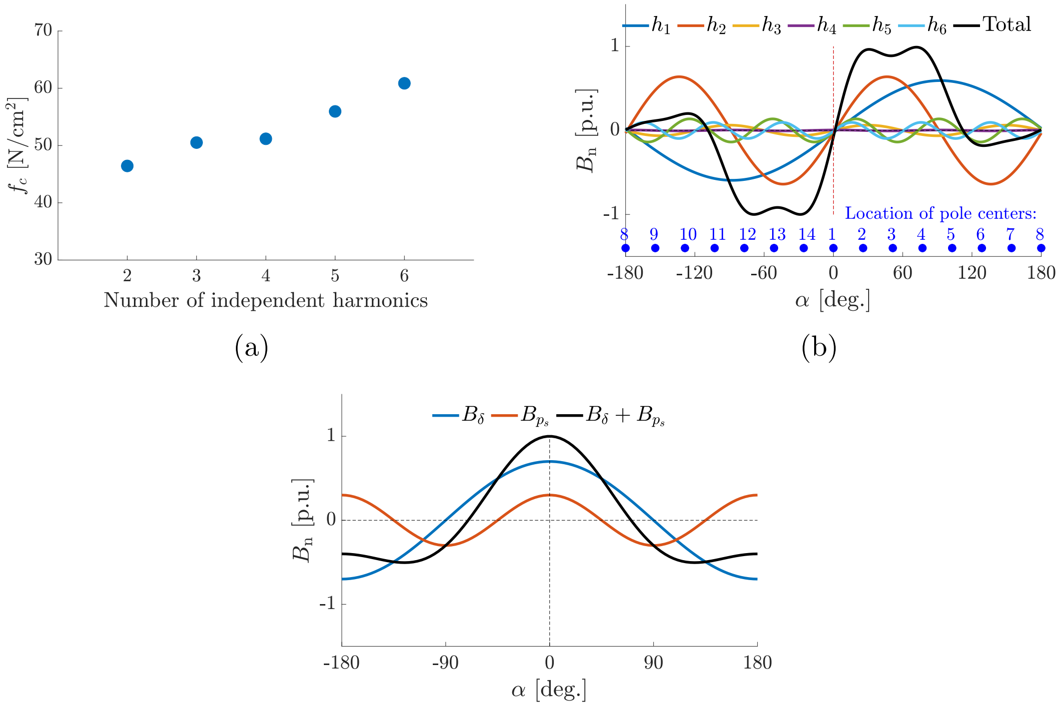

Figure 5.3: (a) Results of force capacity analysis in AMBs for different numbers of independent harmonics n_{ind}, (b) optimal airgap field distribution in AMBs for $n_{\text{ind}} = 6$ and $\phi = 0°$, and (c) optimal airgap field distribution in bearingless machines for $n_{\text{ind}} = 2$ and $\phi = 0°$.

5.4 Force Capacity in Bearingless Motors

This section presents the second and third contributions of the chapter. Section 5.4.1 explains force capacity in bearingless motors when only two space harmonics are controlled, identifies optimal magnetizing field values, and provides an analytical estimation of the torque-force capability using the p.u. model for different magnetizing field values. Section 5.4.2 proposes potential force capacity enhancement by controlling multiple harmonics. As the primary contribution of this chapter, this section finds that, enhancement of force capacity in bearingless machines equivalent to that of AMBs can be achieved through the control of multiple airgap harmonics.

5.4.1 Torque-Force Capability from Two Airgap Harmonics

The standard method of creating torque and suspension force in bearingless motors is through controlling p and p_s pole-pair fields. The p pole-pair field consists of a torque creating (q-axis) and a magnetizing field (d-axis) component B_δ, which impacts both torque and force creation. In addition to the force capacity calculation steps described in Section 5.3, the magnetizing field harmonic p must have a fixed amplitude at $\hat{B}_\delta$ and an angular location at the rotor rotational angle θ. This subsection identifies the optimal magnetizing field values $\hat{B}_\delta$ when there are two harmonics p and p_s. The optimal magnetizing field is defined as the value creating the maximum force or torque without exceeding the airgap field limit.

First, the optimal $\hat{B}_\delta$ to create the maximum force is identified. With two harmonics in the airgap, the maximum force that can be created at any angle has the magnitude of $F'_{\text{rated}} = \hat{B}'_\delta \hat{B}'_{p_s}$, according to the normalized form of (5.2). The peak airgap field must not exceed $B_{\max}$, which in p.u. is $\hat{B}'_\delta + \hat{B}'_{p_s} = 1$, as shown in Fig. 5.3c. Substituting $\hat{B}'_{p_s} = 1 - \hat{B}'_\delta$ gives $F'_{\text{rated}} = \hat{B}'_\delta(1 - \hat{B}'_\delta) = -\hat{B}'^2_\delta + \hat{B}'_\delta$. This is an inverted parabola with the peak $F'_{\text{rated}} = 0.25$ p.u. at $\hat{B}'_\delta = 0.5$ p.u., which gives 35.2 N/cm^2 at $B_{\max} = 1.5$ T and 10 N/cm^2 at $B_{\max} = 0.8$ T. AMBs have approximately 28% higher force capacity at these

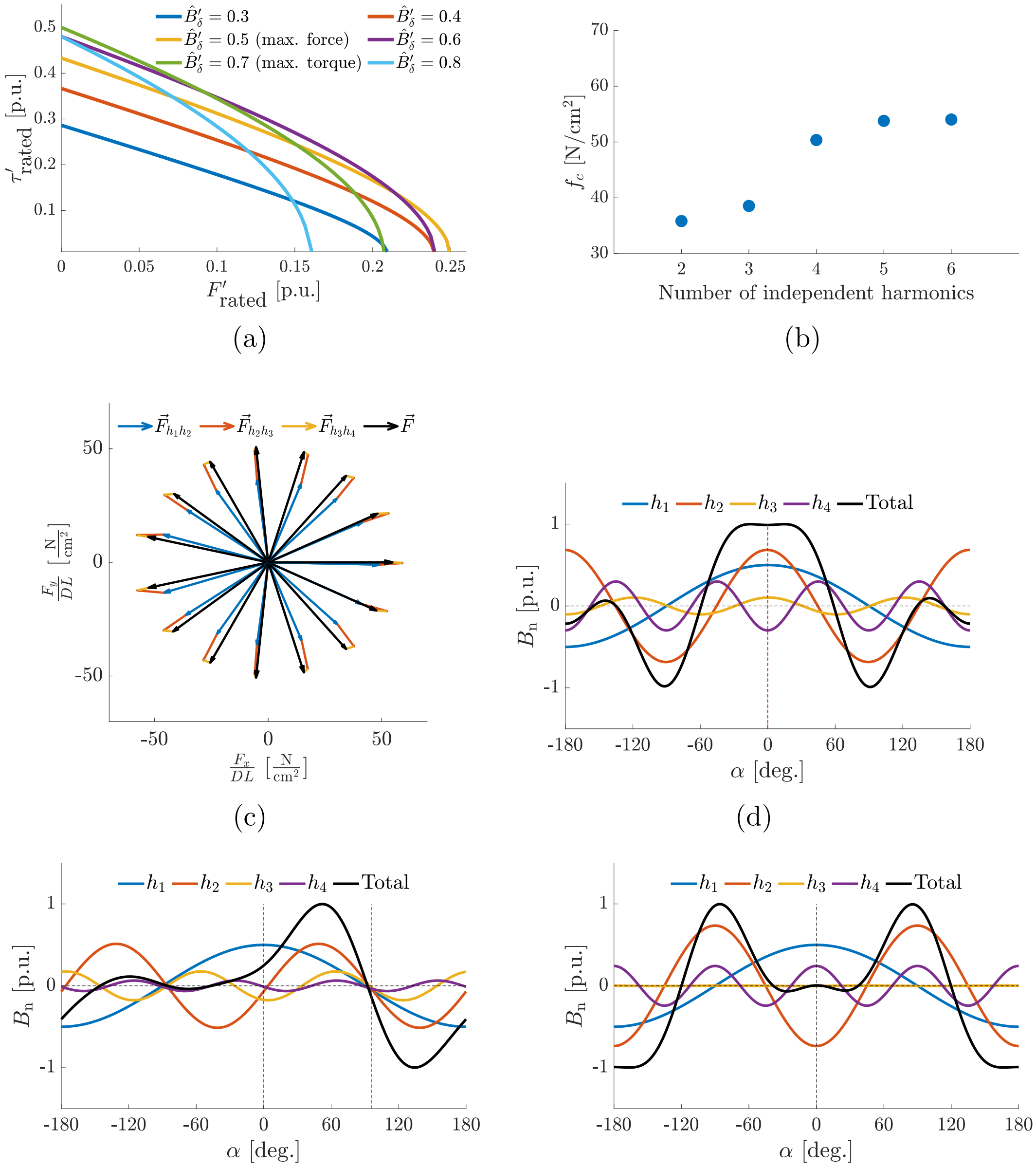

(a)

(b)

(c)

(d)

(e)

(f)

Figure 5.4: Analysis of force enhancement in bearingless motors: (a) rated torque-force curves for different magnetizing field values when $n_{\text{ind}} = 2$, (b) force capacity vs. number of independent harmonics n_{ind} when $B_{\max} = 1.5$ T and $\hat{B}_\delta = 0.75$ T, (c) optimal force vector components when $n_{\text{ind}} = 4$, and (d)-(f) optimal airgap field distributions for $n_{\text{ind}} = 4$ and $\phi = 0^\circ,\ 90^\circ,\ 180^\circ$.

field values (45 N/cm^2 and 12.8 N/cm^2, see Section 5.3) because AMBs do not have the requirement to create the magnetizing field.

Now, the optimal $\hat{B}_\delta$ to create the maximum torque is identified. The maximum torque is created when torque creating and magnetizing field components of harmonic p are 90° phase separated electrically, so that $\hat{B}_\delta'^2 + \hat{B}_\tau'^2 = 1$. The torque is expressed in terms of the normal field components as $\tau_{\text{rated}} = k_\tau \hat{B}_\delta \hat{B}_\tau$, where $k_\tau = V_r p \delta_{\text{eff}}/\mu_0 r$. Defining the base torque value as $\tau_{\text{base}} = k_\tau B_{\max}^2$ (which includes fixed parameters), the normalized form of the torque expression becomes $\tau'_{\text{rated}} = \hat{B}'_\delta \hat{B}'_\tau = \hat{B}'_\delta(1 - \hat{B}_\delta'^2)^{1/2}$. Solving $d\tau'_{\text{rated}}/d\hat{B}'_\delta = 0$, the optimal magnetizing field is found as $\hat{B}'_\delta = 1\sqrt{2} = 0.707$ p.u. with the maximum $\tau'_{\text{rated}} = 0.5$ p.u. The above calculations show that the optimal magnetizing fields for the maximum force ($\hat{B}_\delta = 0.5$ p.u.) and torque ($\hat{B}_\delta = 0.707$ p.u.) creation are different.

The above analysis can be extended to the case when maximum torque and suspension forces are created simultaneously. In this case, the peak airgap field is constrained by $(\hat{B}_\delta'^2 + \hat{B}_\tau'^2)^{1/2} + \hat{B}'_{p_s} = 1$. Using this expression, $F'_{\text{rated}} = \hat{B}'_\delta \hat{B}'_{p_s}$, and $\tau'_{\text{rated}} = \hat{B}'_\delta \hat{B}'_\tau$, the relationship between the rated force, torque, and magnetizing field can be derived:

$$\tau_{\text{rated}}'^2 = F_{\text{rated}}'^2 - 2\hat{B}'_\delta F'_{\text{rated}} + \hat{B}_\delta'^2(1 - \hat{B}_\delta'^2) \tag{5.6}$$

This equation can be used to determine torque-force capabilities of a bearingless machine for different magnetizing fields, as demonstrated in Fig. 5.4a. This plot shows that the optimal range of $\hat{B}'_\delta$ is between approximately 0.5-0.707 p.u. depending on the desired range of τ'_{rated} and F'_{rated}. These results can be used to select a magnetizing field value based on the torque and force requirements when designing a bearingless motor.

5.4.2 Force Enhancement Using Multiple Airgap Harmonics

This section shows that enhancement of the force capacity can be achieved in bearingless motors by controlling more than two rotating space harmonics. Analytic expressions for optimal fields and currents estimated from Matlab calculations are provided, which help increase the force capacity under the maximum airgap field limit. To find the force capacity, a similar approach to that described in Section 5.3 is used with the additional constraints on the magnetizing field harmonic to have fixed magnitude and angle at any force angle ϕ. This reduces the number of degrees of freedom to $2n_{\text{ind}}-2$ for bearingless motors as opposed to $2n_{\text{ind}}$ in AMBs.

Analysis results are now presented by comparing bearingless motors with different numbers of controllable airgap harmonics n_{ind}. The results are obtained for $p = 1$ and $\hat{B}_\delta = 0.5$ p.u., with the remaining space harmonics $h = 2, 3, 4, ..., n_{\text{ind}}$ being used to create force. Figure 5.4b shows the plot of the force capacity vs. n_{ind} for $B_{\text{max}} = 1.5$ T. This result shows that increasing the number of controllable harmonics from $n_{\text{ind}} = 2$ to $n_{\text{ind}} = 4$ can significantly increase force capacity by approximately 42%, which agrees with the results from Chapter 4.7. Figure 5.4c shows the optimal force vector components from each harmonic interaction required to create F_{rated} at different force angles ϕ for $n_{\text{ind}} = 4$. Figures 5.4d-5.4f show the optimal field distributions for this example when $\theta = 0°$ and $\phi = 0°$, 90°, and 180°. An interesting trend is observed from the optimization results: the harmonic peaks are typically aligned or opposite when creating forces at angles 0° and ±180°, and they all have one intersection point when creating forces at angles ±90°. At certain angles, additional harmonics are used to improve the total airgap field distribution, but not to contribute to the total force creation. This can be observed in Fig. 5.4f where the third harmonic is zero and the fourth harmonic is used to reduce the peak airgap field, helping to increase the force capacity.

5.4.3 Comparison of Force Capacity between AMBs and Bearingless Motors

Based on the force capacity results presented earlier, Fig. 5.5 compares the force capacities between AMBs and bearingless machines for different harmonics in per-unit quantities and for magnetic field limits of $B_{\text{max}} = 0.8$ T and 1.5 T. These comparisons reveal that, in order to achieve equivalent force capacities, bearingless machines need to exert control over at least one additional harmonic compared to AMBs. This discrepancy arises because,

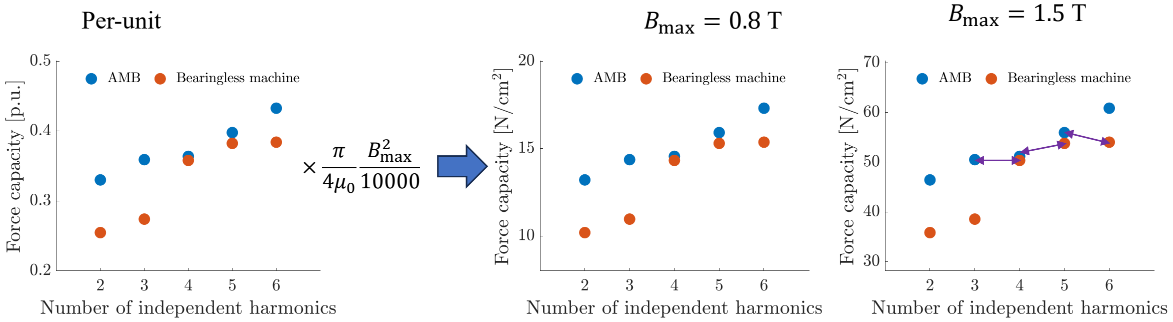

Figure 5.5: Comparison of force capacity between AMBs and bearingless motors

in AMBs, none of the harmonics are constrained to fixed amplitudes and angles, whereas in bearingless machines, one harmonic must be a magnetizing field with a predetermined amplitude and angle. Therefore, to attain a comparable force capacity, bearingless machines need one extra controllable harmonic than AMBs, resulting in an equivalent number of free variables (field amplitudes and angles).

5.4.4 Fields and Currents for Increased Force Capacity

This subsection presents a simple and efficient approach for calculating magnetic fields and currents, aiming to maximize the force rating in 10-phase bearingless machines. The approach is based on numerical calculations from Section 5.4.2. In this approach, sequence 4 is used for flux weakening, enabling sequences 1 and 2 to generate a larger force. This allows maintaining simplicity for implementation in a controller without the need for complex lookup tables.

Table 5.1 provides estimations for optimal field magnitudes and angles derived from numerical calculations for magnetizing fields $\hat{B}'_\delta \approx$ 0.5-0.7 p.u. Based on the desired force requirement $F'^* = \hat{B}'_\delta \hat{B}'_{\mathrm{n},h_2}$, if $\hat{B}'_{\mathrm{n},h_2} \leq 1 - \hat{B}'_\delta$ (column 2), there is no need to excite sequence 4, as the total airgap field remains below the maximum limit of 1 p.u. For a larger force requirement with $\hat{B}'_{\mathrm{n},h_2} > 1 - \hat{B}'_\delta$, $\hat{B}'_{\mathrm{n},h_2}$ can be increased up to $1.2 - \hat{B}'_\delta$ (column 3) and harmonic 4 can be actuated according to Table 5.1, ensuring that the airgap field remains within

	Sequences 1-2	Sequences 1-2-4
$\hat{B}'_{\mathrm{n},h_2}, \phi_{s_2}$	$\leq 1 - \hat{B}'_\delta$, $\theta + \phi$	$\leq 1.2 - \hat{B}'_\delta$, $\theta + \phi$
$\hat{B}'_{\mathrm{n},h_4}, \phi_{s_4}$	NA	$\hat{B}'_\delta + \hat{B}'_{\mathrm{n},h_2} - 1$, $\pi + 3\theta + \phi$

Table 5.1: Optimal Fields for Maximum Force Rating with Sequences 1-2 vs. 1-2-4.

1 p.u. Using these optimal fields, the required current sequences for phase k are computed using (4.8). This requires knowledge of the tesla per ampere parameter for each harmonic-sequence pair, which can be calculated using (4.13), FEA simulations, or measurements.

5.5 Conclusion

This chapter researches force capacity of AMBs and bearingless motors using multiple airgap space harmonic field interactions. It is found that the key factors affecting the force capacity are the peak allowable airgap field and the distribution of the harmonic fields along the inner bore of the stator. The chapter finds that, for the same number of controllable currents, bearingless machines generally have lower force capacity than AMBs due to two main reasons. First, AMBs inherently use more harmonics by individually controlling currents. Second, AMBs do not have the requirement to create the magnetizing field harmonic. This increases the degrees of freedom to find the optimal field distribution in AMBs because harmonic magnitudes and angles do not have to be fixed with respect to the force and rotor angles. It has been identified that the optimal range of the magnetizing field magnitude to have the maximum torque-force capability is between 50% (max force) and 70% (max torque) of the peak airgap field. The chapter also showed that, by increasing the number of controllable harmonics and optimally manipulating their magnitudes and angles, enhancement of force capacity in bearingless motors is achievable. The results demonstrate that potential force enhancement of over 40% can be achieved in bearingless machines when controlling four airgap harmonics (10 phases) as opposed to the typical approach of controlling only two harmonics (six phases). For example, with 0.8 T peak field, the force capacity of a bearingless motor can be enhanced from 10 N/cm^2 to 14.3 N/cm^2. Overall, this chapter proposes a comprehensive framework for analysis of force creation capabilities in AMBs and bearingless motors, and demonstrates the importance of controlling multiple airgap harmonics for achieving high-performance bearingless motor designs.

Chapter 6

Design and Control of a 10-Phase Bearingless Induction Machine

6.1 Introduction

Chapters 4 and 5 results showed that controlling multiple airgap harmonic fields in bearingless machines has benefits of increasing force capacity and providing multiple force actuation approaches. Based on these findings, this chapter develops a framework to design a 10-phase bearingless induction motor, which can independently control four airgap harmonic fields. This motor has benefits of increased force capacity and levitation operation under varying magnetizing field and torque. The main contribution of this chapter is to develop a design framework and a control strategy for a 10-phase bearingless machine with enhanced force creation capabilities. Section 6.2 reviews the operating theory and highlights advantages of using a 10-phase motor based on the findings from Chapters 4 and 5. Section 6.3 proposes and develops a design study methodology for a 10-phase bearingless induction motor. Section 6.4 presents optimization results, comparing Pareto optimal fronts for six- and 10-phase machines, and Section 6.5 provides design details for the selected 10-phase machine. Section 6.6 presents control architecture and simulation results for speed and levitation control of a 10-phase bearingless induction machine.

6.2 Operating Theory and Advantages

In 10-phase bearingless machines, four airgap field harmonics can be created independently, which adds more flexibility when creating suspension forces. Equations for the phase currents, fields, and forces are obtained based on the equations (4.8), (4.12), and (4.27), and are summarized below:

$$\begin{aligned} i_k &= \sum_{s_i=1}^{4} \hat{I}_{s_i} \cos\left(\phi_{s_i} - [k-1] s_i \frac{2\pi}{10}\right) \\ B_{\mathrm{n}} &= \sum_{h_i=1}^{4} \hat{B}_{\mathrm{n},h_i} \cos\left(h_i \alpha - \phi_{h_i}\right) \\ \vec{F} &= F e^{j\phi} = \bar{k}_{h_{12}} \vec{i}_1^{\,*} \vec{i}_2 + \bar{k}_{h_{23}} \vec{i}_2^{\,*} \vec{i}_3 + \bar{k}_{h_{34}} \vec{i}_3^{\,*} \vec{i}_4 \end{aligned} \tag{6.1}$$

where sequence s_i can independently create one airgap harmonic field. Each sequence has its space vector representation $\vec{i}_{s_i} = \hat{I}_{s_i} e^{j\phi_{s_i}}$ obtained through the GCT. Harmonic h_i amplitude $\hat{B}_{\mathrm{n},h_i}$ and angular location ϕ_{h_i} are directly controlled by sequence s_i amplitude $\hat{I}_{s_i}$ and phase angle ϕ_{s_i}. One of these harmonics is a p pole pair field used to create the magnetizing field and torque in the motor, while other harmonics contribute to the suspension force creation.

Force vector equation in (6.1) shows that there are multiple ways of creating the radial suspension forces, which can have several benefits. One advantage is having an increased force capacity, as was shown in Chapters 4.7 and 5.4.2. Chapter 5.4.2 showed that, when the force is created using sequences 1 and 2, additionally exciting sequence 4 (harmonic 4) for weakening the airgap field allows further increasing the force until the maximum airgap field limit is reached. This increases the force capacity. Another advantage is an enhanced force performance under varying magnetizing field and torque values. Consider that sequence 1 is used to create $p = 1$ pole pair field, which consists of the magnetizing and

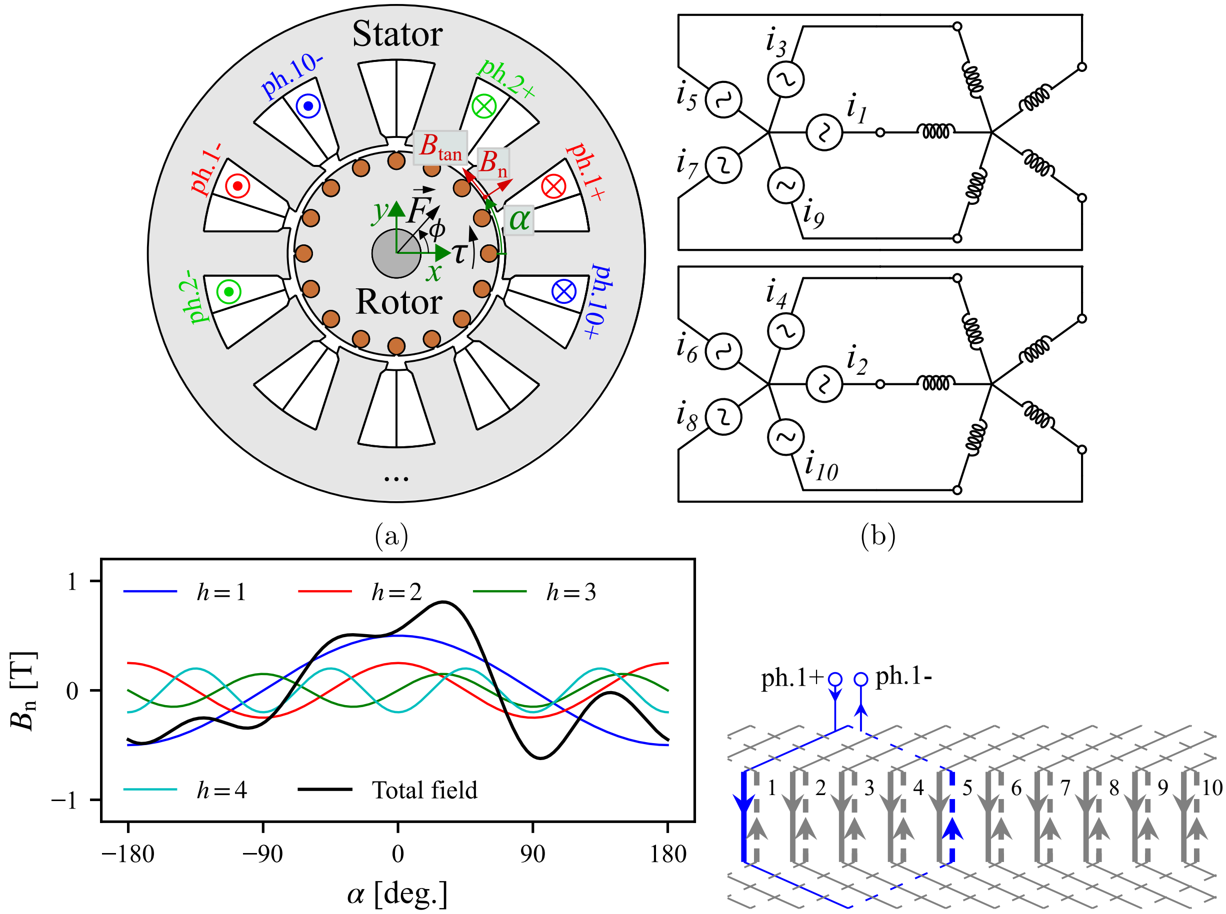

(a) (b)

(c) (d)

Figure 6.1: Ten-phase bearingless induction machine: (a) cross-section, (b) drive connections, (c) example plot of airgap harmonic fields, and (d) winding layout for phase 1.

torque creating quantities. The variations in these quantities have undesirable effects on the force creation, causing error in force vector magnitude and angle. Equation (6.1) shows that keeping sequence 2 current zero and creating forces only with sequences 3 and 4 eliminates these undesirable effects.

6.3 Design Study Methodology

This section presents the design study approach used to design a 10-phase bearingless induction motor, which is the primary contribution of this chapter. The design space is searched using a multi-objective genetic algorithm (GA) to find Pareto optimal designs. Each candidate design is evaluated using finite element analysis (FEA) software FEMM and JMAG, which are linked to the GA using Python scripts. Section 6.3.1 presents the details about the motor topology with the focus on the winding design, Sections 6.3.2-6.3.3 describe optimization design variables and performance metrics (objectives and constraints), and Section 6.3.4 provides evaluation steps for each design during optimization. The developed design study approach can also be extended for machines with a different number of phases. The approach provided in this section will be used for the design studies of six- and 10-phase examples in Section 6.4.

6.3.1 Selected Motor Topology

The induction motor topology selected for the design study is provided in Fig. 6.1a. The motor consists of the stator with a 10-phase winding and the pole-specific squirrel cage rotor [7]. This motor is designed to create four airgap harmonic fields of orders $h = 1,\ 2,\ 3,$ and 4, as illustrated in Fig. 6.1c. The reason for selecting an induction motor is that it has a small effective airgap length δ_{eff} compared to other motors. This facilitates the creation of four airgap harmonic fields as their amplitudes are inversely proportional to δ_{eff}. Harmonic $h = p = 1$ is selected as a magnetizing and torque creating field, while harmonics $h = 2,\ 3,\ 4$ are used for suspension force creation and field weakening. Details of the stator winding and rotor design are now provided.

6.3.1.1 Stator Winding Design

The stator winding is designed using the methodology presented in [100], resulting in the phase terminal connections shown in Fig. 6.1a and the winding layout shown in 6.1d for phase 1. The winding must be designed to independently create four airgap harmonic fields, which requires the winding factors $\hat{k}_{\text{w},h_i}$ at these harmonics to be maximized. With a double-layer winding, a feasible number of stator slots are $Q = 10,\ 20,\ 30, \ldots$. A number of winding designs have been compared, and it is found that a double-layer distributed winding with

Stator slots Q	10	Rotor slots Q_r	16
$\hat{k}_{\mathrm{w},1}$ and $\hat{k}_{\mathrm{w},4}$	0.95	$\hat{k}_{\mathrm{w},2}$ and $\hat{k}_{\mathrm{w},3}$	0.59

Table 6.1: Induction Machine Number of Slots and Winding Factors

$Q = 10$ slots (one coil per phase) and a coil span of $y = 4$ slots yields the highest winding factors, as summarized in Table 6.1. It is important that harmonic 1 has the highest winding factor as this harmonic is used to create the magnetizing field and torque. The motor phases are connected to the drive terminals in a double five-phase configuration, shown in Fig. 6.1b. This configuration allows having no sequences of orders 0 and 5 (zero- and 180° sequences); otherwise, these sequences would have to be regulated to zero to avoid creating oscillating harmonic fields, according to (4.14).

6.3.1.2 Rotor Design

The rotor is a pole-specific squirrel cage rotor designed to have no induced bar currents from $h = p_s = 2$ and its integer multiples $4,\ 6,\ 8, ...$ [7]. This indicates that harmonics 2 and 4 created by 10-phase stator currents do not induce rotor bar currents and do not contribute to the ohmic losses in the rotor bars. Harmonic 1 is expected to induce rotor currents as the torque creating field. While harmonic 3 does induce rotor bar currents, it will be shown in Chapter 7 that the torque from this harmonic is small.

6.3.2 Design Variables

The geometric parametrization of the motor is depicted in Fig. 6.2. For the optimization, the design is characterized by 9 free variables, as listed in Table 6.2. This table also shows the bounds for each variable.

6.3.3 Objectives and Constraints

There are three objectives used in this optimization: electric motor efficiency η, torque per rotor volume TRV, and force capacity/specific load capacity f_c. This is a minimization

Design variable	Bounds	Design variable	Bounds
δ_{eff}	[1.3, 2.9] mm	w_{st}	[8.4, 20.2] mm
α_{st}	[18, 32.4] deg.	d_{so}	[0.5, 3] mm
d_{st}	[21.7, 22.8] mm	d_{sy}	[30.1, 31.7] mm
r_{rb}	[2, 3] mm	w_{so}	[0.5, 3] mm
d_{rso}	[0.5, 3] mm		

Table 6.2: Machine Design Variables

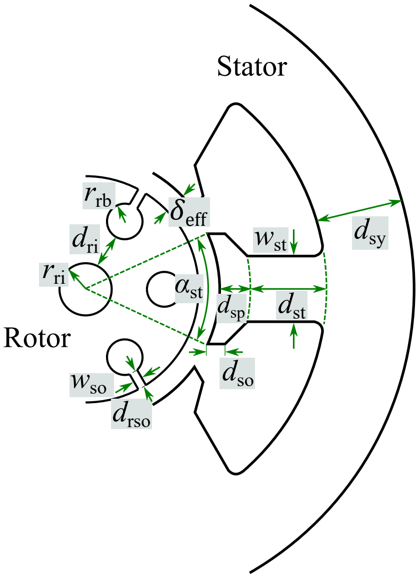

Figure 6.2: Geometric parametrization of a squirrel cage induction machine.

problem. Therefore, objective functions are formulated based on these performance variables as:

$$O_1 = -\eta = -\frac{P_{\text{out}}}{P_{\text{out}} + P_{\text{losses}}},\ O_2 = -\text{TRV} = -\frac{\tau_{\text{rated}}}{\pi r^2 L},\ O_3 = -f_c = -\frac{F_{\text{rated}}}{2rL} \tag{6.2}$$

where P_{out} and P_{losses} are the average output power and power losses (stator ohmic and iron losses, rotor ohmic and iron losses, and windage loss); r and L are the rotor radius and axial length; τ_{rated} and F_{rated} are the rated torque and force found by averaging the created torque and force over one rotor revolution. F_{rated}, which indicates the force the motor can create at any angle without exceeding the airgap field limit, is calculated following the steps in Chapter 4.7.1.

There are four constraint parameters that the designs must satisfy during the optimization process: torque ripple TR, force vector magnitude error E_m and error angle E_a, and force per rotor weight FRW:

$$\mathrm{TR} \leq 30\%,\ E_m \leq 30\%,\ E_a \leq 10^\circ,\ \mathrm{FRW} \geq 0.75 \tag{6.3}$$

These constraints ensure that the designs have reasonably low ripple characteristics and are able to create suspension forces to support the rotor's weight. Torque ripple is calculated as the peak-to-peak torque over a rotor revolution divided by the average torque. The metrics E_m and E_a show the maximum deviation from the average force magnitude and the desired force angle, as was described in Section 1.2.3.1. FRW is calculated when 5% of the rated coil current is used to create a nominal force F_{nom} and 95% is used to create torque.

6.3.4 Motor Performance Evaluation Process

This section presents the evaluation process used during the optimization study. Each of the optimization algorithm's design candidate is evaluated following the steps summarized in Fig. 6.3. A design variant is created using the design specifications (winding, materials, fixed parameters, ratings) and free design variables (geometric dimensions) from the optimization algorithm. The performance of this design variant is evaluated by following time-harmonic and transient FEA analysis steps and calculating objectives and constraints, which are then passed to the optimization algorithm. The entire design study process is implemented in our research group's open source codebase "eMach" designed to facilitate the modeling, evaluation, and optimization of electrical machines. FEA analysis steps are based on [102] and additional force capacity calculation steps for a 10-phase machine are introduced by this dissertation. These steps are described in the following subsections.

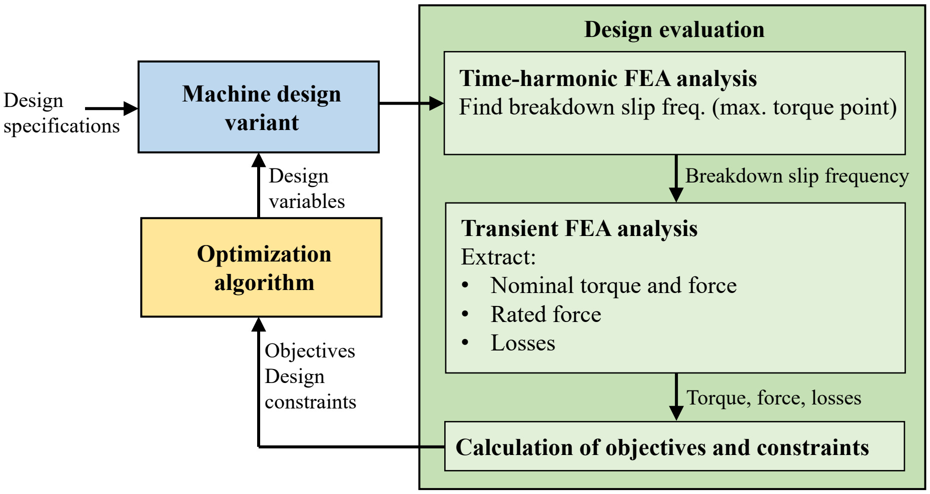

Figure 6.3: Optimization design study steps.

6.3.4.1 Time-Harmonic Analysis

The main goal of this evaluation step is to find a breakdown slip frequency $f_{\text{br,slip}}$ of an induction motor design. This frequency determines the point where the maximum torque is achieved and is used to set the excitation frequency in the transient analysis step in Section 6.3.4.2. The stator is excited with currents at the slip frequency and the rotor position is held fixed. To accelerate the searching process, five instances of time-harmonic FEA at different slip frequencies are executed in parallel using FEMM.

6.3.4.2 Transient Analysis

The main goal of this evaluation step is to compute all performance metrics needed to calculate the design objectives and constraints. FEA simulations are conducted in JMAG, which computes created torque, suspension forces, and losses as functions of the rotor angle. This analysis consists of two main steps described below.

1. Calculation of performance metrics at nominal operation. An FEA simulation in this step consists of two sections that have different time step settings, which greatly reduces simulation time [102]. The first section has a relatively large time step, which allows for a faster simulation of a transient state. The second section has a fine time step with respect to the stator frequency in order to evaluate performance metrics in a steady state. Phase currents are excited by sequences 1 and 2 (6.1) with 95% and 5% of the rated current to create torque and suspension forces, respectively. The excitation frequency for both sequences is set at $f_{e,s_{1/2}} = f_{\mathrm{rotor}} + f_{\mathrm{br,slip}}$, where f_{rotor} is the rotor speed in rev/s and $f_{\mathrm{br,slip}}$ is calculated in the time-harmonic analysis step in Section 6.3.4.1. The outputs of the simulation are torque, force, and losses (ohmic, eddy current, and hysteresis losses) at nominal operating conditions vs. rotor angular position θ. These performance metrics are necessary to evaluate the objectives O_1 and O_2 in (6.2) and constraints in (6.3).

2. Calculation of the rated force. This step computes the rated force of a machine, which is the force that a motor can create at any angle without exceeding the maximum airgap field limit. A motor winding is excited with sequences 1, 2, and 4, sequence 4 being used for flux weakening. The maximum airgap field is set at $B_{\mathrm{max}} = 0.8$ T and the magnetizing field at $\hat{B}_\delta = 0.7B_{\mathrm{max}}$. This magnetizing field is found to yield the highest force rating when sequences 1, 2, and 4 are used, as was discussed in Chapter 5.4.2. The following steps are used to calculate the rated force:

1. Find tesla per ampere parameter for each harmonic-sequence pair ($\mathrm{TPA}_{h_i} = \hat{B}_{\mathrm{n},h_i}/\hat{I}_{s_i}$). These parameters are computed by exciting current sequences 1, 2, and 4 with equal amplitudes $\hat{I}_{s_i} = \hat{I}_{\mathrm{rated}}/3$ at a fixed rotor angle, extracting the radial airgap magnetic field distribution $B_{\mathrm{n}}(\alpha)$, and performing the Fourier transform of $B_{\mathrm{n}}(\alpha)$ to find $\hat{B}_{\mathrm{n},h_i}$ for space harmonics of orders 1, 2, and 4.

2. Apply current sequences 1, 2, and 4. These currents are calculated by knowing tesla per ampere parameters from step 1 and the desired airgap field harmonics that maximize the force rating, as discussed in Chapter 5.4.4.

3. Extract force with respect to the rotor angular position θ. This result is used to calculate F_{rated} and E_m and E_a constraints.

The same evaluation steps are used for the optimization of a six-phase design with $p = 1$

and $p_s = 2$. The only difference is that the maximum F_{rated} is created at $\hat{B}_\delta = 0.5B_{\max}$ (see Fig. 4.4b) and the optimal field distribution to create F_{rated} along x-axis is $B_{\text{n}} = B_{\max}[0.5\cos(\alpha - \theta) + 0.5\cos(2\alpha - \theta)]$.

After following the transient FEA evaluation steps, optimization objectives and constraints are calculated in post-processing and provided to the optimization algorithm.

6.4 Design Study Results

This section presents design study results using the optimization approach from Section 6.3. Optimization results for six- and 10-phase bearingless induction machines are presented and their performances are compared. The rated parameters and other constants used in the optimization study are given in Table 6.3. In both cases, the rotor has the same topology, shown in Fig. 6.1a. For a six-phase case, the stator consists of $Q = 24$ slots with the winding layout provided in Fig. 3.8.

Figure 6.4a presents the Pareto optimal fronts for six- and 10-phase bearingless induction machines. Since there are three objectives, the Pareto front is a 3D surface, which can be visualized on a 2D plot by using a colormap for the third objective. To facilitate the comparison, Fig. 6.4b provides the Box and Whisker plot for each performance metric using Fig. 6.4a results. These results show that both six- and 10-phase designs have comparable torque densities and efficiencies. While the median values (indicated by an orange line) for torque density TRV are similar for both cases (21.3 kN/m^3 for $m = 6$ and 22 kN/m^3 for $m = 10$), 25% of 10-phase designs have torque densities in the range of 26.3-27.8 kN/m^3. This is partly due to a higher winding factor in the selected 10-phase winding topology (0.95 vs. 0.88). Results in Fig. 6.4b show that 10-phase designs can achieve a considerably higher force capacity f_c compared to six-phase designs with the median values at 15.3 N/cm^2 and 12.3 N/cm^2, which is an improvement by approximately 24.4%. For comparison, the highest reported force capacity for bearingless machines is 9.9 N/cm^2 [36].

Parameter	Value	Parameter	Value
Rated power	50 kW	Rated speed	30 kRPM
Current density	4 Arms/mm^2	Copper fill-factor	0.5
Torque current ratio	95%	Suspension current ratio	5%
Lamination stacking factor	96%	Iron material	Arnon-5
Winding material	Copper	Rotor bar material	Aluminum

Table 6.3: Design Study Parameters

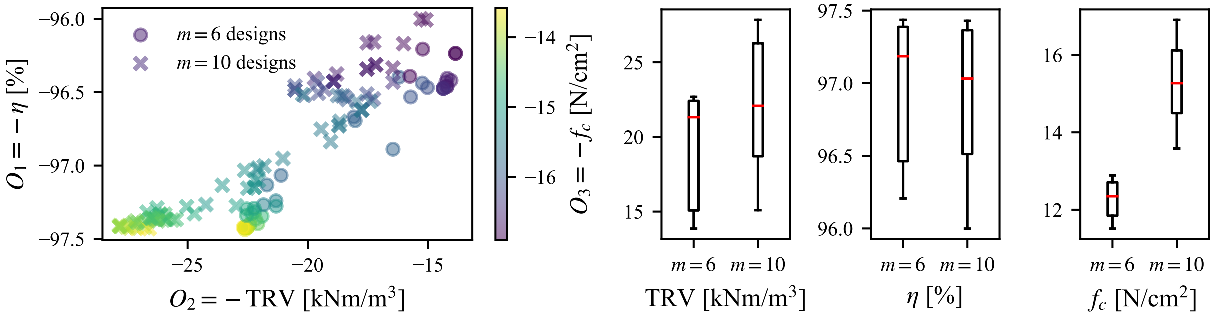

(a) (b)

Figure 6.4: Design study results for six- and 10-phase bearingless induction motor designs: (a) Pareto optimal fronts and (b) box and whisker plot.

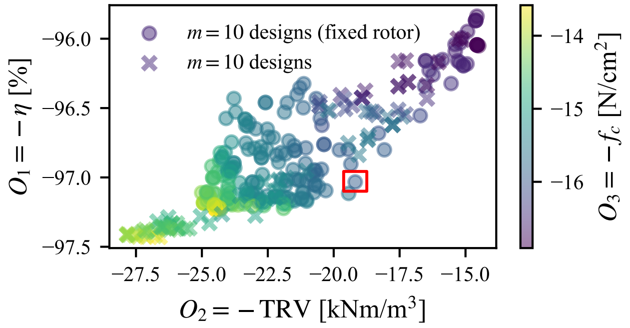

Figure 6.5: Pareto optimal fronts for the design study with fixed rotor dimensions from [7].

6.5 Selected Design

Another optimization study is conducted to select a 10-phase stator design for prototyping and hardware validations in Chapter 7. In this study, the rotor of the prototype in Fig 3.10a [7] is reused; therefore, rotor dimensions are held fixed during the study. Figure 6.5 present the Pareto optimal front for this design study, along with the Pareto front for $m = 10$ designs from Fig. 6.4a. While the rotor dimensions are held fixed during optimization, this result shows that high-performance designs can be obtained. The design selected for prototyping

Parameter	Six-phase design	Ten-phase design
Torque and power	1.17 Nm, 3.6 kW	1.55 Nm, 4.7 kW
Torque-suspension current ratio (FRW ≈ 1)	87.5%-12.5%	93%-7%
Breakdown slip frequency	12.5 Hz	8 Hz
Stator outer diameter, total volume	150 mm, 0.88 liters	154.6 mm, 0.94 liters
Airgap length	2.65 mm	2.05 mm
Rotor current density	6.98 Arms/mm^2	8.7 Arms/mm^2
TRV, efficiency	7.37 kNm/m^3, 92.8%	9.76 kNm/m^3, 94.5%
Torque ripple, E_m, E_a	3.9%, 2.5%, 0.45°	7.7%, 5.1%, 2.9°
Force capacity	11.6 N/cm^2	15.2 N/cm^2

Table 6.4: Comparison of six- and 10-phase designs

is highlighted by a red rectangle.

For prototyping, adjustments are made to the selected design dimensions to have a lower copper fill-factor of 30% (achievable by hand-winding for a distributed winding) and keep the current density in the rotor bars below 10 Arms/mm^2. The final design cross-section is shown in Fig. 6.1a and the key parameters and performance metrics are provided in Table 6.4. This table also provides the key metrics for a six-phase prototype from [7]. These results demonstrate that the selected 10-phase design has higher force capacity, efficiency, and torque density.

6.6 Control Architecture

This section presents speed and levitation control architecture for a 10-phase bearingless induction motor. The block diagram of the control architecture is presented in Fig 6.6, where the blocks highlighted in blue are proposed and developed by this dissertation. The following subsections present the main parts of this architecture and present simulation results using the 10-phase bearingless induction motor design from Section 6.5.

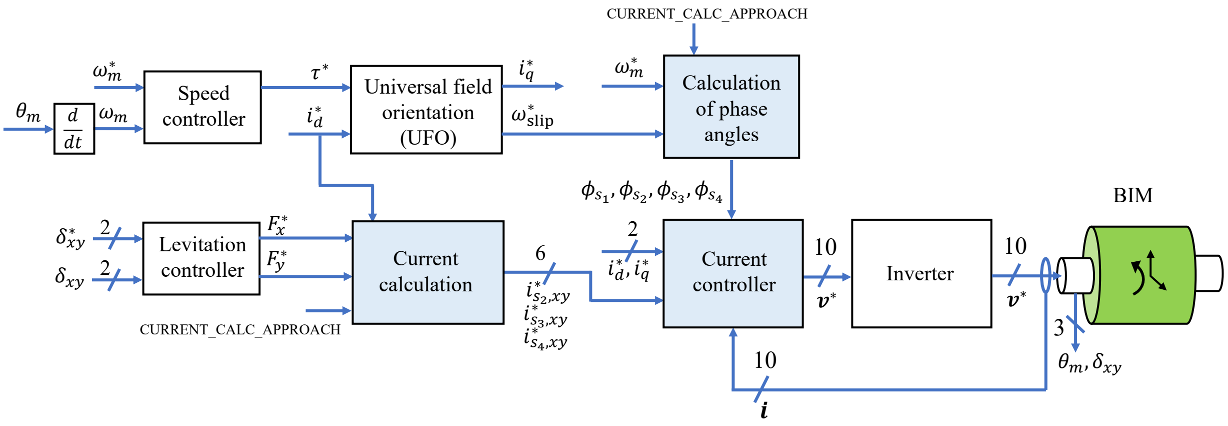

Figure 6.6: Speed and levitation control block diagram for a 10-phase bearingless induction motor.

6.6.1 Speed and Levitation Controllers

Speed and levitation controllers are used to control the desired angular speed ω_m^* and the radial position δ_{xy}^* of a rotor with $x^* = y^* = 0$. The speed controller is realized through a PI controller. The levitation controller employs two Proportional-Integral-Derivative (PID) controllers along with a low-pass filter for x and y positions. Tuning these controllers involves estimating the rotor's inertial and damping coefficients (for the speed controller), as well as the rotor mass and unstable stiffness coefficients. (for the levitation controller). The unstable stiffness coefficient characterizes the pull force per unit radial displacement of a rotor toward the stator, and its estimation will be detailed in Chapter 7.4 using hardware tests. This coefficient can be obtained using FEA or experiment, as will be shown in Chapter 7.4. The output of these controllers consists of torque command τ^* and radial force commands F_x^* and F_y^*, which are used to calculate the required current sequence commands.

6.6.2 Universal Field Orientation

The Universal field orientation (UFO) block is used to estimate the torque current command i_q^* and slip frequency ω_{slip}^* based on the torque command from the speed controller and the user-specified magnetizing current command i_d^*. The implementation of the UFO block is based on the principles of field-oriented control theory, as presented in [103, Ch 9.2]. This block relies on the knowledge of the induction motor equivalent circuit parameters. These parameters include the stator and rotor resistances, leakage inductances, and the magnetizing inductance. In the context of 10-phase machines, the estimation of these parameters involves exciting magnetizing field and torque creating sequence current (which is 1 for the selected design) during no-load and locked rotor tests.

6.6.3 Current Calculation

This block implements three distinct approaches to current calculation, as proposed and developed in this dissertation:

1. The first one is based on the textbook model, as detailed in Chapter 4.3. The force vector is regulated by sequence 2 current, expressed as $\vec{F} = \bar{k}_f \vec{i}_{s_2}$, where $\bar{k}_f$ is a function of the magnetizing current i_d.

2. The second approach employs sequence combinations 1, 2, and 4 to increase force capacity. Analytic equations for currents can be estimated for specific magnetizing field values, as discussed in Chapter 5.4.4. Lookup tables may be required for variable magnetizing fields or when incorporating sequence 3 into the calculation.

3. The third approach utilizes sequences 3 and 4 for enhanced force performance. In this scenario, forces are fully decoupled from torque and magnetizing currents, and the force equation is given by $\vec{F} = \bar{k}_{h_{34}} \vec{i}^{*}_{s_3} \vec{i}_{s_4}$. Under the condition that only sequences 3 and 4 are used to create the force (sequence 1 contributes torque and magnetizing field, sequence 2 is regulated to zero), setting $\hat{I}_{s_3} = \hat{I}_{s_4}$ minimizes ohmic losses in the stator winding.

6.6.4 Calculation of Phase Angles

This block calculates phase angles necessary for Park transformations (rotation matrix) in the current controller block so that sequence currents are controlled in their synchronous reference frames. Sequence 1 phase angle is calculated as $\phi_{s_1} = \theta_m + \theta_{\text{slip}}$. For current calculation approach 1, sequence 2 phase angle $\phi_{s_2} = \phi_{s_1} + \phi$ is set to to regulate force angle ϕ. For approach 2, phase angles from Table 5.1 are used. For approach 3, ϕ_{s_3} can be set to have any frequency, but preferably $f_{e,s_3} = 3f_{\text{rotor}}$, so that the mechanical speeds of airgap harmonic $h = 3$ and the rotor are synchronous. This alignment aids in preventing induced currents in the rotor bars. Sequence 4 phase angle $\phi_{s_4} = \phi_{s_3} + \phi$ regulates force angle ϕ.

6.6.5 Current Controller

This block is structured similarly to the block diagram depicted in Fig. 2.8, but encompasses all current sequences from 1 through 4. This block comprises PI controllers, direct and inverse Park transformations for converting between synchronous and stationary quantities, and direct and inverse GCT for transforming between stationary and phase quantities. The output of this block consists of 10-phase voltage commands, subsequently applied to the power electronic inverter connected to the bearingless induction motor.

6.6.6 Simulation Results

Simulation results of speed and levitation control using the selected design from Section 6.5 are presented in Fig. 6.7. The two scenarios are compared when torque and suspension forces are created using sequences 1-2 in Fig. 6.7a and sequences 1-3-4 in Fig. 6.7b. In both scenarios, the shaft is fully displaced at $t = 0$ s ($y = -1$ mm), and a subsequent position command is issued to recenter it, followed by a speed command up to 3600 RPM under no load. Armature reaction compensation is not implemented to visualize the torque's impact on force creation. The plots in Fig. 6.7a-6.7b show the rotor speed (column 1), radial

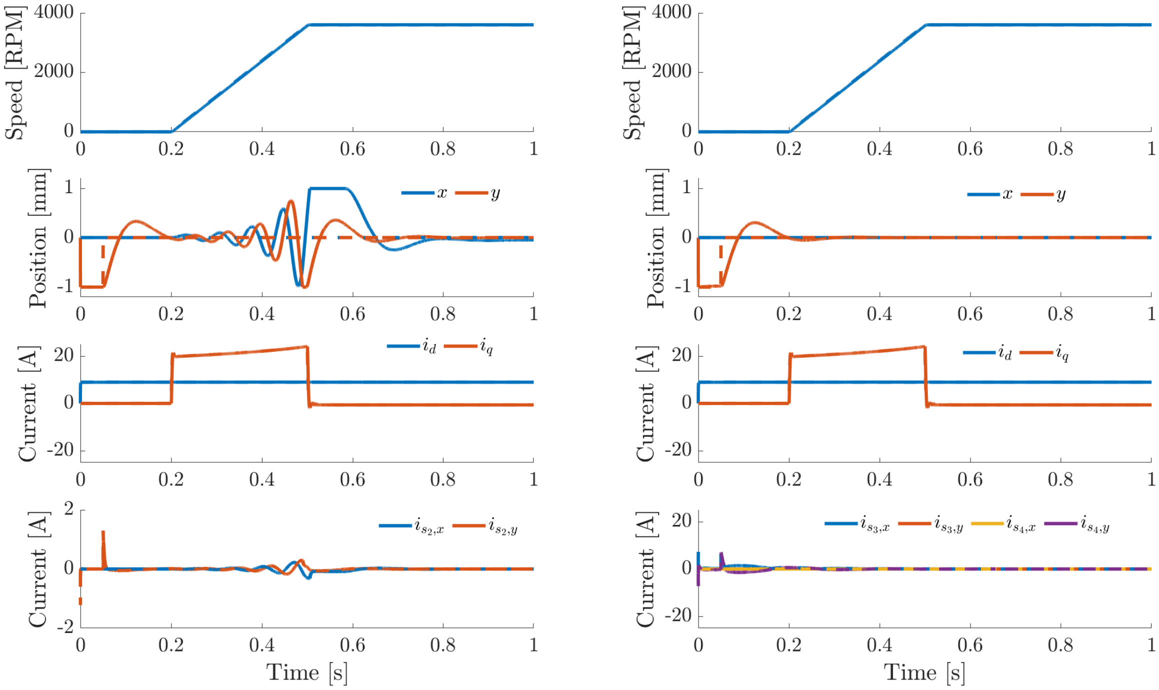

(a) (b)

Figure 6.7: Simulation results of speed and levitation control (speed, radial position, and torque and force creating currents) for the selected 10-phase design from Section 6.5 using the following sequences (without armature reaction compensation): (a) sequences 1 and 2 and (b) sequences 1, 3, and 4.

positions (column 2), sequence 1 currents responsible for generating magnetizing field and torque (column 3), and force creating sequence currents (column 4). These plots confirm the suitability of both approaches for speed and levitation control. The results show that using sequences 1-2 for force creation may have the advantage of lower current requirement for sequence 2, but is affected by non-zero torque during acceleration. On the other hand, utilizing sequences 3-4 for suspension force creation demonstrates enhanced force performance through independent operation from armature reaction, as demonstrated by the results in Fig. 6.7b.

6.7 Conclusion

This chapter develops a design study framework and control architecture for a 10-phase bearingless induction machine, leveraging insights from earlier sections. The results demonstrate that the control of multiple harmonics is critical to achieving high performance bearingless machine designs. It is found that 10-phase bearingless machine designs can achieve a considerably high force capacities of over 15 $\mathrm{N/cm^2}$ compared to 12.3 $\mathrm{N/cm^2}$ for six-phase designs. Furthermore, these designs achieve torque densities over 22 $\mathrm{kNm/m^3}$ and efficiencies close to 97%. The control of current sequences 1, 3, and 4 enhances force performance, fully decoupling force creation from the magnetizing field and torque. The successful implementation of an indirect field-oriented control technique highlights the motor's ability for effective speed control. Overall, these findings underscore the potential of the proposed design and control strategies for high-performance motor systems.

Chapter 7

Experimental Validation

7.1 Introduction

This section provides experimental validation of the theories and performance improvement strategies proposed for bearingless motors in this dissertation. A 10-phase bearingless induction motor from Chapter 6, which is capable of controlling four airgap harmonic fields, is constructed and used for hardware measurements. Section 7.2 provides the hardware description used for the measurements. Section 7.3 validates the proposed exact model (Chapter 4) and machine design considering multiple harmonics (Chapters 3 and 6). Section 7.4 presents hardware measurements to estimate bearingless induction motor equivalent circuit parameters and unstable stiffness. These parameters are necessary in the implementation of a bearingless motor control from Chapter 6.6. Section 7.5 validates an increase in force capacity by controlling multiple airgap harmonic fields (Chapters 4.7 and 5). Section 7.6 confirms an enhanced force creation using sequence combinations 1, 3, and 4 under varying magnetizing fields and torque and Section 7.7 validates speed control in the prototype motor (Chapter 6.6).

Stator slots Q	10	Rotor slots Q_r	16
Rated torque	1.57 Nm	Rated current	10 Arms
Rated speed	29.5 kRPM	Rated slip	8 Hz
$I_{s1,\text{rated}}$	8.6 Arms	$I_{s2,\text{rated}}$	1.4 Arms
$I_{d,\text{rated}}$	6.35 Arms	$I_{s2,\text{FRW}\approx 1}$	0.6 Arms
Experimentally measured:		k_f (at $I_{d,\text{rated}}$)	18.6 N/A
$k_{h_{12}}$	2.07 N/A^2	$k_{h_{23}}$, $k_{h_{34}}$	0.43 N/A^2

Table 7.1: Induction Machine Prototype Parameters

7.2 Hardware Description

The test stand shown in Fig. 7.1a is used for hardware measurements in this Chapter. The setup consists of the 10-phase induction motor and the drive, a load cell [97], and fixtures to support the stator and the rotor, all mounted within a mill. Key motor parameters are summarized in Table 7.1 and drawings are provided in Appendix C. This winding is designed to independently create four airgap space harmonic fields of orders $h = 1$ to 4 with current sequences $s = 1$ to 4, as described in (4.11). Sequence 1 ($p = 1$) is used to create torque, while three other sequences are used to create suspension forces. The motor phases are connected to the drive terminals in a double five-phase configuration, shown in Fig. 6.1b. The rotor is a pole-specific squirrel cage rotor designed to have no induced bar currents from $h = p_s = 2$ and its integer multiples [7].

In the following tests, the motor is excited by the phase currents described in (4.7)-(4.8). These currents are expected to create the fields described by (4.12), creating the force:

$$\vec{F}_{\text{10-ph}} = Fe^{j\phi} = \bar{k}_{h_{12}}\vec{i}_1^*\vec{i}_2 + \bar{k}_{h_{23}}\vec{i}_2^*\vec{i}_3 + \bar{k}_{h_{34}}\vec{i}_3^*\vec{i}_4 \tag{7.1}$$

Reaction torque and forces acting on the stator are measured using the load cell [97], which is fixed to the mill's X-Y table. The rotor is supported by the mill's spindle and locked at magnetic center. For magnetic field measurements in Sections 7.3.1 and 7.5, the radial airgap field is measured in front of each stator tooth using a hall probe [96], as shown in Fig 7.1b.

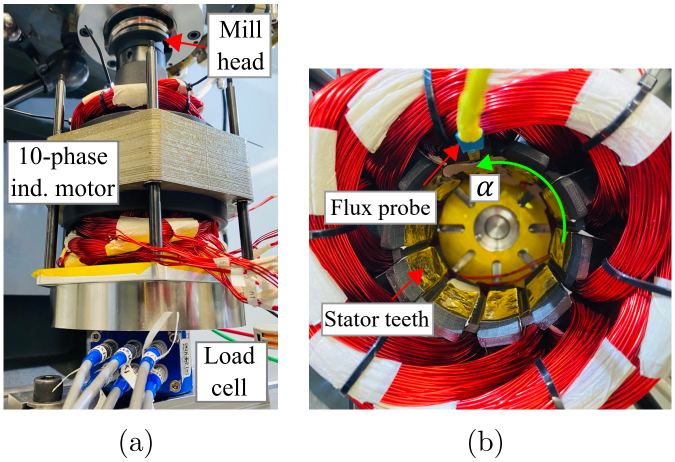

(a) (b)

Figure 7.1: Ten-phase bearingless induction machine test setup: (a) test setup used for all tests and (b) test setup for magnetic field measurements.

7.3 Validation of the Proposed Exact Model and Machine Design

This section presents experimental results that validate the exact model proposed in Chapter 4.4 and machine design with multiple controllable airgap harmonics in Chapter 6. This is done by exciting the stator winding with different combinations of current sequences and measuring the resulting fields, torque, and forces on the rotor.

7.3.1 Airgap Magnetic Field Measurements

In this test, the normal airgap magnetic field B_n is measured with a hall probe [96] in front of each tooth (36° increment) along the inner bore of the stator (along α), as shown in Fig. 7.1b. The rotor is fully inserted during the test, as shown in Fig. 7.1a. At each tooth, measurements are taken when a sequence s_i described in (4.8) is excited with an amplitude equal to the rated current (10 Arms) and a phase angle ϕ_{s_i} swept over $0 - 2\pi$ rad. The measurements are repeated for each sequence (sequences 1, 2, 3, 4).

The measurement results for each sequence are provided in Fig. 7.2, which shows a 3D

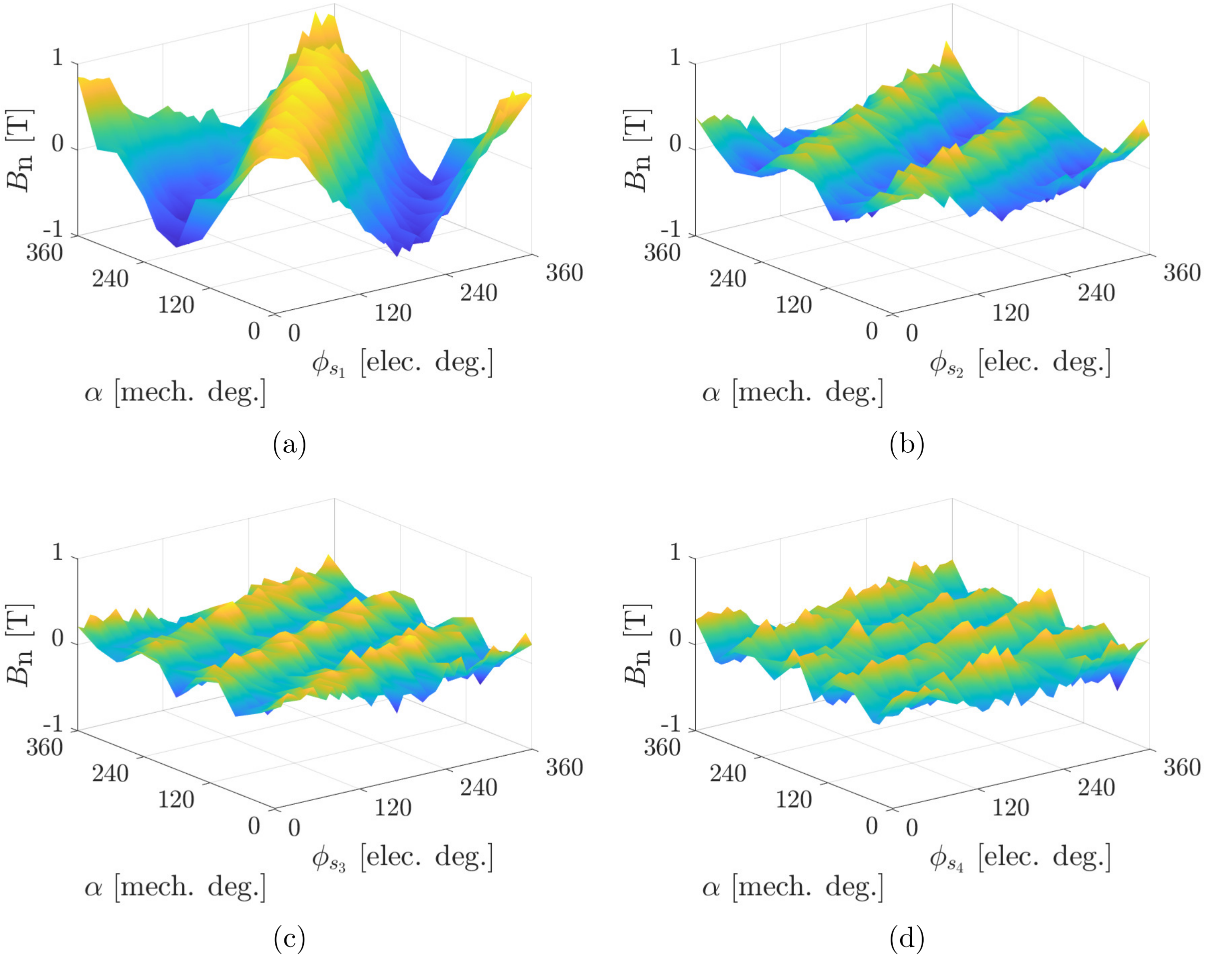

(a) (b) (c) (d)

Figure 7.2: Magnetic field measurements vs. α and ϕ_{s_i} when a sequence s_i is excited with an amplitude equal to the rated current ($I_\mathrm{rated} = 10$ Arms): (a) sequence 1, (b) sequence 2, (c) sequence 3, and (d) sequence 4.

plot of the measured normal magnetic field B_n as a function of α and ϕ_{s_i}. These plots show that sequences 1, 2, 3, and 4 create airgap harmonics of orders 1, 2, 3, and 4 when viewed along α at any fixed ϕ_{s_i} value. In each plot, as ϕ_{s_i} increases, the angular location of the field along α also increases and the field behavior in each measurement can be described by the rotating field equation $B_\mathrm{n} = \hat{B}_{\mathrm{n},h_i} \cos(h_i\alpha - \phi_{s_i})$.

The observations made above validate multiphase machine design with multiple controllable harmonics–rotating harmonic fields can be created when motor windings are excited by balanced currents.

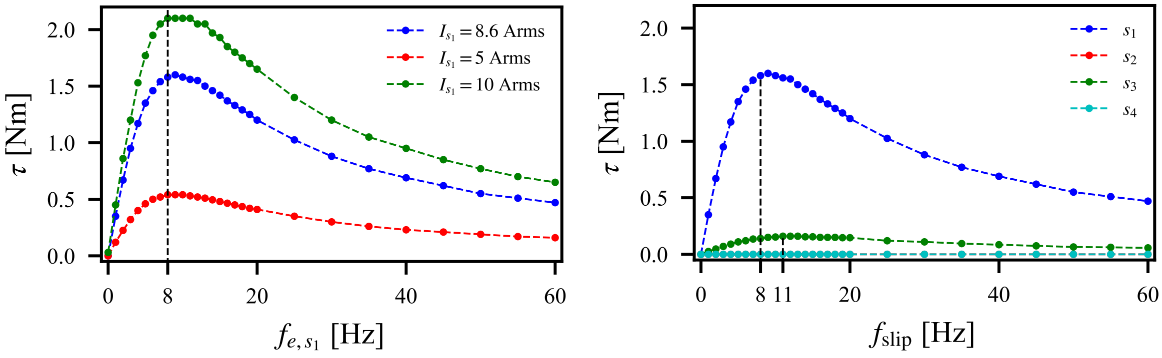

(a) (b)

Figure 7.3: Measured torque vs. slip frequency due to each sequence ($I_{\text{rated}} = 10$ Arms): (a) sequence 1 with different current values and (b) all sequences 1 through 4 (sequence 2, 3, and 4 amplitudes are set to the rated current value). Note that $f_{\text{slip}} = f_{e,s_i}/h_i$.

7.3.2 Torque Performance

This test is conducted to validate the torque capability of the prototype motor different slip frequencies. Since the rotor is locked, slip frequency is related to sequence frequencies as $f_{\text{slip}} = f_{e,s_i}/h_i$.

Figure 7.3a presents measurement results of torque vs. slip when sequence 1 is excited with different amplitudes. The plot exhibits the characteristic appearance of a typical torque-slip curve, showcasing maximum torque at a specific slip frequency. This frequency is identified as 8 Hz, which agrees with the results from Table 6.4 in Chapter 6. The slip frequency and corresponding torque at this point are indicated as the rated values of the machine in Table 7.1.

Figure 7.3b presents the torque measurement results against slip for additional current sequences. These results confirm that sequences 2 and 4 do not create any torque. As was described in Chapter 6.3.1, this is because of the pole-specific structure of the rotor, where harmonics 2 and 4 (and harmonics with multiples of 2) do not induce currents in the rotor bars. Sequence 3, on the other hand, is expected to produce some torque, as shown in Fig. 7.3b, having a breakdown slip frequency at 11 Hz ($f_{e,s_3} = 33$ Hz). However, this torque is relatively small compared to the torque produced by sequence 1.

7.3.3 Force Vector Relationship to Current Sequences

This test is conducted to confirm the first result of Section 4.4.1, that all combinations of adjacent current sequences create controllable forces. In each test, two sequences s_i and $s_j = s_i + 1$ are applied and the average forces are measured. The results are used to validate the relationship between forces and current sequences given in (4.24).

First, measurements are conducted to find the $\bar{k}_{h_{ij}}$ values in (7.1). The phase angles ϕ_{s_i/s_j} are set to create force at $\phi = 0$ degrees, $\hat{I}_{s_i}$ is held constant, and forces are measured for various values of $\hat{I}_{s_j}$. Figure 7.4a presents the measured force vs. sequence 2 current for different sequence 1 currents. Figure 7.4b shows similar force measurements for sequences 2-3 and 3-4. The slopes of these lines (shown in Fig. 7.4a-7.4b) are used to calculate k_f and $k_{h_{ij}}$ values, provided in Table 7.1.

Second, measurements are conducted to confirm that each pair of adjacent current sequences can create force at any angle. Magnitudes $\hat{I}_{s_i/s_j}$ are held constant and the force is measured against $\Delta\phi_{s_{ij}} = \phi_{s_j} - \phi_{s_i}$ for several different frequencies. The angle $\Delta\phi_{s_{ij}}$ is expected to control the force angle based on (4.24). Figure 7.5a presents the measured force vs. $\Delta\phi_{s_{12}}$ for the given currents and frequencies (rated slip frequency). Similarly, Fig. 7.5b shows the results for sequences 2-3 and 3-4. These results confirm that a constant magnitude force vector can be created at any angle using sequence pairs 1-2, 2-3, and 3-4. Sequence 1 in Fig. 7.5a also creates torque, which is independent of the force angle. Due to the armature reaction, a shift in force angle is observed (red and blue curves in Fig. 7.5a subplot 3), which can be adjusted when implementing a levitation control.

7.3.4 Forces from Non-Adjacent Sequences

The goal of this test is to confirm Section 4.4.1's finding that non-adjacent current sequences $s_j \neq s_i \pm 1$ do not contribute to radial force creation. All non-adjacent sequence combinations are tested (1-3, 1-4, and 2-4). In each combination, each current sequence magnitude is set to 5 Arms and the force is measured with respect to the difference in phase angles $\Delta\phi_{s_{ij}}$.

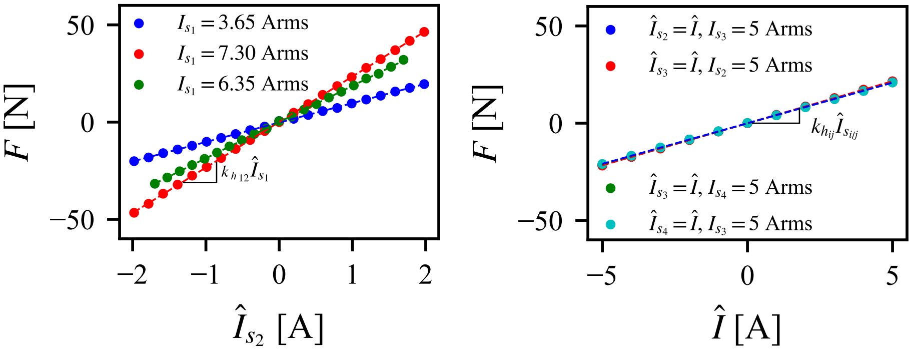

(a) (b)

Figure 7.4: Experiment results for the validation of the proposed model: forces vs. current magnitudes for (a) sequences 1-2 and (b) sequences 2-3 and 3-4

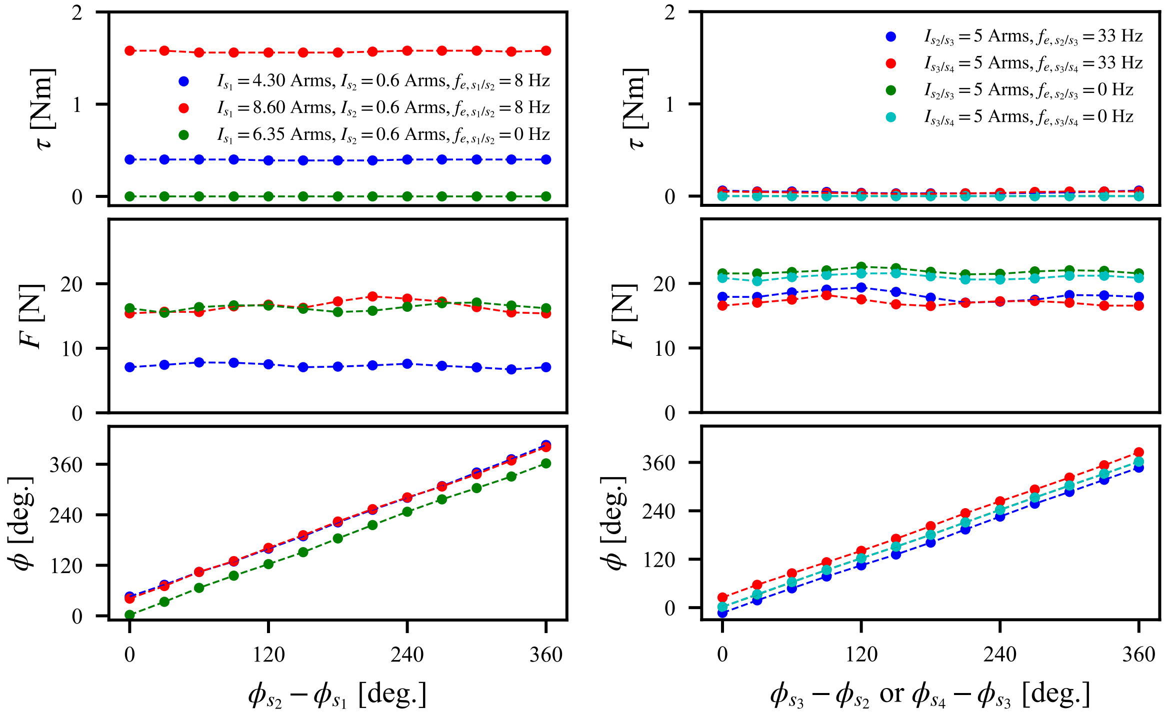

(a) (b)

Figure 7.5: Torque and force measurements vs. phase angle differences when adjacent sequences are excited with different amplitudes and frequencies: (a) sequences 1-2 and (b) sequences 2-3 and 3-4.

Figure 7.6a presents the test results, which confirm that force is not created by non-adjacent sequences.

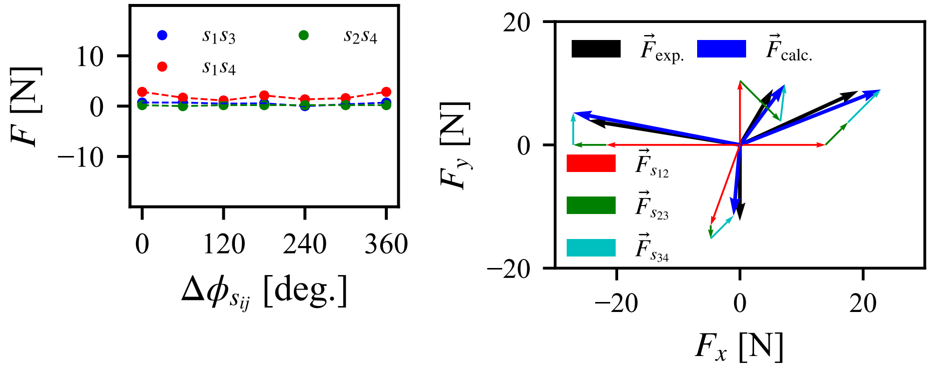

(a) (b)

Figure 7.6: Experiment results for the validation of the proposed model: (a) forces from non-adjacent sequences and (b) comparison between measured and calculated force vectors at four different points.

7.3.5 Forces from Multiple Sequences

This test is conducted to validate that the superposition of multiple force vectors created by multiple current sequences matches (4.29). For each set of currents, the "calculated" force vector is determined by using the $k_{h_{ij}}$ values found in Section 7.3.3 in (7.1). Figure 7.6b shows the test results for four different current sequence combinations. The three components of the calculated force vector in (7.1) are also shown. These results demonstrate the accuracy of the proposed force vector model.

7.4 Equivalent Circuit Parameters and Unstable Stiffness

A set of hardware measurements are conducted to estimate induction motor equivalent circuit parameters and unstable stiffness, which are necessary for the implementation of speed and levitation controllers.

Equivalent circuit parameters for each current sequence are estimated using the voltage and current measurements from the no-load and locked rotor tests in induction motors. During the no-load test, both the rotor and airgap field rotate synchronously at 8 Hz, creating

Sequence order	R_s [mΩ]	R'_r [mΩ]	$L_{\sigma,s}$, $L_{\sigma,r}$ [mH]	L_m [mH]	k_δ at 10 Arms [N/mm]
1	251	107	1.8	3.5	580
2	247	-	-	0.81	72
3	248	-	-	0.49	39
4	246	-	-	0.89	126

Table 7.2: Equivalent Circuit Parameters and Unstable Stiffness Estimated from the Hardware Measurements

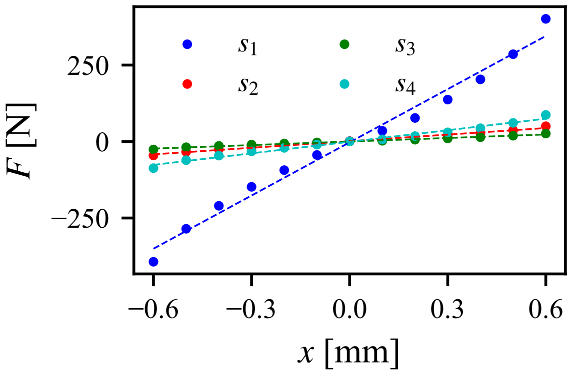

Figure 7.7: Measured force vs. radial position for different sequences.

no torque (zero slip). During the locked-rotor test, the rotor is locked and a current sequence frequency is set to create a field rotating at 8 Hz, creating the rated torque at the rated slip for sequence 1. Using the voltage and current measurements from these tests, equivalent circuit impedances are calculated and used to estimate equivalent circuit parameters, summarized in Table 7.2. Note that, for sequences 2 and 4, the equivalent circuit simplifies to a series RL circuit as no torque can be created with these sequences. A similar simplification is assumed for sequence 3 due to its negligible torque production.

Figure 7.7 shows the measured force when the rotor is radially displaced. The test is conducted for each sequence with an amplitude equal to the rated current of 10 Arms. The results show a higher pull force for sequence 1 compared to the other sequences. This is because harmonic 1 in the prototype has the highest magnetic field strength per unit of current. Through curve fitting, the unstable stiffness is estimated and presented in Table 7.2.

7.5 Increase in Force Capacity

This section presents the test results that validate force enhancement results of Chapters 4.7 and 5. Results of force enhancement within a maximum airgap field limit and transient force response under variable magnetization are presented. Furthermore, force enhancement under iron saturation is demonstrated using FEA.

7.5.1 Force Capacity within a Maximum Airgap Field Limit

This test demonstrates force enhancement when the airgap field must not exceed $B_{\max}$ similar to the analysis in Section 4.7. Sequences 1 and 2 are excited to create force. Force enhancement is achieved by additionally exciting sequence 4 current for field weakening and further increasing sequence 2 current until reaching $B_{\max}$. The results are provided in Fig. 7.8a. First, only sequences 1 and 2 are excited to create a force at $\phi = 0$ deg. (see Fig. 7.8a at $\hat{I}_{s_4} = 0$), and the peak airgap field is measured and set as $B_{\max}$. This is followed by injecting sequence 4 current ($\hat{I}_{s_4} = 4$ or 8 A) for field weakening based on the discussion in Chapter 5.4.4. Finally, sequence 2 current is further increased for force enhancement until reaching $B_{\max}$, as summarized in Fig. 7.8a. At $B_{\max} = 0.83$ T, the force can be enhanced by approximately 12% and 38% with $\hat{I}_{s_4} = 4$ A and 8 A, respectively.

The fields in front of the stator teeth are measured to ensure that the airgap field is below $B_{\max}$, as shown in Fig. 7.8b for $B_{\max} = 0.83$ T. The dashed lines represent the magnetic fields estimated analytically using (4.12). This plot confirms that the peak airgap field is below $B_{\max}$ before (red curve) and after (green and cyan curves) force enhancement.

7.5.2 Force Capacity at Iron Saturation

An FEA study is conducted to demonstrate force enhancement under iron saturation. Due to the limit in current sensor measurements, this test is conducted in FEA. The results are shown in Fig. 7.8c. First, the force capability from only sequences 1-2 is found. Sequence 1 is held at $I_{d,\text{rated}}$ and the force is extracted for various $\hat{I}_{s_2}$ values. The result (blue curve) shows

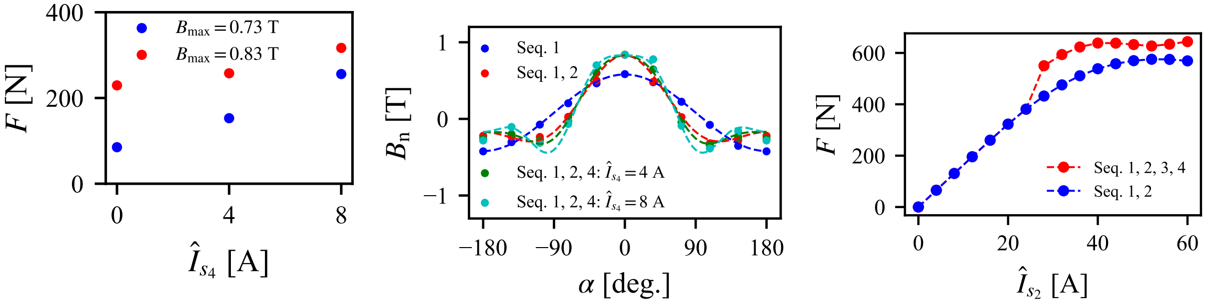

(a) (b) (c)

Figure 7.8: Experiment results for the validation of force enhancement: (a) experiment results of force enhancement using sequence 4 for field weakening, (b) measured airgap magnetic fields corresponding to the $B_{\max} = 0.83$ T case of Fig. 7.8a, and (c) FEA results of force enhancement under iron saturation.

that increasing $\hat{I}_{s_2} \geq 28$ A decreases force creation capability as the iron starts saturating at $B_{\max} \approx 1.03$ T. Second, sequences 3 and 4 are additionally injected to enhance the force for $\hat{I}_{s_2} \geq 28$ A. These currents are calculated following the steps from Section 4.7 with $B_{\max} \approx 1.03$ T and loaded into the FEA model. The result (red curve) demonstrates the potential for force enhancement using sequences 3 and 4. At $\hat{I}_{s_2} \approx 28$ A, the highest force enhancement by 27% is observed.

7.6 Enhanced Force Creation Using Sequences 1, 3, and 4

This section presents the results from a set of hardware measurements that validate an enhanced force creation using sequence combinations 1-3-4 under varying magnetizing fields and torque (Section 7.6.1) and rotor speeds (Section 7.6.2). The results validate that using sequences 3 and 4 for force creation can fully decouple force creation from different magnetizing fields and torque conditions.

7.6.1 Force Performance under Varying Magnetizing Currents and Torque

This test aims to validate force creation independent of the magnetization state of the motor. Figure 7.9a shows the torque and force measurements at various sequence 1 excitation frequencies f_{e,s_1}, which affects the magnetizing field and torque acting on the rotor. The two cases are compared when the force is created with sequences 1-2 and 3-4. These results show that the force magnitude from sequences 3-4 remains relatively constant across f_{e,s_1}, while the force from sequences 1-2, with the armature reaction affecting the force angle. Additionally, Fig. 7.9a presents another set of measurements, varying sequence 1 amplitude $\hat{I}_{s_1}$. Similar observations are made that the forces from sequences 3-4 remain unaffected by changes in the magnetizing field and torque.

Further confirmation of independent force creation under dynamic magnetization variations is provided in Fig.7.10. This figure compares two cases: force creation by sequences 1-2 (column 1) and 3-4 (column 2). In both cases, a series of step commands is applied to the magnetizing current i_d to observe its impact on the forces. As shown in Fig. 7.10 (column 1), the change in the magnetizing current directly impacts the force creation because i_d in this motor is created by sequence 1. The results for case 2 (column 2) show that the force created from sequences 3-4 remains approximately constant regardless of the changes in i_d. This is expected based on (7.1) because sequence 2 is zero and i_d does not affect the force. These findings demonstrate the potential to enhance bearingless motor performance under variable magnetization conditions.

7.6.2 Force Performance under Different Rotor Speeds

The objective of this test is to confirm that sequences 3-4 can create suspension forces for different rotor speeds. The rotor is rotated using a mill spindle (see Fig. 7.1a), current sequences 1, 3 and 4 are excited, and the resulting torque and forces are measured at every

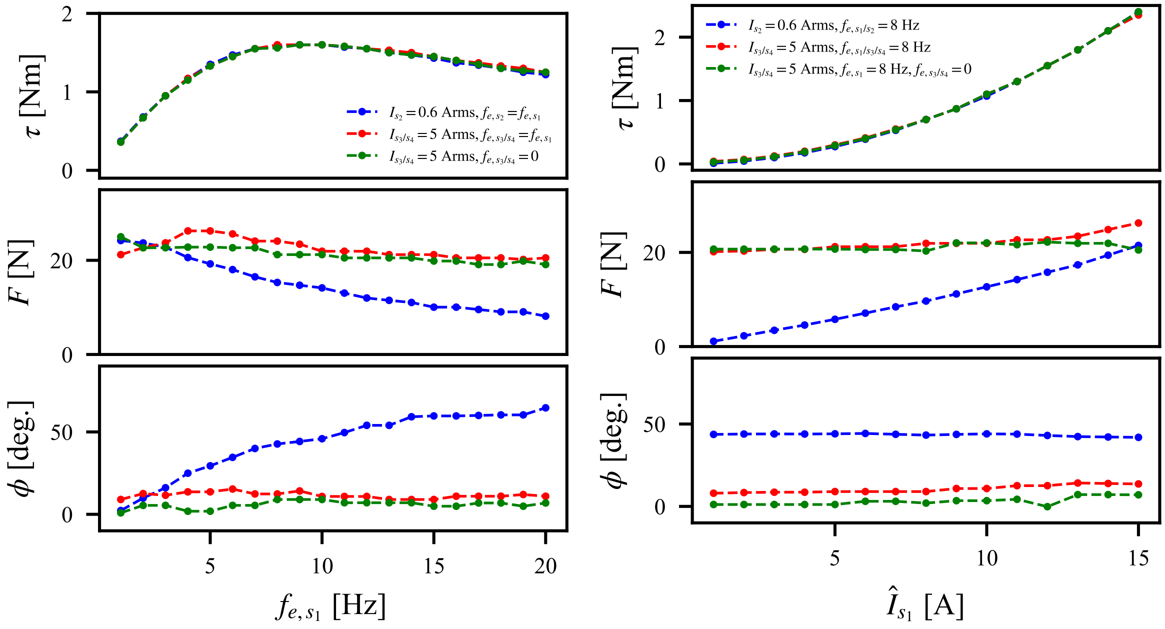

(a) (b)

Figure 7.9: Torque and force measurements under varying magnetizing currents.

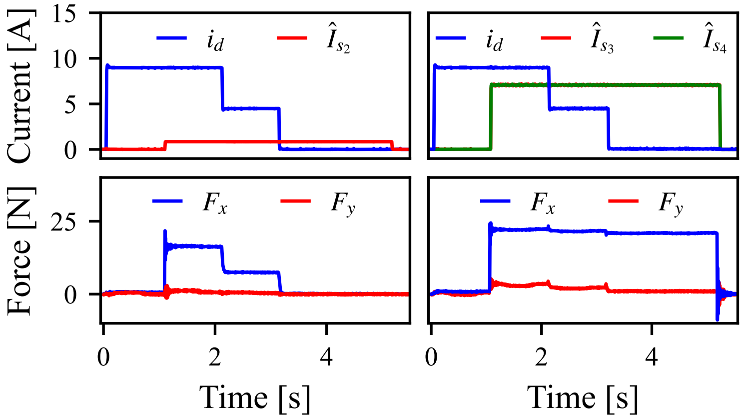

Figure 7.10: Measured transient force response using sequences 1-2 and 3-4 under different i_d magnetizing currents.

speed. Sequence 1 is excited to create the rated torque with $f_{e,s_1} = f_{\text{rotor}} + 8$ [Hz]. Figure 7.11 presents the measurement results, which confirm constant torque and force creation using the combination of sequences 1-3-4. This is shown for two cases when sequence 3-4 frequencies are set to $3f_{\text{rotor}}$ and f_{e,s_1}. By aligning current sequence 3 with $f_{e,s_3} = 3f_{\text{rotor}}$, harmonic 3 and the rotor synchronize, inducing no current in the rotor bars (no ohmic losses from sequence 3).

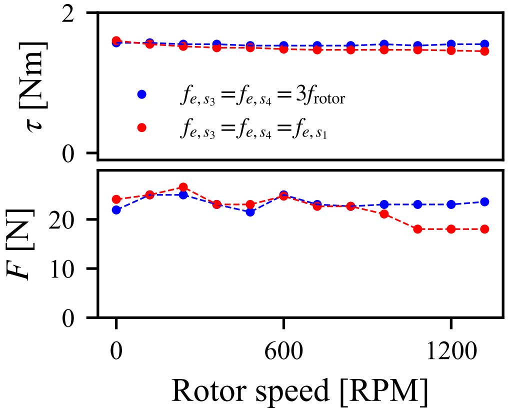

Figure 7.11: Torque and force measurements at different rotor speeds for current sequence combinations 1-3-4.

7.7 Speed Control

Measurement results in this section validate induction motor speed control discussed in Chapter 6.6. The control structure presented in Fig. 6.6 is implemented in the advanced motor drive controller (AMDC) [104]. Position measurements are obtained using the mill's encoder from Fig.7.1a (the mill spindle is set to freely rotate). Torque current i_q and slip frequency are estimated using the equivalent circuit parameters from Table 7.2 for sequence 1. Figure 7.12 displays the actual and measured speed results for various cases. Magnetizing i_d and torque i_q currents are also provided for a rotor speed of 1200 RPM. These results confirm that the indirect field-oriented control technique with torque and slip estimation used in three-phase induction machines can be similarly applied to 10-phase induction machines, enabling speed control.

7.8 Conclusion

This chapter provides experimental validation for the theories and strategies developed throughout this dissertation, utilizing a 10-phase bearingless induction machine selected from the design study and constructed in the lab. The hardware measurements validate the winding design approach and the proposed exact model. The experimental results further

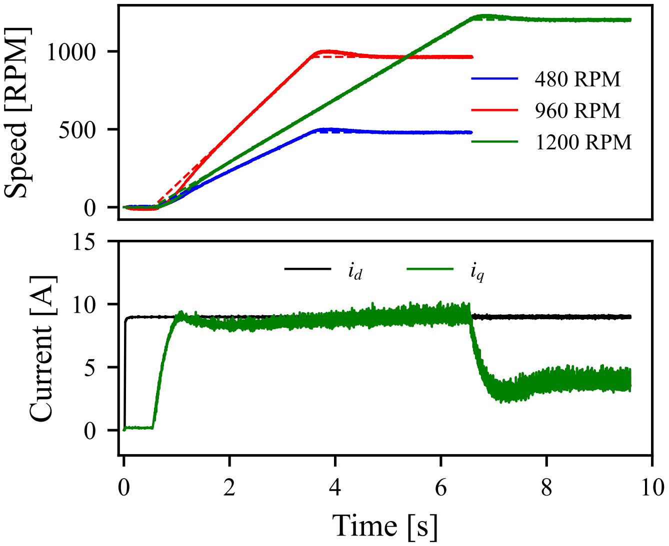

Figure 7.12: Speed control validation for different speed commands. Measured currents are shown for 1200 RPM.

confirm the earlier findings on force capacity increase, with a 38% improvement under a maximum airgap field limit of 0.83 T. Additionally, the tests confirm the enhanced force performance achieved with sequences 3 and 4, demonstrating the force creation independent of the variations in the magnetizing fields and torque. Moreover, the validation of speed control incorporating slip and torque current calculations is presented.

Chapter 8

Conclusions and Future Work

This dissertation introduced and developed new winding design theory, an exact electric machine model considering magnetic shear and normal pressure on the shaft of an electric machine, a framework for investigating potential benefits of controlling multiple airgap harmonic fields, and the design and experimental validation of a 10-phase bearingless induction motor with enhanced force performance. These developments enable creating higher performance bearingless machines for significant power applications than are currently found in the literature. This chapter presents the conclusions and future work.

8.1 Conclusions

This section presents a summary of the conclusions for each chapter.

8.1.1 Introduction and State-of-the-Art

This chapter reviewed state-of-the-art on bearingless machines, identified research opportunities, and presented research contributions of this work. This leads to the following conclusions:

1. Bearingless machine design space is more constrained than conventional machine de-

sign space. Relaxing force vector error constraints can significantly improve motor performance (torque increase by approximately 30% or more, according to [3]).

2. Development of combined winding designs and improved precise force vector regulation techniques have the potential to yield high performance bearingless machines.

3. Redefining an electric machine model to encompass both force and torque creation is necessary for studying the system physics, investigating potential performance improvements, and developing force/torque regulation techniques and bearingless machine design studies.

8.1.2 Comparison of Combined Winding Strategies

This chapter made a comprehensive comparison between two popular combined winding topologies, multiphase and DPNV combined windings, and identified operating conditions when each topology is more advantageous. The following conclusions can be drawn:

4. From the machine perspective, both multiphase and DPNV windings are the same winding type and result in the same winding layout and stator slot currents. However, their power electronics and control implementations are different.

5. The multiphase winding drive is most advantageously used in bearingless motor designs that require substantially more torque current than suspension current, while the parallel DPNV winding drive is most advantageous in motors with high force requirements or applications with limited DC bus voltage available.

8.1.3 Analysis and Design of Multiphase Combined Windings

This chapter proposed and developed multiphase combined winding design technique for bearingless machines. These windings can be used to create the specified airgap field harmonics necessary for independent torque and suspension force generation. This resulted in the following conclusions:

6. The classical stator winding star of slots can be extended to study and aid in the design of multiphase combined windings by considering both the motor and suspension field spatial harmonics.

7. The proposed rules determine which sets of slots, poles, and phases can be used to obtain a symmetric winding capable of producing torque and suspension pole pair fields independently.

8. The proposed winding design technique can be used by motor designers to rapidly design multiphase combined windings for various slot-pole combination motors, including popular winding designs such as concentrated and fractional-slot windings.

9. Reducing the drive connections to three or four allows for the implementation of feasible asymmetric winding designs as a cost-saving measure. However, these designs have higher torque and force ripple compared to the designs with symmetric windings.

8.1.4 Exact Torque and Force Vector Modeling Framework for Bearingless Electric Machines

This chapter proposed and developed a new modeling approach that describes force and torque creation on an electric machine incorporating multiple airgap magnetic field harmonic interactions. The proposed model is then used to investigate the potential advantages of controlling multiple harmonics for performance improvement. The following can be concluded:

10. The proposed model is applicable to all motor types, is analytic-based, and captures the underlying physics of the machine accurately.

11. Suspension forces can be created by exciting two adjacent current sequences in machines with any number of phases or by exciting a single highest sequence in machines

with an odd number of phases.

12. Applying the Generalized Clarke Transform in the modeling of torque and force facilitates the integration of any number of phases and spatial harmonics within the airgap magnetic field. This is expressed through a set of space vector matrix equations of order 2.

13. Previous attempts at developing the exact models for magnetic bearings and bearingless motors can be viewed as special cases of the generalized model developed in this chapter.

14. All three-phase combined windings and some three-phase separated windings have quadratic force vector components, which have been neglected in previous literature, and can result in force vector error if not modeled properly when calculating phase currents.

15. Solving for the currents using the proposed exact model and subsequently exciting motor windings with these currents can eliminate force ripple (errors in force magnitude and angle).

16. Increasing the number of phases/controllable airgap harmonic fields can increase force rating, which is useful when a bearingless machine operates close to iron saturation or requires large amount of force.

8.1.5 Analysis of Force Capacity in Magnetic Bearings and Bearingless Motors from the Perspective of Airgap Space Harmonic Fields

This chapter provided an in-depth analysis of force capacity in AMBs and bearingless motors from the perspective of airgap harmonic fields. The analysis uses the model developed in Chapter 4. The following conclusions can be drawn:

17. The key factors affecting the force capacity are the peak allowable airgap field and constraints on the distribution of the harmonic fields.
18. For the same number of phases, AMBs have higher force capacity than bearingless machines because 1) AMBs inherently use more harmonics by individually controlling pole currents and 2) AMBs have more degrees of freedom to control airgap harmonic fields as there is no constant magnetization requirement and no dependence on the rotor angle.
19. The optimal range of the magnetizing field magnitude to have the maximum torque and force capability in bearingless machines is between 50% (maximum force) and 70% (maximum torque) of the peak airgap field.
20. Bearingless machines can achieve the same force capacity as AMBs by controlling at least one additional harmonic compared to AMBs. When the maximum airgap field limit is 1.5 T, achieving force capacities of over 50 N/cm^2 requires three harmonics for AMBs and four harmonics for bearingless motors (8 vs. 10 controllable currents). This additional harmonic facilitates field weakening and contributes to the increase in force capacity in bearingless machines.
21. A potential increase in force capacity by over 40% can be achieved in bearingless machines when controlling four airgap harmonics (10 phases) as opposed to the typical approach of controlling only two harmonics (six phases).
22. Controlling more than four airgap harmonic fields in bearingless machines requires more than 10 phases and results in diminishing returns on force capacity increase due to increased winding and drive complexity.

8.1.6 Design and Control of a 10-Phase Bearingless Induction Machine

This chapter developed a design study framework for a 10-phase bearingless induction motor. Based on the findings from Chapters 4 and 5, this motor can independently control four airgap harmonic fields to enhance its performance. A design is selected for prototyping, and control model and simulation results are presented. The conclusions are listed below:

23. The design of bearingless machines with multiple controllable airgap harmonic fields serves to mitigate the recognized limitations of bearingless motors and enable a broader range of design possibilities.

24. Ten-phase bearingless machine designs can achieve a considerably high force capacity exceeding 15.3 N/cm^2, in contrast to 9.9 N/cm^2 reported in the literature (for an IPM motor). Further improvements can be achieved with higher airgap field limits.

25. In addition to an improvement in force capacity, 10-phase motors with torque densities of over 22 kNm/m^3 and efficiencies close to 97% can be designed. This exceeds the IE4 efficiency standard unlike most published results.

26. Controlling current sequence combinations 1, 3, and 4 enables an enhanced force performance in bearingless motors, which fully decouples force creation from both the magnetizing field and torque.

27. An indirect field-oriented control technique with torque and slip estimation used in three-phase induction machines can be similarly implemented in 10-phase induction machines, realizing speed control.

8.1.7 Experimental Validation

This chapter presented experimental validation of the theories and bearingless motor performance improvement strategies developed in this dissertation. A 10-phase bearingless induction machine was selected from the design study results of Chapter 6. The following conclusions are drawn:

28. Results of hardware measurements from the 10-phase bearingless induction motor validate the winding design approach developed in Chapter 3 and the exact model developed in Chapter 4, showing that controlling multiple airgap harmonic fields can be used to control force vector magnitude and angle independent of torque.

29. Results of hardware measurements and FEA simulations validate an increase in force capacity from Chapters 4-5. With the maximum airgap field limit of 0.83 T, an increase in force capacity up to approximately 38% can be achieved, which confirms conclusion 21.

30. Test results validate enhanced force performance achieved with sequences 3 and 4. Altering sequence 1 current magnitude and slip frequency, which, in turn, changes the magnetizing field, did not impact the generated force from sequences 3 and 4.

31. Test results validate speed control that incorporates slip and torque current calculations using estimated induction motor equivalent circuit parameters for sequence 1.

8.2 Future Work

The potential future works are now suggested for continuing this work:

1. Investigation of motor performance under parameter uncertainties. Exploring motor performance under parameter uncertainties is crucial for robust designs. It is suggested to investigate the influence of variations in the excitation frequency and rotor speed on equivalent circuit parameters and torque and force creation.

2. Cost optimization of a 10-phase motor drive and sensors. Achieving cost-effective solutions is important for widespread adoption of bearingless motors. Future work can

focus on more cost-effective power electronics and sensor configurations. Efforts can be made to investigate the effectiveness of using 10 phases for self-sensing.

3. Investigation of performance improvement using multiple harmonics in other motor topologies such as interior permanent magnet (IPM) and synchronous reluctance motors. IPM motors have a relatively small airgap length compared to other motors, which helps increase the strength/amplitude of magnetic field harmonics. Synchronous reluctance motors can have multiple harmonics created due to saliency. More investigations can be made to identify the benefits of actuating multiple harmonics in these machines.

Appendix A

Generalized Clarke Transformation

This work makes extensive use of the generalized Clarke transformation to analyze the machine phase currents and establish requirements for independently controlling torque and force. The generalized Clarke transformation was first introduced by Fortescue in 1918 [105] and is more recently described in [60, 85]. The transformation and key properties used by this dissertation are now summarized.

For a vector $\boldsymbol{x_1}(\theta) = [x_{1,1}(\theta)\ x_{1,2}(\theta)\ ...\ x_{1,m}(\theta)]^T$ consisting of m sinusoidal terms, the generalized Clarke transform calculates a space vector $\boldsymbol{x}$ of order k as

$$\vec{x}_k = c\sum_{i=1}^{m} x_{1,i}(\theta)a^{k(i-1)} \tag{A.1}$$

where $a = e^{j2\pi/m}$ and c is a transformation coefficient.

Now, consider $\boldsymbol{x}(\theta)$ to be the sum of several sets of m-phase balanced sinusoidal terms $\boldsymbol{x}(\theta) = \boldsymbol{x_1}(\theta) + \boldsymbol{x_2}(\theta) + ...$, each with a distinct phase separation of $\Delta\alpha_j$ as (A.2).

$$\boldsymbol{x_j}(\theta) = \begin{bmatrix} \cos\theta \\ \cos(\theta - \Delta\alpha_j) \\ \cos(\theta - 2\Delta\alpha_j) \\ ... \\ \cos(\theta - [m-1]\Delta\alpha_j) \end{bmatrix} \tag{A.2}$$

$$\Delta\alpha_j = \frac{2\pi}{m}j \tag{A.3}$$

Here, j is restricted to be an integer value based on the number of phases m. For even m, j can be $0, \pm1, ..., \pm m/2$, for an odd m, j can be $0, \pm1, ..., \pm(m-1)/2$.

When (A.1) is used to calculate space vectors for $\boldsymbol{x}(\theta)$, the following properties can be shown:

1) The only $\boldsymbol{x_j}(\theta)$ set that will contribute to a space vector of order k is the set with $|j| = k$. Therefore, an independent space vector exists for each $\boldsymbol{x_j}(\theta)$ component.

2) Space vectors of order $k = 0$ and $k = m/2$ will be one dimensional (zero sequence); all other space vectors will have two degrees of freedom (real and imaginary).

3) Increasing the number of phases m increases the number of independent space vectors of $\boldsymbol{x}(\theta)$.

4) A set $\boldsymbol{x_k}(\theta)$ with $\Delta\alpha_k > 0$ is considered to be positive sequence and produces a constant magnitude space vector $\vec{x}_k$ that rotates counterclockwise at speed $\omega = \frac{\mathrm{d}\theta}{\mathrm{d}t}$; negative sequence has $\Delta\alpha_k < 0$ and $\vec{x}_k$ rotating clockwise.

Appendix B

Dimensionless Force Vector Model

This dissertation (Chapters 4 and 5) makes use of the p.u. force vector model to find the force capacity in bearingless machines and AMBs. The model is expressed in terms of the p.u. radial field quantities, which are normalized by a maximum allowable airgap field $B_{\max}$. By setting the base value $F_{\mathrm{b}} = \frac{V_r}{2\mu_0 r} B_{\max}^2$ in (4.19), it can be shown that (4.29)-(4.30) can be expressed in a p.u. form as

$$\vec{F}' = \sum_{i=1}^{n_f} C_{h_{ij}} \hat{B}'_{\mathrm{n},h_i} \hat{B}'_{\mathrm{n},h_j} e^{j(\phi_{s_j} - \phi_{s_i})} \tag{B.1}$$

where $h_j = h_i + 1$, n_f is the total number of force vectors, and $\hat{B}'_{\mathrm{n},h_{i/j}}$ is a p.u. radial field amplitude.

The base values for currents, ohmic losses, and torque that are used in Chapter 4.7 are given by

$$I_{\mathrm{b}} = \frac{\pi \delta_{\mathrm{eff}}}{\mu_0 m z_Q z_c B_{\max}},\ P_{\mathrm{b}} = I_{\mathrm{b}}^2 R_{\mathrm{ph}} m,\ \tau_{\mathrm{b}} = \frac{V_r p \delta_{\mathrm{eff}}}{\mu_0 r} B_{\max}^2 \tag{B.2}$$

Note that these base values are same for all designs compared in Section 4.7, which allows comparing them in p.u. I_{b} is set using (4.13), resulting in the p.u. relationship between current and field quantities as $\hat{I}'_s = h\hat{B}'_{\mathrm{n},h}/\hat{k}_{\mathrm{w},h}$. P_{b} is set based on its relationship to currents; τ_{b} is set using (4.21), resulting in the p.u. equation for torque $\tau' = \hat{B}'_{\delta}\hat{B}'_{\mathrm{n,w},p}$. Note that, if machines with various pole pairs are being compared, the torque base value τ_{b} in (B.2) needs to be adjusted not to have p, resulting in the p.u. torque equation of $\tau' = p\hat{B}'_{\delta}\hat{B}'_{\mathrm{n,w},p}$.

Appendix C

Motor Assembly

This appendix presents a 3D model of the motor assembly constructed and used for experimental validation in Chapter 7. Figure C.1 presents the primary components of the assembly. Figure C.2 provides a cross-sectional drawing of the stator. Further information regarding the rotor structure is available in [7].

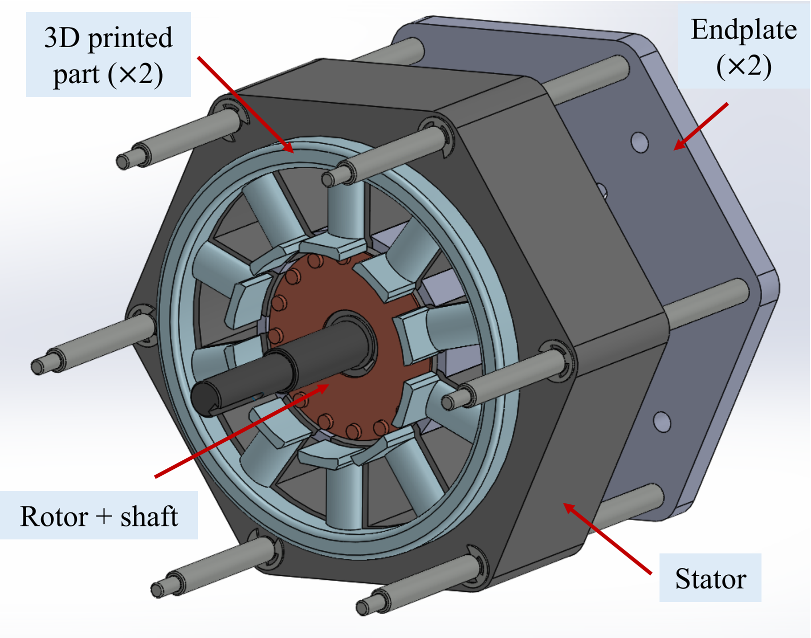

Figure C.1: 3D model of the motor assembly.

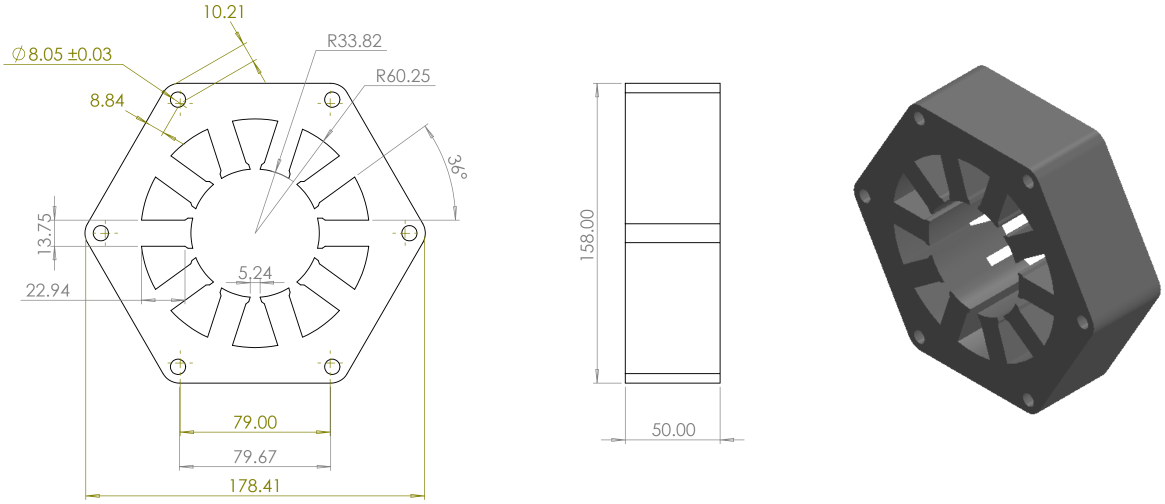

Figure C.2: Dimensions of the stator lamination in mm.

Bibliography

[1] W. Gruber, R. Remplbauer, and E. Göbl, "Design of a novel bearingless permanent magnet vernier slice motor with external rotor," in *2017 IEEE International Electric Machines and Drives Conference (IEMDC)*, 2017, pp. 1–6.

[2] T. Stallinger, E. Göbl, R. Remplbauer, and W. Gruber, "Performance evaluation of a novel bearingless pm vernier motor," in *2017 IEEE 12th International Conference on Power Electronics and Drive Systems (PEDS)*. IEEE, 2017, pp. 408–413.

[3] J. Chen, J. Zhu, and E. L. Severson, "Review of bearingless motor technology for significant power applications," *IEEE Transactions on Industry Applications*, vol. 56, no. 2, pp. 1377–1388, 2020.

[4] A. Khamitov, W. Gruber, G. Bramerdorfer, and E. L. Severson, "Comparison of combined winding strategies for radial non-salient bearingless machines," *IEEE Transactions on Industry Applications*, 2021.

[5] N. R. Hemenway and E. L. Severson, "Three-pole magnetic bearing design and actuation," *IEEE Transactions on Industry Applications*, vol. 56, no. 6, pp. 6348–6359, 2020.

[6] N. Turk, N. Bulić, and W. Gruber, "Nonlinear control of a bearingless flux-switching slice motor with combined winding system," *IEEE/ASME Transactions on Mechatronics*, vol. 25, no. 1, pp. 152–163, 2020.

[7] J. Chen, M. W. Johnson, A. Farhan, Z. Wang, Y. Fujii, and E. L. Severson, "Reduced axial length pole-specific rotor for bearingless induction machines," *IEEE Transactions on Energy Conversion*, 2022.

[8] F. J. T. E. Ferreira, G. Baoming, and A. T. de Almeida, "Reliability and operation of high-efficiency induction motors," *IEEE Transactions on Industry Applications*, vol. 52, no. 6, pp. 4628–4637, 2016.

[9] M. Key, "The high cost of ignoring chiller oil buildup," *RSES Journal*, pp. 1–4, 2002.

[10] D. Eaton, J. Rama, and S. Singhal, "Magnetic bearing applications & economics," in *2010 Record of Conference Papers Industry Applications Society 57th Annual Petroleum and Chemical Industry Conference (PCIC)*. IEEE, 2010, pp. 1–9.

[11] J. Pyrhonen, T. Jokinen, and V. Hrabovcova, *Design of rotating electrical machines.* John Wiley & Sons, 2013.

[12] H. Mitterhofer, W. Gruber, and W. Amrhein, “On the high speed capacity of bearingless drives,” *IEEE Transactions on Industrial Electronics*, vol. 61, no. 6, pp. 3119–3126, June 2014.

[13] T. Reichert, T. Nussbaumer, and J. W. Kolar, “Bearingless 300-w pmsm for bioreactor mixing,” *IEEE Transactions on Industrial Electronics*, vol. 59, no. 3, pp. 1376–1388, 2012.

[14] B. Warberger, T. Reichert, T. Nussbaumer, and J. W. Kolar, “Design considerations of a bearingless motor for high-purity mixing applications,” in *SPEEDAM 2010*, 2010, pp. 1454–1459.

[15] P. Puentener, M. Schuck, D. Steinert, T. Nussbaumer, and J. W. Kolar, “A 150 000-r/min bearingless slice motor,” *IEEE/ASME Transactions on Mechatronics*, vol. 23, no. 6, pp. 2963–2967, Dec 2018.

[16] M. T. Bartholet, T. Nussbaumer, S. Silber, and J. W. Kolar, “Comparative evaluation of polyphase bearingless slice motors for fluid-handling applications,” *IEEE Transactions on Industry Applications*, vol. 45, no. 5, pp. 1821–1830, 2009.

[17] W. Gruber, *Bearingless Slice Motor Systems Without Permanent Magnetic Rotors, Schriftenreihe Advances in Mechatronics, Bd. 45 - E-Book.* Trauner Verlag + Buchservice GmbH, 2019. [Online]. Available: https://books.google.com/books?id=Y1nUzQEACAAJ

[18] W. Gruber, W. Briewasser, M. Rothböck, and R. Schöb, “Bearingless slice motor concepts without permanent magnets in the rotor,” in *2013 IEEE International Conference on Industrial Technology (ICIT).* IEEE, 2013, pp. 259–265.

[19] A. Chiba, T. Fukao, O. Ichikawa, M. Oshima, M. Takemoto, and D. Dorrell, *Magnetic Bearings and Bearingless Drives.* Newnes, 2005.

[20] A. Chiba, T. Deido, T. Fukao, and M. Rahman, “An analysis of bearingless ac motors,” *IEEE Transactions on Energy Conversion*, vol. 9, no. 1, pp. 61–68, Mar 1994.

[21] B. Liu, “Survey of bearingless motor technologies and applications,” in *2015 IEEE International Conference on Mechatronics and Automation (ICMA).* IEEE, 2015, pp. 1983–1988.

[22] G. Munteanu, A. Binder, and T. Schneider, “Loss measurement of a 40 kw high-speed bearingless pm synchronous motor,” in *2011 IEEE Energy Conversion Congress and Exposition*, Sept 2011, pp. 722–729.

[23] Q. Li, P. Boesch, M. Haefliger, J. W. Kolar, and D. Xu, “Basic characteristics of a 4kw permanent-magnet type bearingless slice motor for centrifugal pump system,” in *2008 international conference on electrical machines and systems.* IEEE, 2008, pp. 3037–3042.

[24] M. Ooshima, A. Chiba, A. Rahman, and T. Fukao, "An improved control method of buried-type ipm bearingless motors considering magnetic saturation and magnetic pull variation," *IEEE Transactions on Energy Conversion*, vol. 19, no. 3, pp. 569–575, 2004.

[25] Y. Fu, M. Takemoto, S. Ogasawara, and K. Orikawa, "Investigation of a high speed and high power density bearingless motor with neodymium bonded magnet," in *2017 IEEE International Electric Machines and Drives Conference (IEMDC).* IEEE, 2017, pp. 1–8.

[26] T. Baumgartner, R. M. Burkart, and J. W. Kolar, "Analysis and design of a 300-w 500 000-r/min slotless self-bearing permanent-magnet motor," *IEEE Transactions on Industrial Electronics*, vol. 61, no. 8, pp. 4326–4336, 2013.

[27] T. Hiromi, T. Katou, A. Chiba, M. A. Rahman, and T. Fukao, "A novel magnetic suspension-force compensation in bearingless induction-motor drive with squirrel-cage rotor," *IEEE Transactions on Industry Applications*, vol. 43, no. 1, pp. 66–76, 2007.

[28] A. Sinervo and A. Arkkio, "Rotor radial position control and its effect on the total efficiency of a bearingless induction motor with a cage rotor," *IEEE Transactions on Magnetics*, vol. 50, no. 4, pp. 1–9, 2013.

[29] J. Chen, Y. Fujii, M. W. Johnson, A. Farhan, and E. L. Severson, "Optimal design of the bearingless induction motor," *IEEE Transactions on Industry Applications*, vol. 57, no. 2, pp. 1375–1388, 2020.

[30] M. Johnson, K. Hanson, and E. L. Severson, "Normalized analytical model of stresses in a surface mounted permanent magnet rotor," in *2021 IEEE Energy Conversion Congress and Exposition (ECCE).* IEEE, 2021, pp. 3928–3935.

[31] E. H. Maslen and G. Schweitzer, *Magnetic bearings: theory, design, and application to rotating machinery.* Springer, 2009.

[32] A. Chiba, T. Fukao, O. Ichikawa, M. Oshima, M. Takemoto, and D. G. Dorrell, *Magnetic bearings and bearingless drives.* Elsevier, 2005.

[33] R. P. Jastrzebski, A. Putkonen, E. Kurvinen, and O. Pyrhönen, "Design and modeling of 2 mw amb rotor with three radial bearing-sensor planes," *IEEE Transactions on Industry Applications*, vol. 57, no. 6, pp. 6892–6902, 2021.

[34] S. E. Mushi, Z. Lin, and P. E. Allaire, "Design, construction, and modeling of a flexible rotor active magnetic bearing test rig," *IEEE/ASME transactions on mechatronics*, vol. 17, no. 6, pp. 1170–1182, 2011.

[35] E. E. Swanson, E. H. Maslen, G. Li, C. H. Cloud *et al.*, "Rotordynamic design audits of amb supported machinery," in *Proceedings of the 37th Turbomachinery Symposium.* Texas A&M University. Turbomachinery Laboratories, 2008.

[36] Z. Liu, A. Chiba, Y. Irino, and Y. Nakazawa, “Optimum pole number combination of a buried permanent magnet bearingless motor and test results at an output of 60 kw with a speed of 37000 r/min,” *IEEE Open Journal of Industry Applications*, vol. 1, pp. 33–41, 2020.

[37] D. Dietz and A. Binder, “Comparison between a bearingless pm motor with separated and combined winding for torque and lateral force generation,” in *2019 21st European Conference on Power Electronics and Applications (EPE’19 ECCE Europe)*. IEEE, 2019, pp. P–1.

[38] R. P. Jastrzebski, P. Jaatinen, O. Pyrhönen, and A. Chiba, “Current injection solutions for active suspension in bearingless motors,” in *2017 19th European Conference on Power Electronics and Applications (EPE’17 ECCE Europe)*. IEEE, 2017, pp. P–1.

[39] S. M. Mirić, R. V. Giuffrida, D. Bortis, and J. W. Kolar, “Enhanced complex space vector modeling and control system design of multiphase magnetically levitated rotary–linear machines,” *IEEE Journal of Emerging and Selected Topics in Power Electronics*, vol. 8, no. 2, pp. 1833–1849, 2020.

[40] A. Chiba, K. Sotome, Y. Iiyama, and M. A. Rahman, “A novel middle-point-current-injection-type bearingless pm synchronous motor for vibration suppression,” *IEEE Transactions on Industry Applications*, vol. 47, no. 4, pp. 1700–1706, 2011.

[41] M. Sokolov, W. Gruber, S. E. Saarakkala, and M. Hinkkanen, “Modeling of a bearingless synchronous reluctance motor with combined windings,” in *2019 IEEE Energy Conversion Congress and Exposition (ECCE)*, 2019, pp. 7084–7090.

[42] W. Gruber and S. Silber, “Dual field-oriented control of bearingless motors with combined winding system,” in *2018 International Power Electronics Conference (IPEC-Niigata 2018 -ECCE Asia)*, May 2018, pp. 4028–4033.

[43] W. Gruber, T. Nussbaumer, H. Grabner, and W. Amrhein, “Wide air gap and large-scale bearingless segment motor with six stator elements,” *IEEE Transactions on Magnetics*, vol. 46, no. 6, pp. 2438–2441, 2010.

[44] S. Silber and W. Amrhein, “Power optimal current control scheme for bearingless pm motors,” in *Proc. 7th Int. Symp. Magn. Bearings*, 2000, pp. 401–406.

[45] Min Kang, Jin Huang, Hai-bo Jiang, and Jia-qiang Yang, “Principle and simulation of a 5-phase bearingless permanent magnet-type synchronous motor,” in *2008 International Conference on Electrical Machines and Systems*, 2008, pp. 1148–1152.

[46] V. F. Victor, J. de Paiva, A. O. Salazar, and A. L. Maitelli, “Performance analysis of a neural flux observer for a bearingless induction machine with divided windings,” in *2009 Brazilian Power Electronics Conference*, 2009, pp. 498–504.

[47] W. K. S. Khoo, “Bridge configured winding for polyphase self-bearing machines,” *IEEE Transactions on Magnetics*, vol. 41, no. 4, pp. 1289–1295, 2005.

[48] R. Oishi, S. Horima, H. Sugimoto, and A. Chiba, "A novel parallel motor winding structure for bearingless motors," *IEEE Transactions on Magnetics*, vol. 49, no. 5, pp. 2287–2290, 2013.

[49] E. Severson, S. Gandikota, and N. Mohan, "Practical implementation of dual-purpose no-voltage drives for bearingless motors," *IEEE Transactions on Industry Applications*, vol. 52, no. 2, pp. 1509–1518, March 2016.

[50] G. Valente, A. Formentini, L. Papini, P. Zanchetta, and C. Gerada, "Position control study of a bearingless multi-sector permanent magnet machine," in *IECON 2017 - 43rd Annual Conference of the IEEE Industrial Electronics Society*, 2017, pp. 8808–8813.

[51] E. L. Severson, R. Nilssen, T. Undeland, and N. Mohan, "Design of dual purpose no-voltage combined windings for bearingless motors," *IEEE Transactions on Industry Applications*, vol. 53, no. 5, pp. 4368–4379, 2017.

[52] K. Raggl, T. Nussbaumer, and J. W. Kolar, "Comparison of separated and combined winding concepts for bearingless centrifugal pumps," *J. Power Electron*, vol. 9, no. 2, pp. 243–258, 2009.

[53] R. P. Jastrzebski, P. Jaatinen, O. Pyrhönen, and A. Chiba, "Design optimization of permanent magnet bearingless motor using differential evolution," in *2018 IEEE Energy Conversion Congress and Exposition (ECCE)*. IEEE, 2018, pp. 2327–2334.

[54] Y. gu Kang and E. L. Severson, "Optimal design of 50kw concentrated winding bearingless motor," in *2018 IEEE Energy Conversion Congress and Exposition (ECCE)*. IEEE, 2018, pp. 4411–4418.

[55] A. Farhan, M. Johnson, K. Hanson, and E. L. Severson, "Design of an ultra-high speed bearingless motor for significant rated power," in *2020 IEEE Energy Conversion Congress and Exposition (ECCE)*, 2020, pp. 246–253.

[56] T. Schneider, J. Petersen, and A. Binder, "Influence of pole pair combinations on high-speed bearingless permanent magnet motor," 2008.

[57] Y. g. Kang and E. L. Severson, "Optimization framework for a large, high speed bearingless permanent magnet motor," in *Sixteenth International Symposium on Magnetic Bearings*, August 2018, pp. 1–10.

[58] R. P. Jastrzebski, P. Jaatinen, O. Pyrhönen, and A. Chiba, "Design of 6-slot inset pm bearingless motor for high-speed and higher than 100kw applications," in *Electric Machines and Drives Conference (IEMDC), 2017 IEEE International*. IEEE, 2017, pp. 1–6.

[59] Y. Jiang, R. A. Torres, and E. L. Severson, "Current regulation in parallel combined winding bearingless motors," *IEEE Transactions on Industry Applications*, vol. 55, no. 5, pp. 4800–4810, 2019.

[60] G. Grandi, G. Serra, and A. Tani, “General analysis of multi-phase systems based on space vector approach,” in *2006 12th International Power Electronics and Motion Control Conference*. IEEE, 2006, pp. 834–840.

[61] J. Chen, A. Farhan, M. Johnson, and E. L. Severson, “Design of bearingless permanent magnet motors using no voltage combinedwindings,” in *The 10th International Conference on Power Electronics, Machines and Drives (PEMD 2020)*, vol. 2020, 2020, pp. 803–808.

[62] W. Gruber, K. Radman, and R. T. Schöb, “Design of a bearingless flux-switching slice motor,” in *2014 International Power Electronics Conference (IPEC-Hiroshima 2014-ECCE ASIA)*. IEEE, 2014, pp. 1691–1696.

[63] Y. Fu, M. Takemoto, S. Ogasawara, and K. Orikawa, “Investigation of operational characteristics and efficiency enhancement of an ultrahigh-speed bearingless motor at 100 000 r/min,” *IEEE Transactions on Industry Applications*, vol. 56, no. 4, pp. 3571–3583, 2020.

[64] B. Ramadas and E. L. Severson, “Suspension force design guidelines for bearingless permanent magnet machines,” in *2021 IEEE Energy Conversion Congress and Exposition (ECCE)*. IEEE, 2021, pp. 4554–4561.

[65] N. R. Hemenway and E. L. Severson, “Exact force vector regulation of the three-pole magnetic bearing,” *IEEE Transactions on Industry Applications*, 2021.

[66] D. Steinert, T. Nussbaumer, and J. W. Kolar, “Slotless bearingless disk drive for high-speed and high-purity applications,” *IEEE Transactions on Industrial Electronics*, vol. 61, no. 11, pp. 5974–5986, 2014.

[67] S. Silber, W. Amrhein, P. Bosch, R. Schob, and N. Barletta, “Design aspects of bearingless slice motors,” *IEEE/ASME Transactions on Mechatronics*, vol. 10, no. 6, pp. 611–617, Dec 2005.

[68] H. Grabner, W. Amrhein, S. Silber, and W. Gruber, “Nonlinear feedback control of a bearingless brushless dc motor,” *IEEE/ASME Transactions on Mechatronics*, vol. 15, no. 1, pp. 40–47, Feb 2010.

[69] H. Mitterhofer, B. Mrak, and W. Gruber, “Comparison of high speed bearingless drive topologies with combined windings,” in *2014 International Power Electronics Conference (IPEC-Hiroshima 2014 - ECCE ASIA)*, 2014, pp. 1701–1706.

[70] M. Kang, J. Huang, J. Yang, and H. Jiang, “Analysis and experiment of a 6-phase bearingless induction motor,” in *2008 International Conference on Electrical Machines and Systems*, 2008, pp. 990–994.

[71] J. Huang, B. Li, H. Jiang, and M. Kang, “Analysis and control of multiphase permanent-magnet bearingless motor with a single set of half-coiled winding,” *IEEE Transactions on Industrial Electronics*, vol. 61, no. 7, pp. 3137–3145, 2014.

[72] R. L. A. Ribeiro, F. E. F. Castro, A. O. Salazar, and A. L. Maitelli, “A suitable current control strategy for split-phase bearingless three-phase induction machine,” in *2005 IEEE 36th Power Electronics Specialists Conference*, 2005, pp. 701–706.

[73] V. F. Victor, F. O. Quintaes, J. S. B. Lopes, L. d. S. Junior, A. S. Lock, and A. O. Salazar, “Analysis and study of a bearingless ac motor type divided winding, based on a conventional squirrel cage induction motor,” *IEEE Transactions on Magnetics*, vol. 48, no. 11, pp. 3571–3574, 2012.

[74] W. Amrhein, “Bearingless single-phase motor with concentrated full pitch windings in interior rotor design,” *ISMB1998*, 1998.

[75] W. K. S. Khoo, K. Kalita, and S. D. Garvey, “Practical implementation of the bridge configured winding for producing controllable transverse forces in electrical machines,” *IEEE Transactions on Magnetics*, vol. 47, no. 6, pp. 1712–1718, 2011.

[76] F. Ahmed, G. Kumar, M. D. Choudhury, and K. Kalita, “Bridge configured wounded switched reluctance motor,” *Procedia Engineering*, vol. 144, pp. 817–824, 2016.

[77] G. Valente, L. Papini, A. Formentini, C. Gerada, and P. Zanchetta, “Radial force control of multisector permanent-magnet machines for vibration suppression,” *IEEE Transactions on Industrial Electronics*, vol. 65, no. 7, pp. 5395–5405, July 2018.

[78] G. Sala, D. Gerada, C. Gerada, and A. Tani, “Radial force control for triple three-phase sectored spm machines. part i: Machine model,” in *2017 IEEE Workshop on Electrical Machines Design, Control and Diagnosis (WEMDCD)*, 2017, pp. 193–198.

[79] ——, “Radial force control for triple three-phase sectored spm machines. part ii: Open winding fault tolerant control,” in *2017 IEEE Workshop on Electrical Machines Design, Control and Diagnosis (WEMDCD)*, 2017, pp. 275–280.

[80] G. Valente, A. Formentini, L. Papini, C. Gerada, and P. Zanchetta, “Performance improvement of bearingless multisector pmsm with optimal robust position control,” *IEEE Transactions on Power Electronics*, vol. 34, no. 4, pp. 3575–3585, 2019.

[81] P. Kascak, R. Jansen, T. Dever, A. Nagorny, and K. Loparo, “Motoring performance of a conical pole-pair separated bearingless electric machine,” in *IEEE 2011 EnergyTech*, 2011, pp. 1–6.

[82] F. Nishanth, A. Khamitov, and E. L. Severson, “Design of multiphase motor windings for control of multiple airgap fields,” in *2022 IEEE Energy Conversion Congress and Exposition (ECCE)*. IEEE, 2022, pp. 1–8.

[83] W. Gruber, W. Amrhein, and M. Haslmayr, “Bearingless segment motor with five stator elements - design and optimization,” *IEEE Transactions on Industry Applications*, vol. 45, no. 4, pp. 1301–1308, July 2009.

[84] A. Khamitov and E. L. Severson, “Design of multi-phase combined windings for bearingless machines,” *IEEE Transactions on Industry Applications*, vol. 59, no. 3, pp. 3243–3255, 2023.

[85] A. Wilamowski and M. Bogdan, “The industrial electronics handbook power electronics,” *Taylor and Francis Group*, 2011.

[86] E. Severson, S. Gandikota, and N. Mohan, “Practical implementation of dual-purpose no-voltage drives for bearingless motors,” *IEEE Transactions on Industry Applications*, vol. 52, no. 2, pp. 1509–1518, March 2016.

[87] N. Petersen, A. Khamitov, T. Slininger, and E. L. Severson, “Machine design and precision current regulation for the parallel dpnv bearingless motor winding,” *IEEE Transactions on Industry Applications*, 2021.

[88] E. Levi, M. Jones, S. N. Vukosavic, and H. A. Toliyat, “A novel concept of a multiphase, multimotor vector controlled drive system supplied from a single voltage source inverter,” *IEEE transactions on Power Electronics*, vol. 19, no. 2, pp. 320–335, 2004.

[89] E. L. Severson, R. Nilssen, T. Undeland, and N. Mohan, “Design of dual purpose no-voltage combined windings for bearingless motors,” *IEEE Transactions on Industry Applications*, vol. 53, no. 5, pp. 4368–4379, Sept 2017.

[90] S. Rubino, O. Dordevic, E. Armando, R. Bojoi, and E. Levi, “A novel matrix transformation for decoupled control of modular multiphase pmsm drives,” *IEEE Transactions on Power Electronics*, 2020.

[91] E. Levi, R. Bojoi, F. Profumo, H. Toliyat, and S. Williamson, “Multiphase induction motor drives–a technology status review,” *IET Electric Power Applications*, vol. 1, no. 4, pp. 489–516, 2007.

[92] G. Sala, M. Mengoni, G. Rizzoli, L. Zarri, and A. Tani, “Decoupled d–q axes current-sharing control of multi-three-phase induction machines,” *IEEE Transactions on Industrial Electronics*, vol. 67, no. 9, pp. 7124–7134, 2019.

[93] E. Levi, “Advances in converter control and innovative exploitation of additional degrees of freedom for multiphase machines,” *IEEE Transactions on Industrial Electronics*, vol. 63, no. 1, pp. 433–448, 2015.

[94] J. Asama, T. Oi, T. Oiwa, and A. Chiba, “Simple driving method for a 2-dof controlled bearingless motor using one three-phase inverter,” *IEEE Transactions on Industry Applications*, vol. 54, no. 5, pp. 4365–4376, 2018.

[95] J. Chen, Y. Fujii, M. W. Johnson, A. Farhan, and E. L. Severson, “Optimal design of the bearingless induction motor,” *IEEE Transactions on Industry Applications*, vol. 57, no. 2, pp. 1375–1388, 2021.

[96] *AN180KIT for AKM HG-106C-2U Hall Element Y axis, Thin, High Magnetic Field Sensor*, GMW Associates, 2016. [Online]. Available: https://gmw.com/wp-content/uploads/2019/01/AN$_$180KIT-AKM-HG-106C-2U-9$_$27$_$16.pdf

[97] *MCS10, Multicomponent sensor*, HBM, 2017. [Online]. Available: http://spectromas.ro/wp-content/uploads/2017/12/Fisa-tehnica-MCS10.pdf

[98] A. Khamitov and E. L. Severson, "Exact torque and force model of bearingless electric machines," in *2022 IEEE Energy Conversion Congress and Exposition (ECCE)*. IEEE, 2022, pp. 1–8.

[99] G. Sala, G. Valente, A. Formentini, L. Papini, D. Gerada, P. Zanchetta, A. Tani, and C. Gerada, "Space vectors and pseudoinverse matrix methods for the radial force control in bearingless multisector permanent magnet machines," *IEEE Transactions on Industrial Electronics*, vol. 65, no. 9, pp. 6912–6922, Sep. 2018.

[100] F. Nishanth, A. Khamitov, and E. L. Severson, "Design of electric machine windings to independently control multiple airgap harmonics," *IEEE Transactions on Industry Applications*, pp. 1–12, 2023.

[101] T. A. Lipo, *Analysis of synchronous machines*. Crc Press, 2017.

[102] J. Chen and E. L. Severson, "Design and modeling of the bearingless induction motor," in *2019 IEEE International Electric Machines Drives Conference (IEMDC)*, 2019, pp. 343–350.

[103] R. W. De Doncker, D. W. Pulle, and A. Veltman, *Advanced electrical drives: analysis, modeling, control*. Springer Nature, 2020.

[104] N. Petersen and E. Severson, "Amdc: Open-source control and sensing platform for advanced electric motor drives," in *2023 IEEE International Electric Machines and Drives Conference (IEMDC)*, 2023, pp. 1–7.

[105] C. L. Fortescue, "Method of symmetrical co-ordinates applied to the solution of polyphase networks," *Transactions of the American Institute of Electrical Engineers*, vol. 37, no. 2, pp. 1027–1140, 1918.